UNIVERSITY OF LEEDS

Electron Microscopy of Macromolecular Complexes, and their Interactions with Membranes

Rebecca Faith Thompson

Submitted in accordance with the requirements for the degree of Doctor of Philosophy

The University of Leeds

Faculty of Biological Sciences, School of Molecular and Cellular Biology

December 2015

Intellectual property and publication

The candidate confirms that the work submitted is her own, except where work which has formed part of jointly authored publications has been included. The contribution of the candidate and the other authors to this work has been explicitly indicated below. The candidate confirms that appropriate credit has been given within the thesis where reference has been made to the work of others. This copy has been supplied on the understanding that it is copyright material and that no quotation from the thesis may be published without proper acknowledgement.

Components of this thesis contain work from jointly authored publications. Work in Chapter 3 contains data from a jointly authored paper published in 2014. The candidate contributed to the work presented in Goodchild, SC, Sheynis, T, Thompson, RT, Tipping, KW, Xue, WF, Ranson, NA, Beales, PA, Hewitt, EW And Radford, SE (2014) β2-microglobulin amyloid fibril-induced membrane disruption is enhanced by endosomal lipids and acidic pH, PloS ONE. 9;e104492. The candidate contributed by performing cryo-electron microscopy to characterise morphology of liposomes, in addition to contributing to the experimental design and editing of the manuscript. S.C. Goodchild performed and designed the experiments and wrote the original manuscript of the paper, T. Sheynis performed confocal microscopy analyses. N.A. Ranson, P.A. Beales, E.W. Hewitt and S.E. Radford provided help with scientific discussions, data interpretation and manuscript preparation.

Work in Chapter 5 contains data from a jointly authored paper published in 2013. The candidate contributed to the work presented in Kyle C. Dent, Rebecca Thompson, Amy M. Barker, Julian A. Hiscox, John N. Barr, Peter G. Stockley, and Neil A. Ranson (2013) The Asymmetric Structure of an Icosahedral Virus Bound to Its Receptor Suggests a Mechanism for Genome Release. Structure 21, 1225–1234. The candidate performed cryo-EM to examine the role of maturation protein in virus binding and contributed to experimental design and editing of the manuscript. K.C Dent designed, performed and analysed results and contributed to writing and editing of the manuscript. A.M Barker synthesized rMS2. J.A Hiscox, J.N Barr, P.G Stockley, and N.A Ranson provided help with scientific discussions, data interpretation and manuscript preparation.

Work in appendix A contains data from a jointly authored paper published in 2015. The candidate contributed to the work presented in Hesketh, E. L, Meshcheriakova Y, Dent K.C,

Saxena P., Thompson R.F., Cockburn J.J, Lomonossoff G.P., Ranson N.A. Mechanisms of assembly and genome packaging in an RNA virus revealed by high-resolution cryo-EM. Nat. Commun. 6:10113 doi: 10.1038/ncomms10113 (2015). The candidate performed cryo-EM on CPMV virus samples. E.L.H., K.C.D., P.S., G.P.L. and N.A.R. conceived and designed the experiments; K.C.D., Y.M., P.S. and the candidate performed the experiments; E.L.H., Y.M., J.J.C., G.P.L. and N.A.R. analysed the data; E.L.H., Y.M., G.P.L. and N.A.R. wrote the paper.

Work in appendix A contains data from a jointly authored published in 2015. In situ formation of magnetopolymersomes via electroporation for MRI. (2015) Jennifer Bain, Lorena Ruiz-Pérez, Aneurin J. Kennerley, Stephen P. Muench, Rebecca Thompson, Giuseppe Battaglia & Sarah S. Staniland. Scientific Reports 5, Article number: 14311. The candidate performed and processed cryo-electron tomography on magnetopolymersomes. S.S Staniland, G Battaglia and J Bain conceived of the original idea of using electroporation of polymersomes to precipitate MNPs. G Battaglia and L Ruiz-Pérez developed and optimized the original polymersome electroporation method. S.P Muench carried out cryo-EM and processed images. A.J Kennerley carried out all MRI measurements and analysis. All remaining analyses were carried out by J Bain. The manuscript was written by J Bain and S.S Staniland with contributions from all authors.

Acknowledgements

First and foremost I need to thank my fantastic supervisors Neil Ranson, Eric Hewitt and Sheena Radford for their enthusiasm and advice throughout the project, and for guidance during the thesis writing process. I feel extremely privileged to have worked with you all. I would like to say a special thank you to Neil (TGSB) for unwavering support, extreme levels of patience, and encouraging me to take advantage of the many opportunities that have presented themselves over the last 4 years. It really has been a joy working with you.

'A learning experience is one of those things that says, "You know that thing you just did? Don't do that." ' ***Douglas Adams, The Salmon of Doubt***

I am grateful to all members, past and present, of the Ranson, Hewitt, Radford and Muench labs for stimulating scientific discussion and practical assistance throughout my PhD. I need to thank Kyle Dent for teaching cryo-EM, and for help with collection of soft-X ray data at Diamond Light Source. Thanks to my lab 'big sister' (the very responsible) Emma Hesketh, for help with processing in RELION and keeping this thesis on track, Daniel 'The Honey Badger' Hurdiss for being a Chimera boss, Matthew Iadanza for keeping me company in the world of amyloid EM, and Ethan Morgan for attempting to teach me virology. Stephen Muench deserves a large amount of cake (at least another 3 years worth!) for teaching me cryo-EM and generally being exceptionally supportive. Extra special thanks goes to the Shaun Rawson, who wins the awards for 'Best in-office IT support' and 'Best value in exchange for a tea spoon' for insightful discussions and help with RELION and Rosetta.

I am grateful for the assistance of Andrew Hellewell, Morwenna Porter, and especially Toral Jakaria and Matthew Jackson, in all things cell biology. Matt, I owe you much gin (again). I am grateful to Kevin Tipping for all his help, and for determining fibril lengths by AFM described in Figure 3-10. A massive thanks to Sophia Goodchild for providing advice and support with the lipid work, and performing DLS experiments, and dye release experiments presented in Figure 3-21. I would like to thank Peiyi Wang for his assistance with the electron microscopes and Shaun Killen for maintaining the servers and IT support. I am grateful to Helen Saibil for providing access to their FEI Polara Microscope at Birkbeck, London, and to Daniel Clare for assistance with data collection. I also need to thank the MRC LMB for providing access to their FEI Titan Krios, and Shaoxia Chen and Christos Savva for their assistance with data collection.

Abstract

Over the last ~4 years, cryo-electron microscopy (EM) has undergone a 'revolution', thanks to advances in microscope hardware, such as direct electron detectors, and image processing algorithms. This has improved the quality of data that can be obtained using cryo-EM, and so a diverse range of biological problems can now be effectively tackled using this technique. Here, two biological systems are examined using different cryo-EM imaging modalities.

A large number of human diseases are associated with the formation of amyloid fibrils. Amyloid-membrane interactions may play a key role in amyloid mediated cytotoxicity. In Chapter Three, a combination of liposome dye release assays and cryo-EM is used to investigate the effect of amyloid fibrils on membranes of varying compositions. Solution conditions such as pH, alongside lipid composition, were found to have a profound effect on the propensity of β-2-microglobulin (β_2m) amyloid fibrils to perturb membranes. In Chapter Four, subcellular fractionation and cryo-EM and tomography were used to further probe the nature of interactions between β_2m amyloid fibrils and cellular membranes. Cryo-electron tomography was used to reveal 3D detail of unique interactions at molecular resolution.

In Chapter Five, structural properties of the *Leviviridae* family of bacteriophages, a model family of spherical viruses, were investigated using cryo-EM. The structure of Qβ bacteriophage at 4.2 Å is presented. Using this electron density map, an existing X-ray crystal structure is refined to yield a better quality model of the Qβ capsid. Asymmetric reconstructions were used to generate insight into genome organisation and capsid assembly.

This work demonstrates the utility of cryo-EM as a flexible technique to tackle a broad range of research questions by providing structural information at different resolutions.

Table of Contents

List of figures

List of tables

Abbreviations

1-anilinonaphthalene-8-sulfonate	ANS
1-palmitoyl-2-oleoyl-*sn*-glycero-3-phospho-1'-*rac*-glycerol	POPG
1-palmitoyl-2-oleoyl-sn-glycero-3-phospho-L-serine	POPS
1-palmitoyl-2-oleoyl-sn-glycero-3-phosphocholine	POPC
1-palmitoyl-2-oleoyl-sn-glycero-3-phosphoethanolamine	POPE
1,2-dimyristoyl-sn-glycero-3-phospho-L-serine	DMPS
3-(4,5-Dimethylthiazol-2yl)-2,5-diphenyltetrazolium Bromide	MTT
4-(2-hydroxyethyl)-1-piperazineethanesulfonic acid	HEPES
Adenosine triphosphate	ATP
Alexa Fluor® 647	AF647
Alpha-N-acetylgalactosaminidase	NAGA
Alzheimer's disease	AD
Amyloid β	Aβ
Apolipoprotein E	APOE
APP amyloid precursor protein	Aβ
Atomic force microscopy	AFM
β-2-microglobulin	β_2m
Bis(monoaclglycero)phosphate	BMP
Bovine serum albumin	BSA
Charged coupled device	CCD
Contrast transfer function	CTF
Correlative light electron microscopy	CLEM
Crude lysosomal pellet	CLP
Cryo-EM of vitreous sections	CEMOVIS
Deoxyribonucleic acid	DNA
Detective quantum efficiency	DQE
Dialysis related amyloidosis	DRA
Dimethyl sulfoxide	DMSO
Direct electron detectors	DED
Dithiothreitol	DTT
Double stranded	ds
Dulbecco's modified eagle's medium	DMEM
Dynamic light scattering	DLS
E Pluribus Unum	EPU
Electron microscope/microscopy	EM
Electron Microscopy Data Bank	EMDB
Electron tomography	ET
Electrospray ionisation mass spectrometry	ESI-MS
Ethylenediaminetetraacetic acid	EDTA
Fibrils with long, straight morphology	Ls
Field emission gun	FEG
Fluorescence *in situ* hybridisation	FISH
Fluorescence microscope	FM
Focused ion beam	FIB
Foetal calf serum/foetal bovine serum	FCS
Fourier shell correlation	FSC
Fourier transform	FT
Fourier transform infrared spectroscopy	FTIR
Fragmented fibrils with long, straight morphology	Ls-f
Gatan Energy Filter	GIF
Glycosaminoglycans	GAGs
Green fluorescent protein	GFP
High Tension	HT
High-pressure freezing	HPF
Horseraddish peroxidase	HRP
Horseradish peroxidase	HRP
Hour	h
Hydrochloric acid	HCL
Hydrodynamic radius	R_h
Islet amyloid polypeptide	IAPP

Isopropyl β-D-1-thiogalactopyranoside	IPTG
Large unilamellar vesicles	LUVs
Liquid nitrogen	LN_2
Lysogeny broth	LB
Lysosomal membrane permeabilisation	LMP
Lysosome-associated membrane glycoprotein	LAMP
Major histocompatibility complex I	MHC I
Mannose 6-phosphate receptor	MPR
Maturation protein	MP
Maximum likelihood	ML
Metallothionein	MT
Mini-singlet Oxygen generator	mini-SOG
Modulation transfer function	MTF
Molecular weight cut off	MWCO
Monolithic active pixel sensors	MAPS
Multivesicular body	MVB
Niemann-Pick type C	NPC
Nuclear magnetic resonance	NMR
Parkinson's disease	PD
Phenylmethylsulfonyl fluoride	PMSF
Phosphate buffered saline	PBS
Photoactivated localisation microscopy	PALM
Photon Technology International	PTI
Point spread function	PSF
Polytetrafluoroethylene	PTFE
Post nuclear supernatant	PNS
Primary	1°
Prion protein	PrP
Protein Data Bank	PDB
Pure deionised water	dH_2O
Q-beta	Qβ
Quasi-elastic light scattering	QELS
Quantum dots	QD
Recombinantley expressed MS2	rMS2
Research Collaboratory for Structural Bioinformatics	RCSB
Ribonucleic acid	RNA
Scanning electron microscope	SEM
Scanning transmission electron microscopy	STEM
Secondary	2°
Signal to noise ratio	SNR
Simulated emission depletion	STED
Simultaneous iterative reconstruction technique	SIRT
Single particle analysis	SPA
Single stranded	ss
Sodium dodecyl sulphate polyacrylamide	SDS-PAGE
Standard deviation	SD
Standard error	SE
Stochastic optical reconstruction microscopy	STORM
Structured illumination microscopy	SIM
Tetramethylethylenediamine	TEMED
Thioflavin-T	ThT
Three-dimensional	3D
Transmissible Spongiform Encephalopathies	TSEs
Transmission electron microscopy	TEM
Transmission soft X-ray cryo microscopy/tomography	cryoXM/T
Two-dimensional	2D
Ubiquitin-proteasome system	UPS
Volta potential phase plates	VPPP
Zernike phase plate	ZPP

1 Introduction

1.1 Imaging life at the molecular level

The average human body is composed of ~3.7 x 10^{13} cells (Bianconi *et al.*, 2013). Mammalian cells range from 100-10,000 μm^3 in volume (Andersen *et al.*, 2003; Frank *et al.*, 1997), and in each cubic micron of the cell, there are 2-4 million individual protein molecules (Milo, 2013). This means even in the smallest cell, there are over 200 million proteins. The cellular environment is thus immensely crowded, and in this environment, proteins, lipids, nucleic acids and other constituents assemble into complex molecular machines that carry out all the biological processes necessary for life (Figure 1-1). Understanding the three-dimensional (3D) spatial arrangement of these components helps to explain how they interact and function.

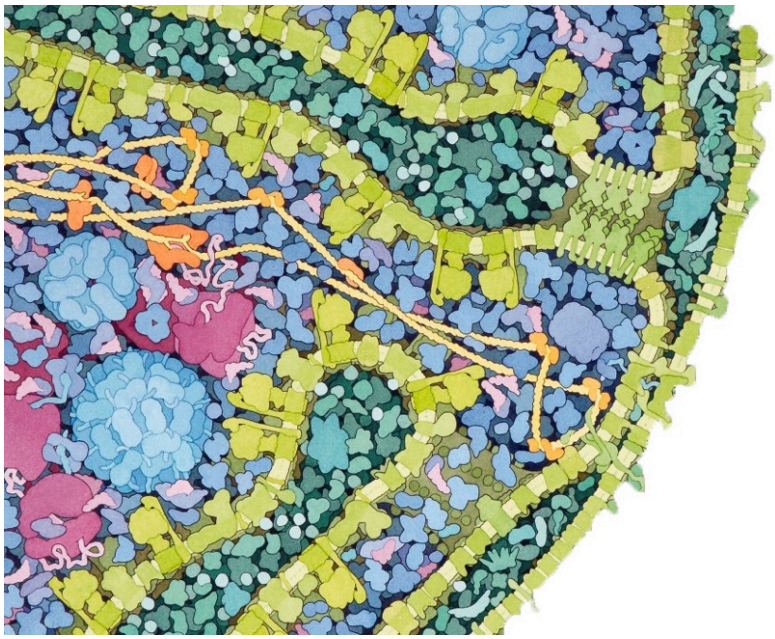

Figure 1-1 The crowded cellular environment. An illustration of a cross-section through a mitochondrion. Soluble proteins are shown in blue, membranes/membrane bound proteins in green, RNA in pink, DNA in yellow and DNA associated proteins in orange. Adapted from Goodsell, 2010.

A variety of techniques have been developed to help understand life at the cellular and molecular level. Structural biology, imaging and biochemical analyses used together can provide complementary information on different resolution scales, aiding our understanding of biological processes (Figure 1-2). Here, some of the most widely used imaging and structure determination techniques will be discussed.

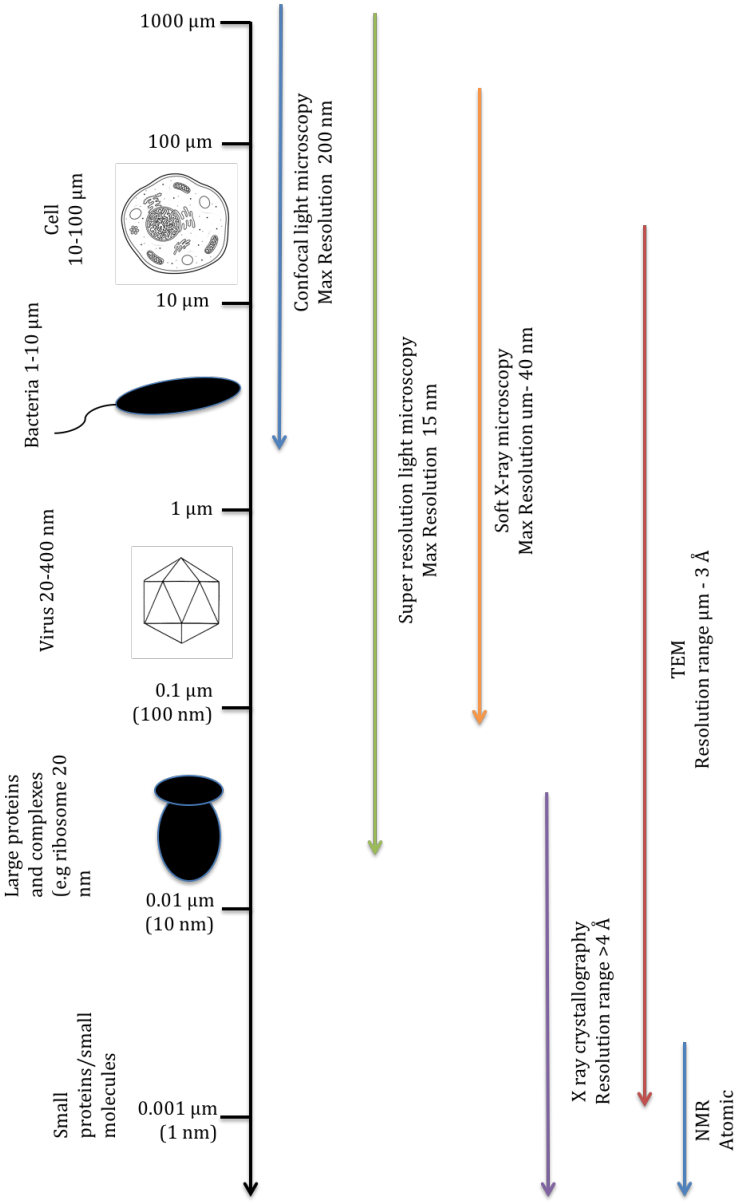

Figure 1-2 Techniques to study cellular and macromolecular complexes. These include transmission electron microscopy (TEM) and nuclear magnetic resonance (NMR).

1.1.1 Light and fluorescence microscopy

Simple light microscopes were the first devices used to significantly extend our capacity to visualise small objects beyond the resolving power of the human eye. In the 17th century, Hooke and van Leeuwenhoek used glass lenses and basic microscopes to observe a previously unseen world, uncovering the existence of cells and single-celled organisms (Amos, 2000; Gest, 2004). Since then, light microscopy has revolutionised our understanding of the microscopic world, and advances in technology have greatly increased the resolution at which specimens can be imaged. A significant innovation that has made optical microscopy one of the most widely used, and powerful tools in cell biology were the advent of fluorescence microscopy (FM), and the accompanying development of a wide range of staining and tagging methods. These allow specific cellular

constituents to be localized in both chemically fixed and live cells. For example, fluorescence *in situ* hybridisation (FISH) allows specific sequences of nucleic acids to be detected, while cloneable fluorescence tags such as Green Fluorescent Protein (GFP) enable visualisation of fusion proteins in live cells. Other useful variants of GFP, including yellow fluorescent protein and calcium sensitive GFP, have been developed, facilitating the study of secondary-messenger cascades and other forms of intracellular signalling, as well as intracellular localization (Pedelacq *et al*., 2006; Miyawaki *et al*., 1997). A whole host of fluorescent proteins and tags that can be expressed recombinantly are now available. Additionally, fluorescent tags with a broad range of chemistries have been developed to allow multiple protein labelling strategies to be applied. FM is thus a flexible tool to study a broad range of cellular processes (van Roessel & Brand, 2002; Correa, 2014).

While traditional light microscopy has revolutionised our understanding of the cell, structures on the molecular scale, such as viruses, molecular chaperones like GroEL, and molecular motors like dynein, cannot be visualised using traditional light microscopy. The resolution of light microscopy is fundamentally limited by the wavelength of light to around 200-300 nm laterally (x and y axes, perpendicular to the beam) and 500-700 nm axially (z axis, parallel to the beam)(Huang *et al*., 2009). When light is focused by the microscope's objective lens, it does not converge to an infinitely sharp focal point, but to a blurred point of a finite size defined by the numerical aperture of the lens and the wavelength of light, the size of which limits the resolution that can be achieved. This was first described by Ernst Abbe and is known as the Abbe limit (Schermelleh *et al*., 2010). Other methods are therefore needed if we are to examine the architecture of subcellular structures and molecular machines.

1.1.2 Super resolution light microscopy

Several super resolution methods have been developed that improve the resolution that can be obtained using light microscopy. There are two main approaches. The first uses patterned illumination to spatially modulate fluorophores within a diffraction limited region, so that the fluorophores do not emit simultaneously (Schermelleh *et al*., 2010). Examples of this include simulated emission depletion (STED) microscopy and structured illumination microscopy (SIM). Instant SIM is well suited for live cell imaging as it can acquire images at >100 frames per second, and offers a resolution of ~145 nm laterally and 320 nm axially at 488 nm excitation wavelength and a 1.49 NA objective lens, in addition to real-time display of super resolution images (Curd *et al*., 2015).

Stochastic optical reconstruction microscopy (STORM)(Rust *et al*., 2006) and photoactivated localisation microscopy (PALM)(Betzig *et al*., 2006) use fluorophores that

stochastically activate or photo-switch at different times. Within single images of sparsely emitting fluorophores, the positions of individual fluorphores can be calculated with very high accuracy, and are then combined to yield a sub diffraction limit image. In order to perform STORM/PALM, fluorescent probes need to have emission/excitation spectra that do not overlap with the dark state, and that are bright (i.e. emit a high number of photons in one duty cycle and a low spontaneous fluorophore activation rate)(Huang *et al*., 2010). Many such probes are now available, including fluorescent proteins and organic dyes. Resolutions better than 10 nm can now be achieved through these techniques, but as image acquisition can take minutes, samples are usually fixed before imaging (Huang *et al*., 2010).

1.1.3 X- ray crystallography and small angle X ray scattering

Compared with visible light which has a wavelength of 400-700 nm, a typical X-ray source has a wavelength of ~ 0.01 nm, allowing a theoretical maximum resolution of ~0.5 Å to be obtained, which is approximately half the length of a carbon bond. X-ray crystallography is a powerful technique for studying the atomic structure of proteins. In pioneering work in the field, X-rays were used to examine the structural properties of biological samples by William Astbury at the University of Leeds, who used fibre diffraction to study proteins including keratin (Astbury & Sisson 1935; Astbury & Marwick, 1931). Fibres such as keratin and deoxyribonucleic acid (DNA) produce diffraction patterns with layer line reflections, however X-rays can also be, and are now most commonly used, to study 3D crystals. Proteins in a crystal are arranged in a lattice, with the smallest repeating unit known as a unit cell. The points recorded from X-ray diffraction through the crystal correspond to points on a reciprocal lattice. This pattern of diffraction spots, or Bragg peaks, are predicted by Bragg's Law, which describes how constructive interference gives rise to the diffraction pattern (Drenth, 2007; Bragg 1913). Each spot of the diffraction pattern represents a sampling of the unit cell of the crystal. Typically, large, well-ordered crystals consist of more unit cells, and so can amplify the diffraction signal better than disordered or smaller crystals. For most crystals, in order to adequately sample the 3D reciprocal lattice of the crystal, several diffraction patterns must be recorded with the crystal rotated at different angles. The intensity of the diffraction spots are recorded and converted to wave amplitudes that, along with phase information, can be used to calculate the electron density of the unit cell. Phase information is not recorded in the diffraction pattern, and so must be determined using other approaches, such as multiple isomorphous replacement, molecular replacement, or anomalous dispersion (Ladd *et al*., 2013).

As of November 2015, over 113,000 X-ray crystallography structures have been deposited in the Research Collaboratory for Structural Bioinformatics (RCSB) Protein Data Bank (PDB). Many proteins and complexes of interest form well-ordered 3D crystals, making X-ray crystallography a viable technique to study their structure. However, some specimens have eluded crystallisation, such as many virus capsids and membrane proteins. Here we will consider the reasons virus capsids may not crystallise. Firstly, the capsid itself may disassemble, creating heterogeneity in the sample, become insoluble at concentrations required for crystallisation, or be intrinsically heterogeneous, all factors preventing the formation of well-ordered 3D crystals. Other challenges present themselves because of the size of capsids; the asymmetric unit of a capsid crystal is very large compared with a typical protein, meaning many more X-ray reflections are present in the diffraction pattern, which are typically weak, complicating structure determination (Fry *et al*., 1999). Even where crystallisation is possible, elements of the structure may not be visible in an X-ray crystallography experiment for example, flexible N-terminal or C-terminal extensions and the genome are typically disordered and so invisible during crystallographic analysis, although there are some interesting exceptions such as bean pod mottle virus where the symmetry of the capsid is reflected in part by the structure of the genome (Fry *et al*., 1999).

1.1.4 Soft X-ray cryo-microscopy

Transmission soft X-ray cryo microscopy/tomography (cryoXM/T) is a technique that uses photons with wavelengths of 4.37-2.29 nm to image cryo-immobilised (Section 1.2.1.3) biological specimens such as whole eukaryotic cells (Dent *et al*., 2014). Photons at these energies are in the 'water window', where contrast arises from the differential absorption of X-rays. A biological specimen, such as a cell, primarily comprises of carbon, nitrogen, oxygen and phosphate. These atoms will strongly absorb X-rays at these energies, so the resulting image reflects the specimen's elemental makeup. Prominent features include lipid bodies, the nuclear envelope and vesicles. As cryoXM is dependent on the absorption contrast of the sample, it is possible that the linear absorption coefficient of different parts of the specimen could be used for sample identification, for example characterizing different compartments in a cell. Photons at 510-520 eV are routinely used, allowing samples ~20 μM thick to be imaged. Resolutions of 36-70 nm can be achieved for biological specimens (Müller *et al*., 2012).

The cryoXM is maintained under a high vacuum, typically < 10^{-7} torr, with the sample mounted in a frozen hydrated state on an electron microscopy (EM) grid, or in a capillary tube (depending on the microscope)(Dent *et al*., 2014). The cryoXM has two primary optical components, a condenser and objective Fresnel zone plate, used to illuminate the

specimen and form the magnified image onto the detector, respectively. Zone plates are a circular diffraction grating with a series of concentric, strongly X-ray absorbing metal rings overlaid with a ~ 100 nm silicone nitride membrane, and function by using diffraction to focus X-rays. The maximum possible resolution is dependent on the smallest zone width and so zone plate technology is currently a major limiting factor to improving resolution. Work is being undertaken to produce superior zone plates which may (theoretically) enable resolutions of better than 12 nm to be achieved (Chao *et al*., 2009).

As cryoXM is usually applied to relatively thick samples such as cells, two-dimensional (2D) images, which represent a projection view of the sample, can be hard to interpret. Consequently, the most useful data is obtained when a tomographic approach is used (Section 1.4.3). Such experiments involve the collection of many images of the sample, each tilted at a different angle. The back-projection of these images is then used to calculate a 3D reconstruction of the sample. Using these data, the 3D relationship between cellular components can be determined. The technique has achieved resolutions approaching 30 nm and better for test objects (Müller *et al*., 2012). CryoXM is increasingly being used as a complementary technique in conjunction with both cryo-EM and optical techniques, and correlative approaches are being developed (Section 1.5.1)(Carlson *et al*., 2013).

1.2 Transmission electron microscopy

Transmission electron microscopy (TEM) overcomes many of the resolution and practical limits of the techniques described above. In the 1920's Louis de Broglie theorised that electrons had wave-like properties, but with significantly shorter wavelengths than that of visible light, allowing them, in principle, to be used for imaging. A 100 keV electron has a wavelength of ~0.004 nm, smaller than the diameter of an atom (Williams & Carter, 1996). The first demonstration that electrons could be used for imaging was published by Knoll and Ruska in 1932 (Ruska, 1986). Electron microscopes (EMs) were then commercialised and since the 1940's their use in both biological and material sciences has grown dramatically (Harris, 2015). One of the first examples of biological TEM was in 1944, where cells were fixed with osmium tetroxide and supported on formvar (Figure 1-3)(Porter *et al*., 1945). From here TEM has been continuously developed, and has provided the first detailed views of cellular ultrastructures, such as the nucleus, mitochondria and cytoskeleton, and now allows direct visualisation of macromolecular complexes such as ribosomes, the proteasome, molecular chaperones and viruses at near-atomic resolution (Bai *et al*., 2013; Campbell *et al*., 2015; Haguenau *et al*., 2003).

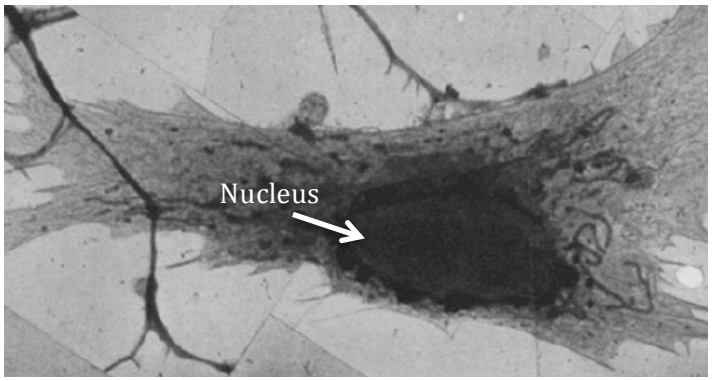

Figure 1-3 An early example of biological TEM. Fibroblast like cell fixed with osmium tetroxide on formvar plastic. Adapted from Porter *et al*., 1945.

1.2.1 Sample preparation

To image with electrons, a microscope must be maintained under a high vacuum, excluding air molecules that will scatter the beam. However, hydrated biological specimens would dehydrate rapidly into a non-native state under a high vacuum. To image a biological specimen, it must therefore first be preserved in a native (or native-like) state. Another consideration is sample thickness. In some cases, the sample may be too thick for electrons to be 'transmitted', a prerequisite for TEM, and so the specimen may need to be processed to make it thinner. The choice of preparation technique is ultimately determined by the nature of the sample and the resolution needed to achieve the intended biological insight.

1.2.1.1 Negative stain

Negative stain is a common method for examining a specimen, especially macromolecular complexes, at room temperature. Specimens are adsorbed onto a thin (~10 nm) carbon support film and stained with a solution of heavy metal salt, commonly 1-2 % (w/v) uranyl acetate, and dried. This quickly dehydrates the specimen and envelops it in stain (where the sample is visualised by the absence of stain, negative staining occurs; where the sample itself becomes stained, positive staining)(1-4). Typically, negative staining yields more informative images. The resulting shell of heavy metal atoms generates amplitude contrast, (Section 1.3.1) which results in images with a relatively high signal to noise (SNR) ratio. The correct stain depth must be achieved for optimal imaging, if the structure is too deeply embedded, or is incompletely embedded, information can be lost. The thicker the specimen, the deeper the stain needs to be to ensure full embedding, and the noisier the images will be (due to inelastic electron scattering and multiple scattering events, section 1.3.1). Other drawbacks include dehydration and deformation of the specimen, and resolution is limited by the grain size of the stain, which determines how well the stain envelope reflects the structure of the object (Booth *et al*., 2011). Despite these limitations, negative stained samples can generate 3D data and provide invaluable biological insight (Burgess *et al*., 2004; Bakker *et al*., 2013). For example, negatively

staining can be used to elucidate the binding of small molecule inhibitors in a timeframe of weeks, (Muench *et al.*, 2014), assess conformational changes (Hesketh *et al.*, 2015a; A.J. Roberts *et al.*, 2009), complex stability (Wu *et al.*, 2012) and subunit stoichiometry/position (Rasmussen *et al.*, 2011; Low *et al.*, 2014). The process of negative staining has been reviewed in (Ohi *et al.*, 2004).

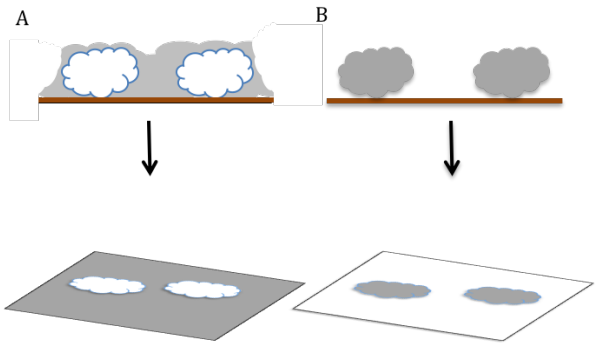

Figure 1-4 Positive and negative staining using heavy metal salts. Negative staining (A), the stain fully envelops the macromolecular complex; the complex appears light on a dark background. Positive staining (B) results in a small amount of stain forming a thin shell around the molecule, meaning the sample appears dark on a light background.

1.2.1.2 Plastic embedding and thin sectioning of cells

When imaging cells or tissues in the TEM, specimen thickness becomes a limiting factor. To overcome this, samples can be chemically fixed, embedded in plastic and sectioned. This involves fixation (e.g. with gluteraldehyde), staining with osmium tetroxide and dehydration in alcohol or acetone. The specimen is then embedded in a resin and sectioned using a microtome. Sections are mounted onto a support grid and further stained with heavy metal such as uranyl acetate. Each step is harsh and can introduce artefacts, making image interpretation difficult. However, despite these problems this technique has revolutionised our understanding of cell ultrastructure (Knott & Genoud, 2013).

1.2.1.3 Cryogenic preparation

Staining, plastic embedding and sectioning dehydrate the biological specimen, fundamentally removing it from its native, aqueous environment. To better preserve such specimens in their native state in the high vacuum of the EM, cryogenic immobilisation can be used. Cryo-immobilisation has the dual benefits of preserving the specimen in an aqueous environment inside the EM, and also the low temperature ameliorates the damaging effect of the electron beam. The sample must be frozen extremely rapidly, at a rate of $\sim 10^6$ °C/s, so that the water in, and surrounding, the specimen is fixed in a vitreous state (Dubochet *et al.*, 1988). If freezing occurs more slowly, ice crystals form from the hydration shell of the complexes, or even within the sample, disrupting the atomic

structure of the specimen. Image quality is also reduced owing to electron diffraction by ice crystals (Figure 1-5). Hexagonal ice can form during freezing, while cubic ice forms when vitreous ice layers warm (Dubochet & Lepault, 1984).

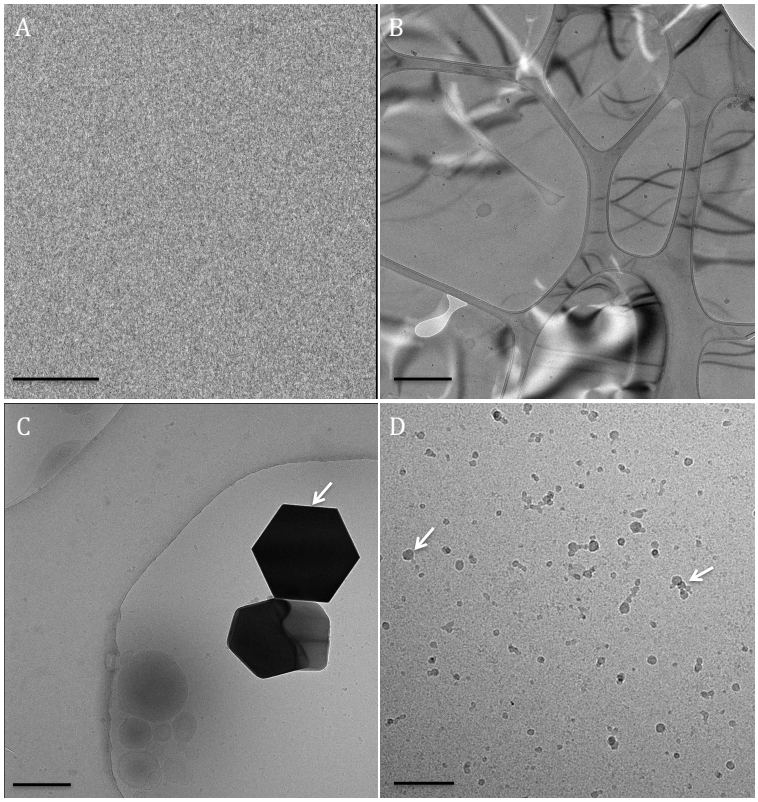

Figure 1-5 Examples of vitreous and non-vitreous ice, and ice contamination. A) Empty, vitreous ice (Scale bar 50 nm). B) Hexagonal ice (scale bar 400 nm). C) Large ice crystal (white arrow)(scale bar 400 nm). D) Ethane contamination (scale bar 200 nm).

For thin specimens such as suspensions of macromolecules and small cells, or the thin edge of larger cells, cryo-immobilisation can be achieved by blotting the sample to generate a thin film of liquid, and then rapidly freezing it by plunging into a cryogen. The most widely used cryogens are liquid ethane or propane, cooled by liquid nitrogen. Both ethane and propane are closer to their freezing point than their boiling point at -180 °C, meaning when the sample is plunged into the cryogen a layer of insulating gas does not form (such as occurs with plunging into liquid nitrogen)(Tivol *et al*., 2008). The specific heat capacity of liquid ethane and propane is also higher than liquid nitrogen (LN_2). Plunge freezing thin films of macromolecules/thin samples is a widely applied technique used with great success for a range of specimens. Blotting and plunging can be achieved with simple devices, often built in house (Dobro *et al*., 2010). However, these often lack humidification control, and produce grids with variations within and between batches of EM grids. There are several commercial instruments available that control and monitor a

larger number of variables during the blotting and plunging process to achieve more reproducible results, including models by FEI, Leica and Gatan.

A key consideration in cryogenic specimen preparation is the support film to be used. EM grids are traditionally 3.05 mm across, and made from a mesh of metal such as copper, gold, nickel, molybdenum or rhodium. The mesh size, or number of squares across the grid, is defined as the number of squares in one inch. For example, a 200-mesh grid has 20 squares across in one direction, and a 300 mesh 30 squares. 200-400 mesh grids are most commonly used in cryo-EM. The next consideration is support film. Generally, perforated carbon films are used so the specimen is imaged in ice suspended in holes in such films. However, samples have differing affinities for the carbon film, with some almost exclusively depositing on the carbon. The surface properties of the carbon can be altered by a variety of processes, including exposure to UV radiation and glow discharge, which render the carbon film hydrophilic (Grassucci *et al*., 2007). Altering the charge properties of the carbon film can aid the partition of the sample into the holes, but this needs to be optimised for each sample. Some samples have very high affinities for the carbon, these samples sometimes benefit from a thin (~10 nm or thinner, although there is a trade off between carbon stability and thickness) continuous carbon film over the surface of the grid to improve particle distribution. Perforated films are available commercially, and can consist of regular arrays of equal sized holes, as with Quantifoil and C-flat grids, or irregular as in lacy carbon (Figure 2-1). Carbon support films are widely used, but are not without their problems. Instability of the carbon film contributes to beam induced particle motion, blurring the image of the specimen (Russo & Passmore, 2014). Novel support films have been recently developed to tackle this problem, including gold supports and doped silicone carbide films. Both appear to reduce beam induced particle movement (Russo & Passmore, 2014; Yoshioka *et al*., 2010).

While thin samples, such as macromolecular assemblies, or the thin edge of larger cells may be cryogenically fixed by plunge freezing, thicker samples (< 1 μm) such as the nuclear and perinuclear regions of eukaryotic cells, or tissue sections are likely to experience some crystalline ice formation. For these specimens, high-pressure freezing (HPF) is an effective alternative. HPF involves raising the pressure of the sample to ~2000 bar while dropping the temperature using liquid nitrogen (McDonald & Auer, 2006). Samples over 100 μm thick can be vitrified using HPF. Vitrified samples must then sectioned to be thin enough for TEM. Sectioning can be performed under cryogenic conditions, which gives the best preservation of the sample. The technique known as cryo-EM of vitreous sections (CEMOVIS) uses cryo-ultramicrotomy with a diamond knife under

cryogenic conditions to produce sections 40-100 nm thick (Al-Amoudi *et al.*, 2004; Chlanda & Sachse, 2014). It is a useful technique to image thick specimens in a native-like state, but it is technically challenging. A common alternative approach is to perform freeze substitution, which enables sectioning and imaging at room temperature (Walther & Ziegler, 2002; Matsko & Mueller, 2005). Freeze substitution involves gradually warming the specimen and replacing the water with acetone. The sample can then be stained, embedded in resin and sectioned. This technique introduces fewer artefacts compared to traditional plastic embedding. However, some small ice crystals do form causing rearrangement of cell structures, and staining is not uniform so interpreting images can be challenging.

Frozen-hydrated samples must be visualised at cryogenic temperatures, known as cryo-EM. A major technical challenge in cryo-EM is transferring the specimen at -180 °C to the microscope without warming it above -137 °C, the temperature of water devitrification (Dubochet *et al.*, 1988), while also maintaining the thermal and mechanical stability of microscope components to allow imaging.

1.2.1.4 Focus Ion Beam Milling

For thicker samples, such as whole eukaryotic cells or networks of cells, focused ion beam (FIB) milling can be used to reduce specimen thickness or to perform serial block-face imaging (Schertel *et al.*, 2013; K. Wang *et al.*, 2012). FIB milling is carried out on frozen hydrated specimens in a dual beam scanning EM/FIB. In this approach, a focused beam of ions blasts material from the surface of the sample in a defined manner, while the scanning electron microscope (SEM) allows simultaneous non-destructive monitoring of the milling process (Rigort & Plitzko, 2015). In FIB milling, incoming ions expel surface atoms in a process known as sputtering, and the beam is rastered across the surface of the specimen removing material in a layer-by-layer manner. Gallium ions are the most popular due to their volatility (Rigort & Plitzko, 2015). The ion beam is generated by a liquid metal ion source and liberated by an extraction electrode. Electromagnetic lenses and apertures are used to focus the ion beam, and deflectors to control the pattern of milling.

FIB milling can introduce artefacts. Sputtered material can redeposit on the surface of the specimen, although an anti-contaminator device close to the specimen can reduce this. Milling can also produce streaking or curtaining across the surface when differential milling occurs. Another concern is the transfer of thermal energy to the specimen, causing local heating and devitrification. However it has been shown that under set conditions FIB milling does not raise temperatures sufficiently for this to be a routine problem (Marko *et*

al., 2006). It would be very interesting to perform FIB milling on a crystal and assess how it affects diffraction, as this may reveal how the process degrades high-resolution features of the specimen.

Since the first successful cryo-FIB experiment in 2003 (Mulders, 2003), workflows have been developed to improve and optimise the technique including *in situ* cryo-lamella preparation of cells grown on EM grids (Figure 1-6). Cryo-FIB technology is still being developed, one particularly exciting development is the implementation of correlative light microscopy in combination with FIB milling, as discussed in Section 1.5.1.2 (Rigort *et al*., 2012).

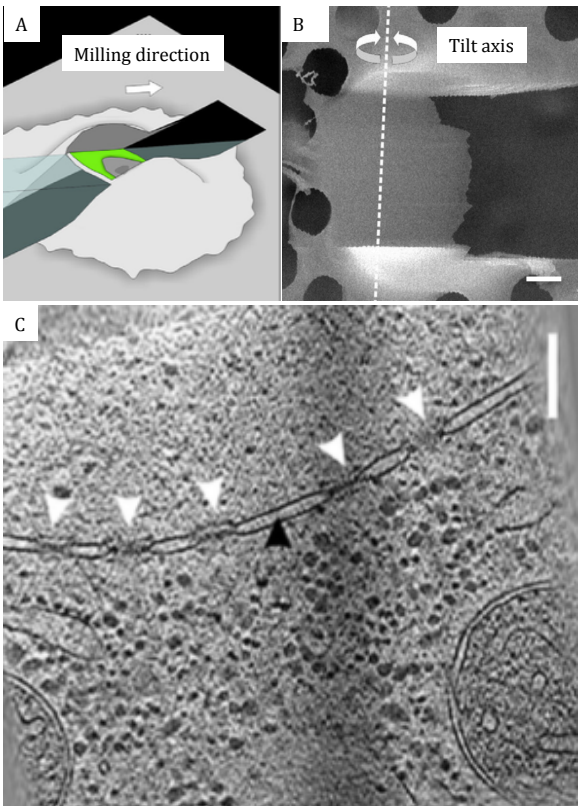

Figure 1-6 Preparation of *in situ* cryo-lamellar using focused ion beam milling. Milling patterns can be adapted to produce lamellar (A, green lamellar) in perinuclear regions of a cell. The lamellar can be viewed in the SEM (B- top down view of lamellar, scale bar 2 μm), and transferred into the TEM for cryo-electron tomography (discussed in Section 1.4.3), a slice through a tomogram of a perinuclear region of the cell (C- scale bar 200 nm) revealing the nuclear envelope (black arrow) and nuclear pore complexes (white arrow). Adapted from Rigort & Plitzko, 2015.

1.2.1.5 Time resolved electron microscopy

Macromolecular complexes can be dynamic, undergoing conformational changes under certain stimuli, such as binding to a ligand. These conformational changes can occur over variable timescales, from femtoseconds to hours (Evans & Browning, 2013). Studying conformational changes which occur on short time scales can be especially challenging, and so sample preparation methods for cryo-EM have been adapted to enable time resolved analysis down to ~ 10 ms (Shaikh *et al*., 2014). Specimens for cryo-EM are trapped within that conformation upon vitrification, and so by mixing two reactants, for example an enzyme and its substrate, a set time before vitrification, a temporal dimension can be incorporated into the experiment.

One of the most common approaches to achieving time resolution utilises microfluidics where one reactant is sprayed onto the grid and a second reactant sprayed on before freezing (White *et al*., 2003). In an alternative approach, rapid mixing of the two reagents is performed, which are then sprayed onto a thin film that is rapidly vitrified. The fastest reported time resolution has been achieved using a monolithic micro-fabricated silicon device that incorporates a mixing mechanism, incubation channel and pneumatic sprayer in a single chip (Shaikh *et al*., 2014). It is capable of achieving mixing within 0.4 ms and a minimum reaction time of 9.4 ms (Shaikh *et al*., 2014). Using this methodology, the dynamics of bridges associating the 30S and 50S bacterial ribosomal subunits was examined (Shaikh *et al*., 2014). While improvements in microfluidic devices may yield improvements in time resolution, it has been suggested that the use of photo-activatable complexes may enable even faster time resolution to be achieved. For example, by fitting a fibre optic cable or another bright light source very close to the cryogen before the sample is plunged, a conformational change may be induced and fixed by vitrification on the ns time scale. Depending on the temporal resolution of the approach and the timescales under which the reaction or conformational change is occurring, often the cryogenically fixed sample will represent a range of conformations or reaction states. New developments enable *in silico* purification of heterogeneous mixes of conformations (Voorhees *et al*., 2014), as discussed in Section 1.4.2.2.

1.3 Design of the EM

In its most basic form, the TEM consists of an electron source/gun, a series of electromagnetic lenses to focus the electron beam, and a mechanism for viewing or recording an image of the specimen, all maintained under high vacuum (Figure 1-7). Many different EM's are available commercially from companies including FEI and JEOL, which share similar main components and designs. Here the principal components of the EM and process of image formation are discussed.

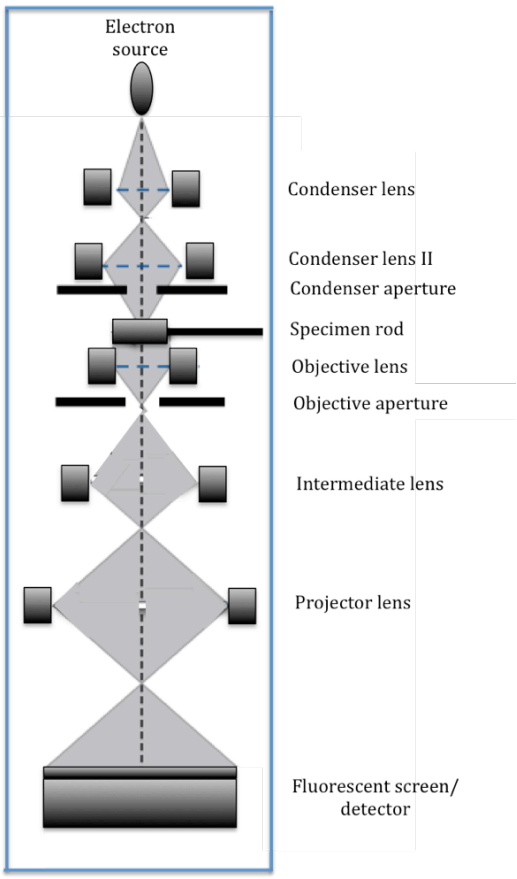

Figure 1-7 Schematic of a typical TEM. The electron beam (light grey) is directed down the central axis (dashed black line) of the column, directed by electromagnetic lenses (black) and through apertures, producing a magnified image, which can be viewed on the fluorescent screen or detector.

1.3.1 Image formation in the TEM

In the TEM, electrons are transmitted through the specimen, and the projected image consists of areas of light and dark, which provide information about the electron density of the specimen. Electrons can be scattered by the specimen in two main ways (Figure 1-8). Elastic scattering causes the path of the electron to be altered with no energy loss, while inelastic scattering transfers energy to the specimen. For biological specimens, for every elastic scattering event that contributes positively to image formation, 3-4 inelastic scattering events also occur (Henderson, 1995). Energy transfer from incoming electrons to the specimen can cause ionisation, induce free radical formation, X-ray emission and chemical bond rearrangement, as well as induce secondary electron scattering, limiting the resolution of the image both by damaging the specimen and introducing noise. Multiple electron scattering events can also occur; sample thickness is minimised to reduce this.

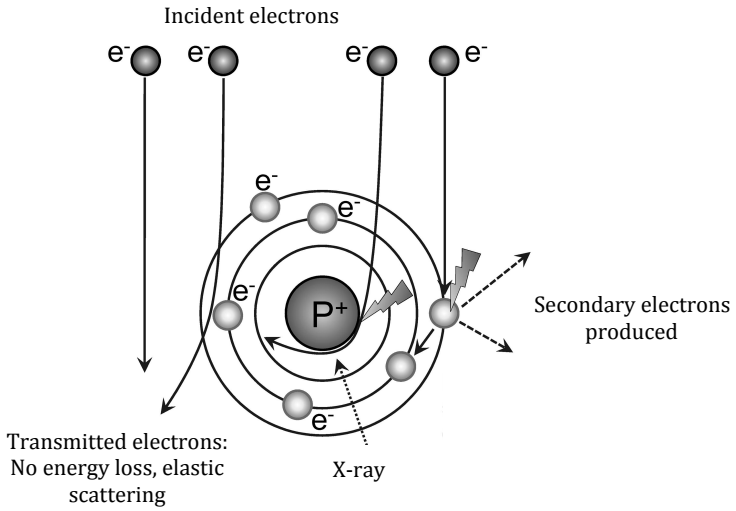

Figure 1-8 Interactions of the electron beam with the sample. As incident electrons hit the electron cloud of a specimen, no energy is lost but the incident electron is deflected (elastic scattering). If incoming electrons collide with electrons of the nucleus, energy is lost (inelastic scattering) and secondary electrons may be produced or X-rays emitted. Adapted from Orlova & Saibil, 2011.

The generation of contrast in the images, can be split into two primary categories, amplitude and phase contrast. Phase contrast arises from interference between electron waves, while amplitude contrast arises from the absorption of electrons by the specimen, or exclusion of widely scattered electrons from the image. The method of specimen preparation defines which process contributes most to contrast. Biological specimens are primarily made of light atoms such as carbon, nitrogen, oxygen and hydrogen. These atoms do not absorb electrons strongly from the incident beam and so amplitude contrast is low when performing cryo-EM of thin aqueous films. However, if the biological specimen is encapsulated in a heavy metal stain, as in negative staining, the heavy metal atoms absorb electrons introducing amplitude contrast.

Frozen-hydrated biological specimens in thin films are classified as weak phase objects as they cause a weak phase shift of the incident electron beam and extremely low amplitude contrast. As this is so small, it must be converted into an amplitude-varying signal. In practice this is achieved by defocusing the microscope. Which in combined with spherical aberrations, induces a phase shift between scattered and unscattered electrons, producing stronger image contrast.

1.3.2 Electron Source

The electron gun extracts and accelerates electrons; it consists of an electron source, a cathode, and an anode. TEM's are typically fitted with either thermionic electron sources

or Schottky emission guns, known as a field emission gun (FEG)(Williams & Carter, 2009). Common thermionic sources include tungsten filaments or lanthanum hexaboride crystals, which are heated so the voltage potential exceeds the work function required to free electrons from the source. Most thermionic sources operate at an extraction voltage of 80-200 kV (Williams & Carter, 2009). The Schottky emission gun is an extremely fine tungsten filament coated with zirconium oxide, typically operated at an extraction voltage of 200-300 kV and a temperature of 1800 K (1526 °C) (Williams & Carter, 2009). In true field emission, the cathode electron source is held at a negative potential compared with the anode, so the electric field at the tip is strong enough that the electrons can 'tunnel' and leave the cathode without the thermal energy input needed in thermionic sources (Joy *et al*., 1986). In Schottky emission electron sources the field strength is not sufficiently strong for quantum mechanical tunnelling, and so thermal energy input is required to overcome the potential barrier (Williams & Carter, 2009). As a result Schottky emission guns are 'field assisted thermionic emitters' rather than true FEGs. Schottky emission guns result in a much brighter and coherent electron beam compared with thermionic sources.

1.3.3 Electromagnetic lenses

Electrons are negatively charged and so can be focused using electromagnetic lenses. These lenses function by passing an electric current through a coil of wire, generating a magnetic field, which deflects electrons. The first set of lenses the electron beam encounters upon leaving the source is the condenser lens system, or illumination system, which comprises the condenser lens and condenser aperture. Most commonly the illumination system has two or three lenses, with the three-lens system enabling parallel illumination to be more easily achieved. Further down the column, the electron beam meets the objective lens, the most important lens for image formation. It provides the first magnification and focuses the beam onto the image plane after electrons have been scattered by the sample. In most EMs the specimen sits within the objective lens, meaning it is immersed in the magnetic field. The objective aperture sits in the back focal plane of the lens, removing electrons scattered at high angles and so improving contrast. The image is then magnified by intermediate and projector lenses onto the detector. The lens system allows a wide range of magnifications to be achieved, typically from 20 to 200,000 times.

1.3.4 Electron detectors

Once the different lenses of the TEM form the image, it must be visualised or recorded. The high-energy electrons used in TEM are invisible (and damaging) to the human eye, and so they are viewed indirectly using a phosphorescent screen or detector. The images recorded, known as electron micrographs, can be captured on film, charged coupled device (CCD) cameras or direct electron detectors (DED).

Cryo-EM images of biological specimens are intrinsically noisy due to the low electron doses used. A perfect detector would add no additional noise. However, in practice, all detectors introduce additional noise. This can be expressed as the detective quantum efficiency (DQE) of the detector at a given spatial frequency, the square ratio of the output SNR (SNRo) over the input SNR (SNRi)(McMullan *et al*., 2014). A perfect detector would have a DQE of 1.

$$DQE = SNRo^2/SNRi^2$$

Historically, film was the most common detector. It has a large field of view, an extremely small 'pixel' (the grain size of silver halide crystals in the emulsion), and relatively good DQE. However, recording large data sets using film is inconvenient, expensive and time consuming. Film emulsion contains water and introduces contamination into the column of the EM. It also needs developing, and digitisation using extremely expensive and delicate densitometry. As a result, CCD cameras are currently the most commonly used detectors. CCDs utilise a phosphor scintillator, which induces the emission of photons when electrons strike it. The CCD camera then transforms these photons into electrical signals. The DQE of a CCD camera is inferior to film at the electron energies typically used for imaging. The scintillator layer results in electron and so photon scattering, causes a loss in sensitivity as well as introducing an accelerating voltage dependent point spread function (PSF). Despite these problems, data collected on a CCD camera under appropriate imaging conditions can be processed to sub-nanometre resolution (Cheng *et al*., 2010). CCD cameras are also much more convenient than film, and allow images to be inspected immediately after collection.

In the last few years, the use of DEDs has revolutionised biological TEM. Combining the benefits of a high DQE detector with the convenience of an electronic read out, DED's are now the recording medium of choice. Several detector designs were developed, including monolithic active pixel sensors (MAPS) and hybrid pixel detectors (Faruqi & McMullan, 2011), but MAPS based DED's are becoming prevalent (Bai, McMullan, *et al*., 2015).

MAPS detectors detect incident electrons directly as they pass through a semiconductor membrane ~10 μm in depth where they deposit energy. Some electrons are back scattered from the support matrix and pass through the membrane again, generating noise. As a result, high DQE DEDs are 'back thinned', which involves removing as much of the support matrix as possible (to less than 50 μm), meaning most electrons pass right

through the detector. Monte Carlo simulations show the thinner the substrate the less scattering is observed (McMullan *et al*., 2009). DEDs are available commercially from three manufacturers, FEI, Direct Electron and Gatan, all of which have a DQE better than film (McMullan *et al*., 2014). Currently, the FEI Falcon II and some Direct Electron solutions work by integrating signal from electrons hitting the detector. The limitation of this approach is that incoming electrons may have different energies, and so contribute differently to the output signal (McMullan *et al*., 2014). By contrast, counting detectors such as the Gatan K2, FEI Falcon III and Direct Electron DE-20 can count individual electrons as they hit the detector. This enables some counting detectors to image in 'super resolution mode', providing information beyond the Nyquist limit, by analysing the point spread function (PSF) of the incoming electron and localising its location within the pixel. Low spatial frequencies are better preserved on detectors which operate in counting mode, however longer exposure times are used as a low electron dose rate is required in order for counting (and super resolution) mode to function. Other limitations arise from errors in counting. For example, single events may be split over several pixels, and even with careful dark and gain references some pixels will be hit by multiple electrons which will produce noise (Ruskin *et al*., 2013). The counting algorithm may also misinterpret the path of an electron (McMullan *et al*., 2014). A major benefit of DED's is the ability to spread the dose across several frames, creating a movie of the exposure. This is useful as it allows correction for specimen movement during the exposure (Section 1.4.2.5). Structures at near-atomic resolution have been determined using all three manufacturers' DEDs (Parent *et al*., 2014; Voorhees *et al*., 2014; Lu *et al*., 2014).

1.3.5 Phase plates and energy filters

As discussed fully in Section 1.3.1, cryo-EM produces images with poor SNR, and in order to retain high-resolution information in our images, they must be taken close to true focus, again reducing overall image contrast. To combat this, two complementary technologies have been developed to increase SNR in images: phase plates and energy filters.

When imaging, a proportion of electrons that interact with the specimen are inelastically scattered, i.e. they deposit energy in the specimen. Their resulting lower energy, and thus longer wavelength causes these inelastically scattered electrons to be focused in a different plane to the elastically scattered electrons (Orlova & Saibil, 2011). Inelastically scattered electrons can be considered a form of chromatic aberration, introducing noise. Energy filtering can prevent inelastically scattered electrons from contributing to the recorded image. There are two commercialised energy filters currently available, the in-column Omega (Ω) filter and post-column Gatan Energy Filter (GIF)(Williams & Carter, 2009). Both work on the principle that electrons of different energies/wavelengths can be

deflected along different paths, meaning that only electrons that interact elastically (or not at all) with the specimen contribute, improving the signal to noise ratio. Energy filtering is particularly useful when collecting tilt series, as at high tilts the specimen effectively becomes thicker in the direction of the beam, and the amount of inelastic scattering is proportional to specimen thickness.

When imaging unstained biological specimens, there is little amplitude contrast. However, phase contrast can be introduced to mitigate this problem. This can be achieved by defocusing the microscope, but this causes a loss of information (Section 1.3.8.1). Phase plates have been developed to introduce an additional phase shift, allowing imaging at (or close to) focus, retaining information while generating sufficient contrast to see the specimen. While the concept has been in development for many years, the practical application of phase plates has only been realised in the last few years. There are two main types of phase plate: Zernike and Volta potential.

The Zernike phase plate (ZPP) is a thin carbon film with a small (~1 μm) hole, which is aligned so the unscattered beam passes through (Figure 1-9)(Dai *et al*., 2014). Scattered electrons pass through the carbon film and undergo an approximate $\pi/2$ shift relative to the unscattered beam. This causes the contrast transfer function (CTF) to switch from a sine to a cosine function, boosting SNR at low spatial frequencies and thus providing image contrast. ZPPs are commercially available in JEOL EMs and have been use in electron tomography (ET) experiments to great effect (Dai *et al*., 2013). However, images taken using a ZPP suffer from fringing artifacts around high contrast features, owing to the sudden onset of the CTF (Sui *et al*., 2014). ZPPs are also time consuming to align, and have a short, unpredictable lifetime (~ 1 week), which is independent of use.

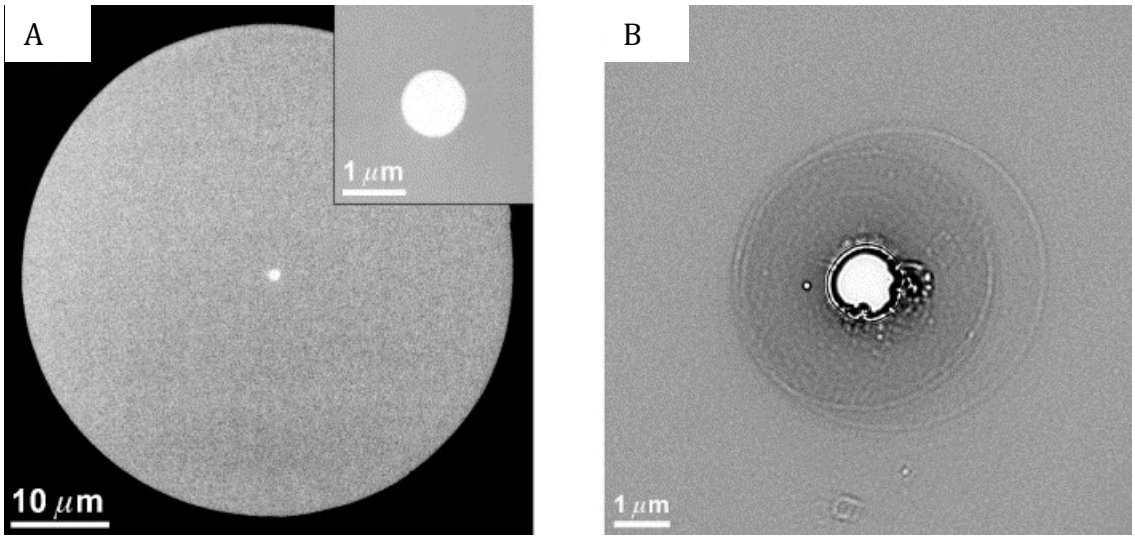

Figure 1-9 Zernike phase plates. An unused Zernike phase plate with 1 μm aperture (A) and a phase plate used for several experiments (B), the wide dark grey circle around the central aperture is where beam induced damage of the carbon has occurred. Adapted from Danev & Nagayama, 2001.

Volta potential phase plates (VPPP) uses an ~12 nm film of amorphous carbon heated to 200 °C to introduce a phase shift (Danev *et al.*, 2014). The physics underlying this phenomenon remains unclear, but it is hypothesized to function by a beam-induced Volta potential (Danev *et al.*, 2014). This potential is thought to arise from beam-induced surface modification of the carbon combined with a chemical equilibrium between the carbon surface and residual gases in the EM column. VPPPs do not introduce fringing artefacts, and they are reported to be stable for months (Danev *et al.*, 2014). As VPPPs have been developed recently, they have not been extensively tested.

As both phase plate designs boost SNR at low spatial frequencies, they are particularly useful when performing ET. For single particle work it remains to be seen how much benefit phase plates will yield, as CTF correction compensates (Section 1.3.8.1) for the information lost by introducing a phase shift by defocusing the microscope. In principle however, they may reduce the amount of data needed to generate a structure to the same resolution compared with a dataset collected with no phase plate (Murata *et al.*, 2010), and may be beneficial for samples that are particularly small or hard to align.

1.3.6 Use of low electron dose conditions

Biological specimens are sensitive to radiation damage (Baker & Rubinstein, 2010). Electrons destroy the specimen, with damage occurring in three stages. Firstly, primary damage is caused as electrons ionize the sample, break chemical bonds, and produce secondary electrons and free radicals. Secondary damage occurs as these reactive species

migrate and cause further reactions. Tertiary damage occurs as hydrogen gas is produced within the sample, causing gross damage.

Radiation damage thus dictates that total electron dose should be minimised, but without sufficient dose the specimen cannot be visualised. Dose is thus a compromise between contrast and damage. During data collection, areas suitable for imaging must be identified, and the appropriate focus chosen. These processes expose the sample to the electron beam contributing to the total dose the specimen receives. Low dose imaging protocols have been developed to minimise this exposure prior to imaging, thereby allowing maximal dose to be applied during the acquisition of the final image. Low dose imaging occurs in three modes. Firstly, a low magnification 'Search' mode, with a very low electron dosage per $Å^2$, is used to identify the field of interest. Then, the microscope is focused a short distance away from the area of interest. Finally, the image is acquired, with a typical total electron dose of 15-100 $e^-/Å^2$.

1.3.7 Automated data collection software

Alongside recent advances in EM hardware, software has been developed to aid data collection. The SNR of cryo-EM images is very low and so many images are usually needed to generate a structure. As a result, several software packages have been developed to automate data collection, making efficient use of microscope time. One commonly used commercial package is FEI's E Pluribus Unum (EPU). EPU generates an atlas of the grid, identifying suitable grid squares. Suitable holes within the square can then be identified, and a recording template defined. Depending on the magnification used, multiple images can be taken in one hole. EPU will collect images independent of human intervention, according to this template, until stopped or there are no more selected areas. However, EPU only functions on FEI microscopes. Open-source programmes with similar functionality have been developed, such as Leginon (Carragher *et al.*, 2000; Stagg *et al.*, 2006) and TOM² (Unverdorben *et al.*, 2014; Korinek *et al.*, 2011). Software to allow the automated collection of tilt series has also been developed, including SerialEM (Mastronarde, 2005), UCSF Tomo (Zheng *et al.*, 2010), Xplore3D (FEI) and Leginon (Suloway *et al.*, 2009).

1.3.8 Microscope aberrations

The lens system of the EM gives rise to aberrations, the most significant of which are chromatic, astigmatic and spherical. Chromatic aberration arises from the lens focusing long wavelengths more strongly than shorter wavelengths so that the image is formed in different planes. In the EM, this can be caused by energy ('colour') spread in the electron beam, as well as inelastic scattering. Astigmatic aberrations are caused by asymmetry in

the electromagnetic lenses used to focus the beam, and causes an imaged point to become elliptical. It can be corrected to a large extent by adjusting stigmator coils to symmetrise the magnetic field strength with the lens. Spherical aberration (C_s) is caused by electron waves being refracted differentially by different parts of the lens; waves passing through the lens periphery are refracted more strongly compared with paraxial waves. Methods have been developed to correct for C_s during imaging, by the use of a second set of electromagnetic lenses and apertures, but while they have been used to generate structures to high resolutions, such as of the *E. coli* ribosome–EF-Tu complex to 2.9 Å (Fischer *et al.*, 2015). C_s correctors are complex to align and expensive, so their use is currently limited in biological TEM.

1.3.8.1 Contrast transfer function

Cumulatively, imperfections in the lens system of a microscope lead to the recorded image being distorted by a contrast transfer function (CTF), which describes the transfer of information as a function of spatial frequency (or resolution). The effect of the CTF on the observed image can be described by a Fourier Transform (FT,) that produces a power spectrum which relates a signal (the image) to the frequencies of which it is composed. In real space, the effect of the CTF is as a PSF, where information from one part of the image is spread into adjacent areas. The CTF is thus the Fourier space representation of the microscope's PSF.

The recorded image of the object is the convolution of the real image with the microscope's point spread function (PSF). The CTF serves as a mathematical description of the relationship between the recorded image and the weak phase object that generated it. Thus the FT of the recorded image (I) is the multiplication of the microscopes CTF (M) with the weak phase object's FT (O), plus noise (N);

$$I = M * O + N$$

In Fourier space, the CTF appears as a sinusoidal function with increasing frequency and decreasing amplitude. The function γ(s) describes the wave aberration function of the microscope. The microscope's CTF is influenced by spherical aberration (C_s), electron wavelength (λ) and defocus (ΔZ). The CTF can be described as;

$$\text{CTF} = \sin \Upsilon(s)$$

With

$$\Upsilon_{(s)} = 2\pi \frac{Cs}{4} \lambda^3 s^4 - \frac{\Delta Z}{2} \lambda s^2$$

While an ideal CTF would possess a uniform value for information transfer across all spatial frequencies, the oscillations of the real CTF results in zero contrast at some spatial frequencies for any given defocus. The greater the defocus, the higher the frequency of the oscillations and so the lower amount of high-resolution information collected.

The overall CTF also suffers from attenuation of high spatial frequency information due to other imperfections in imaging, including imperfect coherency of the electron source, lens and mechanical instability, and detectors imperfections. Computational methods to correct the CTF have been developed and are described in 1.4.2.1.

1.4 Image processing

Each recorded EM image (micrograph) represents all the information of a 3D sample projected onto a single 2D plane. However, computational processing of 2D images can reconstruct 3D information about the specimen. There are two primary ways this is done. Firstly, single particle analysis (SPA). By recording many images of an identical macromolecular complex randomly orientated within a vitreous ice layer, different 'views', or orientations can be classified and averaged to obtain a 2D projection with improved SNR. If the angular relationships between these 2D projections can be determined a 3D object can be reconstructed. Secondly, a tilt series can be collected, where many images are taken across range of tilt angles (typically +/- 60° for tomographic reconstruction), back projecting such a series generates a 'tomogram', or 3D volume representing the specimen. Tilting the specimen can also be applied to 2D crystals as discussed in Section 1.4.1.

1.4.1 Electron crystallography

Electron crystallography applies many of the principles discussed in X-ray crystallography (Section 1.1.3) to '2D crystals'. 2D crystals are one unit cell thick, compared with crystals used for X-ray crystallography which are typically many unit cells wide in X, Y and Z. In order to record sufficient information to extrapolate a 3D structure, the crystal must be tilted and imaged at many tilt angles. This approach has been applied successfully to many proteins, one of the first structures obtained by this technique was bacteriorhodopsin to 3.5 Å resolution (Henderson *et al*., 1990). Other proteins studied using this technique include aquaporins, in one study 1.9 Å resolution was achieved, sufficient to visualise and build a model of protein-lipid interactions (Gonen *et al*., 2005). Electron diffraction can also be performed using very small 3D crystals, a method known as MicroED (Iadanza & Gonen, 2014; Rodriguez *et al*., 2015; Shi *et al*., 2013). Electron crystallography can provide high-resolution information, but ultimately requires the specimen to be crystallised. For

many proteins, especially membrane proteins, this can be challenging and thus limits the applications of this technique.

1.4.2 Single particle analysis

As of December 2015, the Electron Microscopy Data Bank (EMDB) had over 2600 electron density maps generated by SPA, with resolutions below 10 Å becoming routine, and many at near atomic resolution. Below 4.5 Å, the Cα backbone can be resolved, separating beta strands in the density map, and some side chains are visible. Between 4.5-9 Å α helices are resolved. Information above 10 Å can still be invaluable, especially when combined with other structural techniques. For example, homology models of protein subunits of the V-ATPase have been fitted into an EM density map (Rawson *et al*., 2015). Single particle reconstruction has many advantages over crystal-based techniques. Besides the obvious advantage of not needing to grow crystals, outside the confines of a lattice the specimen is able to sample a range of native conformations in solution before being trapped by cryo-fixation. This allows information about conformational changes, and to some extent flexibility, to be elucidated.

SPA traditionally assumes a homogenous population of macromolecular complexes, which are orientated randomly over a full range of orientations. A data set may contain hundreds or thousands of micrographs, containing potentially millions of particles, although many data-sets are much smaller. Particles can then be 'boxed' out of their micrographs, aligned, classified into orientations and averaged to produce 2D 'class averages'. Each particle in a micrograph corresponds to a 2D projection of the 3D structure. SPA relies upon Projection Theorem, which shows that Fourier transforms of the 2D projections represent central slices through the 3D Fourier transform of object (Figure 1-10). In SPA, the angular and translational relationships between each 2D projection are calculated, allowing the generation of a 3D structure. The accuracy of particle alignment is dependent on SNR the of the particle, and the presence of features that can guide alignment. Larger, more 'featured' objects tend to align better, and so SPA has historically most commonly been applied to samples larger than ~1 MDa. However, improved EM and detector hardware, alongside improved imaging processing algorithms mean that ever-smaller complexes are being studied with great success. For example, the structure of beta galactosidase, 0.465 MDa, has been solved to 4.2 Å resolution (Scheres, 2015) and the 0.17MDa γ -secretase complex to 3.4 Å resolution (Bai, Yan, *et al*., 2015).

There are many software packages available for SPA, including SPIDER (Shaikh *et al*., 2008), IMAGIC (van Heel *et al*., 2000), EMAN2 (Tang *et al*., 2007), RELION (Scheres, 2012), Xmipp (la Rosa-Trevin *et al*., 2013) and SIMPLE (Elmlund & Elmlund, 2012). Many of the

steps taken in generating a model in SPA are common to all programs, and so an overview of the general process is now given.

1.4.2.1 Initial processing of micrographs

For data collected on a DED, the first step is usually to perform sub-frame alignment of the micrographs, although due to computational expense this is sometimes performed later in processing (Section 1.4.2.5). As the CTF of the micrograph is dependent on the microscope's defocus, this is determined () A series of concentric rings in the power spectrum of the micrograph, known as Thon rings, are caused by the CTF, and the position of these rings is dependent on the defocus. A number of programmes have been developed to determine defocus and fit the CTF of the power spectrum (the square of the FT), from semi-automated to fully automated methods. One of the most widely used is CTFFIND, developed by Grigorieff and colleagues (Mindell & Grigorieff, 2003; Rohou & Grigorieff, 2015). Once CTF parameters are known for the micrograph, they can be accounted for in later processing stages. For example, phase flipping is commonly applied, which involves phase inversions where the amplitude of the CTF signal drops below zero.

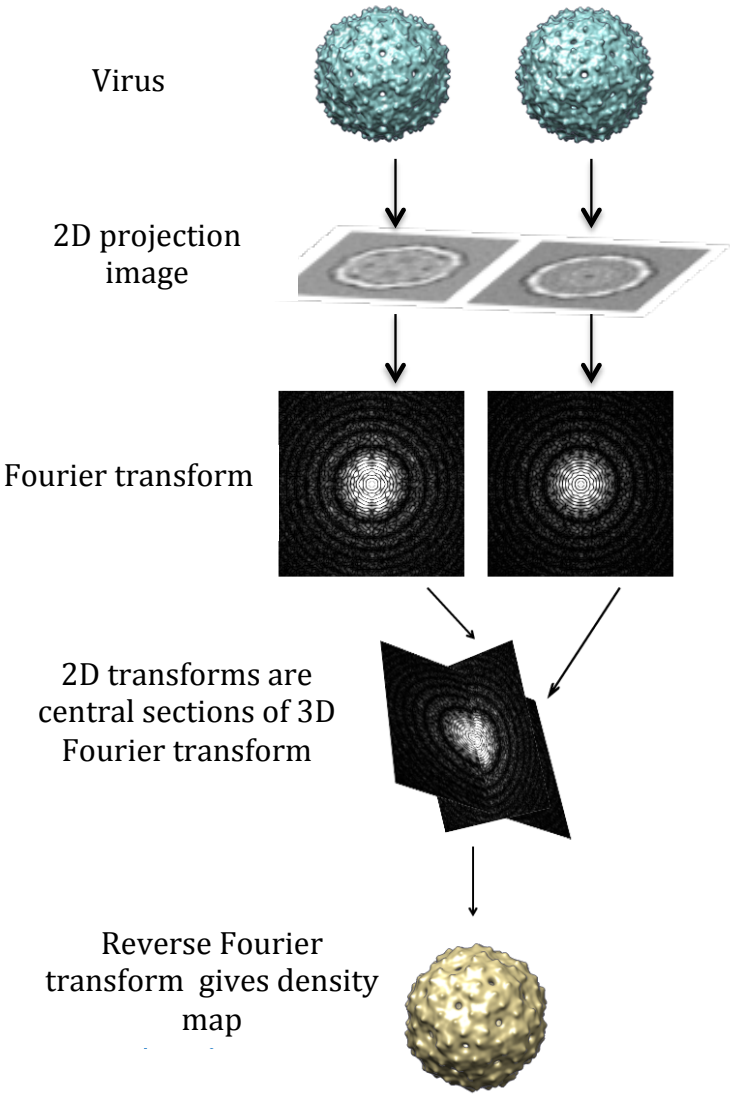

Figure 1-10 Schematic of Projection Theorem. A macromolecular complex adopts an orientation in real/physical space. When imaged by TEM, a 2D projection view is seen. A Fourier transform of this projection represents a central section through the 3D Fourier transform of the 3D structure.

Particles are averaged from different micrographs, taken at a range of defocuses, and so their power spectrum differ (Figure 1-11). This can be utilised during averaging to 'fill in' missing information at certain spatial frequencies in different micrographs. A full CTF correction incorporating Weiner filtering is more usually applied, which flips the image phases as well as rescaling amplitudes at higher spatial frequencies.

Particles are then 'boxed' out, which involves the centre of the particle being defined and a box of a set size being digitally cut out of the micrograph. Defining the centre of the particle is sometimes done manually, but automated and semi-automated particle selection procedures have been implemented as datasets get bigger (Scheres, 2015; Sorzano *et al*., 2009). In RELION, particles from manually picked micrographs are used to generate reference free 2D classes (heavily filtered to prevent the 'Einstein from nose' effect (Henderson, 2013)), which are then used as a template to pick particles from the full data set. The algorithm uses an additive model with white Gaussian noise in real space (Scheres, 2015). Particles are then extracted and normalised to a common mean and standard deviation, as different micrographs in a cryo-EM data set do not have equal SNR and pixel values. In some cases, dust-correction type procedures, which remove pixels that are particularly dark or light, which can bias alignment, are used. Particle sorting methods can also be used to identify and remove incorrectly auto-picked particles (Scheres, 2015).

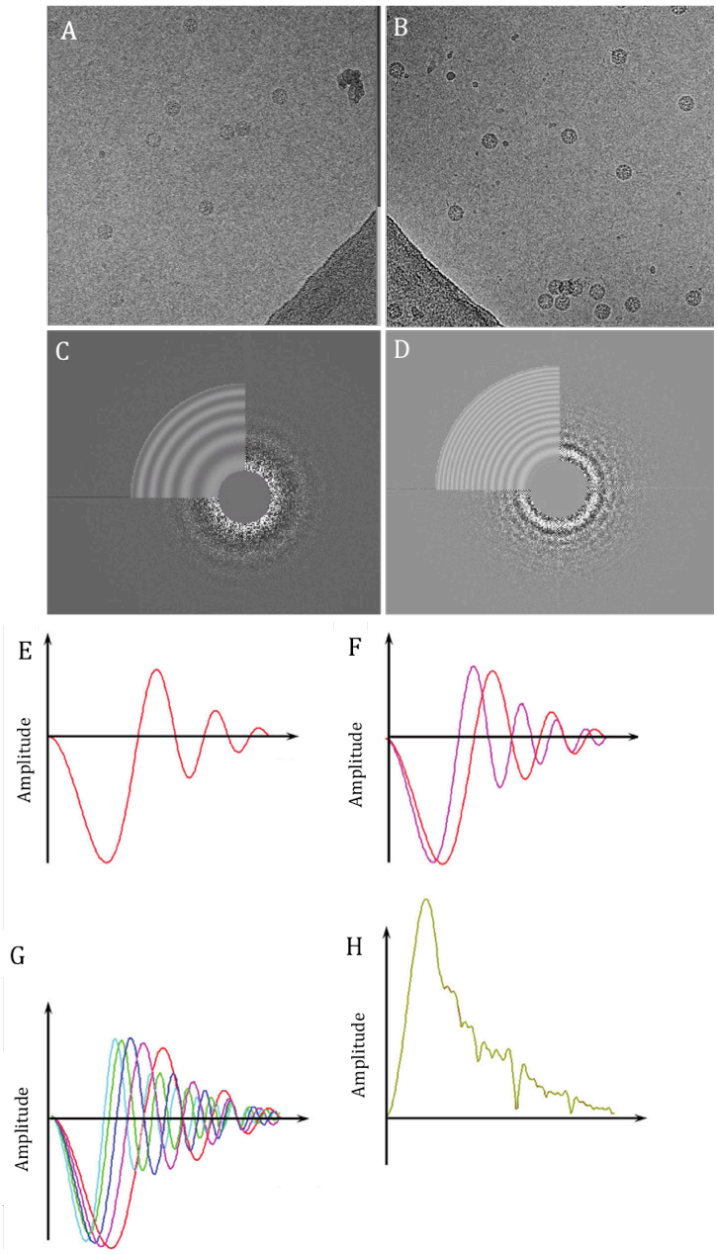

Figure 1-11 CTF correction. Micrographs in a data series are collected at different defoci such as A (1 µm defocus) and B (4 µm defocus); the more defocused the micrograph, the greater the contrast. The power spectrum of the images (C and D) shows the Thon rings, whose position relative to the origin and oscillations can be used to calculate defocus and CTF curves such as shown in E. The CTF is defocus dependent (F- red CTF curve of image closer to focus, purple line further from focus), and so when multiple CTFs are summed (G) and phase flipped (H), the sum total of the spatial frequencies represented in the data can be seen. E-H adapted from Orlova & Saibil, 2011.

1.4.2.2 Classification and alignment

Particle classification and alignment aims to take a series of unaligned, noisy images, calculate their angular relationships and separate a homogenous subset of particles that can be used to generate a 3D structure (Section 1.4.2). Programs such as RELION and XMIPP implement maximum likelihood (ML) algorithms for classification, in order to account for the low SNR of cryo-EM data. In ML classification, probabilities are assigned to class assignments, to account for the fact that there is uncertainty in the assignment. If data were perfect, there would be no difference in the output of ML approaches compared with 'standard' cross correlation approaches.

2D classification can be used to assess the data and remove poor quality particles, although 2D classes are often informative in their own right (Imai *et al.*, 2015). Many

programs use referenced based 2D alignment, which involves using aligning particles to references and calculating the cross correlation in an iterative manner. RELION implements a multi-reference maximum likelihood alignment scheme to simultaneously align and classify particle images. These reference free averages are generated in an unsupervised manner, with the user simply defining the number of classes. The ML approach means all images are compared with all references, in all possible orientations. Probability weights are calculated for each possibility. The classes produced are weighted averages, so every particle contributes to every class. In reality, particles often contribute strongly to one class or a set of similar classes, and weakly to every other class. This process is iterated, typically 25 times. Particles from 'good' classes can then be analysed or taken forward for 3D classification (Scheres, 2010).

A key challenge in 3D reconstruction is the introduction of bias from false assumptions about the spatial relationship between classes. Complexity is also introduced when heterogeneity is present in the dataset, e.g. different conformations of a complex, or different complexes are present (Fernández *et al*., 2013). This can result in a low resolution, or even a completely artefactual map being generated. These issues can be tackled by the use of multi-reference ML refinement, such as implemented in RELION, which can be used to perform unsupervised classification of structurally heterogeneous datasets (Scheres *et al*., 2007). A low-resolution (~60 Å) starting model is used, and the user defines an arbitrary number of 3D models to be simultaneously refined, which should ideally reflect the number of conformations present in the dataset. The process is iterated until the number of particles that change their optimal orientation/class has stabilised, and the log-likelihood increase has levelled off, indicating the refinement has converged. 3D classification can be performed in a hierarchical manner, enabling structures of lowly populated conformations to be generated (Fernández *et al*., 2013). One drawback of the 3D ML classification is that it is computationally expensive, and so down-sampling or binning the particles and/or limiting the angular sampling rate is sometimes necessary, depending on the computational resources available and the size of the particle.

Once a subset of sufficiently homogenous particles has been generated, the structure can be refined to high resolution. The 'gold standard' Fourier Shell Correlation (FSC) is used to calculate the agreement between two independently refined halves of the dataset, and provide a measure of the resolution. In RELION, the procedure estimates the accuracy of angular assignments and automatically determines when the refinement has converged (Scheres, 2012).

1.4.2.3 B-factor correction and map sharpening

Sub-nanometer resolution SPA structures are now routine (Bai *et al*., 2013). At these high resolutions, information is lost both because of experimental factors, including beam induced movement and radiation damage, and computational factors such as inaccurate determination of angular orientations. Traditionally, this loss was modelled by a Gaussian decay of structure factors with a temperature factor, or *B*-factor, but this approach significantly affects high-resolution features and makes identification of secondary structure elements challenging (Fernandez *et al*., 2008). These high-resolution features must be restored, or 'sharpened' to bring out features in the map. A method was developed to estimate the amplitude decay of the structure factors by comparison with a theoretical scattering curve, along with a weighting function to account for the noise in the map (Rosenthal & Henderson, 2003). The weighting function is needed to avoid the amplification of noise and increase robustness against over-fitting. This method removes the need for *ad hoc B*-factor assignment. Programs are available to implement this *B*-factor correction method, such as EM-BFACTOR (Fernandez *et al*., 2008), and sharpening by this method is implemented in RELION (Chen *et al*., 2013).

The assessment of resolution and model validation is the subject of (heated) on-going discussion in the EM community. Over fitting of data can lead to inflated resolution claims and erroneous interpretation of the resulting density. Tilt pair validation can be used to validate 3D structures, which involves taking a micrograph of the sample at 0^0 and at a tilt, typically $\sim 30^0$. These images are then compared with their predicted projections of the 3D map. The output from this process is a tilt pair parameter plot, clustering patterns of can provide a confident validation of the structure (Henderson *et al*., 2011). An online server is available to enable tilt pair validation to be achieved (Wasilewski & Rosenthal, 2014).

The use of a 'gold standard FSC' procedure is currently generally accepted as the optimal method for assessing the resolution of cryo-EM density, which measures self-consistency within the dataset. A correlation threshold is used to assign the resolution to the final reconstruction. 0.143 has been suggested as the most appropriate threshold to use as an indication of the true resolution of the map (Scheres & Chen, 2012).

The gold standard FSC calculates the global resolution for a density map, but algorithms have been developed to assess local resolution. This can be extremely informative, as resolution can vary considerably across the structure. One such tool is ResMap, which functions by testing each voxel 3D pixel (Kucukelbir *et al*., 2014). The theory is based on the idea that if a λ- Å feature exists at a voxel, a 3D local sinusoid of λ is statistically

detectable above the noise (calculated from the surrounding voxels). At a given λ, a likelihood ratio test is used to evaluate the λ- Å sinusoid model, and a false discovery rate control is applied. The local resolution at a voxel is defined as the smallest λ at which the local sinusoid is detectable. Using this method there are no parameters to tune, and the local resolution is defined unambiguously at a given *P* value (Kucukelbir *et al*., 2014). Local resolution analysis is most commonly applied to sub-nanometer structures, but can also be performed on tomographic data and other imaging modalities, whose resolution may be much lower (Kucukelbir *et al*., 2014).

To assess the quality and features of density maps, it is often useful to visualise the full map rather than simply 2D figures in a paper. As a prequisite for publication, many journals now require the deposition of EM derived density maps into public archives such as the EMDB, which is the single biggest global archive for EM derived structures, with over 3400 entries to date from single particle experiments, 2D electron crystallography, helical reconstruction, tomography and sub-tomographic averaging (Patwardhan *et al*., 2014).

1.4.2.4 Applying symmetry

Many biological specimens possess symmetry; there is a strong tendency for symmetry in complexes, even for heteromeric complexes, and many viruses possess icosahedral symmetry (Chapter 5)(Levy *et al*., 2006; Bhella & Bakker, 2013). This symmetry can be exploited when generating 3D reconstructions. For example, icosahedrons are built from 60 asymmetric units. In the projection of an icosahedral structure, the asymmetric unit is visualised in 60 orientations. The redundancy of information can be utilised by averaging when the orientation of the view is known. While utilising a sample's symmetry greatly improves reconstructions, any asymmetric features, which do not conform to that symmetry, will be lost. For example, the genomes of icosahedral viruses will be inappropriately symmetrised when icosahedral symmetry is applied. Computational methods are now being developed to aid structure determination of complexes with symmetry mis-matches (Liu & Cheng, 2015).

1.4.2.5 Movie processing

Under cryo-EM imaging conditions, biological samples undergo radiation damage and beam induced movement, and charging of the specimen is sometimes observed. These factors contribute to typical images being poorer than they might be in theory (Henderson, 1992). Recent advances in detector technology, specifically the development of DEDs (Section 1.3.4), help to ameliorate some of these effects. Along with their high DQE, DEDs record images at a high rate (16-44 images/s), meaning that 'movies' of an

exposure can be taken (Bai *et al*., 2013). In RELION, a trajectory for particles can be calculated through the exposure, and has subsequently corrected. There are several algorithms available for this calculation/correction (Li *et al*., 2013; Scheres, 2014). This methodology was initially developed on large (>1 MDa) complexes such as the ribosome and icosahedral viruses (Bai *et al*., 2013), and subsequently been used to correct smaller specimens (X. Li *et al*., 2013; Scheres, 2014; Rubinstein & Brubaker, 2015).

1.4.3 Electron tomography

The word tomography originates from two Greek words; Tomos meaning 'to slice' and graph meaning 'image' (Luci c *et al*., 2005). Whereas SPA allows (relatively) homogenous specimens to be examined, ET can be used to generate 3D information of 'unique' structures, including areas of the cell, organelles and pleomorphic viruses such as HIV, herpes and measles (Liljeroos *et al*., 2011; Ibiricu *et al*., 2011; Carlson *et al*., 2010; Van Driel, *et al*,. 2009). ET provides molecular resolution, typically between 4-10 nm. Tomography involves taking a tilt series of images, each representing a slice of information related by the known angular relationship between each tilt. The tilt series is aligned and back projected, creating a 3D volume known as a tomogram.

Single axis tilt series are routinely collected from +/- 60°, with a tilt increment of 1-3° (Figure 1-12), although dual axis data collection is possible The tilt range that can be achieved is limited by the thickness of the sample and hardware constraints of the EM, which requires the grid to be secured by a specimen arm, which is much thicker than the grid itself. As the tilt series collected does not represent the full angular sampling of the specimen, some information is missing. In a single axis tilt series this is known as the 'missing wedge', and in a dual axis tomogram a 'missing pyramid'. This missing information leads to distortion and elongation along the Z-axis, but sub-tomographic averaging of repeating features within tomograms can be used to correct for this (Section 1.4.3.2).

ET is typically carried out using 200-300 keV microscopes, whose electrons can penetrate the specimen better and are less likely to be inelastically scattered compared with lower energy electrons. Electron dose is a key consideration when collecting tilt series. As many images are collected in one area, very low electron doses must be used for each image to prevent radiation damage. For specimens under cryogenic conditions, typical doses are below 120 $e^-/Å^2$. However, for some specimens, total dose must be kept even lower. Weibel-Palade bodies exposed to a total dose of > 50 $e^-/Å^2$ 'bubble' and become damaged, compared with surrounding organelles which are unaffected, possibly because of their extensive glycosylation (Berriman *et al*., 2009).

1.4.3.1 Construction of the tomogram

There are two main methods used to reconstruct an aligned tilt series into a tomogram; back-projection and simultaneous iterative reconstruction technique (SIRT). Back-projection reconstructions can be carried out in real or reciprocal space. In real space, 2D density is 'smeared' along lines into a 3D volume at angles predefined by the relative orientations of each 2D projection. This is an 'unweighted' back-projection, and results in blurry reconstructions. Many programs to reconstruct tilt series use weighted algorithms, such as IMOD which has the option of R-weighted back projection (Gilbert, 1972; Kremer *et al*., 1996). SIRT initially generates a trial tomogram, reprojecting images at the stated tilt angles, and then adjusts the tomogram for the differences between the original projections and the new reprojections. This process is iterated to achieve a balance between noise and signal. In the first iterations, the tomogram is dominated by low frequencies, leading to blurry features. As iterations progress, higher frequency information is added, but so is some noise. SIRT will not intrinsically produce a reconstruction where different spatial frequencies possess the correct relative magnitudes, as back-projection does.

For images collected with the sample tilted, CTF correction is challenging. Not only do the images possess poor signal to noise ratio due to the low doses used, but the defocus also varies across the image due to the tilt. Programs have been developed to enable CTF correction of this type of data, such as CTFPLOTTER (Xiong *et al*., 2009). It functions by taking a 1D power spectrum by periodogram and rotational averaging, then estimates the noise background by comparing with micrographs of no specimen. The background is then subtracted from the power spectrum. Regions of the image at different defocus values are then shifted to align their first zeros, and averaged together. This averaging improves the SNR so that it becomes possible to determine the defocus for subsets of the tilt series. Once the defocus is known, phase flipping can then be applied as in Section 1.3.8.1.

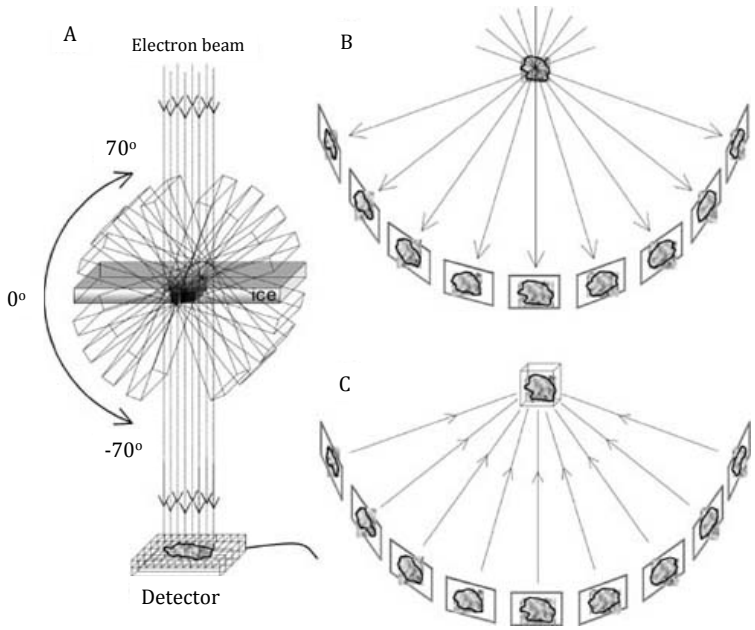

Figure 1-12 Electron tomography. A) The specimen holder is tilted incrementally around an axis perpendicular to the electron beam. Projection images of the same object of interest are recorded at each tilt angle. Tilt increments are typically 0.5° to 5° and the tilt range is about ±70°. B) The 2D projection images of specimen at successive tilt angles. These are translationally and rotationally aligned. C) Aligned 2D projection images are reconstructed into a 3D density map or tomogram by a weighted-back projection or SIRT. Adapted from Steven & Belnap, 2005

1.4.3.2 Interpretation of tomograms and sub-tomographic averaging

The interpretation of cryo-ET data can be challenging, not only because of the poor SNR of the tilt series, the microscopes' CTF, and the missing wedge of information, but also because the samples are crowded. As a result, tomograms are often 'segmented' to make visualisation and interpretation easier. Segmentation involves tracing features of interest through the slices of a tomogram, so that when the tomogram is removed, a 3D representation of the features remains. Segmentation can be performed manually, and often is for noisy cryo-data. Programs are available to aid the segmentation process, including IMOD and Amira (FEI) (Kremer *et al.*, 1996). Manual segmentation can be time consuming and is subjective. Various surface fitting approaches have been developed to improve upon manual segmentation, such as spatial gradient optimisation in 2D (Volkmann, 2010). Other approaches include those that detect distinct regions, such as watershed algorithms (Volkmann, 2002).

Just as in SPA, where averaging is used to increase the SNR of a particle of interest; sub-tomographic averaging is used to align and average copies of identical features, which can be taken from multiple tomograms. This increases the SNR and fills in the missing

wedge/pyramid of information. Commonly, classification is carried out prior to averaging, as all features may not be identical.

Sub-tomographic alignment of randomly orientated objects is complicated by the presence of the missing wedge/pyramid of information. As a result, weighted averaging algorithms must be used to compensate. These function by locating the missing wedge and mapping each non-zero Fourier component into the aligned volume (Nicastro *et al*., 2006). Methods have also been developed to enable the classification of features with missing wedges of information. These algorithms constrain similarity comparisons to regions of Fourier space outside of the missing wedge, but which are shared between features (Förster *et al*., 2008). This constrained approach is known as constrained cross-correlation, and enables classification of sub-tomograms on structural features rather than missing wedge artefacts. Sub-tomographic averaging has been used to study the structure of many complexes to sub nanometer resolution for example the features of the HIV-1 capsid at 8.8 Å resolution (Schur *et al*., 2015).

1.5 Finding the needle in the haystack

Cryo-electron tomograms have poor SNR, so how can features by unambiguously identified? Objects such as mitochondria and cytoskeleton can be confidently assigned based on morphology, but this is not the case for many structures. In addition, increasingly EM is being used to study spatially and temporally rare events, such as endocytosis and virus entry into cells (Ibiricu *et al*., 2011; Gan & Jensen, 2012). As a result, methods have been developed to enable researchers to find the 'needle in the haystack' in a sample, and to aid functional interpretation.

Fluorescence microscopy in combination with fluorescent markers and cloneable fluorescent tags have lead to huge advances in cell biology (Tsien, 1998; Chang *et al*., 2014; Paez-Segala *et al*., 2015). Through the use of different fluorescent labels, the spatial and temporal location of many proteins or cellular components can be simultaneously tracked. There have been two main approaches to replicate this kind of functionality in EM, the generation of tags/markers of points of interest, and correlative light electron microscopy (CLEM).

1.5.1 Correlated light-electron microscopy

Correlative methods have been developed to combine information from two or more types of microscope that offer complementary information, overcoming the limitations of each individual technique and allowing more complex biological questions to be addressed. The two key questions when designing a CLEM experiment are which microscopy techniques

to combine, and how to perform the correlations. Many different microscopy techniques have been combined and solutions for correlation determination developed.

1.5.1.1 Performing correlations

Methods for correlating information from two or more microscopy techniques fall into two categories. The first are integrated microscopes, capable of two imaging modalities. Often, software is available with these set-ups to aid correlations, which usually relies on a fiducial marker system to ensure accuracy. As the sample does not move between instruments, the risk of damage and contamination is reduced, and an area of interest can be located in one imaging mode then imaged directly using another. Dual mode imaging instruments are very convenient. The second category involves performing the imaging on two separate instruments, and a fiducial marker system to navigate to the region of interest in the second imaging mode. While correlations of this kind can be more difficult to implement, they are often cheaper and more flexible than integrated systems.

Two of the most commonly combined imaging techniques are fluorescence microscopy with TEM. One commercially available option is the FEI iCorr system, which integrates a fluorescence microscope (FM) into a Tecnai G^2 microscope (Agronskaia *et al*., 2008). A 15 x 0.5 NA lens is integrated; one laser line is fitted allowing the imaging of GFP, AlexaFluor488 or other spectrally similar fluorophores. The FM sits within the vacuum of the EM and is mounted perpendicular to the electron beam of the TEM, meaning the grid is rotated by 90° to switch between imaging modes. In-column fluorescent microscopes have also been implemented for cryo-XM. For example, a system is available at the BESSY II U41-XM beamline with an integrated 100 x objective with a 0.75 NA (Schneider *et al*., 2012). Bright field, fluorescence and DIC images can be collected, with a retractable objective lens (Schneider *et al*., 2012). A similar system has been implemented at the Diamond Light Source, a Carl Zeiss cryo-XM, which has an integrated epi-fluorescence microscope with a 20 x 0.42 NA lens (Dent *et al*., 2014). In this set up, the sample is rotated to enable imaging in bright field, epi-fluoresence or reflective modes (Dent *et al*., 2014).

While integrated dual mode microscopes are convenient, commercially available equipment can be prohibitively expensive. The technical complications of combining two microscopes into one often mean that compromises are made, for example in the FEI iCorr system a poor magnification and NA of the lens. Integrated systems are also inflexible and have a fixed configuration. An alternative to integrated dual mode microscopes is to image on two separate instruments and perform correlations to allow navigation back to the point of interest. Cryo-FM is now increasingly being used in conjunction with TEM. It has

been demonstrated that fluorophores still fluoresce under cryo-conditions, and in fact photobleaching is slowed (Schwartz *et al*., 2007).

Several stages have been designed to perform cryo-FM on both upright and inverted optical systems, and a wide range of microscopy techniques can be performed under cryogenic conditions including confocal microscopy and z stack imaging (Sartori *et al*., 2007; Schwartz *et al*., 2007; Van Driel *et al*., 2009). Very low cost cryo-light microscopy stages (< $40 USD) have been developed from materials commonly found in hardware stores, although their functionality and stability is limited compared with commercial models (Carlson & Evans, 2011). The most commonly used commercial cryo-FM stages are the cryostage^2 by FEI, developed with Baumeister and colleagues (Rigort *et al*., 2010), and the Linkam cryostage (Linkam Scientific Instruments) in collaboration with Koster and colleagues. The Linkam stage can be fitted to a variety of commercially available upright confocal microscopes, and can function with a 0.75 NA 100 x lens, which sits in the lid of the holder. The resolution of cryo-FM is limited by the NA of the lens used, for the Linkam system ~ 400 nm. The lens has a relatively long working distance (4 mm), which allows it to sit in the heated lid close to the specimen without freezing. The stage has been designed to minimise contamination in both sample transfer and during imaging, although contamination is still a significant problem when performing grid transfer and imaging. Stages of this design have been widely used to perform cryo-FM and correlate with TEM and cryo-XM (Section 1.5.1.2).

With cryo-FM stages, markers across several orders of magnitude in scale must be used to navigate to the region of interest between the FM and TEM. Grids with large visual markers such as numbers, letters or symbols can be used for crude navigation. Features within a grid square, such as regular Quantifoil carbon holes can also be used for crude correlations. For greater accuracy, different systems and software programs have been developed. In many approaches, a low magnification 'map' of the grid is generated. These maps are likely to be different scales, magnifications, rotations and even mirrors of each other and so several transformations may be needed to bring the maps into register. Different features in the maps may have very different contrast levels in the different imaging techniques, for example cells in the light microscope appear light/translucent but in the TEM are dark, and as a result simple cross correlation approaches are often not effective. Algorithms have been developed to enable featured based transformations, for example scale invariant feature transformation, which is implemented in the TOM^2 software program (Korinek *et al*., 2011). Accuracy of correlations in each of these approaches is limited to 1-2 μm. Methods have been developed to perform more accurate

correlations. For example, when imaging resin embedded sections, correlations with an accuracy of ~100 nm can be performed by using fluorescent, electron dense microspheres as fiducial markers (Kukulski *et al*., 2011; Kukulski *et al*., 2012). A similar system has now been developed for cryo-FM/EM, using a combination of TetraSpek fluorescent microspheres and fluorescent electron dense microspheres to perform accurate correlations to ~ 60 nm (Schellenberger *et al*., 2014).

Fluorescent, electron dense markers such as quantum dots (QD) are ideal for correlations. QDs are typically made of cadmium selenide or similar, with a shell such as zinc sulphide (Giepmans *et al*., 2005). They can be covered with a polymer which allows a wide range of functionalisation, for example with streptavidin or $F(ab)_2$ fragments (Giepmans *et al*., 2005). The fluorescence properties of QDs are 'tuneable' by their size, with smaller QDs typically fluorescing at shorter wavelengths (E. Brown & Verkade, 2010). In theory, this enables different QDs to be distinguishable in the TEM, however in practice this can be challenging, as their core is not very electron dense (Brown & Verkade, 2010). It has been shown in plastic embedded sections up to three QD sizes can be distinguished (Giepmans *et al*., 2005) QDs are photostable and bright, making them ideal for fluorescence imaging (Medintz *et al*., 2005).

1.5.1.2 Complementary imaging techniques

Many microscopy techniques have now been combined to answer different questions. As shown in Table 1.1, combining different types or resolutions of information has yielded insights into a wide range of biological questions.

In many cases, live cell FM is used to identify the region of interest and the sample is then quickly immobilised (time scale of minutes, typically). Using this method, at the very least, there is a ~30 second gap between the FM image and the EM image, and as a result it is not suitable for studying rapid processes. The alternative approach is to prepare samples for EM prior to imaging with FM. Recently, protocols for preserving the fluorescence of GFP and other fluorophores when processing samples by high pressure freezing followed by freeze substitution and resin embedding/sectioning have been developed (Kukulski *et al*., 2011). This has resulted in a large number of CLEM studies, which perform FM and EM on resin embedded sections. This combination of imaging techniques has been powerful for studying rare temporal events such as endocytosis (Kukulski *et al*., 2012), and is technically less challenging than other forms of CLEM as all imaging can be performed at room temperature. However, freeze substitution, resin embedding and sectioning can introduce artefacts as discussed in section 1.2.1.2. Vitrification of samples is widely

regarded as the best way to retain native-like samples for visualisation in the EM, and so cryo-FM can be used.

CLEM is a developing field, and in coming years many more imaging techniques are likely to be combined. For example, stages are under development to allow super resolution imaging (e.g. PALM/STORM) of frozen-hydrated specimens (Kaufmann *et al.*, 2014). Another interesting area that is likely to expand is using cryo-FM to guide cryo-FIB milling and cryo-ET, which has already been shown to be technically feasible (Rigort *et al.*, 2010). By using this combination of techniques, a molecular resolution view of rare spatial or temporal events in thick regions of the cell such as the nucleus or perinuclear region can be generated (Rigort & Plitzko, 2015).

Study	Imaging technique 1	Imaging technique 2	Reference
Intracellular dynamics	Live cell FM	Immunogold labelling resin embedded cell sections	Polishchuk *et al.*, 2000
GFP labeled proteins	Live cell FM	ET of resin embedded sections (di-aminobenzidine photo conversion using GFP bleaching)	Grabenbauer *et al.*, 2005
Endosome dynamics	Live cell FM	Ultrathin cryo-sections with immunogold labelling	van Rijnsoever *et al.*, 2008
Endocytosis in yeast	FM on resin embedded sections	ET on resin embedded sections	Kukulski *et al.*, 2012
HIV-1 infection	Time lapse live cell FM/cryo-FM	Cryo-ET at thin edge of whole HeLa cells	Jun *et al.*, 2011
Mitochondria	Cryo-FM	Cryo-ET at the thin edge of HUVEC cells	Van Driel *et al.*, 2009
Herpesviridae proteins	Cryo-FM (in column)	Cryo-XM	Hagen *et al.*, 2012
Endosomes	Cryo-FM (Linkam cryo stage)	Cryo-XM	Duke *et al.*, 2014
Adenovirus particles	Cryo-FM (FEI Cryostage^2)	Cryo-EM	Schellenberger *et al.*, 2014

Table 1.1 Topics of study and microscopy techniques combined in CLEM.

1.5.2 EM tags

Recombinantly expressed tags such as GFP have revolutionised optical microscopy, and so researchers have sought to develop similar systems for EM. One of the most developed systems is based on the protein metallothionein (MT). When fused with a protein of interest and treated with gold salts, a single tag will build an electron dense cluster of ~ 1

nm in diameter. This technique has been used to detect intracellular proteins in both eukaryotic and prokaryotic cells (Risco *et al*., 2012; Diestra *et al*., 2009). It can offer improved resolutions compared with immunogold-based techniques, where there can be 15-20 nm between the protein of interest and the marker. MT tags can be used when imaging whole cells, but are also maintained when cells are processed by embedding in acrylic resin and sectioned. While MT tags can replace the need for CLEM in some systems where only one protein must be unambiguously identified, it is possible for the MT tag to be combined with fluorescence tags such as GFP, or smaller cloneable fluorophores such as mini-singlet Oxygen generator (mini-SOG) to ensure the identification of the same macromolecular complexes at different spatial resolutions (Risco *et al*., 2012).

MT tags still have significant barriers to overcome for their use to be as ubiquitous as optical cloneable tags. Complications of this technique include the presence of endogenous MT in many cell types, whose expression is often up regulated upon exposure to metal salts, although studies have shown background from endogenous MT to be negligible (Risco *et al*., 2012). Eukaryotic cells are also particularly sensitive to gold salts and so protocols must be optimised to reduce cytotoxicity. Currently, only one type of tag can be employed, a limitation of the technique. Methods are currently being investigated to enable the labelling of multiple proteins, for example through different sized MT peptides yielding different sized nanoclusters of metal (Fernández de Castro *et al*., 2014).

1.6 Perspectives

For many years, structure determination by electron microscopy was limited to large macromolecular complexes to molecular resolutions, structures much below 10 Å were the exception (Bai, McMullan, *et al*., 2015). Over the last ~ four years, cryo-EM has undergone a 'resolution revolution' as a result of improved hardware such as DEDs and improved image processing techniques (Kuehlbrandt, 2014). For many macromolecular complexes such as the ribosome and proteasome, achieving sub 5 Å resolution is now routine, a feat almost unthinkable a decade ago. Many other samples that historically would have been too small (typically < 500 kDa), or too heterogeneous for high-resolution structure determination by cryo-EM are now within reach, for example the sub 0.5 MDa beta-galactosidase and γ-secretase, and heterogeneous ribosome populations (Scheres, 2014; Bai, Yan, *et al*., 2015; Scheres, 2010). As cryo-EM produces maps of improving resolution, new opportunities are opening to solve structures *de novo* or refine existing crystal structures, using tools originally designed for X-ray crystallography data (Emsley *et al*., 2010; Murshudov *et al*., 1997). Another opportunity for the field is investigating small molecule binding, potentially opening up cryo-EM as a tool for structure based drug design and validation (Bartesaghi *et al*., 2015). Aside from SPA, the new DEDs and phase plate technologies have the potential to revolutionise electron tomography, and correlative microscopy along with FIB milling may revolutionise cryo-EM's contribution to cell biology.

Despite recent advances, many challenges remain. It is still challenging to generate high (< 5 Å) resolution structures for many macromolecular complexes that may be unstable, highly flexible, small (less than 200 kDa), or highly heterogeneous; in reality these challenges may have to be tackled in the laboratory with improved sample preparation. Even the generation of near atomic resolution maps is creating new challenges, for example in model validation. The field has moved rapidly in the last few years, but progress can still be made. Better electron detectors with improved DQEs, implementation of more automation in both data collection and processing, improved understanding of mechanisms of beam induced particle movement and finally improved image processing algorithms are all areas likely to progress the fields ability to generate high resolution structures of a range of macromolecular complexes.

2 Experimental procedures

2.1 Materials

All reagents were supplied by Sigma-Aldrich unless stated in Table 2.1. Buffer and media compositions are shown in Table 2.2. Source of materials is shown in Table 2.3. Pure deionised water (dH_2O) was obtained from a purite water system (Purite ltd).

Reagent	Supplier
1-palmitoyl-2-oleoyl-*sn*-glycero-3-phospho-(1'-*rac*-glycerol (POPG- 840457)	Avanti Polar Lipids
1-palmitoyl-2-oleoyl-sn-glycero-3-phospho-L-serine (POPS)	Avanti Polar Lipids
1-palmitoyl-2-oleoyl-sn-glycero-3-phosphocholine (POPC)	Avanti Polar Lipids
1-palmitoyl-2-oleoyl-sn-glycero-3-phosphoethanolamine (POPE)	Avanti Polar Lipids
1,2-dimyristoyl-sn-glycero-3-phospho-L-serine (DMPS)	Avanti Polar Lipids
2-[[5-[5-(4-hydroxyphenyl)thiophen-2-yl]thiophen-2-yl]methylidene]propanedinitrile (NIAD-4)	ChemShuttle
bis(monoaclglycero)phosphate (BMP)	Avanti Polar Lipids
Complete protease inhibitor mix, ETDA free	Roache Applied Science
Foetal bovine serum (FBS)	Biosera
Isopropyl β-D-1-thiogalactopyranoside (IPTG)	Melford
Luria Bertani (LB) containing per L, 10 g bacto-tryptone, 5 g yeast extract and 10 g NaCl.	Melford
Lysotracker deep red	Molecular Probes
sphingomyelin purified from porcine brain	Avanti Polar Lipids
Supersignal West Pico chemiluminescent substrate	Perbio

Table 2.1 Suppliers of reagents.

Buffer	Components
2 x Laemmli buffer	100 mM Tris-HCl pH 6.8, 20 % (v/v) glycerol, 4 % (w/v) SDS, 0.2 % (w/v) bromophenol blue, 100 mM dithiothreitol (DTT)
Acid phosphatase substrate	5 mM 4-nitrophenyl phosphate in 0.09 M citric acid, pH 4.5
Alkaline phosphatase substrate	5 mM 4-nitrophenyl phosphate in 5 mM magnesium acetate, 70 mM KCl, 5 mM glycine, 0.2% (v/v) Triton X-100, pH 9
Alpha-N-acetylgalactosaminidase (NAGA) substrate	2 mM 4-nitrophenyl N-acetyl- β-D-glucosaminide in 100 mM citric acid, 0.2% (v/v) Triton X-100 pH 4.5
Anode buffer	400 mM Tris-HCl pH 8.8
Bacterial lysis buffer	25 mM Tris-HCl pH 8.0, lysozyme 100 µg/ml, PMSF 50 µg/ml, DNase 20 µg/ml, 1mM EDTA
Blocking buffer	Phosphate buffered saline (PBS), 0.2 % (v/v) Tween-20, 5 % skimmed milk power
Carboxyfluorescein buffer	50 mM sodium phosphate buffer, pH 7.4 containing 50 mM carboxyfluorescein, 10 mM NaCl and 1 mM EDTA
Cathode buffer	200 mM Tris-HCl, 200 mM Tricine, 0.2% (w/v) Sodium dodecyl sulfate,pH 8.25
Cell culture medium	Dulbecco's modified eagle's medium (DMEM), 10 % (v/v) foetal bovine serum, 2 mM L- glutamine, 100 IU/ml penicillin, 100 µg/ml streptomycin
Coomassie brilliant blue stain	50% methanol (v/v), 10% acetic acid (v/v) and 0.25% (w/v) Coomassie Brilliant Blue
Coomassie destain	50 % (v/v) methanol, 10 % (v/v) acetic acid
Dye release buffer pH 4.5	50 mM citric acid/sodium phosphate buffer, pH 4.5, 107 mM NaCl and 1 mM EDTA
Dye release buffer pH 6.5	50 mM citric acid/sodium phosphate buffer, pH 6.5, 107 mM NaCl and 1 mM EDTA
Dye release buffer pH 7.4	50 mM citric acid/sodium phosphate buffer, pH 7.4, 107 mM NaCl and 1 mM EDTA
Optiprep	60 % w/v iodixanol in water
Percoll homogenisation buffer	10 mM acetic acid, 1 mM EDTA, 190 mM sucrose, 10 mM triethanolamine, pH 7.4
pH 2.0 β_2m fibril buffer	10 mM sodium phosphate buffer, 50 mM NaCl, pH 2.0
SDS-PAGE running buffer	25 mM Tris-HCl, pH 8.0, 192 mM glycine, 0.1 % (w/v) SDS
Transfer buffer	15 mM Tris-HCl, 150 mM glycine, 0.02 % (w/v) SDS, 20 % (v/v) methanol

Table 2.2 Buffer and media compositions

Material	Supplier
0.2 μm syringe filter	Millipore
0.4 μm polycarbonate pore	Whatmann
1.5 ml glass vial	Chromacol
3 cm glass bottomed imaging dish- FluoroDish	World Precision Instruments
6 well dish	Corning Costar
96 well plate	Corning Costar
Cell scraper	Grenier Bio-one
Continuous carbon EM grids	Agar Scientific
Lacey EM grids	Agar Scientific
Polyvinylidene fluoride membranes	GE healthcare
Quantifoil EM grids	Quantifoil
Zeba™ spin desalting column	Thermo Fisher
SnakeSkin™ Dialysis Tubing, 3.5K Molecular weight cut off (MWCO)	Thermo Fisher
Tissue culture flasks (75 cm^3 or 175 cm^3)	Corning Costar
Whatman No.1 filter paper	Agar Scientific

Table 2.3 Suppliers of materials.

Antibody	Host	Clonality	Working concentration/ dilution	Supplier (Catalogue number)
Anti- β_2m	Rabbit	Polyclonal	11 μg/ml	DakoCytomation (A0072)
Anti-Calreticulin	Rabbit	Polyclonal	1/2000	Calbiochem (208910)
Anti-Cathepsin D	Goat	Polyclonal	0.4 μg/ml	R&D systems (AF1029)
Anti-Complex I	Mouse	Monoclonal	0.5 μg/ml	Molecular Probes (A21344)

Table 2.4 Primary antibodies used in western blotting.

Antibody	Host	Clone	Working concentration	Buffer	Supplier
A11 Anti-Oligomer	Rabbit	Polyclonal	0.5 ng/ml	PBS, 0.05 % (v/v) Tween-20	Charles Glabe, University of California, Irvine
Anti- β_2m	Rabbit	Polyclonal	11 μg/ml	PBS, 0.2 % (v/v) Tween-20	Dako
WO1 Anti-Fibrillar	Mouse	Monoclonal (WO1)	1 μg/ml	PBS, 0.2 % (v/v) Tween-20	Ronald Wetzel, University of Pittsburgh

Table 2.5 Primary antibodies used for immunoblotting (dot blotting).

Antibody	Host	Clone	Concentration	Supplier (Catalogue number)
HRP-conjugated anti-mouse IgG	Rabbit	Polyclonal	0.1 µg/ml	GeneTex (GTX213112-01)
HRP-conjugated anti-goat IgG	Rabbit	Polyclonal	50 µg/ml	Dako (Po449)
HRP-conjugated anti-rabbit	Goat	Polyclonal	1/5000	BD Biosciences (554021)

Table 2.6 Horseradish peroxidase (HRP) conjugated secondary antibodies used in immnoblotting and western blotting.

2.2 Gel-based techniques

2.2.1 Sodium dodecyl sulphate polyacrylamide gel electrophoresis

Tris-tricine or tris-glycine buffered sodium dodecyl sulphate polyacrylamide gel electrophoresis (SDS-PAGE) was used to separate proteins according to their molecular weight. Components of the layered gels, consisting of stacking and resolving gels, are shown in Table 2.7 and Table 2.8. Gel plates were assembled according to the manufacturer's instructions (Hoefer). The resolving gel mixture was used to fill the gel plates leaving ~ 2 cm air at the top. ~1 ml water-saturated butanol was added to exclude air and ensure a smooth gel. Once set, water-saturated butanol was poured off, and the stacking gel poured. A comb was immediately inserted to create wells for sample loading.

Samples were diluted two fold in 2x Laemmli buffer (Table 2.2) and heated to 95 °C for five minutes before loading onto the gel. Gel samples were subsequently stored at – 20 °C. 15 µl protein marker (Bio-Rad precision plus dual colour protein) was also loaded. For tris-tricine gels, cathode and anode buffers (Table 2.2) were used in appropriate chambers during electrophoresis of the proteins through the gel. A current of 30 mA was applied until the samples entered the resolving gel, at which point the current was increased to 60 mA until the dye front reached the bottom of the gel. For tris-glycine gels, running buffer was used during electrophoresis, and a current of 15 mA applied until the sample entered the resolving gel, when it was increased to 25 mA.

Gels were then stained with Coomassie or probed by western blotting (Section 2.2.2). For Coomassie blue staining, gels were incubated with Coomassie brilliant blue stain for 30 minutes, rocking at room temperature. Gels were then washed in Coomassie destain (Table 2.2) until bands were clearly visible and background staining minimised. Gels were photographed in the InGenius gel documentation system (Syngene).

Gel component	Resolving Gel (ml)	Stacking gel (ml)
30% (w/v) Acrylamide: 0.8% (w/v) bis-acrylamide	7.5	0.83
3 M Tris.HCl, 0.3% (w/v) SDS pH 8.45	5	1.55
dH_2O	0.44	3.72
Glycerol	2.0	-
10 % (w/v) ammonium persulphate	0.05	0.1
Tetramethylethylenediamine (TEMED)	0.005	0.005

Table 2.7 Tris-tricine buffered gel components.

Gel component	Resolving Gel (ml)	Stacking gel (ml)
30% (w/v) Acrylamide: 0.8% (w/v) bis-acrylamide	3.33	0.83
3 M Tris.HCl, 0.8% (w/v) SDS pH 8.8	1.35	-
1 M Tris.HCl, 0.8% (w/v) SDS pH 6.8	-	0.63
dH_2O	5.31	3.4
10 % (w/v) ammonium persulphate	0.05	0.1
Tetramethylethylenediamine (TEMED)	0.005	0.005

Table 2.8 Tris-glycine buffered gel components

2.2.2 Western Blotting

Tris-glycine SDS-PAGE was carried out as described above. Gels were transferred onto polyvinylidene fluoride membranes using a semi-dry electrophoretic transfer cell (Bio-rad) according to the manufacturers instructions, using transfer buffer, at 12-20 V for 1-2 hours. Membranes were blocked with blocking buffer for 1 hour (h) rocking at room temperature, then incubated with primary (1°) antibodies as specified in Table 2.4 for 16 h at 4 °C. Membranes were then washed at least three times for 5 minutes in blocking buffer (Table 2.2) before being incubated with secondary (2°) antibody for 1 h at room temperature. Membranes were washed a further two times in blocking buffer. Antibody binding to the membrane was detected using chemiluminescene detection with Supersignal West Pico chemiluminescent substrate and medical imaging film (Fujifilm). Film was developed on a Kornica SRX-101A developer.

2.2.3 Immunoblotting (dot blotting)

Fibril samples or controls (2.8 µg protein, monomer equivalent, per dot) were applied to nitrocellulose membrane (Hybond-Enhanced Chemiluminescence, GE Healthcare) and dried at room temperature. Negative controls were used for all blots. The buffer for each antibody varies in concentration of Tween-20, appropriate buffers for each antibody are shown in Table 2.5. For β_2m and A11 blots membranes were blocked with 10 % (w/v) skimmed milk powder (Marvel) in appropriate buffer (Table 2.5) for 16 h at 4 °C. For WO1 blots, blocking was performed by incubation with appropriate buffer containing 3 % (w/v) bovine serum albumin (BSA) for 16 h at 4 °C.

During 1°antibody incubation, for A11 and anti-β_2m dot blots, samples were incubated with 1° antibody in appropriate buffer containing 5 % (w/v) skimmed milk powder for 1 h

at 25 °C (Table 2.5). For WO1 blots, samples were incubated with 1° antibody in appropriate buffer containing 3 % (w/v) BSA for 16 h at 4 °C. For all antibodies, membranes were washed three times in appropriate buffer before incubation with horseradish peroxidase (HRP) conjugated 2° antibody (Table 2.6), in appropriate buffer (Table 2.5). The membranes were washed three times with appropriate blot buffer, before visualisation of antibody binding using Supersignal West Pico chemiluminescent substrate and medical imaging film (Fujifilm), developed on the Konica SRX-101A developer.

2.3 Expression and purification of recombinant β_2m

2.3.1 Expression of β_2m in E.coli

BL21 DE3 cells transformed with pINK plasmid containing the human gene for β_2m (Kad *et al* 2003) were streaked out onto an Lysogeny broth (LB) agar plate. Throughout this expression LB supplemented with 100 mg/ml carbenicillin was used. A single colony was used to inoculate two flasks of 100 ml LB broth. Flasks were incubated at 37 °C in a shaking incubator (200 rpm) for 16 hours. These cultures were then used to inoculate 10 x 1 L LB broth in 2.5 L flasks. 10 ml of culture per flask was used to inoculate each flask, which was incubated at 37 °C, 200 rpm and OD_{600} monitored periodically in a spectrophometer (Amersham Biosciences) until it reached 0.6. IPTG was then added to a final concentration of 1 mM to each flask and the cultures further incubated for 16 h. Cells were harvested using a continual action centrifuge (Heraeus centrifuge stratus 3049 with a continuous flow rotor, 15,000 rpm).

2.3.2 Inclusion body isolation

The cell pellet was resuspended in 100 ml bacterial lysis buffer and agitated at room temperature for 30 minutes. Cells were further lysed using a cell disruptor operating at 20 kPSi (Constantsytem). Lysed cells were centrifuged at 15,000 rpm (Beckman JLA 16.250 rotor) for 30 minutes, 4 °C. The supernatant was discarded and a lipid film on top of the pellet removed by gently scraping with a spatula, before re-suspending the pellet containing inclusion bodies in 25mM Tris-HCL, pH 8.0. This process was repeated until the pellet appeared a pale cream colour devoid of cellular debris (typically 3-5 times). After the final wash step the pellet was resuspended in 25 mM Tris-HCL pH 8.0, 8 M urea, and agitated at room temperature for 16 h to resolubilise β_2m. The solution was then centrifuged at 15,000 rpm at 4 °C, 30 minutes, to remove precipitate and the supernatant taken forward for dialysis.

2.3.3 Refolding by dialysis

Protein from inclusion body isolation was dialysed against 5 L of 25 mM Tris-HCL pH 8.0 in 3500 MWCO dialysis tubing at 4 °C, with the buffer changed 6 x over 48 hours. Post dialysis, precipitate was removed by centrifugation at 15,000 rpm at 4 °C for 30 minutes.

2.3.4 Anion exchange

Refolded protein was separated from contaminants using a XK50 column (GE healthcare) containing ~200 ml fast flow Q-Sepharose. The column was washed with 5 x column volume of dH_2O before being equilibrated with 25 mM Tris-HCL pH 8.0 until steady UV conductivity baselines were achieved. The protein was applied to the column and the column further washed with 2 X column volume of equilibration buffer. Protein was eluted from the column using 0.5 M NaCl. Fractions containing recombinant protein were pooled and freeze-dried before storage at -20 °C.

2.3.5 Gel filtration

Monomeric β_2m was further separated from contaminants and higher order aggregates using a Superdex 75 gel filtration column attached to an AKTA *prime*-GE Healthcare Chromatography System. The column was washed with dH_2O until absorbance at 280 nm (A_{280}) and conductivity traces stabilised, and then washed with 25 mM Tris-HCL pH 8.0. Protein was resuspended to 20 mg/ml in 25 mM Tris-HCL pH 8.0, filtered, and 5 ml injected onto the column. Protein was eluted using the programme illustrated in Table 2.9. Fractions containing β_2m were pooled and dialysed against 5 L dH_2O in 3500 MWCO dialysis tubing at 4 °C, with the buffer changed 3 x over 24 hours before freeze drying and storage at -20 °C. Protein molecular weight was determined by electrospray ionisation mass spectrometry (ESI-MS) by James Ault, University of Leeds.

Parameters for Superdex 75 gel filtration column programme Breakpoint (ml)	Flow Rate (ml/min)	Fraction Size	Buffer Valve position	Inject Valve position	Set Peak collect	Auto zero	Event mark	Time after run start
0	2	0ml	1	Load	No	No	No	-
10	2	0ml	1	Inject	No	Yes	Yes	5 min
20	2	0ml	1	Load	No	No	Yes	10 min
110	2	3ml	1	Load	No	No	Yes	60 min
360	2	0ml	1	Load	No	No	No	180 min

Table 2.9 Programme for the collection of protein using the AKTA *prime* GE Healthcare Chromatography System with Superdex 75 gel filtration column.

2.3.6 Quantifying protein concentration

Protein samples were diluted to obtain UV absorption values at 280 nm of between 0.1 and 1.0. Protein solutions were diluted into 6 M Guanidine-HCL, 20 mM NaPi, pH 6.5 to a final volume of 200 μl. All absorption values were acquired using a reference standard of buffer-only solutions. Protein concentrations were determined using Beer-Lambert's law. Wild-type β_2m has an extinction coefficient of 20065 $M^{-1}.cm^{-1}$ (Gill & Hippel, 1989).

2.3.7 Labelling of β_2m with a fluorescent dye

Alexa Fluor ® 647 succinimidyl ester (10 mg/ml in DMSO) was added dropwise to monomeric β_2m (10 mg/ml 0.1 M sodium bicarbonate pH 8.3) at a volumetric ratio of 1:20 dye:protein and incubated at room temperature for 1 hour. A 2 ml Zeba™ spin desalting column with a 7 K MWCO, was used according to manufacturers instructions. The column was equilibrated with dH_2O and the sample was loaded and eluted in dH_2O. Monomeric β_2m-Alexa Fluor conjugate was lyophilised and stored at -20 °C. ~ 33 % labelling was confirmed using ESI-MS, performed by James Ault, University of Leeds.

2.3.8 Formation of β_2m fibrils

Seeds for β_2m fibrillation were generated by agitating a 500 μl aliquot of 120 μM β_2m monomer in pH 2.0 β_2m fibril buffer (Table 2.2) for three days in a glass vial with a polytetrafluoroethylene (PTFE) coated magnetic stirring bar, stirred in a custom built precision stirrer (Workshop of the School of Physics and Astronomy, University of Leeds) at 1000 rpm, room temperature. Two batches of seeds were used to generate all fibrils for this project. Morphological consistency between seeds was confirmed using negative stain EM.

For the formation of amyloid fibrils, lyophilised β_2m monomeric protein was passed through a 0.2 μM syringe filter and dissolved in pH 2.0 β_2m fibril buffer. Protein concentration was adjusted to 120 μM and seeded with 0.1 % (v/v) seed. Sample was incubated quiescently at room temperature for 24 h to generate long, straight (Ls) β_2m fibrils. Fragmented long, straight fibrils (Ls-f) were generated by agitating a 500 μl aliquot of Ls fibrils (120 μM β_2m monomer equivalent, in pH 2.0 β_2m fibril buffer) in a 1.5 ml glass vial with a PTFE coated magnetic stirring bar, stirred in a custom built precision stirrer at 1000 rpm at room temperature for 48 h.

Fluorescently labelled fibrils were generated by mixing unlabelled monomer with labelled monomer at a ratio of 1:9, resulting in an approximate overall labelling density of ~3/100 monomers labelled with Alexa Fluor® 647.

Amorphous β_2m aggregates were generated as previously described (Jahn *et al*., 2008). 120 µM monomer equivalent β_2m in 10 mM sodium phosphate, pH 5.0 was heated to 60 °C for 1 h.

2.3.9 Small molecule binding to amyloid fibrils

2.3.9.1 Thioflavin-T

Samples containing 6 µM protein and 10 µM thioflavin-T (ThT), pH 2.0 fibril buffer were incubated for 10 minutes at 25 °C. Fluorescence intensity at 440 nm excitation and 480 nm emission was measured using a Photon Technology International (PTI) Quantmaster fluorescence spectrometer, with a slit width of 3 nm.

2.3.9.2 NIAD-4

Samples containing 12 µM β_2m monomer/Ls-f (monomer equivalent) and 7.5 µM NIAD-4 were diluted into pH 2.0 β_2m fibril buffer, dye release buffer pH 4.4 or dye release buffer pH 7.4 (Table 2.2). Samples were incubated at 25 °C for 10 minutes. Fluorescence emission spectra were measured using a PTI Quantmaster fluorescence spectrometer at an excitation wavelength of 500 nm with a slit width of 6 nm, with emission measured between 520-740 nm with a slit width of 8 nm. Emission spectra were normalised against 7.5 µM NIAD-4 in respective buffer.

2.4 Atomic force microscopy

AFM was performed and analysed by Kevin Tipping. Samples were prepared for tapping-mode AFM by diluting samples to 0.4 µM monomer equivalent concentrations in dH_2O. 20 µl of sample was deposited onto freshly cleaved mica and incubated at room temperature for 5 min. Surfaces were then washed with 1 ml of dH_2O before gently aspirating the surface with a stream of N_2 gas to complete dryness. Samples were imaged using a Dimension 3100 scanning probe microscope (Veeco Instruments) and PPP-NCLR silicon cantilever probes (Nanosensors, Neuchatel, Switzerland) with a nominal force constant of 48 N/m. Typically, 10 μm^2 images at a pixel ratio of 1024 x 1024 were collected for analysis. To generate fibril length distributions, images were analysed using scripts generated in Matlab (Mathworks) by Dr Wei-Feng Xue (Xue *et al*., 2009).

2.5 Cell culture

RAW 264.7, HeLa and SH-SY5Y cells were cultured in cell culture media (Table 2.2) at 37 °C, 5 % CO_2, in 75 cm^3 or 175 cm^3 tissue culture flasks and passaged when they reached ~ 80 % confluency. RAW 264.7 cells were passaged using a cell scraper. HeLa and, SH-SY5Y cells with 1 % Trypsin-EDTA solution.

For imaging in the electron microscope, cells were grown on EM grids (Section 2.11) by seeding at 250,000 cells/ml into a 6 well dish, with EM grids pre-irradiated with UV for 30 minutes placed into the bottom of the dish. Cells were incubated at 37 °C, 5 % CO_2 for 16 h before vitrification (Section 2.11.3).

2.5.1 MTT cell viability assay

RAW 264.7 cells were plated into 96 well dishes, 500,000 cells/well and cultured for 16 h. 1.2 μM monomer or monomer equivalent fibril sample, buffer, or 0.1 % w/v sodium azide were added to wells, and cells further incubated for 24 hours. Cells were then incubated with 3-(4,5-Dimethylthiazol-2yl)-2,5-diphenyltetrazolium bromide (MTT) at a final concentration of 0.5 mg/ml for 1 hour. Cell medium was then removed and formazan crystals resuspended in DMSO. Absorbance at 570 nm was measured using a spectrophometer (Powerwave XS2, Biotek). Absorbance at 650 nm was taken and used to correct for background cell debris. Results were normalised to sodium azide treatment (0% MTT reduction) and untreated sample (100 % MTT reduction).

2.6 Liposome dye release

2.6.1 Preparation of lipid film from purchased lipid

The desired mass of lipid (typically 20 mg) required to form LUVs (e.g. 25 mol % cholesterol and 75 % mol 1-palmitoyl-2-oleoyl-*sn*-glycero-3-phospho-(1'-*rac*-glycerol) (PG), 100 mol % 1,2-dimyristoyl-sn-glycero-3-phospho-L-serine (DMPS) or 100 mol % L-α-Lecithin (Sigma P 5394)) was suspended in chloroform which was then evaporated under a stream of N_2 gas to form a thin lipid film over the bottom of a glass tube. The film was further dried under vacuum for approximately 3 h. The film was stored at 4 °C and used within one week.

2.6.2 Preparation of RAW 264.7 lipid film

Lipids were extracted from cells using a lipid extraction kit (Cell Biolabs STA-612) according to the manufacturer's instructions. The kit extracts total lipids by organic extraction, using a proprietary alcohol. Lipid in the upper organic phase was dried under a stream of N_2 gas to form a thin lipid film over the bottom of a glass tube. The film was further dried under vacuum for approximately 3 h. The film was stored at 4 °C and used within one week.

2.6.3 Large unilamellar vesicles preparation

The lipid film (Section 2.6.1, 2.6.2) was resuspended in carboxyfluorescin buffer to give a final lipid concentration of 25 mM. At least four freeze-thaw cycles were performed between LN_2 and 90 °C water bath, vortexing between each cycle. Free lipids were then

extruded using the mini-Extruder apparatus (Avanti) by passing through a 0.4 μm polycarbonate pore up to 35 times to generate 400 nm extruded large unilamellar vesicles (LUVs). For DMPS and RAW 264.7 lipid where stated, extrusion was performed at 50 °C. LUVs were washed by successive rounds (up to 5) of centrifugation at 16,000 x g for 25 min and re-suspension of the lipid pellet in dye release buffer pH 7.4. LUVs were stored on ice and used within 48 h of extrusion.

2.6.4 Dye release assay

For the dye release assay, LUVs were adjusted to 5 μM lipid monomer in dye release buffer of appropriate pH. Each dye release reaction was carried out at least in triplicate in a 96 well plate. In all LUV lipid types, 190 μl of LUV was incubated with 10 μl buffer control or protein condition (final working concentration 6 μM monomer equivalent). For reactions carried out at pH 4.5 and 6.4, after the experimental duration, samples were diluted 1:2 in dye release buffer pH 7.4 (Table 2.2) before fluorescence intensity was quantified. For reactions carried out at pH 7.4, fluorescence was measured every minute for the duration of the experiment. For DMPS LUVs, reactions were carried out at 45 °C. For biological and PG based LUVs, reactions were carried out at 37 °C. Fluorescence spectra were measured using the CLARIOstar plate reader (BMG Labtech) with a monochromator, using an excitation wavelength of 490 +/- 4 nm. Emission spectra were recorded between 510 +/- 4 nm and 600 +/- 4 nm for reactions at acidic pH, and between 510-520 +/- 4 nm for reactions at pH 7.5. Data were initially analysed using CLARIOstar analysis software. 100% dye release values were obtained for each sample by the addition of Triton X-100 to a final concentration of 0.2% (*v/v*). Normalised dye release values for each sample were calculated using the following equation;

$$\%\ Dye\ Release = \frac{F - F_b}{FT - F_b}$$

Where F is the fluorescence intensity of the sample, F_b is the background dye release (carboxyfluorescein fluorescence from LUVs in the presence of appropriate buffer) and FT is the fluorescence intensity after the addition of Triton X-100.

2.6.5 Dynamic light scattering

To characterise LUVs dynamic light scattering (DLS) was performed by Dr Sophia Goodchild on a miniDAWN TREOS system, equipped with a Wyatt quasi-elastic light scattering (QELS) detector (Wyatt Technology), run in batch mode at room temperature. LUVs were measured at ~ 50 μM lipid molecule concentration in dye release buffer pH 7.4. For each sample, three measurements were performed. QELS data was collected at five seconds intervals for three minutes. Data were processed by regularisation analysis using

Wyatt ASTRA 6.0 software. Hydrodynamic radii are reported as the weighted average of three experiments for each sample with an error of 1 standard deviation (SD).

2.7 Enrichment of lysosomes

2.7.1 Homogenisation using a ball bearing homogeniser

Desired numbers of cells were harvested by centrifugation at 500 x g for 5 minutes (Eppendorph 5804 centrifuge) and washed three times with PBS. The cell pellet was resuspended in an appropriate homogenisation buffer and passed through a ball bearing homogeniser (10 μm clearance, Isobiotec) until >90 % breakage was achieved. Cell homogenisation was carried out on ice, with homogeniser and buffers pre-cooled on ice. Homogenisation in this manner maintains the integrity of subcellular organelles (Balch & Rothman, 1985).

2.7.2 Generation of post nuclear supernatant

Whole cell lysate was centrifuged at 1000 x g for 10 minutes at 4 °C (Eppendorf 5415 R microfuge) to pellet the nucleus and large mitochondria. Post nuclear supernatant (PNS) was moved to a clean eppendorf tube and the pellet discarded.

2.7.3 Generation of crude lysosomal pellet

The PNS was centrifuged at 20,000 x g (Sorvall discovery M150 SE micro-ultracentrifuge, S55-S rotor, Sorvall) to generate crude lysosomal pellet (CLP) enriched in lysosomes, endoplasmic reticulum and micochondria. CLP was resuspended in an appropriate homogenisation buffer for imaging or taken forward for subcellular fractionation on an iodixanol gradient.

2.7.4 Subcellular fractionation using a percoll gradient

Subcellular fractionation using percoll was performed using an adaptation of a published protocol (Casey *et al*., 2007). Briefly, 5 x 10^7 cells were homogenised (Section 2.7.1) in percoll homogenisation buffer (Table 2.2) supplemented with protease inhibitor mixture. The PNS was generated (Section 2.7.2) and loaded onto the top of 9 ml 27 % (v/v) percoll, in percoll homogenisation buffer. To separate organelles by their density, the gradient was centrifuged at 48,500 x g for 1 hour at 4 °C (T1270 rotor Sorvall Discovery 90SE). Ten 1 ml fractions were collected from the top of the gradient and enzyme assays (Section 2.7.6) were performed to identify fractions enriched in lysosomes. An aliquot of each fraction was analysed by SDS-PAGE and immunoblotting to identify the location of organelles across the gradient. The enriched lysosomal fraction(s) were centrifuged 241,000 x g for 1 h at 4 °C (TLS-55 rotor, Beckman Coulter TLX ultracentrifuge). The layer of lipid

(lysosomes) on top of percoll pellet was pipetted off to yield the lysosomal fraction, which was taken forward for imaging by cryo-EM.

2.7.5 Subcellular fractionation on an Optiprep™ gradient

CLP was resuspended to 19 % (v/v) Optiprep™ and loaded between 22.5 and 16% (v/v) layers into a discontinuous gradient of 27, 22.5, 16, 12, 6 % (v/v) Optiprep, with the densest fractions at the bottom of the ultracentrifuge tube. The gradient was centrifuged at 150,000 x g 4 hours at 4 °C (Sorvall discovery 90 SE ultracentrifuge, Sorvall AH650 swing out rotor). 200 µl was removed at the interface between layers that were taken forward for further analysis.

2.7.6 Enzyme assays

2.7.6.1 N-acetylglucosaminidase assay

To assess the levels of N-acetyl glucosaminidase (NAGA), a marker for lysosomes (Sellinger *et al*., 1960), the NAGA activity of each subcellular fraction was determined. 100 µl NAGA substrate (Table 2.2) was incubated with 10 µl of sample in a 96 well plate and incubated at 37 °C for 30 minutes (whole cell homogenate and homogenisation buffer acted as positive and negative controls respectively). The reaction was stopped using 200 µl 200 mM glycine, pH 10.3. Absorbance was then read at 405 nm using a plate reader (Powerwave XS2, Biotek).

2.7.6.2 NAGA release from CLP fraction

2 x 10^7 RAW 264.7 cells were used to a generate CLP (Section 2.7.3), which was resuspended to 1 ml in Optiprep™ homogenisation buffer. 100 µl CLP was incubated with a final concentration of 6 µM monomer equivalent β_2m monomer, Ls or Ls-f, 0.5% (v/v) Triton X-100 detergent or fibril buffer for 1 hour, 37 °C under gentle agitation to ensure mixing. The sample was then centrifuged at 100,000 x g for 30 mins at 4 °C (Sorvall discovery M150SE micro-ultracentrifuge, Sorvall S100 AT3 rotor). The soluble fraction was removed and retained on ice. The pellet was surface washed with 1 ml homogenisation buffer, and ultra-centrifuged 100,000 x g 30 mins, 4 °C. The pellet was resuspended into the same volume as the soluble fraction with Optiprep™ homogenisation buffer. NAGA assays were then performed on the soluble and pellet fractions.

2.7.6.3 Acid phosphatase assay

The activity of acid phosphatase., a lysosomal marker (Bull *et al*., 2002) was assessed in each subcellular fraction. 100 µl acid phosphatase substrate (Table 2.2) was incubated with 5 µl of sample in a 96 well plate and incubated at 37 °C for 30 minutes. The reaction

was stopped using 100 µl 0.5 M NaOH. Absorbance was then read at 405 nm using a plate reader (Powerwave XS2, Biotek).

2.7.6.4 Alkaline phosphatase assay

To quantify the levels of alkaline phosphatase, a plasma membrane marker (Emmelot *et al*., 1964), the activity in each subcellular was determined. 100 µl alkaline phosphatase substrate was incubated with 10 µl of sample in a 96 well plate and incubated at 37 °C for 30 mins. Absorbance was then read at 405 nm (Powerwave XS2, Biotek).

2.8 Live cell confocal microscopy

RAW 264.7 cells were seeded at 25,000 cells/ml in 3 cm glass bottomed imaging dishes and cultured for 16 h. Cells were then incubated with treatment for the designated time frame, such as 120 µM monomer equivalent amyloid fibrils or monomeric protein labelled with Alexa Fluor® 647 (Absorbance 647 nm, emission 671 nm). Cells were incubated with 50 nm LysoTracker deep red (Absorbance 647 nm, emission 688 nm) or 50 nM Lysotracker green (Absorbance 504 nm, emission 516 nm) and/or 100 nm NIAD-4 (Absorbance 487 nm emission 625 nm) 30 minutes before imaging. Cells were washed 3 times in preheated phenol red-free medium before imaging. Images were acquired on a Zeiss LSM700 meta laser scanning inverted confocal microscope with a heated stage (37 °C) and 63X objective lens. Montages were generated using FIJI (Schindelin *et al*., 2012).

2.9 Cryo-fluorescence microscopy

Cryo-fluorescence microscopy was performed on cryogenically frozen samples (Section 2.11.3) using a Linkam cryo-stage on a Zeiss LSM510 META Upright confocal, on a Zeiss LD EC Epiplan-Neofluar 100X/.75HDDICd=4 objective.

2.10 Leviviridae expression and purification

Recombinantley expressed MS2 (rMS2) and wtMS2 and F-pili were expressed and purified by Amy Barker, as described previously (Dent *et al*., 2013; Toropova *et al*., 2011; Mastico *et al*., 1993; Lima *et al*., 2006). For MS2 binding to F-pilus studies, wtMS2 or rMS2 was added to F-pilus (~2 mg/ml: ~0.2 mg/ml final concentrations, respectively) (50 mM Tris-HCl (pH 7.8) in 75 mM NaCl, 2 mM EDTA.) and incubated at room temperature for 30 minutes before preparation for cryo-EM (Section 2.11.3).

Bacteriophage Qβ was gifted from Dr. D. S. Peabody and purified by Amy Barker. Qβ was dialysed into 10 mM HEPES, 10 mM NaCl, pH 7.5 (Pierce Slide-A-Lyzer® MWCO 20 kDa). CsCl was added to the Qβ (final density, ρ=1.38±0.01) and mixed overnight at 4 °C. Samples centrifuged at 20,000 rpm, 4 °C for 20 hours (SW40Ti Beckman rotor, 12 mL tubes). Tubes were fractionated (BioComp Gradient Fractionator), dialysed overnight at 4

°C into 10 mM HEPES, 10 mM NaCl, pH 7.5, quantified by UV Spectrophotometer and verified using SDS-Page. The fraction containing bacteriophage Qβ was concentrated (Vivaspin 500 MWCO 100 kDa) to ~7 mg/ml in 10 mM HEPES 10 mM NaCl pH 7.5 and stored at 4 °C.

2.11 Specimen preparation for transmission electron microscopy

2.11.1 Glow discharge of EM grids

Carbon-coated EM grids were rendered hydrophilic by glow discharge in air. EM grids were placed onto a parafilm coated glass slide, carbon side up, and subjected to glow discharge at a High Tension (HT) setting of 10 for 20 seconds using a Cressington 208 Carbon Coating Unit.

2.11.2 Negative staining

3 µl of sample was applied to a glow discharge treated EM grid with continuous carbon film for 30 seconds. Excess sample was blotted away using Whatman No. 1 filter paper. The grid was washed twice using 10 µl droplets of dH_2O on parafilm. The grid was then washed in a droplet of stain (1 % w/v uranyl acetate). A final droplet of 10 µl of stain was applied to the grid and left for 20 seconds. Excess stain was blotted away leaving a small meniscus by which approximate stain depth could be judged.

2.11.3 Cryo immobilisation

The principle of cryo-immobilisation is to fix the structure of interest in a frozen, hydrated, native-like state in a thin layer of vitreous ice. This is achieved by applying an aliquot of an aqueous solution onto an EM grid covered by a carbon support film (Figure 2-1). Blotting away the excess fluid leaves a thin layer containing the specimen suspended in the holes of the carbon support by surface tension. This is then vitrified by plunging into liquid ethane cooled by LN_2. Plunge freezing was performed using automated freezing devices, the Leica EM GP or FEI Vitrobot mark IV.

For the Vitrobot Mark IV, briefly, LN_2 was added to the dewar designed to cool the ethane bucket through the cooling legs. Once ethane bucket was sufficiently cooled, ethane gas was passed into the bucket and allowed to liquefy until the bucket was $4/5^{th}$ full. The chamber of the Vitrobot was adjusted to the appropriate temperature and humidity. The EM grid was loaded into the chamber and the specimen applied to the grid through ports in the side. The liquid ethane bucket was then raised up to meet the chamber area so during plunge freezing the grid remains within the temperature and humidity controlled chamber for as long as possible. The grid was blotted with fresh blotting paper according to parameters that were optimised according to the sample/grids used. After blotting the

EM grid was plunged into the bucket of liquid ethane. The grid was then transferred from the liquid ethane into liquid nitrogen through liquid nitrogen vapour. After vitrification, grids were stored in plastic pucs under liquid nitrogen in storage dewars (Wessington Cryogenics).

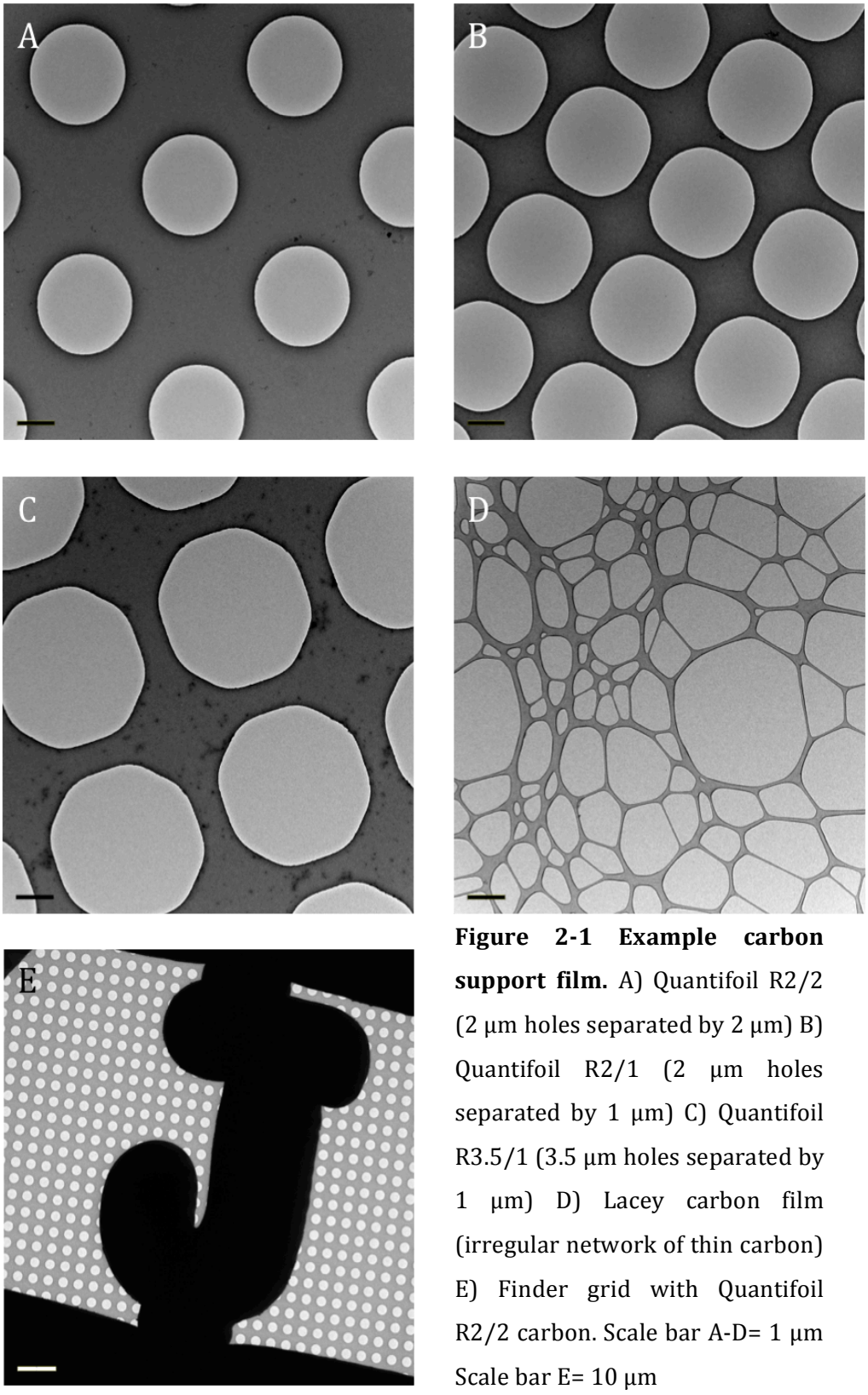

Figure 2-1 Example carbon support film. A) Quantifoil R2/2 (2 µm holes separated by 2 µm) B) Quantifoil R2/1 (2 µm holes separated by 1 µm) C) Quantifoil R3.5/1 (3.5 µm holes separated by 1 µm) D) Lacey carbon film (irregular network of thin carbon) E) Finder grid with Quantifoil R2/2 carbon. Scale bar A-D= 1 µm Scale bar E= 10 µm

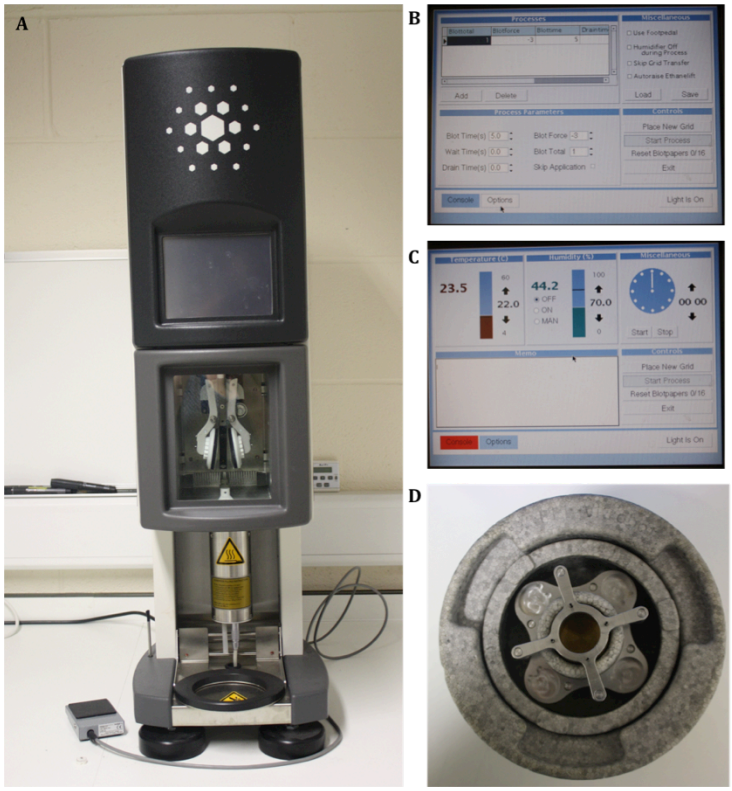

Figure 2-2 The Vitrobot mark IV (FEI) (A). System is controlled through touch screen panels (B,C). Dewar for LN_2 is designed to maintain the ethane bucket at optimal temperature (D).

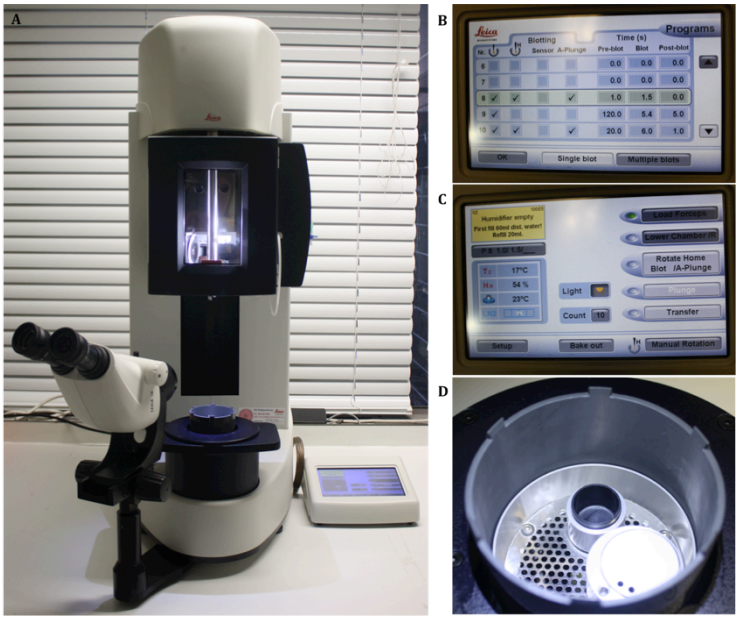

Figure 2-3 The Leica EM GP (A). System is controlled through touch screen panels (B,C). Dewar for LN_2 is designed to maintain the ethane bucket at desired temperature, typically -175 °C (D).

Sample	EM grid	Blot time (s)	Blot force	Wait time/ Drain time (s)	Chamber temperature (°C)	'Chamber humidity'
Eukaryotic cells	Quantifoil R2/2 Au 200 mesh	1.5	0	1,1	10	100 %
Organelles from percoll gradient	Lacy carbon grid	6	6	1,1	4	100 %
Qβ	Quantifoil R2/2 Cu 200 mesh	4	4	1,1	4	100 %

Table 2.10 Example Vitrobot mark IV blotting conditions.

Sample	EM grid	Blot time (s)	Wait time/ Drain time (s)	Chamber temperature (°C)	'Chamber humidity'	Arm position, grid height, ethane height
Organelles from gradient	Quantifoil R2/1 Cu 200 mesh	1.5	1,0	8	95 %	225, 5, 2

Table 2.11 Example Leica EM GP blotting conditions.

2.12 Electron microscopy

2.12.1 Microscopes used

Microscopes used in this project can be found in Table 2.12. Unless otherwise stated, cryo-EM data was collected on an F20 microscope, University of Leeds.

Microscope	Location	Electron source	Operating Voltage (keV)	Detector	Physical pixel size (µm)	Additional hardware
FEI Tecnai F20	University of Leeds	FEG	200	Gatan US4000/SP CCD camera	15	
FEI Tecnai T12	University of Leeds	LaB6	120	Gatan US1000XP CCD camera	14	
FEI Titan Krios	MRC LMB, Cambridge	FEG	300	FEI Back-thinned Falcon II Direct detector	14	
FEI Polara	Birkbeck College, London	FEG	300	Gatan K2 bioquantum 967 direct electron detector	5	Quantum energy filter

Table 2.12 Electron microscopes used.

Tilt series were collected on FEI Polara microscope with a sampling of of 5.38 Å/pixel, using a 6 second exposure, with an electron dose of 0.177 $e^-/Å^2$/second, leading to a total dose of ~ 1 e^-/ Å per exposure. Dose was fractionated at 0.25 s intervals, with drift correction carried out by Gatan software. Tilt series were collected +/- 65°, with a 2° tilt

increment and a target defocus of -8 µm. Tilt series were collected using SerialEM. Microscope alignments were performed by Dan Clare.

Data collected on the FEI Titan Krios magnification of 103,704 x, resulting in a sampling of 1.35 Å per pixel and a total dose of ~50 e-/Å^2. Dose was fractionated across 34 frames during a 2 s exposure. Target defocus range was from -1 to -3 µm. Microscope alignments were performed by Shaoxia Chen and Christos Savva. Data was collected using FEI EPU software.

2.12.2 Microscope alignments at University of Leeds

EM alignments were carried out to ensure the electron beam passes down the microscope column through the centre of the apertures and lenses, keeping optical aberrations to a minimum. Microscope alignments were performed starting from the top of the column. Gun and C2 aperture alignments were performed by Dr Peiyi Wang (EM facility, University of Leeds). The objective aperture was centred in diffraction mode. The grid was bought to eucentric height and focus (contrast minima). Beam tilt pivot points were then corrected to make the electron beam parallel to the axis of the objective lens. The rotation centre alignment was performed to ensure the electron beam passes through the centre of the objective lens. To minimise beam shifts during magnification changes in low dose mode, beam shift alignments were performed.

2.12.3 Electron microscopy at University of Leeds

At the beginning of each session, the anti-contaminator was cooled using LN_2, and left to equilibrate for 20 minutes before specimen loading. Imaging was performed using standard low-dose imaging as described in Section 2.12.3.3.

2.12.3.1 Negative stain electron microscopy

Negatively stained grids were placed into a single tilt holder and inserted into the microscope.

2.12.3.2 Cryo electron microscopy

Every tool/surface that comes into contact with the cryo-grid is dried thoroughly before use and then pre-cooled using LN_2. The cryo-holder was inserted into the EM and cooled to ~-180 °C. using LN_2. Several designs of cryo-holder for side entry microscopes are available, here Gatan 626b and Oxford instruments 3500 holders were used. Once the holder reached a stable temperature, the cryo-transfer station was cooled with LN_2. The cooled cryo-holder was then transferred quickly out from the microscope into the cryo-station. The clip ring, which holds the grid in place, was removed using the clip ring tool. A grid was transferred through LN_2 or LN_2 into the grid slot of the cryo holder and the clip

ring replaced. In order to keep the grid cool during transfer to the microscope, the cryo shield was closed.

During transfer from the cryo-station to the microscope, the goniometer was set to -60° so some nitrogen is retained in the dewar whilst the cryo-holder was loaded into the microscope. The air lock of the microscope was pre-pumped before cryo-holder loading to ensure the high vacuum of the column was maintained, and transfer of the holder into the column occurred in ~one minute. The temperature of the cryo-holder was monitored during transfer and typically stayed cooler than -165 °C. The goniometer was reset to 0° and the dewar topped up with LN_2. At the end of the session the cryo holder was inserted into a pumping station (Gatan 655 pumping station, Gatan Pleasanton CA) and the zeolite cycle was initiated. This heats the dewar so an improved vacuum can be generated in the vacuum chamber of the holder. Finally, the LN_2 was removed from the microscope's anti-contaminator and the cryo-cycle initiated for 4-8 hours. This removes contaminants adsorbed to the anti-contaminator.

2.12.3.3 Low-dose imaging

As biological specimens are highly susceptible to radiation damage, low dose imaging was performed to minimise sample exposure to the electron beam and so minimise total electron dose. Three imaging modes are operated in low-dose, search, focus and exposure. Search mode allows the user to examine a relatively large grid area and identify regions of interest while exposing the sample to very little electron dose. Using search mode, areas of good quality ice can be identified. Once an area has been identified for imaging, focus mode was used to find focus (contrast minima). Focusing is performed at high magnification, typically over 100,000 X magnification at the specimen level, and ~ 2 µm from the area to be imaged. Exposure mode is set to magnification and dose required in the final image, and a micrograph is taken. Calibrations were performed to minimise beam shift when switching between modes.

2.12.3.4 Liposome diameter measurements

Liposome diameters were assessed using cryo-EM. For each lipid condition, 200 liposome diameters were calculated in FIJI (Schindelin *et al*., 2012).

2.12.3.5 Cryo-electron tomography

SerialEM version 3.1.1 (Kremer *et al*., 1996) was used to collect tilt series. In addition of basic microscope alignments described above, SerialEM calibrations were performed including stage shift, image shift and electron calibrations. Tilt series were collected up to a maximum tilt range of +/-55°, with a step size of 2° or 3°. Tilt series were collected using low dose imaging (Table 2.13).

	View	Focus	Record
Magnification	2900	23,000	13,000
Spot size	8	8	8
Dose ($e^-/Å^2$)			1
Exposure (seconds)	0.3	0.5	1
Binning	4	1	1

Table 2.13 Low-dose imaging settings used in SerialEM during tilt series collection at University of Leeds.

2.13 Soft X-ray microscopy

Soft X-ray microscopy was performed at Diamond Light Source (Beamline B24 cryo-transmission X-ray microscopy) using an Xradia UltraXRM-S/L220c microscope and PIXIS-XO 1024B (Princeton Instruments) detector, using a laboratory X-ray source and 40 nm zone plate. Tilt series were processed using IMOD as in Section 2.14.2.

2.14 Image processing

2.14.1 Single particle processing

Micrograph defocus and astigmatism was determined using CTFFIND4 (Rohou & Grigorieff, 2015). Micrographs with unacceptable astigmatism, drift or defocus were discarded. Single particle processing was performed in RELION version 1.3 (Scheres, 2012). Approximatley 2000 particles were manually picked and classified using reference free 2D classification. These 2D classes were used as templates for automated particle picking (Scheres, 2015). Particles were extracted with 'dust correction' applied, where pixels with values higher and lower than five times the image standard deviation are replaced with values from a Gaussian distribution.

Reference free 2D classification and particle sorting were performed iteratively to obtain a 'homogenous' particle stack (Scheres, 2015). 2D classification was performed into 50 classes for 25 iterations with a regularisation parameter T value of 2. Image alignment was performed with an in-plane angular sampling (psi) of 5°, an offset search range of five pixels and offset search step of one pixel. CTF correction was performed in RELION according to parameters calculated by CTFFIND4; Wiener filtering was applied.

3D classification was performed over 25 iterations with a regularisation parameter T value of 2. A sphere generated in Spider, or a previous map filtered to 50 Å was used as a starting model. Classification was performed into two classes, with I3 symmetry was imposed. RELION uses XMIPP's libraries for symmetry operations. CTF correction was performed. In 3D classification, image alignment was performed with auto-sampling, where the angular sampling interval decreases automatically through the refinement. An

offset search range of 5 pixels and offset search step of 1 pixel was used, with no local angular searches.

For 3D autorefine, the output from 3D classification filtered to 50 Å was used as a starting model. CTF correction was performed (Scheres, 2012). Auto-sampling was performed with an initial angular sampling of 7.5°, an initial offset range of 5 pixels and initial offset step of 1 pixel. Local searches were performed when angular sampling dropped below 0.9°.

To correct for drift and beam-induced movement of particles, movie processing and particle polishing was performed (Bai *et al*., 2013). For movie processing a running average of 3 frames and a standard deviation on the translations of 2 pixels, with no rotational searches was used. For particle 'polishing', linear particle movements were fitted. Polishing was performed using a running average of 3 movie frames. Each particle was fitted individually. *B*-factor weighting was performed. The *B*-factors across movie frames were plotted, and as a result of this particle 'polishing' was performed again only using frames 5-25 of the movie. The resulting 'shiny' particle stack was reprocessed using the 3D autorefine procedure with either I3 (icosahedral) or C1 (asymmetric) symmetry applied.

The final 3D structures were subjected to post-processing that included masking and *B*-factor correction. Resolution was calculated using the gold standard Fourier shell correlation (FSC=0.143) criterion (Scheres & S. Chen, 2012). Local resolution was calculated using ResMap, with a P-value of 0.05 (Kucukelbir *et al*., 2014). UCSF Chimera was used for map visualisation, generation of figures and as a fitting tool to fit (Pettersen *et al*., 2004).

2.14.1.1 Refinement of X-ray crystal structure

Refinement of X-ray crystal structures was performed in Rosetta using RosettaScripts the 'relax' protocol, with an additional tool to assess agreement with the density (DiMaio *et al*., 2015). Agreement to density is implemented as an additional energy term, calculated by computing the expected density for a given model and measuring the agreement of the expected and experimental density. Rosetta scoring was performed to assess agreement between existing PDB structures and electron density. The MolProbity server was used to assess structures generated in Rosetta (Chen *et al*., 2010).

2.14.2 Tilt series processing

Tilt series were reconstructed into tomograms using the ETOMO program within the IMOD package (Kremer *et al*., 1996). Initially, CCD Eraser was used to remove strong pixel intensities which may be attributed to X-rays, and which may interfere with cross-correlation calculations later in processing. Tiltxcorr was then used to perform cross-correlation calculations and align the images. Tilt series were either aligned using patch tracking or gold fiducial markers to make a fiducial model. A sample tomogram was then created and the boundaries of the specimen marked using 6 contours (2 for each axis). Aligned tilt series were binned by 2 and a 3D tomogram calculated using weighted back projection or SIRT. Tomograms were then inspected and trimmed in 3DMOD.

2.14.3 Tomogram segmentation

Tomogram segmentation was performed using Amira (FEI). Amira uses a modular system, where each process applied to the tomogram can be tracked. The filter sandbox tool was used to select the most appropriate filter to maximise signal to noise in the tomograms; commonly Gaussian, median, anisotropic diffusion and non-local means filters were useful. The interactive thresholding tool was used to select density automatically. This typically yielded a very noisy segmentation that was cleaned using the 'remove small spots' tool was used. This was used iteratively in both 2D and 3D planes, where segmented density smaller than the defined pixel volume/dimensions was removed. The resulting segmented density can be visualised as a surface. Typically, no smoothing or constrained smoothing was applied during surface generation; this was assessed on a tomogram by tomogram basis, depending on the features the segmentation sought to reveal. Where needed, the segmentation editor tool was used to assign voxels from each frame to a material, such as membrane or material. These selected voxels can then be independently manipulated. All figures of tomogram segmentation were generated in Amira.

3 Preparation and characterisation of β_2m amyloid fibrils, and their propensity to perturb membranes

3.1 Introduction

Amyloid is the name given to a protein conformation defined by a highly ordered, β-sheet-rich structure that has a cross-β motif. The term 'amyloid' was first used in a disease context by Virchow in 1854 (Sipe & Cohen, 2000). The name was given originally as amyloid was thought to be starch, and although the fibrils are now known to be proteinaceous, the name has persisted (Toyama & Weissman, 2011; Dobson, 2001). Proteins and polypeptides possessing a diverse range of native structures have been shown to form amyloid, including proteins rich in α-helices, β-sheet, and intrinsically disordered proteins (Chiti & Dobson, 2006)(Table 3.1). Although the propensity to do so varies with sequence; it has been suggested that the ability to adopt the amyloid conformation is an inherent property of polypeptide chains (Stefani & Dobson, 2003).

Despite the heterogeneity of amyloid precursor proteins, all amyloid assemblies share common characteristics. Fibrils are long, unbranched filaments of variable length, typically 7-20 nm in width, that are readily observed by atomic force microscopy (AFM) and EM. The core of the amyloid fibril is β-sheet rich, where the β-strands are highly ordered and perpendicular to the fibril length. The repeat produced by the cross-β architecture gives rise to a characteristic X-ray fibre diffraction pattern (Astbury *et al*., 1935; Jahn *et al*., 2010). Other characteristic properties of amyloid include its apple green birefringence under polarised light upon binding with Congo Red dye (Puchtler *et al*., 1962). Amyloid also increases the fluorescence of some dyes such as ThT and NIAD-4 (Bae *et al*., 2015). Amyloid fibrils also share conformational epitopes recognised by specific antibodies (O'Nuallain & Wetzel, 2002). These generic properties are shared by *ex vivo* and *in vitro* formed amyloid fibrils (Jahn *et al*., 2008). Fourier transform infrared spectroscopy (FTIR) has been used to compare the structural properties of β-2-microglobulin (β_2m) amyloid fibrils formed at pH 2.5, 7.0 or *ex vivo* fibrils, and all share the same structural characteristics (Jahn *et al*., 2008; Kawai-Noma *et al*., 2010).

3.1.1 Amyloidosis

Protein misfolding and aggregation is the basis for much human disease (Reynaud, 2010; Dobson, 2003). Although eukaryotic cells have extensive quality control mechanisms for proteostasis which prevent aberrant protein misfolding and aggregation, these can be ineffective (Baumeister & Walz, 1998; Trombetta & Parodi, 2003). The amyloidoses are a group of diseases associated with the conversion of proteins and peptides from their functional (normally soluble) forms into amyloid, which deposit as extracellular

aggregates or intracellular inclusions. To date, 31 proteins are known to form extracellular amyloid fibrils, and several more form intracellular inclusions (Table 3.1) (Sipe *et al*., 2014), but they share no apparent similarity in amino acid sequence, tertiary structure or biological function in their soluble forms (Knowles *et al*., 2014). These amyloid-forming proteins are associated with ~ 50 diverse disorders, including the debilitating neurodegenerative conditions Alzheimer's and Parkinson's Diseases (AD and PD, respectively), organ-specific disorders such as diabetes mellitus type 2 and systemic disorders such as dialysis related amyloidosis (Selkoe, 2003; Knowles *et al*., 2014).

With increased life expectancy globally, the prevalence of these diseases will increase. Although the relationship between ageing and amyloid formation is poorly understood, proteostasis is thought to become less effective with age, increasing the susceptibility to misfolding diseases (Labbadia & Morimoto, 2015). Here some of the most prevalent amyloidoses are discussed.

Disease	**Extracellular deposits/ Intracellular inclusions**	**Target site**	**Precursor protein (fold)**
Dialysis related amyloidosis	Extracellular deposits	Musculoskeletal system	β_2m (predominantly β sheet)
Amyloid light chain amyloidosis	Extracellular deposits	Systemic	Immunoglobulin Light Chain (predominantly β sheet)
AA amyloidosis	Extracellular deposits	Systemic	Serum amyloid A protein (predominantly α helical)
Alzheimer's Disease	Extracellular deposits	CNS	Amyloid β (intrinsically disordered)
Transthyretin amyloidosis	Extracellular deposits	Systemic	Transthyretin (predominantly β sheet)
Spongiform encephalopathies including Creutzfeldt-Jakob Disease and Fatal Familial insomnia	Extracellular deposits	CNS	Prion protein (PrP) (intrinsically disordered)
Diabetes mellitus type 2	Extracellular deposits	Islets of Langerhans, Insulinomas	Islet Amyloid Polypeptide (intrinsically disordered)
Parkinson's Disease	Intracellular inclusions 'Lewy bodies'	Neurons, intracytoplasmic	α-synuclein (intrinsically disordered)
Huntington's Disease	Intracellular inclusions 'Huntington bodies'	Neurons, intranuclear	PolyQ expanded Huntingtin (intrinsically disordered)
Alzheimer's Disease	Intracellular inclusions 'Neurofibrillary tangles'	Neurons intracytoplasmic	Tau (intrinsically disordered)
Lysozyme amyloidosis			Lysozyme (α and β content, lysozyme fold)

Table 3.1 Selection of amyloidosis. Adapted from Sipe *et al*., 2014, Chiit *et al,.* 2006.

3.1.1.1 Alzheimer's disease

AD is a neurodegenerative disease first described in 1906, and is the most common cause of dementia (Haass, 2004). The hallmarks of AD are extracellular amyloid plaques and neurofibrillary tangles formed from amyloid β (Aβ) peptides and tau respectively (Table 3.1)(Hardy & Higgins, 1992). Aβ is a proteolytic cleavage product of amyloid precursor protein (APP), which is processed by β-secretases and ϒ-secretases to a peptide of 39-43 residues (Zhang *et al*., 2011). Longer Aβ peptides are more amyloidogenic than their shorter counterparts (Haass *et al*., 2012). $A\beta_{1-40}$ and $A\beta_{1-42}$ are the most common forms in amyloid plaques, with $A\beta_{1-42}$ being less prevalent, but more toxic (Kayed *et al*., 2003). The normal physiological role of APP is unclear, although roles in inter-cell interactions and cell adhesion, cell migration, calcium homeostasis, and neuroprotection have been proposed (Young-Pearse *et al*., 2007; Nalivaeva & Turner, 2013; Corrigan *et al*., 2014). Mutations in APP are linked with familial and early-onset AD, implicating Aβ in the pathogenesis of AD (Karch & Goate, 2015). Other genes identified as risk factors, include apolipoprotein E (*APOE*) gene polymorphs (Van Cauwenberghe *et al*., 2015; Medway & Morgan, 2014).

In addition to Aβ, hyperphosphorylation of Tau has been long been implicated in AD, through loss of normal physiological function and aggregation into intracellular aggregates known as neurofibrillary tangles (Medeiros *et al*., 2011). Tau is a microtubule-associated protein found primarily in axonal cells, where it modulates microtubule-dependent transport of organelles and biomolecules (Ballatore *et al*., 2007).

People with AD are typically > 65 years old and have symptoms including progressive memory loss, especially short-term memory, hallucinations, personality change, agitation and anxiety. It is projected that by 2050 there will be 1 million new cases per year in the USA alone, with a total of 11-16 million people living with the disease (Alzheimer's Association, 2015). AD is set to become a global epidemic in the coming decades. By 2040 there will be an estimated 81.1 million people living with AD (Prince *et al*., 2013). People with dementia often require round the clock care, especially in the advanced stages of the disease. Globally in 2010 healthcare expenditure on dementia was estimated to be $604 billion, with these costs expected to rise in line with increased prevalence of the disease (Schaller *et al*., 2015).

There is currently no cure for AD, and no treatments that significantly slow disease progression. Given the global economic burden, intensive research is underway to develop therapeutics. One drug under investigation, is a humanized monoclonal IgG1 antibody

directed against Aβ peptide, known as solanezumab (Siemers *et al*., 2015). Initial research indicates that this antibody may slow cognitive decline in patients with mild dementia by 34 % (Siemers *et al*., 2015), although further research is required to validate these findings. Other approaches include vaccination; a phase III trial of a vaccine called CAD106 is due to start late 2015 (Underwood, 2015). The vaccine is composed of a fragment of Aβ linked to a virus-like particle, which will, in theory, prompt the immune system to clear Aβ peptide. Another approach by Novartis is treating carriers of the *APOE4* gene variant early in their life with inhibitors of BACE, an enzyme involved in the proessing of APP (Underwood, 2015). All these approaches target patients before symptoms emerge or at the very earliest stages, before extensive neurodegeneration has occurred. This further increases the need for biomarkers to enable early diagnosis, which is itself a significant challenge (Sancesario & Bernardini, 2015).

3.1.1.2 Parkinson's disease

PD is the second most common neurodegenerative condition that specifically affects the dopaminergic neurons of the substantia nigra (Herva & Spillantini, 2015). It is a chronic and progressive disease, with an average life expectancy of 15 years after diagnosis (Shulman *et al*., 2011). Those living with PD exhibit a broad range of motor and non-motor symptoms including resting tremor, bradykinesia and loss of postural reflexes; cardinal symptoms of PD (Jankovic, 2008). Non-motor symptoms include dementia, hallucinations and sleep disorders (Jankovic, 2008). On a cellular level, intracellular aggregates known as Lewy bodies, are observed, which contain many proteins including primarily α-synuclein (Dickson *et al*., 2009). A range of other disorders, together termed the α-synucleinopathies are associated with the aggregation of α-synuclein, including dementia with Lewy bodies and multiple system atrophy.

α-synuclein is an intrinsically disordered protein that is widely expressed throughout the nervous system, and is enriched in presynaptic terminals, where it is thought to play a role in synaptic vesicle trafficking and the fast kinetics of synaptic vesicle endocytosis (Vargas *et al*., 2014). Its expression has also been reported in kidney, liver and heart (Ltic *et al*., 2004). Mutations in the *SNCA* gene encoding α-synuclein are found in familial cases of PD, and single nucleotide polymorphisms at the *SNCA* locus have been linked to incidence of sporadic forms of the disease (Shulman *et al*., 2011). α-synuclein undergoes several post-translational modifications which affect pathology, including N-terminal acetylation, ubiquitination and phosphorylation, and may be present in a tetrameric form *in vivo* (Trexler & Rhoades, 2012; Bartels *et al*., 2011).

Currently, the motor symptoms of PD are managed through dopamine replacement therapy, such as Levodopa (Chase, 1998). While this partially relieves motor symptoms and extends life expectancy, it does not address neurological symptoms or the underlying neurodegeneration, and may in fact accelerate the loss of nigrostriatal cells. Currently, there is only one approved treatment of dementia associated with PD, rivastigmin, which temporarily slows progression of symptoms, but does not modify underlying disease progression (Ding *et al*., 2015; Shulman *et al*., 2011).

3.1.1.3 Diabetes mellitus type II

Diabetes mellitus type II is a common metabolic disease, with more than 300 million people currently living with the disease (Knowles *et al*., 2014). Diabetes mellitus type II occurs when cells become insulin resistant, leading to hyperglycemia. Patients also have lower insulin levels compared with healthy individuals. Secondary complications include blindness, stroke, heart attack and loss of blood flow to extremities leading to amputations, leading to life expectancy of patients decreasing by 10 years, compared with healthy individuals (Patel *et al*., 2008).

Islet amyloid polypeptide (IAPP) is strongly associated with diabetes mellitus type II. IAPP and insulin are under the control of the same regulatory elements; they are co-expressed and co-secreted (20:1 molar ratio insulin:IAPP) in pancreatic islet β cells (Cluck *et al*., 2005; Martin, 2006). As an individual becomes insulin resistant, expression of both insulin and IAPP is increased. It may be that these increased concentrations promote the formation of amyloid fibrils from IAPP. It is currently unclear whether islet amyloid deposition, or intermediate oligomers, are the causative agents of pathogenesis, but evidence from *in vivo* mouse models suggests that both may be toxic and pathogenic factors (Höppener *et al*., 1993; Höppener & Lips, 2006; Lin *et al*., 2007).

The incidence of diabetes mellitus type II is predicted to rise over the coming decades, and while the disease can be controlled, current therapies have limited efficacy, side-effects and high cost (Rochester, 2014). Targeting amyloid formation, preventing or delaying β-cell loss, is an attractive avenue for the development of new therapeutics.

3.1.1.4 Dialysis related amyloidoisis

The formation of β_2m fibrils is associated with the systemic disorder dialysis related amyloidosis (DRA). *In vivo,* β_2m is a component of the major histocompatibility complex I (MHC I) that presents 8-10 residue long peptides on the surface of nucleated cells, which are then recognized by T-lymphocytes as part of self-recognition and the immune response (Williams *et al*., 2002). In healthy individuals β_2m is constitutively expressed and

transported to the cell surface as part of the MHC I complex, where it dissociates and is transported to the kidney for degradation (Williams *et al*., 2002). β_2m is removed from the blood by glomerular filtration followed by proximal tubular reabsorption and finally proteolytic cleavage. Significant quantities of β_2m are synthesised in healthy individuals; 2.4 ± 0.7 mg per kg of body mass per day (Floege *et al*., 1991). When renal function is compromised, β_2m is no longer efficiently removed from the blood and degraded, leading to a 25-60 fold increase in serum β_2m. Current dialysis treatments are unable to efficiently remove all β_2m (Rabindranath *et al*., 2006; Floege & Ehlerding, 1996).

Over many years of compromised renal function, elevated levels of β_2m are thought to promote its aggregation into amyloid fibrils (Figure 3-1) throughout the musculoskeletal system, possibly due to the presence of collagen and glycosaminoglycans (GAGs) in these locations (Otsubo *et al*., 2009; Linke *et al*., 2000). This leads to painful joints. Such extracellular aggregates are primarily formed from full length β_2m, although the highly amyloidogenic truncated form of β_2m, ΔN6, can form up to 30 % total β_2m within the extracellular deposits (Linke *et al*., 1989; Esposito *et al*., 2000). Other modified versions of β_2m are also found in *ex vivo* deposits, and contain other components such as glycosaminoglycans, proteoglycans, collagen, apolipoprotein E and serum amyloid protein (Hodkinson *et al*., 2012). These additional factors are thought to stabilise fibrils and play a role in pathogenesis and disease progression.

Patients undergoing long-term dialysis for renal insufficiency experience symptoms ~ 5 years after treatment starts. Carpal tunnel syndrome, chronic arthropathy, destructive spondyloarthropathy, and cystic bone lesions which can result in bone lesions and fractures can all occur as the disease progresses (Yamamoto *et al*., 2013). Current treatments relieve chronic pain and inflammation (Floege & Ketteler, 2001). However, the only curative treatment is renal transplantation, which rapidly and drastically reduces symptoms (Floege & Ehlerding, 1996), although it has yet to be shown whether β_2m amyloid deposits diminish after transplantation (Campistol, 2001). Transplantation is not always possible due to the age of the patient, availability of organs or cultural reasons. Future treatment options may include improved dialysis membranes, but their long term effects remain unclear (Yamamoto *et al*., 2009). Some studies suggest haemodiafiltration, which more effectively removes β_2m, does not offer any improvement to quality of life over haemodialysis treatments (Mazairac *et al*., 2013). It may be that levels of β_2m are not reduced enough to prevent the onset of pathogenesis. In one study, the mean predialysis serum β_2m concentrations were 33.5 mg/L in the high-flux haemodialysis group versus 26.4 mg/L in the haemodiafiltration (Leypoldt *et al*., 2012). Although haemodiafiltration

may offer an improvement over conventional dialysis, these serum concentrations of β_2m are still over 10-fold higher than in individuals with normal renal function.

More recently, a variant of β_2m was described, D76N, which is associated with autosomal dominant hereditary systemic amyloidosis; patients experience progressive bowel dysfunction and extensive visceral amyloid deposits, while their renal function and serum concentrations of β_2m remain normal (Valleix *et al.*, 2012). Interestingly, compared with dialysis related amyloidosis, no ΔN6 β_2m was detected in plaques. Under physiological conditions *in vitro* the D76N variant was fully converted into amyloid fibrils within 48 hours, compared with wt β_2m which does not aggregate under these conditions (Valleix *et al.*, 2012).

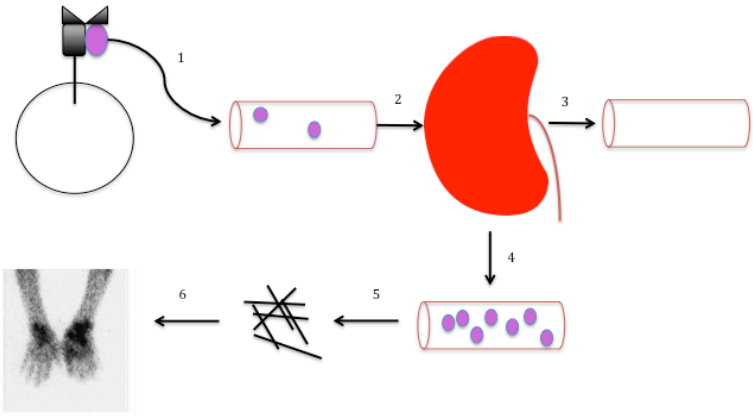

Figure 3-1 Disease progression of dialysis related amyloidosis. β_2m (pink) dissociates from the MHC I complex, on the surface of all nucleated cells (1). β_2m is transported in the blood to the kidneys (2) where in healthy individuals it is removed by glomerular filtration and proteolytic cleavage (3). In patients undergoing dialysis treatment, β_2m is not removed from the blood and so serum concentrations increase (4) and aggregates into amyloid fibrils (5) in the joint environment as shown by the scintigram of a dialysis related amyloidosis patient (6, from Linke *et al.*, 2000).

3.1.2 Amyloid as a prion-like transmissible agent

Proteinaceous infectious particles, or prions, are now generally accepted as the causal agents of Transmissible Spongiform Encephalopathies (TSEs), which include Scrapie in sheep, bovine spongiform encephalopathy in cattle and Creutzfeldt–Jakob disease, Gerstmann–Sträussler–Scheinker syndrome and fatal familial insomnia in humans (Collins *et al.*, 2004). In all TSE's, the ubiquitously expressed cellular prion protein (PrP^{c}) misfolds into Scrapie prion protein (PrP^{Sc}), which then acts as a high fidelity seed, propagating the prion through the cell, and ultimately the organism, via a range of mechanisms including exosomes and tunnelling nanotubes between cells (Prusiner, 1998; Gerdes, 2009). Prions occur as distinct strains; all share the underlying PrP^{c} protein, but differ in their PrP^{Sc}

conformation, and exhibit diverse phenotypes and disease progression (Soto, 2012). Prions can also be transmitted between individuals, with high fidelity of strain preservation (Prusiner, 2012). The precise mechanisms of PrP^{Sc} toxicity are still unclear despite intensive research (Aguzzi & Falsig, 2012). Biochemically, PrP^{Sc} has a high β-sheet content and high levels of resistance to proteinase K digestion compared with PrP^{c}. and can form oligomeric and fibrillar amyloid species (Riesner, 2003).

Interestingly, recent studies have suggested that other protein misfolding diseases share striking similarities to TSE's, and may exhibit prion-like mechanisms of propagation. Shared features such as the ability to seed or template proteins into the amyloid conformation, as well as the mechanisms of cell-cell transmission, have lead many researchers to term a subset of protein misfolding disorders 'prion-like' (Fernández-Borges *et al*., 2015). Some of the strongest evidence for prion-like properties is found in AD and PD. The remaining feature which appears to still separate TSE's from other protein misfolding disorders is that true prions spread not only within the affected organism but also between individuals (Angot *et al*., 2010). An interesting recent study demonstrated that Aβ pathology may have been transmitted through iatrogenic mechanisms; patients injected with human cadaveric pituitary-derived growth hormone showed signs of significant Aβ deposition, despite their young (36-51) age and lack of gene mutations associated with AD (Jaunmuktane *et al*., 2015). This is the first evidence of transmission of AD pathology between humans, and raises concerns that pathology may be transmitted through previously unsuspected routes such as contaminated surgical instruments or blood transfusions. Several groups have reported that Aβ and tau display prion-like transmission between cells (Frost *et al*., 2009; Eisele *et al*., 2009). Brain extracts from a human patient with AD can be injected into the brains of transgenic mice expressing amyloid precursor protein (APP) and induce aggregation and deposition of Aβ extracellular aggregates (Meyer-Luehmann *et al*., 2006). However, in contrast to prions, administration of brain extract through oral, intravenous, intraocular or intranasal mechanisms does not lead to Aβ aggregation (Eisele *et al*., 2009). Other studies have suggested the existence of polymorphic strains of Aβ, further indicating prion like behaviour (Petkova *et al*., 2005). These studies suggest that introducing exogenous aggregates of Aβ or tau can induce aggregation or formation of inclusions from endogenously expressed Aβ or tau, which may spread to neighbouring cells (Angot *et al*., 2010).

For α-synuclein, cell-to-cell transfer of inclusions has been demonstrated in both cell culture and transgenic mice (Desplats *et al*., 2009), although not all studies have

corroborated cell-cell transfer (Luk *et al.*, 2009). Distinct, self propagating strains have also been reported (Yonetani *et al.*, 2009). Recent studies even suggest that a particular prion like stain of α-synuclein may be responsible for causing the disease multiple system atrophy (Prusiner *et al.*, 2015).

Crucial distinctions remain between prions and other protein misfolding disorders. Despite decades of study, no evidence has been found for the spontaneous transmission of AD or PD between individuals (Frost & Diamond, 2010). Serum amyloidosis A is being studied as a potentially infectious amyloid disease which may spread via oral infectivity (Lundmark *et al.*, 2003). There are also differences in the progression rates of disease; most prionopathies exhibit relatively rapid disease progression, patients with CJD typically surviving 4-6 months from the onset of symptoms, compared with AD or PD where patients can survive for decades (Frost & Diamond, 2010). Despite these differences, increasing our understanding of the potential prion-like nature of amyloid species may reveal novel targets for therapeutic intervention (Brundin *et al.*, 2010).

3.1.3 Functional amyloid

Although amyloid is primarily studied as a disease-associated agent, its stability, mechanical strength, proteolytic resistance and prion-like properties have been exploited by evolution to play functional roles in organisms from *E. coli* to humans (Table 3-2)(Shewmaker *et al.*, 2011; Fowler *et al.*, 2007). The prevalence of functional amyloid across different domains of life suggests its quaternary structure may be an evolutionarily-conserved structure underpinning processes vital for normal cell and tissue physiology (Fowler *et al.*, 2006). Functional amyloid fibrils share the generic characteristics of their disease-causing relatives, and it has been suggested that the difference lies in their tight regulation and coordination by other cellular processes to prevent cytotoxicity (Badtke *et al.*, 2009). The study of functional amyloid may help rationalise the cytotoxicity of amyloid species in various disease states. The amyloid fold may also be exploited for biotechnological applications, for example fibrils can form monodisperse microgels and gel shells which may have applications as drug carrier agents (Shimanovich *et al.*, 2015).

Protein	Organisms(s)	Function	Reference
Peptide hormones	Mammals	High Storage Density	(Maji *et al*., 2009).
Melanin formation- Pmel17 proteolytically cleaved into Mα.	Mammals	Melanin formation	(Hearing, 2000; Berson *et al*., 2003; Fowler *et al*., 2006)
Transmissible element- Sup35	Yeast	Modulation of normal translation termination.	(Uptain & Lindquist, 2002; Saibil *et al*., 2012).
Transmissible element- Ure2p	Yeast	Regulation of nitrogen catabolism	(Peter Chien *et al*., 2004).
Curli fimbraie	Bacteria such as *E.coli*	Biofim formation	(Hammer *et al*., 2007; Dueholm *et al*., 2011; Evans *et al*., 2015; Evans & Chapman, 2014)

Table 3.2 Examples of functional amyloid in nature.

1.1.1 Formation of amyloid

The formation of amyloid fibrils from soluble protein is a complex process, with the formation of multiple heterogeneous species en route to the final, mature fibril (Knowles *et al*., 2014). The majority of amyloid species display nucleation-dependent growth kinetics *in vitro* (Collins *et al*., 2004; Xue *et al*., 2008; Ferrone, 1999; Knowles *et al*., 2009). In an *in vitro* setting, using a defined concentration of monomer, a lag phase occurs followed by exponential growth, and finally a plateau as monomer becomes sequestered in aggregates (Figure 3-2). In the lag phase, a dynamic equilibrium exists between different soluble oligomers formed from fully or partially unfolded monomer. In some cases, these associate into higher order assemblies known as protofilaments. These protofilaments and other oligomeric species, may be on or off pathway intermediates of mature fibril assembly (Caughey & Lansbury, 2003). For most proteins, the rate limiting step of fibril formation is the generation of a nucleus which acts as a template onto which soluble species can bind and change conformation to elongate the fibril (primary nucleation), however the rate limiting step can be the conformational conversion of the soluble species or even the dissociation of stable, native complexes to release an aggregation-prone precursor (Lee *et al*., 2011; Hurshman *et al*., 2004; Xue *et al*., 2008). The lag phase can be reduced or eliminated by the addition of pre-formed seeds (Wood *et al*., 1996; O'Nuallain *et al*., 2004). Secondary processes, for example upon fibril fragmentation, can increase the rate of soluble species sequestering into mature fibrils and reduce or eliminate the lag phase. In the exponential growth phase, soluble species are rapidly added to a nucleating particle which acts as a template or seed, enabling the soluble species to adopt the cross-β architecture (Knowles *et al*., 2014).

The process of mature fibril formation can be monitored by the use of fluorescent dyes such as Thioflavin-T or Congo red (Nilsson, 2004; Westermark *et al*., 1999), along with

other techniques such as circular dichroism and mass spectrometry (Knowles *et al.*, 2014). Different species formed en route to fibrils can also be recognised by various conformation-specific antibodies such as A11 (pre fibrillar soluble oligomers), OC (fibillar oligomers) and WO1 (mature fibrils) (O'Nuallain & Wetzel, 2002; Glabe, 2004; Kayed *et al.*, 2007; Kayed *et al.*, 2003). Aggregation kinetics are highly variable, depending on the precursor species and solution conditions (Kad *et al* 2003; Buell *et al.*, 2011; Buell *et al.*, 2014). There is also a potential discrepancy between amyloid fibril formation *in vitro*, which often occurs on the timescale of days, and *in vivo* which occurs over decades.

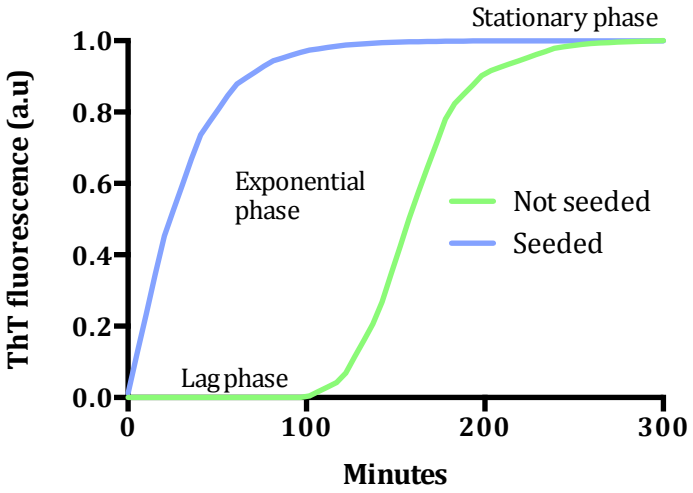

Figure 3-2 Typical amyloid aggregation as measured by ThT fluorescence. A) Typical ThT fluorescence kinetics observed during *de novo* (green) and seeded (blue) amyloid aggregation.

3.1.4 Structure of amyloid

The cross-β motif characteristic of amyloid is formed from the lamination of successive β-sheets (Biancalana *et al.*, 2010). Despite the sequence diversity between proteins that form amyloid, fibrils have structural similarities. The fact that many structurally diverse proteins can form amyloid fibrils suggests that the amyloid fold is governed by protein backbone interactions, while the kinetics and thermodynamics of fibrillation may be modulated by side chain interactions. Amyloid fibrils are commonly identified by their propensity to bind dyes (Bertoncini & Celej, 2011). However, the gold standard for identification remains the characteristic X-ray fibre diffraction pattern (Figure 3-3, A-C) (Sunde *et al.*, 1997; Eanes & Glenner, 1968; Astbury *et al.*, 1935; Jahn *et al.*, 2010), which demonstrates that the strongest repeating feature shared by amyloid fibrils is a set of β-sheets parallel to the fibril axis (Nelson *et al.*, 2005; Jahn *et al.*, 2010).

X-ray crystallography studies of peptides which form amyloid-like fibrils, such as GNNQQNY from the yeast prion Sup35, suggest the fibril core is comprised from β-strands spaced ~ 4.8 Å apart that run perpendicular to the fibril axis, and that these form β-sheets with hydrogen bonding parallel to the axis (Nelson *et al.*, 2005)(Figure 3-3 D, E). It also reveals that side chains from adjacent chains form a steric zipper between pairs of β-

sheets (Nelson *et al*., 2005; Sawaya *et al*., 2007). More recently, electron diffraction has been used to solve the structure of peptide fragments from α-synuclein, which also showed a steric zipper structure (Rodriguez *et al*., 2015)(Figure 3-3 F, G). The cross-β structure suggested in these studies has been independently validated by solid state NMR (Tycko, 2000), and many other structural and biophysical techniques (Boeré *et al*., 1965; Serpell & Smith, 2000; White *et al*., 2009; Knowles *et al*., 2006; Cohen & Calkins, 1959; Shirahama & Cohen, 1965).

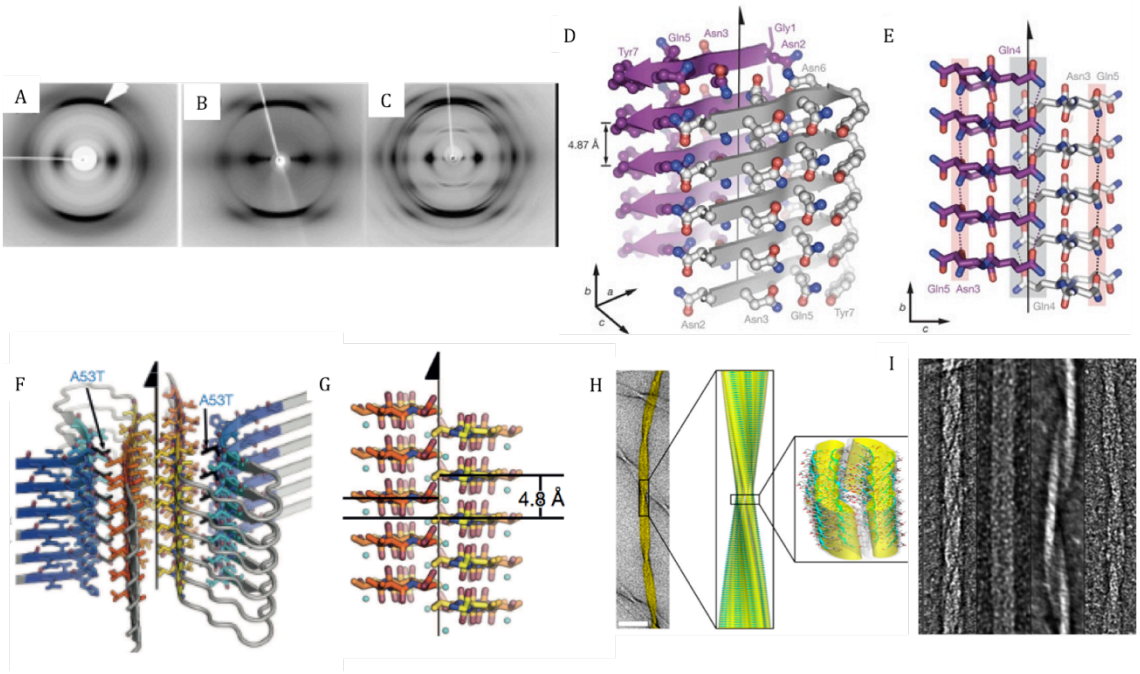

Figure 3-3 Structure of amyloid fibrils. X-ray fibre diffraction patterns from a wide range of fibrils formed from different precursor proteins show characteristic cross-β pattern including $A\beta_{1\text{-}42}$ (A) $IAPP_{1\text{-}37}$ (B) $A\beta_{11\text{-}25}$ (C) (adapted from Jahn *et al.*, 2010). X-ray crystallography has been used to solve the structure of GNNQQNY peptide (D,E). Carbon atoms are coloured in purple or grey/white, oxygen in red, nitrogen in blue. Arrows represent backbone of each β-strand, with side chains protruding. B-strands are spaced by 4.8 Å. The steric zipper viewed edge on shows interdigitation of side chains; Grey line shows dry interface, red lines show wet interface (E) (D,E Adapted from Nelson *et al.*, 2005). Structure of α-synuclein peptides have been solved by electron diffraction of microcrystals (F,G adapted from Rodriguez *et al.*, 2015). Speculative model of an α-synuclein protofibril with the A53T mutation shown in black, where the strong interface of NACore (residues 68–78, orange) forms the core of the fibril (F). Crystal structure of the NACore (G) shows 4.8 Å spacing. Information from a range of structural techniques can be combined to yield a model of an amyloid fibril, such as the magic angle spinning NMR structure of an 11 residue peptide fitted into a cryo-EM density, scale bar 50 nm (H, adapted from (Fitzpatrick *et al.*, 2013). A range of fibril morphologies can be formed from the same precursor protein, as negative stain electron microscopy images show for IAPP fibrils (adapted from Serpell, 2014)

3.1.5 β_2m as a model system

As many amyloid fibrils share similar structural features, common properties of amyloid fibrils can be investigated using a single amyloidogenic protein. In this thesis, β_2m is used as a model system. *In vivo,* β_2m is the non-covalent component of the MHC I complex. It is a 99-residue protein consisting of seven antiparallel β-strands, which form an immunoglobulin, β-sandwich fold consisting of seven β-strands stabilised by a disulphide

bond between β-strands B and F. The structure of β_2m as part of the MHC I molecule and in its monomeric form has been solved by X-ray crystallography (Borbulevych *et al.*, 2010; Trinh *et al.*, 2002) and by solution NMR (Verdone *et al.*, 2002; Eichner *et al.*, 2011). There are 5 proline residues in β_2m, 4 in the trans-conformation, with only proline 32 in the cis conformation; this isomerisation is thought to play a role in β_2m aggregation (Jahn *et al.*, 2006).

Figure 3-4 Structure of human monomeric β_2m
Sheets A, B and E are labelled.
(PDB 1LDS) (Trinh *et al.*, 2002).

3.1.5.1 β_2m amyloid formation

Interestingly, wt β_2m does not form fibrils at physiological pH and temperature, unless in the presence of additional factors such as trifluoroethanol, SDS, glycosaminoglycans (GAGs), proteoglycans, collagen or Cu^{2+} (Eakin & Miranker, 2005; Myers *et al.*, 2006; Relini *et al.*, 2006; McParland *et al.*, 2000). Fibril formation *in vitro* can occur at low pH, with the pathway influenced by salt concentration, agitation, buffer and pH (Kad *et al.*, 2001; Smith *et al.*, 2003; Gosal *et al.*, 2005). At low pH and low ionic strength (pH 2.0, 50 mM NaCl) β_2m amyloid fibril formation proceeds via a nucleation-dependent mechanism (Gosal *et al.*, 2005). Fibrils formed in non-physiological conditions exhibit the classical cross-β fibre diffraction pattern (Platt & Radford, 2009), thioflavin T binding (Xue *et al.*, 2008), Congo red birefringence and WO1 immunoreactivity, (Myers *et al.*, 2006). Vigorous agitation of these β_2m fibrils results in fibrils with the same long straight (Ls) morphology but with shorter lengths due to fragmentation (Ls-f) (Xue *et al.*, 2009). The β_2m variant ΔN6 has been shown to form fibrils under physiological conditions, and therefore is proposed to play a role in initiating amyloid formation (Jones *et al.*, 2003). Further supporting this, truncated β_2m ΔN6 and full length β_2m have been shown to co-polymerise to form heteropolymers, which have distinct biophysical properties compared with fibrils formed from a single monomeric species (Sarell *et al.*, 2013). Using NMR, it has been shown that the truncated β_2m variant ΔN6 promotes conformational changes of full length β_2m at pH 6.2 into an amyloid-competent state (Karamanos *et al.*, 2014). The interaction between β_2m ΔN6 and full length β_2m involves transient, weakly associated, head-to-head

interactions, which destabilises the native state sufficiently to allow fibril formation of wt β_2m (Karamanos *et al.*, 2014).

3.1.6 Morphology of β_2m

β_2m fibrils have been extensively studied using biophysical techniques (Katou *et al.*, 2002; Ladner *et al.*, 2010; Monti *et al.*, 2005; White *et al.*, 2009). The quaternary packing of protofilaments within the mature fibril, and the subunit packing within protofilaments, has been examined using cryo-EM (White *et al.*, 2009). β_2m fibrils formed at pH 2.0 are heterogeneous in their repeat length (120-185 nm), but can be subcategorised into two major types (A and B)(White *et al.*, 2009). The 3D reconstructions show β_2m amyloid fibrils are built from a dimer-of-dimers building block which assemble into protofilaments that associate in an asymmetric fashion into crescent shaped units, which then in turn associate back to back to form the full amyloid fibril. In each crescent, three protofilaments form at least three non-equivalent subunit contacts (Figure 3-5)(White *et al.*, 2009). Scanning transmission electron microscopy (STEM) analysis of mature β_2m fibrils showed a packing density of 52 kDa/nm, indicating that each repeat length (5.25 nm) must be composed of ~24 β_2m monomers (White *et al.*, 2009). NMR and electron paramagnetic resonance demonstrate that β-strands within the mature wt β_2m fibril core are arranged in a parallel, in register order, an architecture found in amyloid fibrils formed from other precursor proteins (Debelouchina *et al.*, 2010).

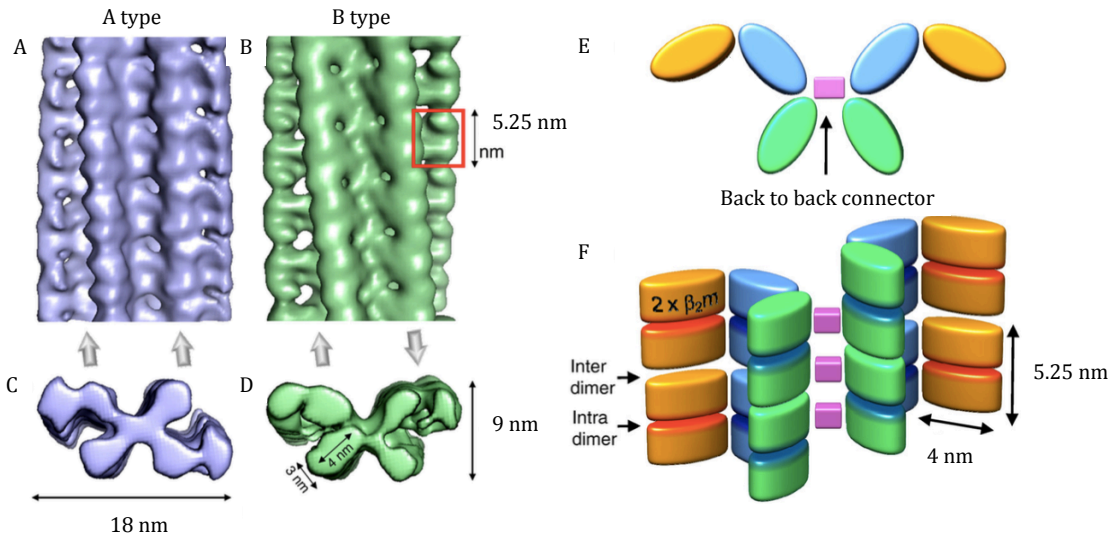

Figure 3-5 Structure of β_2m amyloid fibrils by cryo-EM. 3D reconstructions of type A (A,C) and type B (B,D) forms of β_2m fibrils. One dimeric density unit is indicated by a red box in B. The directions of the half-fibrils are indicated by arrows. Schematic of subunit packing and interfaces in a B-type fibril. E-F) Schematic representation the B type fibril dimer-of-dimers subunit packing for the same fibril orientation; each elliptical cylinder contains to two β_2m monomers. Adapted from White *et al.*, 2009.

In this thesis, β_2m fibrils have been assembled at pH 2.0. FTIR spectroscopy has been used to compare the structural properties of β_2m amyloid fibrils formed at pH 2.5, 7.0 and *ex vivo* fibrils, with all sharing the same structural characteristics (Jahn *et al*., 2008). This suggests it is valid to draw biologically relevant conclusions from the experimental use fibrils formed at non-physiological pH.

3.1.6.1 Oligomers vs fibrils: two sides of a toxic coin

An on-going debate in the field is the relative cytotoxicities of the diverse range of amyloid species that can form (Verma *et al*., 2015). When fibrillar deposits were initially found in patients, they were proposed as the causative agents of disease (Hardy & Higgins, 1992). These deposits are now known to consist primarily of amyloid fibrils. Such fibrils, formed from a wide range of precursor proteins, are associated with disease, including Aβ, lysozyme, IAPP, as well as non-disease associated proteins such as Sup35 and Ure2p, have been shown to exert cytotoxic effects (Gharibyan *et al*., 2007; Petkova *et al*., 2005; Pieri *et al*., 2012; Engel *et al*., 2008; Novitskaya *et al*., 2006; Mossuto *et al*., 2011; Mossuto *et al*., 2010; Picone *et al*., 2009; Qiang *et al*., 2012). However, the observation that the presence of soluble Aβ amyloid species correlated better with AD progression than the deposition of extracellular, fibrillar aggregates, drew attention to these soluble species and their role in cytotoxicity (Fox *et al*., 1999; Naslund *et al*., 2000; McLean *et al*., 1999). It was noted that extensive amyloid plaques have been found in the brain of patients who appear to have normal cognition, while mouse models of Alzhiemer's disease show cell dysfunction and reductions in synaptic plasticity long before extracellular aggregates are detectable (Zhang *et al*., 2011; Moechars *et al*., 1999). This further supports a role for soluble amyloid species in disease.

It has proved difficult to extract oligomers from an *in vivo* setting, but they have been extracted from cell culture and brain tissues. It is noteworthy that the extraction methods often involve harsh steps such as boiling, homogenisation, urea or β-mercaptoethanol treatment, which may destabilise any fibrillar species present, or alter the oligomeric species present in the original sample. With this caveat in mind, both *ex vivo* and *in vitro* oligomeric species have cytotoxic potential (Pountney *et al*., 2004; Lesne *et al*., 2006; Walsh *et al*., 2002; Cleary *et al*., 2005; Townsend *et al*., 2006; Lee & Lee, 2002; Mukai *et al*., 2005). Oligomeric species formed from the Aβ, α-synuclein, huntingtin, IAPP, transthyretin and lysozyme, along with non-disease associated proteins hypf-N and stefin-B, are all cytotoxic (Campioni *et al*., 2010; Rigacci *et al*., 2008; Anderluh *et al*., 2005; Gharibyan *et al*., 2007; Reixach *et al*., 2004; Demuro *et al*., 2005; Nucifora *et al*., 2012). The antibody A11 appears to bind a generic oligomeric conformation, and protects against

cytotoxicity, further supporting the role of oligomers in disease(Kayed *et al*., 2003). This has led to some discounting amyloid fibrils as 'tombstones representing the end point of a past disease process', although this is likely to be a simplistic view in the light of evidence of fibrillar toxicity (Carrell, 2005; Tipping *et al*., 2015).

It is worth noting that in many studies, full biophysical characterisation of the amyloid species is not performed, meaning the presence of oligomeric/fibrillar species, or their interconversion, cannot be discounted. Amyloid polymorphism is now well-documented, with examples of the same precursor protein giving rise to fibrils of different morphology and distinct biological activity (Petkova *et al*., 2005; Mossuto *et al*., 2010; Tycko, 2015; Stein & True, 2014). For example, under different solution conditions β_2m can form both fibrils with long straight (Ls) morphology and 'worm-like' fibrils, which exhibit different cellular effects (Gosal *et al*., 2005; Xue *et al*., 2009) The length of amyloid fibrils can also modulate its biological activity (Xue *et al*., 2009). Both amyloid polymorphism and the difficulty in isolating a stable population of a single amyloid species complicate investigations into precise mechanisms of cytotoxicity.

Fibril and oligomer cytotoxicity need not be mutually exclusive. Fibril disaggregation may act as a source of oligomeric species (Cremades *et al*., 2012). Fibrils exhibit 'molecular recycling' properties, and cytotoxic species could form as part of this process (Sánchez *et al*., 2011). For example, mature Aβ amyloid fibrils can be destabilised and resolubilised by natural lipids into cytotoxic protofilaments (Sánchez *et al*., 2011). Different types of amyloid from the same precursor protein may also cause cell death through different mechanisms, as for hen egg-white lysosome where oligomers and fibrils initiate cell death through apoptotic and necrotic-like mechanisms respectively (Gharibyan *et al*., 2007). $A\beta_{1-42}$ fibrils and oligomers both cause apoptotic cell death, but the oligomeric species acts via caspase-9 activation while fibrils act via caspase-8 activation (Picone *et al*., 2009). Such findings support the hypothesis that disease is not the simple result of one species acting via one mechanism of cytotoxicity, but may be the result of a range of species each contributing or triggering different events, culminating in a complex disease state. This has profound implications for the development of anti-amyloid therapeutics as the old paradigm of 'one bug, one drug' simply will not work for amyloidosis.

3.2 Results

3.2.1 Expression and purification of β_2m

To generate material for the experiments performed in Chapter Three and Four, monomeric β_2m was expressed and purified using established procedures (Section 2.3)(Figure 3-6)(McParland *et al*., 2000). β_2m was expressed in a pINK plasmid transformed into in BL21 (DE3) pLysS *E.coli* cells (Section 2.3.1). After induction of protein expression with IPTG, the protein aggregates into inclusion bodies which were isolated and solubilised (Section 2.3.1, 2.3.2) (Figure 3-7 A)(Kad *et al*., 2001). Protein was refolded by dialysis (Section 2.3.3). β_2m was separated from contaminants by anion exchange chromatography (Section 2.3.4)(Figure 3-7 B). Fractions 8-13 were judged by peaks in absorbance (280 nm) to contain protein and so were pooled, dialysed against 18 MΩ purite water and lyophilised. The lyophilised protein was re-solubilised in 25 mM sodium phosphate buffer (pH 8.0) prior to further purification by size exclusion chromatography, to separate monomeric β_2m from higher order species or other contaminants (Section 2.3.5)(Figure 3-7, C). Fractions 25-35 corresponding to monomeric β_2m were pooled, dialysed against 18 MΩ purite water and lyophilised. Protein purity was assessed by SDS-PAGE and ESI mass spectrometry (James Ault, University of Leeds)(Figure 3-7 D, E). The major peak at 11859 ± 0.86 Da corresponds to the molecular weight of monomeric β_2m protein (expected mass 11,860 Da). The additional low intensity peaks correspond to mono- and bi- phosphate adducts.

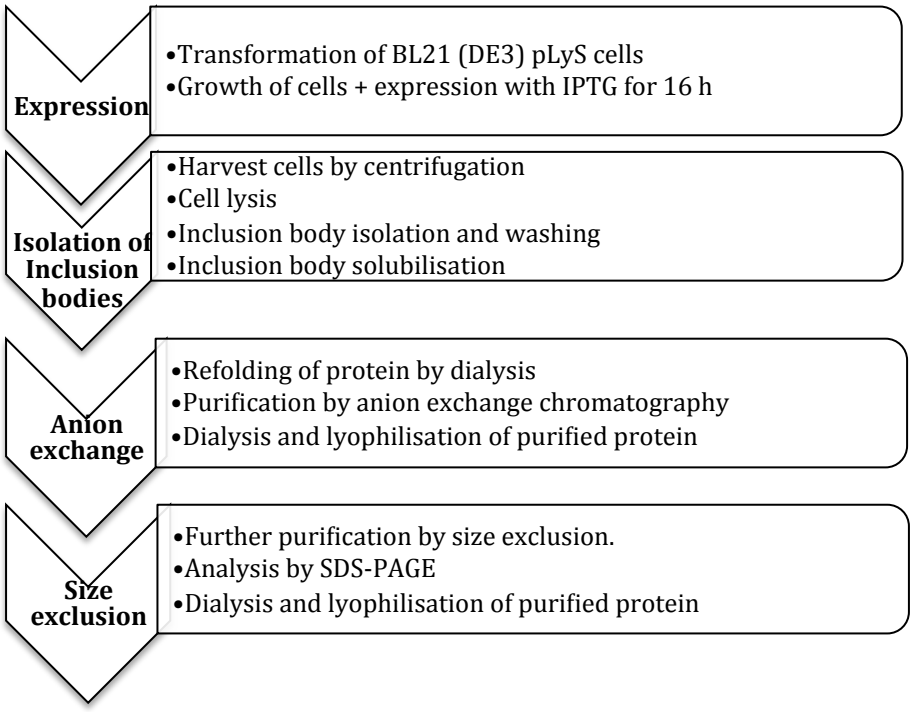

Figure 3-6 Schematic of β_2m expression and purification.

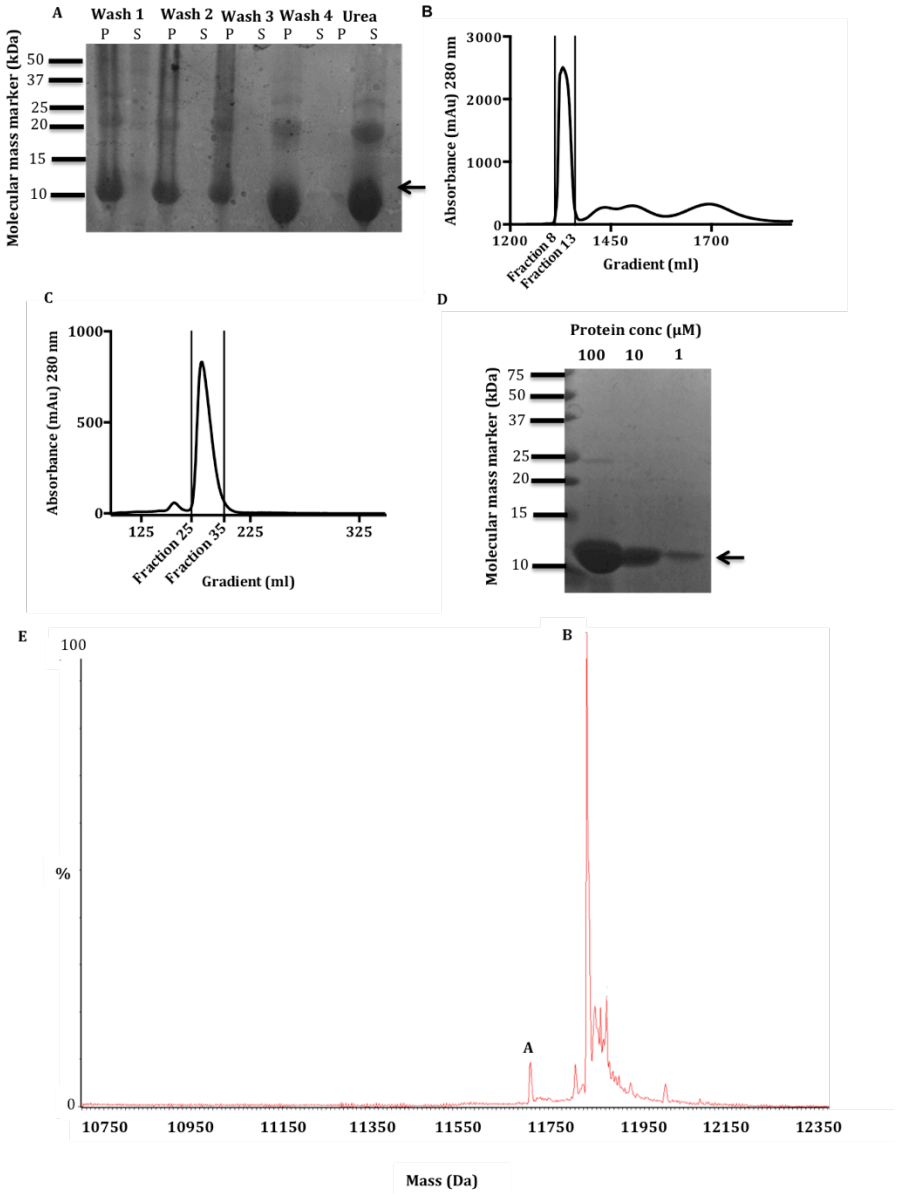

Figure 3-7 Purification of β_2m. A) Protein resolved on 15 % (w/v) Tris-Tricine SDS-PAGE gel stained with Coomassie blue. P=pellet, S=soluble fraction. No protein was visibly lost during washing of the inclusion bodies (Wash lanes-protein remains in the pellet). Upon being solubilised into 8 M urea, protein is fully solubilised (No band visible in the pellet). Black arrow indicates expected mass of β_2m. B) Ion exchange chromatography of solubilised inclusion bodies. Protein was applied to a Q-Sepharose column and eluted using 0.5 M NaCl, fractions 8-13 pooled, dialysed and lyopholised. C) Size exclusion chromatography shows a single major peak, fractions 25-35 were pooled and lyophilised. D) Protein resolved on 15 % Tris-Tricine SDS-PAGE gel stained with Coomassie blue. Arrow indicates expected mass of β_2m. E) Purified β_2m protein analysed by ESI-MS. Peak B (11859 ± 0.86 Da) represents wild type β_2m with disulphide bond. Peak A represents wild type β_2m lacking N-terminal methionine residue. Other peaks are potassium and phosphate adducts. Sample analysis was performed by James Ault, Mass Spectrometry Facility, University of Leeds.

3.2.2 Formation and characterisation of β_2m amyloid fibrils

To form material for experiments in Chapters three and four, β_2m amyloid fibrils with long, straight morphology (Ls) were generated from purified monomeric β_2m in a seeded reaction according to an established protocol (Section 2.3.8). The morphology of fibrils is known to vary depending on the solution conditions (Kad *et al* 2003). Additionally, *de novo* preparations of fibrils may exhibit a broad range of fibril morphologies. Seeding fibril formation means that the same range of fibril morphologies can be propagated between independent samples, increasing consistency between batches of prepared fibrils. Fibrils with a long straight (Ls) morphology were generated because of their similarity to *ex vivo* fibrils (Jahn *et al*., 2008). Ls fibrils were generated by incubating β_2m adjusted to 120 μM in fibril growth buffer (Table 2.2), and seeded with 0.1 % (v/v) β_2m seeds. All Ls fibrils were seeded from one of two β_2m seed batches, which were judged to be morphologically indistinguishable using negative stain EM (Figure 3-8). Fibril formation was allowed to proceed quiescently at room temperature for 24 h.

Ls fibril length is variable, with fibrils growing > 1 μm in length. Fibrils formed showed dimensions consistent with prior work, with a fibril diameter of ~ 20 nm by negative stain EM, and a variable cross-over length (Figure 3-9 A,B) (White *et al*., 2009). It has been previously demonstrated that alterations in the distribution of fibril lengths alters β_2m fibril behaviour in both *in vitro* and cellular assays (Xue *et al*., 2009). To generate fibrils with a shorter length, β_2m Ls fibrils were fragmented for 48 hours at room temperature using a custom build precision stirrer at 1000 RPM (Xue *et al*., 2009), creating Ls-fragmented (Ls-f) fibrils. Ls-f fibrils were morphologically characterised using negative stain EM, and posess the same morphology as their longer counterparts, but a shorter length distribution (Figure 3-9). Average length distributions were determined as ~ 1.3 μm (Ls), and ~ 300 nm (Ls-f) using atomic force microscopy (Figure 3-10).

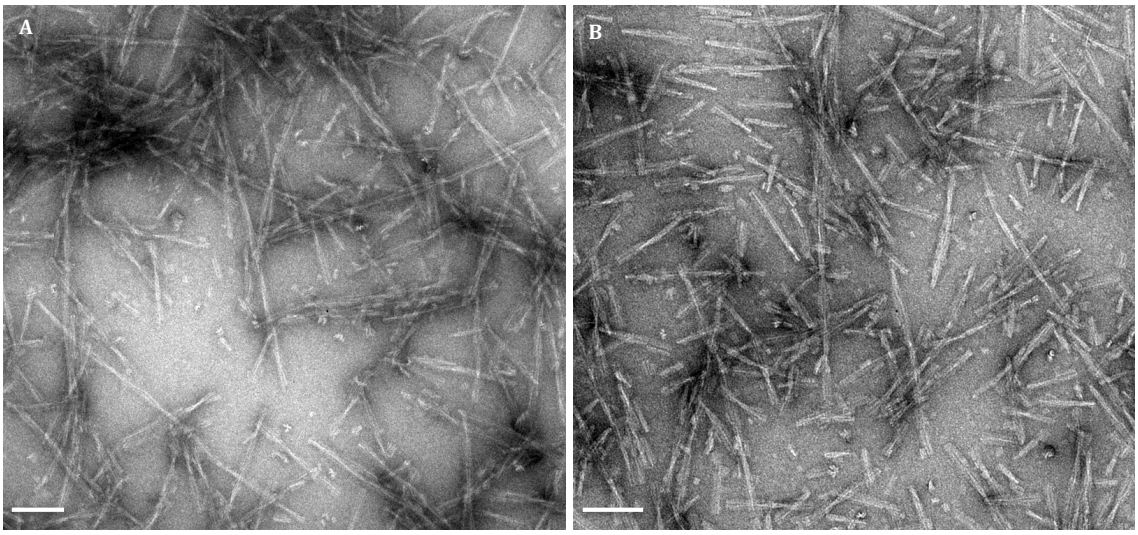

Figure 3-8 Characterisation of β_2m amyloid fibril seeds. Morphology of two completely independent *de novo* β_2m seed batches, imaged by negative stain EM. Scale bar 100 nm.

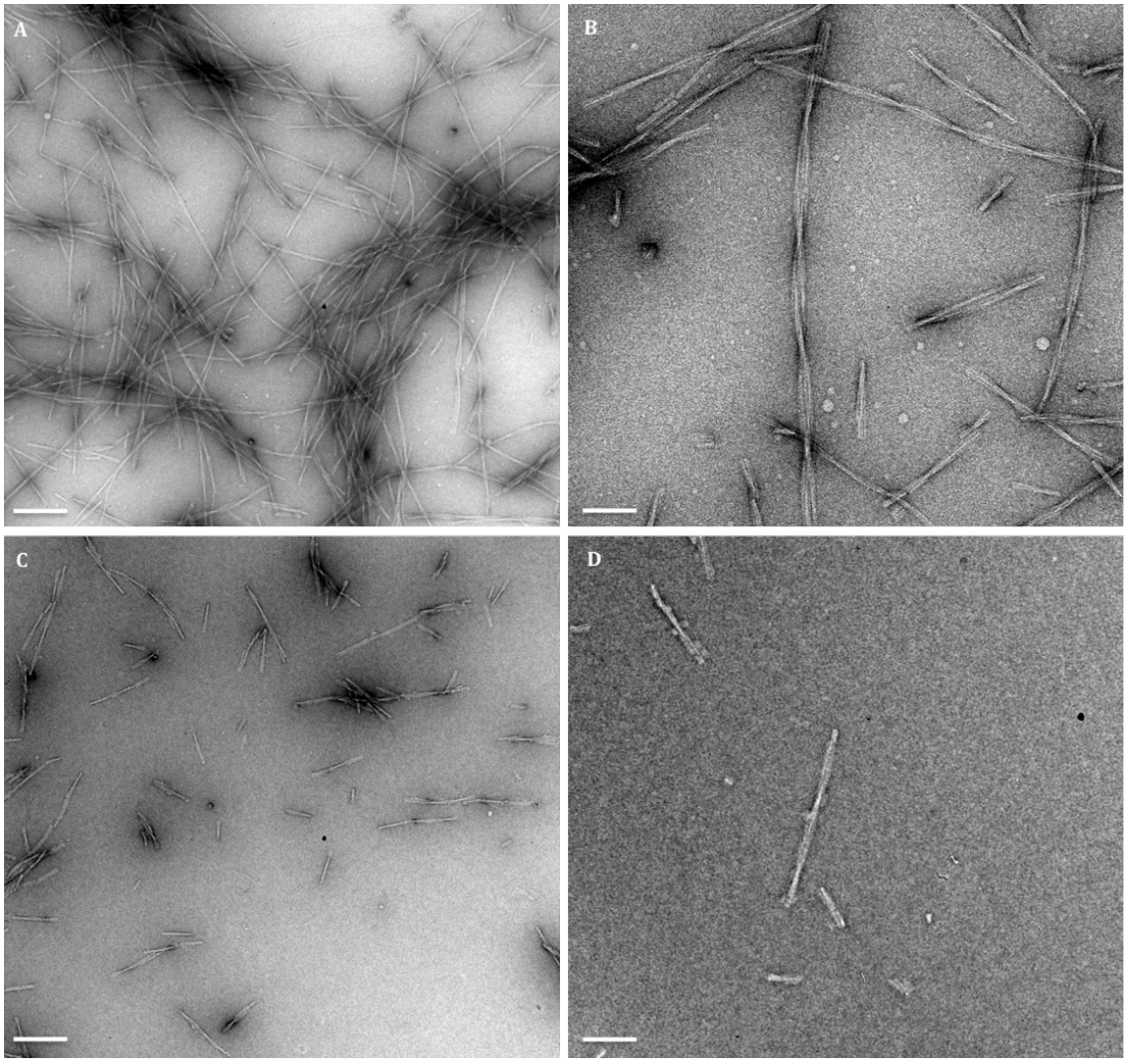

Figure 3-9 Morphological characterisation of Ls and Ls-f β_2m fibrils. Negative stain EM was used to visualise Ls fibrils (A,B) and Ls-f fibrils (C,D). Scale bar 200 nm (A,C) and 50 nm (D,B).

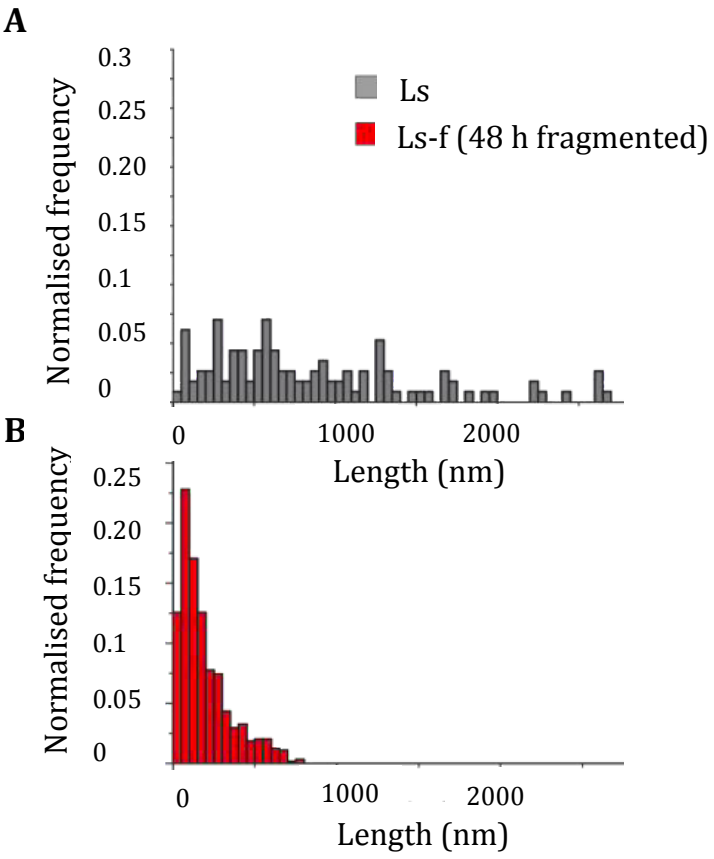

Figure 3-10 Fibril length distributions determined by AFM. Normalised frequency distributions for Ls (grey) and Ls-f (red) fibrils. Average length for Ls fibril is ~ 1.3 μm, and Ls-f ~ 300 nm. Performed and analysed by Dr K Tipping, University of Leeds.

A characteristic property of amyloid is the ability to bind aromatic dyes such as ThT and NIAD-4 (Bertoncini & Celej, 2011). To confirm β_2m amyloid fibrils exhibit the same behaviour, the binding of dye to Ls and Ls-f fibrils was measured, relative to a β_2m monomer control. ThT is an amyloid-binding dye whose fluorescence increases greatly when bound to the amyloid conformation (Biancalana & Koide, 2010; Nilsson, 2004). Increased ThT fluorescence is a consistent observation across amyloid fibrils formed from many precursor proteins. Protein samples were incubated with ThT as described (Section 2.3.9.1). ThT fluorescence increased in the presence of Ls-f and Ls fibrils, 60-fold and 90-fold respectively, compared with the monomer control (Figure 3-11). The increased ThT fluorescence of Ls fibrils compared to Ls-f fibrils may due to the longer length providing more binding sites for ThT compared to fragmented fibrils.

NIAD-4 also exhibits an increase in fluorescence upon binding to amyloid, along with a shift in spectral properties (Nesterov *et al.*, 2005; Olzscha *et al.*, 2011). NIAD-4 is thought to form non-emissive assemblies in aqueous solution, which convert into fluorescent monomers upon diffusion into the hydrophobic voids of amyloid deposits (Peccati *et al.*, 2015). The fluorescence of NIAD-4 with β_2m monomer and Ls-f fibrils was assessed at pH 2.0, 4.4 and 7.4. At each pH tested, a clear increase in fluorescence in the presence of β_2m

Ls-f fibrils compared with the same monomer equivalent concentration of monomeric β_2m (Figure 3-12) was observed. At acidic pH, NIAD-4 has an emission maxima of ~ 595 nm and at pH 7.4, an emission maxima of ~ 580 nm.

A

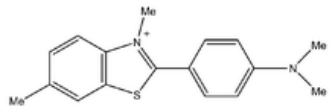

Thioflavin T

B

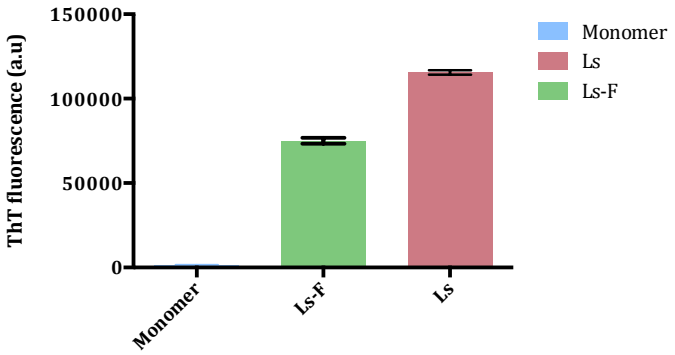

Figure 3-11 Characterisation of ThT fluorescence upon binding to β_2m species. A) Structure of ThT, adapted from (Brandenburg *et al.*, 2012). B) Fluorescence increase of ThT upon binding to β_2m species. Samples containing 6 µM monomer equivalent protein and 10 µM ThT were incubated for 10 minutes. 60 fluorescence intensity readings were taken over 1 minute; ThT fluorescence is the mean of these readings. Error bar represents standard deviation 3 replicates.

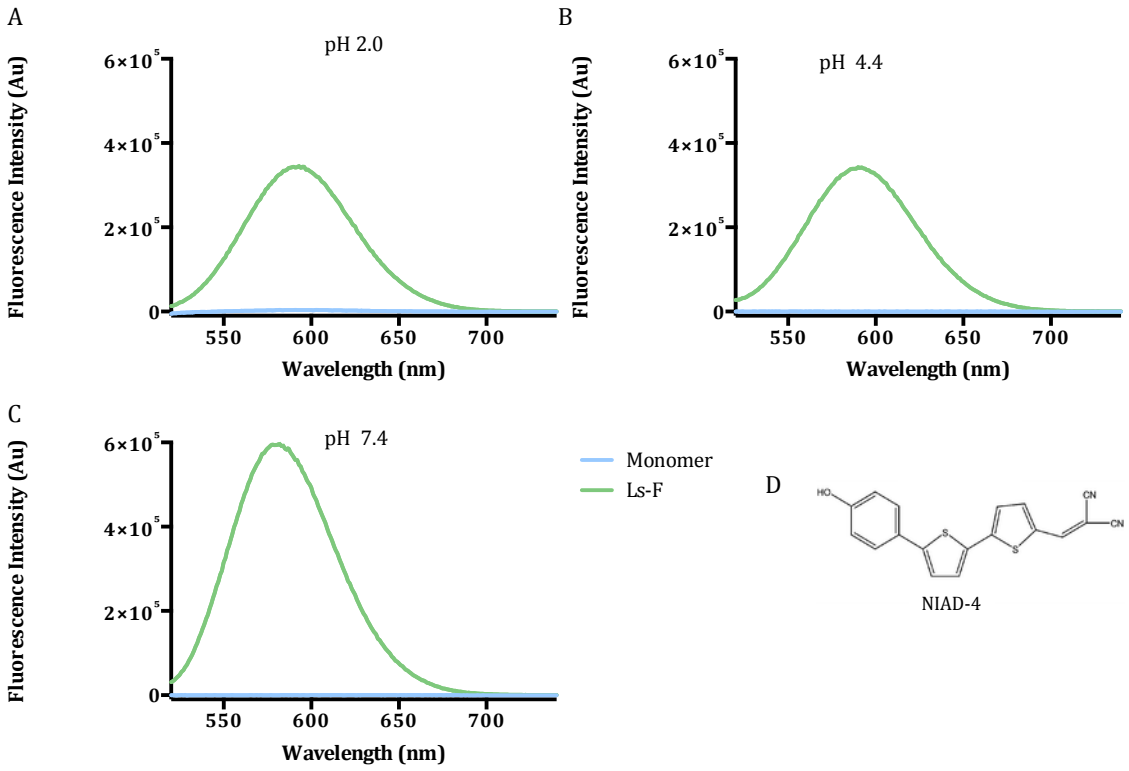

Figure 3-12 Characterisation of NIAD-4 fluorescence upon binding to β_2m species at pH 2.0, 4.4 and 7.4. Fluorescence emission spectra of NIAD-4 (7.5 µM) with monomeric β_2m or β_2m Ls-f (12 µM monomer equivalent) at pH 2.0 (A), pH 4.4 (B) and pH 7.4 (C). Samples were incubated for 10 minutes before a fluorescence emission spectra was collected at an excitation wavelength of 500 nm using at PTI Quantmaster fluorescence spectrometer, slit width 8 nm. Emission spectra are normalised to NIAD-4 in specific pH buffer. D) Structure of NIAD-4, adapted from (Brandenburg *et al*., 2012).

Amyloid species formed from a range of precursor proteins bind conformational-specific antibodies (reviewed in Glabe, 2008). Here, the binding of protein samples to conformational antibodies A11 and W01 was assessed. Protein samples were applied onto a nitrocellulose membrane and immunoblotted with A11, WO1 or β_2m antibodies (Section 2.2.3). Consistent with previously published observations, both Ls and Ls-F fibrils show binding to WO1, which recognises an amyloid fibrillar epitope, while not binding to A11, which binds to an oligomeric conformation (Figure 3-13)(Xue *et al*., 2009).

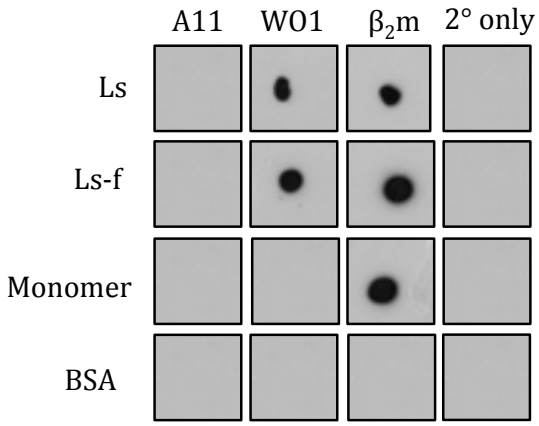

Figure 3-13 Binding of amyloid to conformation-specific antibodies. Samples of β_2m monomer, Ls or Ls-f amyloid fibrils or control protein (2.8 μg protein per dot) were analysed by dot immunoblotting. Fibrils (Ls, Ls-f) show no binding to the anti-oligomer antibody A11, but do show binding to the anti-fibril antibody WO1. Anti-β_2m antibody binding was detected in all β_2m samples, and serves as a loading control. Antibody binding was detected with secondary anti-rabbit IgG-HRP for A11 and β_2m antibodies, and anti-mouse IgM-HRP for WO1 antibody. For secondary antibody only control, samples were treated in the same manner as other samples, but with no primary antibody incubation. Antibody binding was visualised by chemiluminescence.

3.2.3 Characterising cellular effects of β_2m amyloid fibrils

To assess the cellular response to amyloid fibril internalisation, RAW 264.7 cells were used in the MTT assay, a commonly used cell viability assay (Stockert *et al*., 2012)(Section 2.5.1). The MTT assay measures the cell's ability to internalise MTT (yellow) and reduce it to a formazan (blue). Reduction of MTT is performed by mitochondrial and cytosolic dehydrogenases (Saravanan *et al*., 2003). The level of MTT reduction can be assessed by spectroscopic measurement of the formazan salt.

Cells were incubated with β_2m monomer, Ls or Ls-f fibrils, at a concentration of 1.2 μM (monomer equivalent) for 24 h (Section 2.5.1). The percentage of MTT reduction was normalised to 0 % (sodium azide control) and 100 % (pH 2.0 fibril buffer). As has been reported previously, Ls-f fibrils inhibit MTT reduction to a greater extent than Ls fibrils at the same monomer equivalent concentration (Xue *et al*., 2009).

While the MTT assay is a common measure of cell viability, under some circumstances MTT reduction can become uncoupled from cell death. Studies with amylin and Aβ peptide demonstrated that amyloid species inhibit MTT reduction, however, this inhibition is associated with an increase in formazan exocytosis, which can be visualised by needle-like

formazan crystals at the cell periphery, compromising plasma membrane integrity. Under these circumstances, other cell viability assays fail to detect cell death (Isobe *et al.*, 1999; Wogulis *et al.*, 2005; Liu & Hong, 2005). More recently, it has been shown that β_2m amyloid species alter formazan crystal localisation, with Ls and Ls-f treated cells showing a marked increase in the extracellular deposition of formazan crystals compared with monomer and pH 2.0 fibril-treated controls (Jakhria *et al.*, 2014). Additionally, cell viability as measured by adenosine triphosphate (ATP) levels failed to detect cell death, indicating in this instance the MTT assay is not an accurate measure of cell viability, but does reflect a change in cellular behaviour (Jakhria *et al.*, 2014).

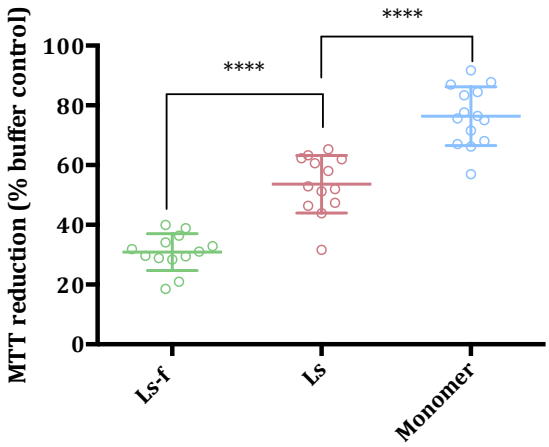

Figure 3-14 Analysis of the effect of fibrils on MTT reduction. MTT assays were performed on RAW 264.7 cells using β_2m monomer, Ls- or Ls-f fibrils at a final monomer equivalent concentration of 1.2 μM. Cells were incubated treatment for 24 h before being tested for MTT reduction. MTT reduction (%) was normalised against the signal from cells incubated with pH 2.0 fibril buffer (100%) and cells treated with 0.1% (w/v) sodium azide (0%). The error bars represent one standard error of mean (S.E.M.) over three independent experiments each containing 3-5 replicates. ****= $P \leq 0.001$.

3.2.4 Role of lipid composition and pH in membrane perturbation by β_2m amyloid fibrils

Some monomeric amyloidogenic proteins and higher order amyloid aggregates interact directly with membranes (Necula *et al.*, 2003; Knight & Miranker, 2004; Choo-Smith *et al.*, 1997; Engel *et al.*, 2008). Under some conditions, these interactions directly permeabilise membranes, a potential mechanism for amyloid-mediated cytotoxicity (Chapter Four)(Stefani, 2010; Berthelot *et al.*, 2013).

The disruption of liposomes can be measured using a liposome dye release assay (Figure 3-15). Large unilamellar vesicles (LUVs) are loaded with carboxyfluorescein dye, which is

pH sensitive and has limited solubility at acidic pH. For all dye-release experiments performed here, carboxyfluorescein was loaded into LUVs at pH 7.5 and high concentration (~50 mM), where carboxyfluorescein fluorescence is self-quenching (Chen & Knutson, 1988). At acidic pH, before measuring carboxyfluorescein fluorescence, the pH was adjusted to 7.5. As carboxyfluorescein fluorescence was always measured at pH 7.5, direct comparisons can be made between experiments performed under different pH conditions. For experiments performed at pH 7.5, carboxyfluorescein fluorescence was measured continuously. For each dye release measurement, β_2m monomer, Ls or Ls-f fibrils were incubated with the CF-loaded LUVs in a total volume of 200 µl at appropriate pH, yielding a reaction mix of 6 µM protein (monomer equivalent) and 5 µM lipid molecule equivalent. β_2m fibrils have a mass/unit length of 53 kDa/nm, which combined with AFM measurements of fibril length distributions for Ls and Ls-f fibrils enabled particle concentration to be calculated as 3.4 nM and 15.5 nM, respectively (White *et al*., 2009; Goodchild *et al*., 2014). Therefore, the approximate fibril particle: lipid molar ratio used here for all liposome dye release equates to ~ 1:300 for Ls-f and ~ 1:1500 for Ls fibrils, which is a typical ratio (Ambroggio *et al*., 2005).

It has been shown previously that Ls-f β_2m amyloid fibrils disrupt synthetic liposomes formed from phosphatidylcholine (PC) and phosphatidylglycerol (PG) at pH 7.4 (Xue *et al*., 2009). Here, the ability of monomeric, Ls and Ls-f β_2m species to disrupt LUVs formed a wider range of lipid compositions and at pH 6.5 and 7.5 was examined. These pH conditions were selected to mimic cytosolic (pH 7.5) and early endosomal (pH 6.5) conditions.

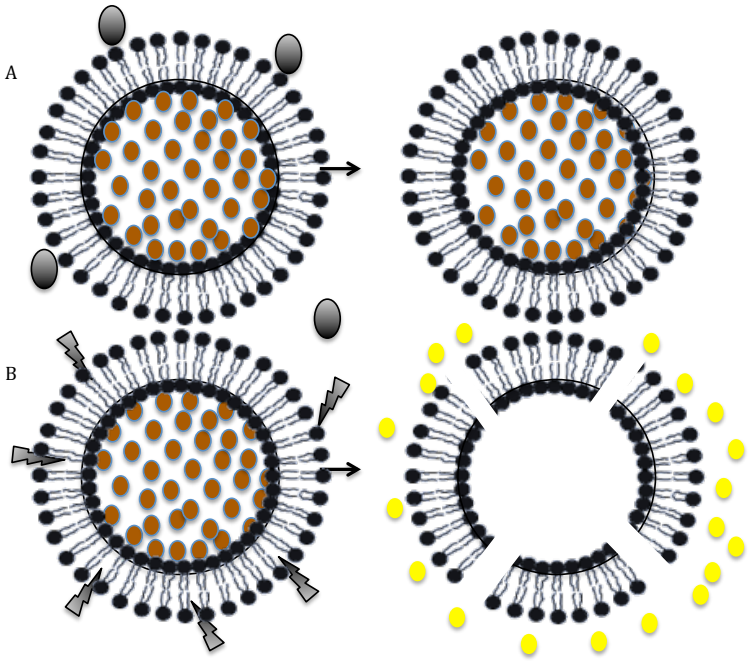

Figure 3-15 Schematic representation of the liposome dye release assay. LUVs are loaded with carboxyfluorescein at a self-quenching concentration (dark orange circles)(A). If LUVs are incubated with protein that disrupts its integrity (B), carboxyfluorescein is released and there is a large increase in fluorescence intensity as carboxyfluorescein is diluted into the reaction volume.

To assess the ability of Ls-f fibrils to disrupt LUVs, 100 mol % DMPS LUVs were used in the liposome dye release assay (Figure 3-16, Table 3-3). DMPS was chosen as this lipid has been shown to modulate the aggregation of amyloid species (Galvagnion *et al.*, 2015). At pH 6.5, LUVs were incubated with Ls, Ls-f and monomeric β_2m species for 60 mins at 45 °C. This temperature was chosen as DMPS has a melting temperature (T_m) of 35 °C. End point fluorescence measurements did not detect LUV disruption in samples incubated with Ls, Ls-f or monomeric β_2m species at pH 6.5 (Figure 3-17 A). Carboxyfluorescin was continually measured over 60 minutes for liposomes treated with Ls, Ls-f and monomeric β_2m species at pH 7.5. Both Ls and Ls-f fibrils were shown to induce low levels of membrane perturbation, with 15-20 % dye release detected (Figure 3-17 B). At the same monomer equivalent concentration, Ls-f fibrils have a greater propensity to disrupt DMPS LUVs compared with their longer counterparts (Figure 3-17 B,C). The addition of monomeric β_2m protein resulted in minimal dye release (< 5 %).

A

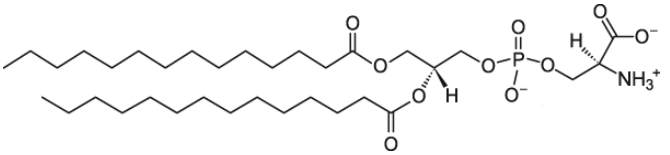

DMPS lipid
1,2-dimyristoyl-sn-glycero-3-phospho-L-serine

B

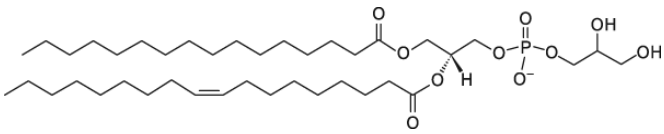

POPG lipid
1-palmitoyl-2-oleoyl-*sn*-glycero-3-phospho-(1'-*rac*-glycerol)

Figure 3-16 Structure of lipid components in simple LUVs

LUV name	DMPS	POPG	Cholesterol
DMPS	100	0	0
POPG:Chol	0	75	25

Table 3.3 Total mol % lipid composition of simple lipid mix LUVs.

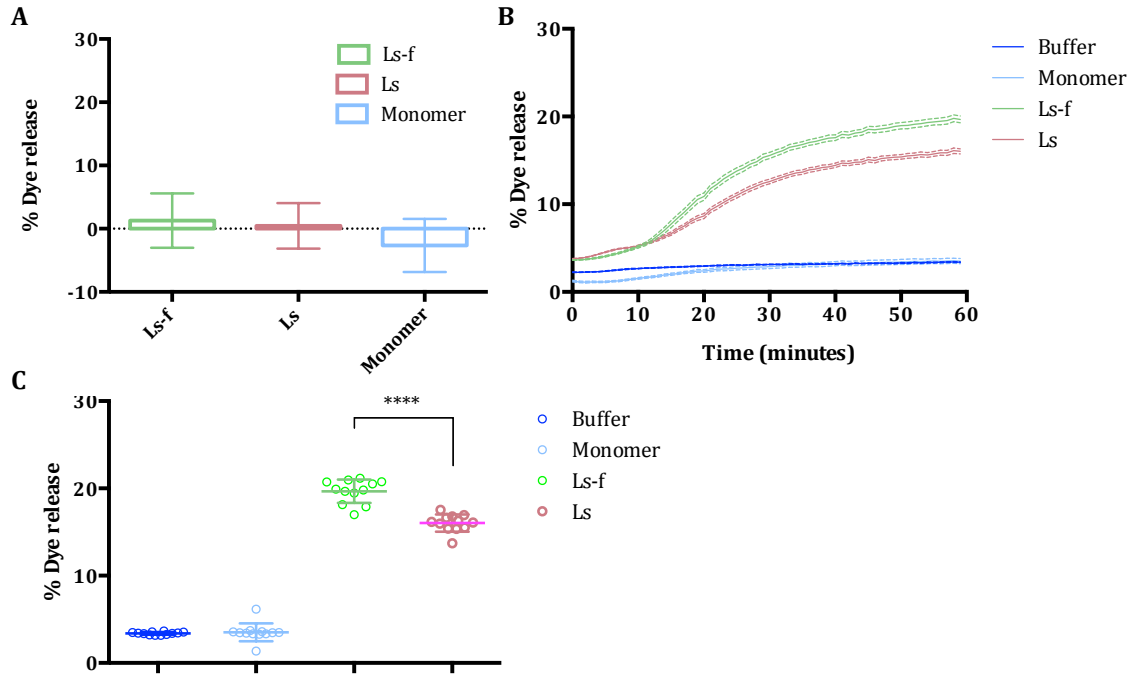

Figure 3-17 Ls and Ls-f β_2m fibrils disrupt LUVs formed from 100 mol % DMPS at pH 7.5 but not pH 6.5. LUVs at pH 6.5 (A) were incubated with 6 μM protein (monomer equivalent) and 5 μM lipid molecule for 60 mins, 45 °C, after which pH was increased to pH 7.5 and fluorescence intensity read. End point fluorescence was normalised to Triton X-100 treated samples (100 % dye release) and appropriate buffer (0% dye release). At pH 7.5, samples were incubated with carboxyfluorescein fluorescence intensity was measured continuously over 60 minutes (B), with dye release normalised to Triton X-100 treated samples (100 % dye release). Error bars represent standard error of three replicates, each containing four repeats. C) Differential fluorescence at 60 minutes, pH 7.5, is represented in a box plot. Statistical significance was calculated using a one-way ANOVA, ****= P ≤ 0.001.

Next, the effect of pH on the ability of Ls-f fibrils to disrupt LUVs formed from POPG:Chol (Table 3.3 ,Figure 3-16) was assessed. At pH 7.5, POPG:Chol LUV disruption was not observed upon incubation with monomeric or fibrillar β_2m, even with a longer incubation period (Figure 3-18). To assess the effect of pH on β_2m species behaviour in the liposome dye release assay, LUVs were prepared in pH 4.5 or 6.5 buffer and incubated with protein or buffer treatment for 10 minutes before measurement of carboxyfluorescein fluorescence. At pH 6.5 and 4.5, high levels of dye release were observed, 46 ± 3.2 % and 50 ± 1 % respectively, indicating that pH plays a key role in mediating β_2m Ls-f fibril disruption. Addition of monomeric protein resulted in minimal dye release, consistent with previous results (< 10 %) (Xue *et al.*, 2009). At pH 7.5, fluorescence was continually measured over 60 minutes. Over this time period, minimal fluorescence was detected, indicating no detectable LUV disruption by monomeric and Ls-f β_2m species.

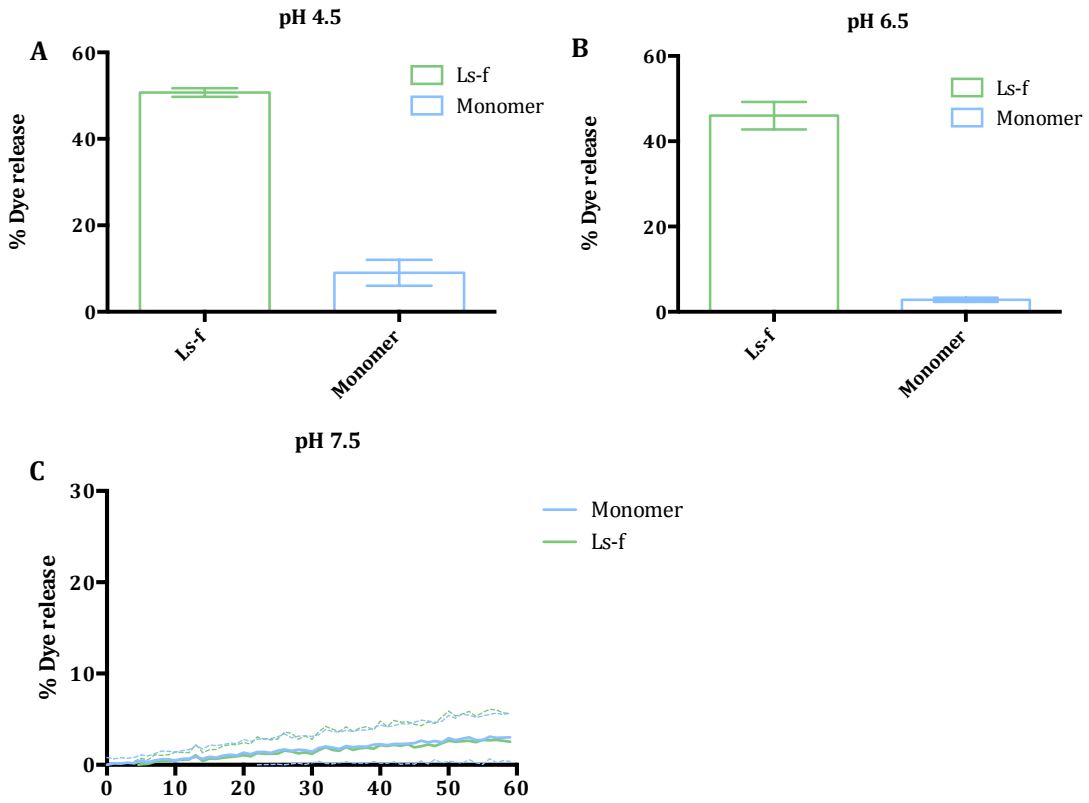

Figure 3-18 Ls-f β_2m fibrils disrupt LUVs formed from 75 mol % POPG, 25 mol % cholesterol at pH 4.5 (A) and pH 6.5 (B) but not pH 7.5 (C). LUVs at pH 4.5 (A) and 6.5 (B) were incubated with 6 μM protein (monomer equivalent) at 5 μM lipid molecule for 10 mins, 37 °C, after which pH was increased to pH 7.5 and carboxyfluorescein fluorescence intensity read. End point fluorescence was normalised to Triton X-100 treated samples (100 % dye release) and appropriate buffer (0% dye release). At pH 7.5, samples were incubated with carboxyfluorescein fluorescence intensity was measured continuously over 60 minutes (C), with dye release normalised to Triton X-100 treated samples (100 % dye release) and appropriate buffer (0 % dye release). Error bars represent standard error of 3 repeats each containing three replicates (A,B) or standard error of three replicates (C).

To characterise the LUVs formed, dynamic light scattering (DLS) was used (Section 2.6.5). All LUVs here were extruded to 400 nm, but changes in lipid composition may influence the size distribution of LUVs, and subsequently their behaviour in the liposome dye release assay. DLS of POPG and DMPS liposomes revealed a hydrodynamic radius (R_h) of 187 ± 78 nm and 136 ± 72 nm, respectively. It is perhaps unsurprising that the DMPS liposomes are slightly smaller on average, as the chain lengths of DMPS is 14 C, compared with 16:0-18:1 for POPG, and chain length is known to affect the process of liposome formation (Figure 3-16)(Zook & Vreeland, 2010).

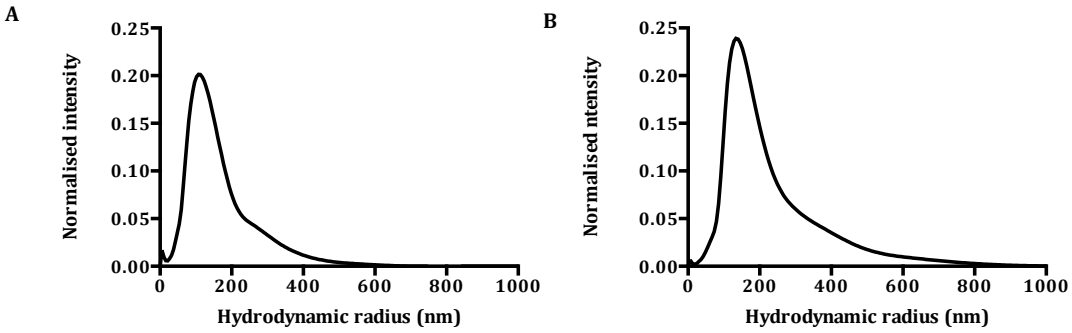

Figure 3-19 DLS of LUVs formed from 75 mol % POPG, 25 mol % cholesterol (A) and 100 mol % DMPS (B). A) R_h 187 ± 78 nm. Average of three mean readings ± 1 SD. B) R_h 136 ± 72 nm. Average of three mean readings ± 1 SD Performed and analysed by Dr Sophia Goodchild.

3.2.5 β_2m fibrils disrupt LUVs with complex lipid mix

Simple lipid mixtures in LUVs formed from DMPS and POPG:Chol are different from biological membranes in several key ways, including complexity of lipid composition, presence of integral membrane proteins and differences in membrane curvature. To assess the propensity of monomer, Ls and Ls-f fibrils to disrupt LUVs that more closely mimic specific biological membranes in lipid composition, LUVs were extruded from synthetic lipid compositions containing different anionic lipids against a background of common cellular lipids (Figure 3-20, Table 3-4).

Physiologically relevant complex lipid mixes were used to reflect the global average of zwitterionic lipids present in various cellular membranes (Van Meer *et al*., 2008). Several different anionic lipid components were varied in LUVs (Figure 3-20). POPS is highly enriched within the inner leaflet of the plasma membrane (Vácha *et al*., 2009). POPG is a minor phospholipid component of many intracellular membranes, accounting for less than 1% of total phospholipids, it is primarily enriched in mitochondrial membranes, and is a precursor of the mitochondrially enriched lipid cardiolipin (Morita & Terada, 2015). BMP is a lipid highly enriched in endocytic compartments, it can comprise > 70 % of some endocytic membranes, and comprises ∼15% of the total lipid composition of late endosomes (Kobayashi *et al*., 2002; Kobayashi *et al*., 1999; Kobayashi *et al*., 1998). BMP is also a structural isomer of POPG. These different anionic lipids were incorporated into 400 nm extruded LUVS at 12 mol % or 50 mol % of the total lipid composition (Table 3-4). In the complex LUVs, 1-palmitoyl-2-oleoyl-sn-glycero-3-phosphocholine (POPC), 1-palmitoyl-2-oleoyl-sn-glycero-3-phosphoethanolamine (POPE), sphingomyelin and cholesterol were chosen for their high levels in biological membranes.

Performing liposome dye release assays on complex lipid mix LUVs demonstrated that dye-release is influenced both by lipid composition and pH conditions. LUVs containing 12 mol % or 50 mol % POPS show minimal membrane disruption in the presence of β_2m Ls-f (Figure 3-21). The membrane disruption observed was comparable to that of control LUVs lacking an anionic lipid component. Contrastingly, for LUVs enriched POPG or BMP, the amplitude of dye release is greater for LUVs enriched in 50 mol % anionic lipid compared with 12% anionic lipid at all pHs.

Dye release experiments were performed at pH 4.5, 6.4 and 7.4, which represent the pH values present through the endocytic pathway of a cell. These experiments showed that pH has a large effect on the propensity of amyloid fibrils to disrupt LUVs. For LUVs enriched in 50 mol % POPG and BMP, there is pH-dependence of membrane disruption, with a significant increase in the amplitude of dye release from pH 7.4 to pH 6.4. The extent of dye-release is similar for these liposomes at pH 5.5 and 6.5, but decreases upon reducing the pH further to pH 4.5. This pH-dependent trend is less pronounced for LUVs containing 12 mol % BMP or POPG LUVs, where the dye release does not change significantly between pH 6.4, 5.5 and 4.5. The greatest extent of dye release is seen in LUVs containing 50 mol % BMP, where ~ 60% membrane disruption is observed at pH 5.5. This is ~1.5-fold greater than that observed for LUVs enriched in 50 mol % POPG (structural isomer of BMP), at the equivalent pH.

A

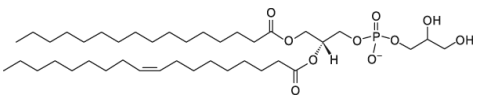

POPG lipid
1-palmitoyl-2-oleoyl-*sn*-glycero-3-phospho-(1'-*rac*-glycerol)

B

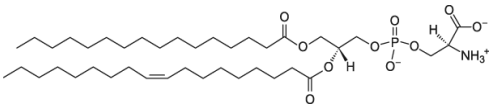

POPS lipid
1-palmitoyl-2-oleoyl-sn-glycero-3-phospho-L-serine

C

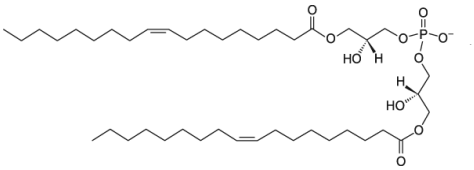

BMP lipid
Bis(monooleoylglycero)phosphate
(8:1 S,R Isomer)

Figure 3-20 Structure of anionic lipid components varied in complex LUVs.

Anionic Lipid	POPC	POPE	Sphingomyelin	Cholesterol
0	41	23	8	28
12	36	20	7	25
50	21	11	4	14

Table 3.4 Total mol % lipid composition of complex lipid LUVs. Anionic lipid component was POPG, POPS or BMP. LUVs containing 0 (control), 12 or 50 mol % anionic lipid component with the remaining lipid zwitterionic components in a mol/mol ratio of 36 POPC: 20 POPE: 7 SM: 25 cholesterol

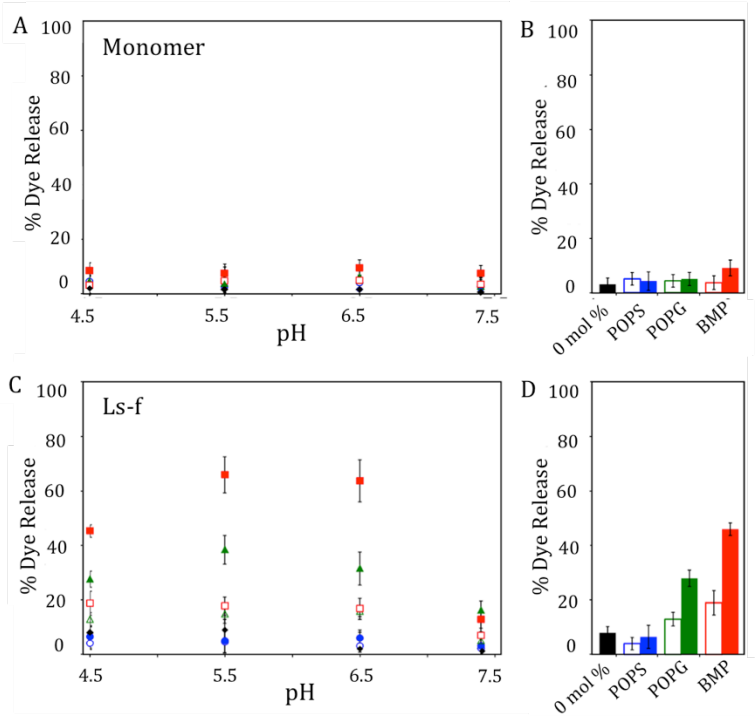

Figure 3-21 Ls-f β_2m fibrils disrupt LUVs in a lipid-specific and pH-dependent manner. For A-D, 0 % (control, black), 12% (open symbols, dashed line) or 50% (solid symbol, solid line) POPS (blue), POPG (green) or BMP (red). Relative dye release induced by native β_2m monomer (A) or Ls-f fibrils (C) from 400 nm extruded LUVs at a range of pH. The corresponding bar graphs (B,D) display the dye release at pH 4.5 in the control (black), 12% (open bar) and 50% (solid bar) of POPG, POPS or BMP containing LUVs. Error on all values is SE from n=3, each of three replicates. Experiments performed and analysed by Dr Sophie Goodchild (Goodchild *et al.*, 2014).

3.2.5.1 Characterisation of complex LUVs

Differing vesicle lipid composition may alter vesicle morphology and size, which in turn may influence behaviour in the liposome dye release assay. For example, the presence of BMP can alter liposome morphology at different pHs (Frederick *et al.*, 2009) and enable small (<100 nm) vesicles to form spontaneously (Chebukati *et al.*, 2010). As different liposome morphologies may rationalise variations in dye release from different lipid

mixes, both DLS and cryo-EM were used to assess liposome morphology (Figure 3-22). DLS revealed an average R_h of ~200 nm for 400 nm extruded LUV. The presence or absence of cholesterol (0 % vs 25 mol %) did not significantly alter R_h. The presence of BMP slightly altered the R_h from ~160 nm for 0 mol % BMP to ~120 nm 50 mol % BMP (Table 3-5). If vesicle size were a key factor in the increase % dye release seen in 50 % BMP liposomes, it would be hypothesised that significantly smaller liposomes would show an increase in % dye release. Dye release data from smaller vesicles (extruded to 100 nm, R_h ~60 nm) show a lower % dye release, and so the size of membrane appears not to be responsible for the efficiency of fibril induced liposome disruption in this case (Goodchild *et al*., 2014) .

Cryo-EM of lipid vesicles revealed no gross morphological differences between the different lipid compositions, at both pH 7.4 and 4.5. In all 400 nm extruded liposome preparations imaged, the primary species were unilamellar, spherical liposomes, with some multilamellar species present. In order to quantitate these observations, 200 liposomes for each condition were counted to obtain a distribution of radii. Radii distributions suggest that 50 mol % BMP liposomes are (on average) slightly smaller than 0 mol % BMP liposomes (85.5 nm vs 72.5 nm radii, average of both pH conditions), in line with DLS data (Figure 3.22).

Interestingly, for the 400 nm extruded vesicles, the R_h reported by DLS ~ double that reported by cryo-EM (Table 3.5). This is consistent with previous studies which found DLS measured sizes to be 30->100 % larger than those obtained by cryo-EM for the same lipid preparation (Crawford *et al*., 2011). In cryo-EM, the sample must become embedded into the vitreous ice layer in order to be imaged. Larger membranes may have a slightly decreased tendency to enter the thin film formed during the blotting process. Supporting this hypothesis, for 100 nm extruded vesicles, the DLS and cryo-EM measurements were in closer agreement compared with 400 nm extruded vesicles, with DLS reported radii 1.2 x greater than cryo-EM measurements. This indicates that, particularly for objects on the 100s of nm scale, cryo-EM may systematically under represent larger species in any given sample.

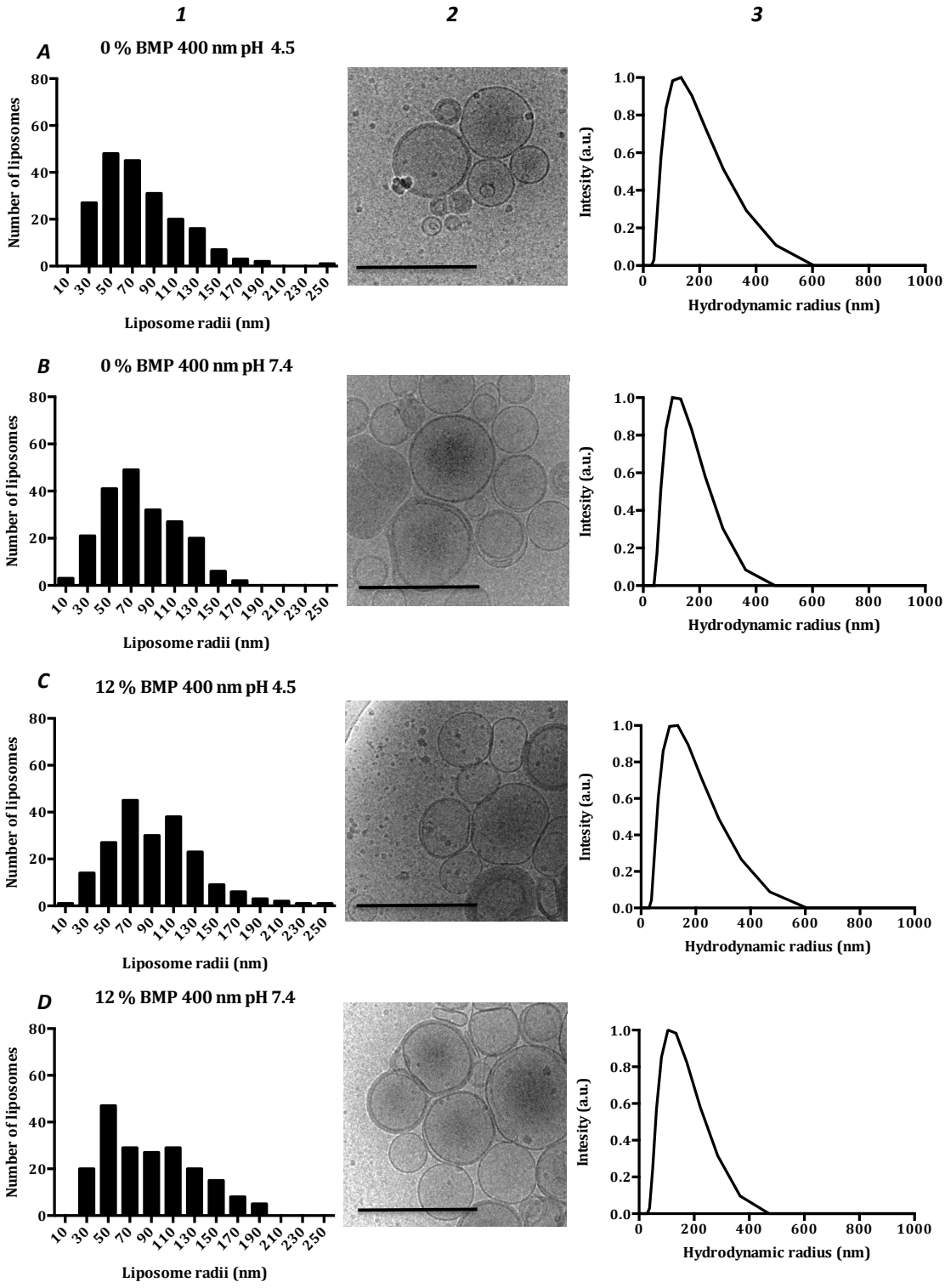
1
2
3
A
0 % BMP 400 nm pH 4.5
Number of liposomes
Liposome radii (nm)
Intesity (a.u.)
Hydrodynamic radius (nm)
B
0 % BMP 400 nm pH 7.4
C
12 % BMP 400 nm pH 4.5
D
12 % BMP 400 nm pH 7.4

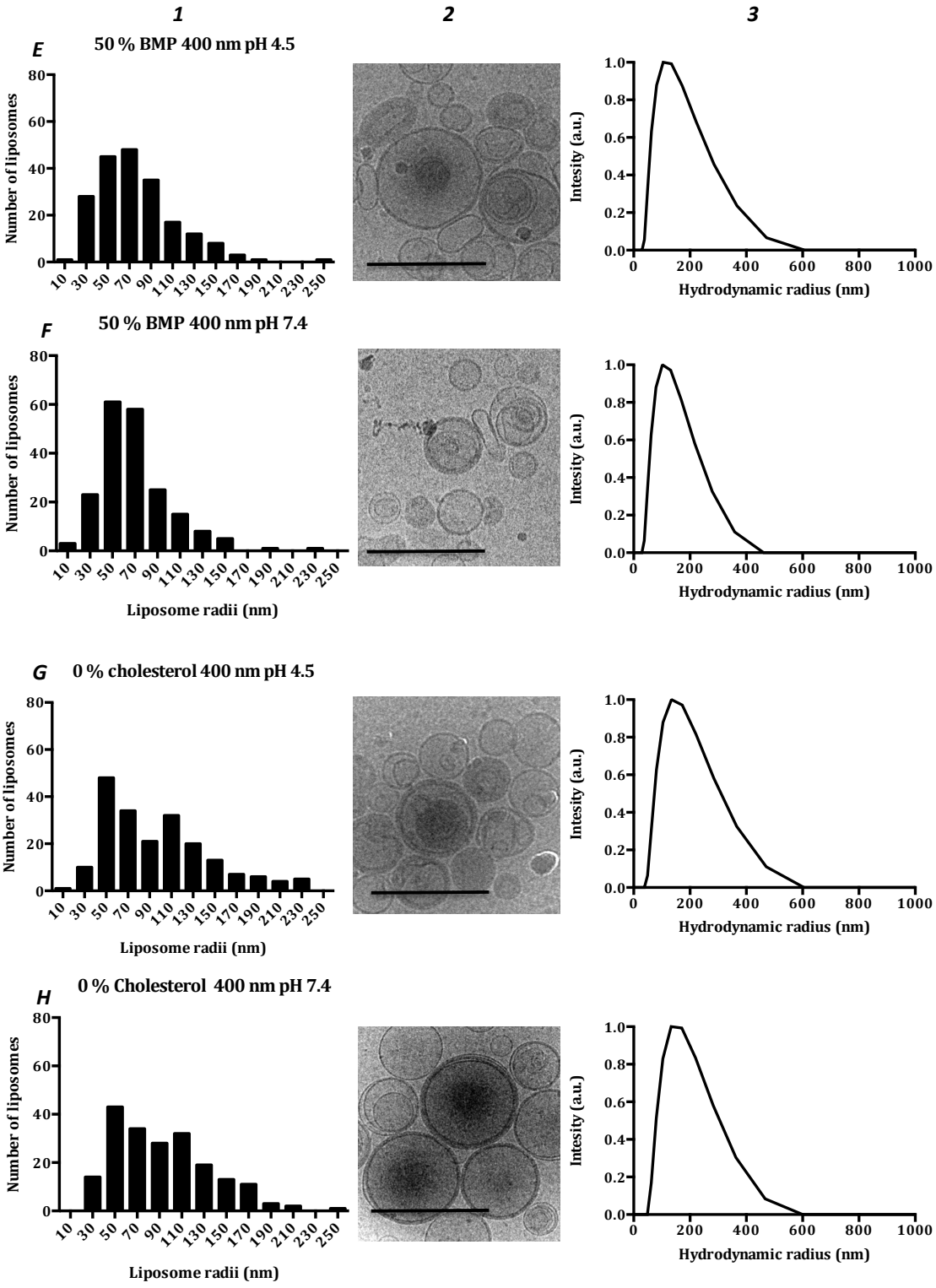
1
2
3
E
50 % BMP 400 nm pH 4.5
Number of liposomes
Intesity (a.u.)
Hydrodynamic radius (nm)
F
50 % BMP 400 nm pH 7.4
Liposome radii (nm)
G
0 % cholesterol 400 nm pH 4.5
H
0 % Cholesterol 400 nm pH 7.4

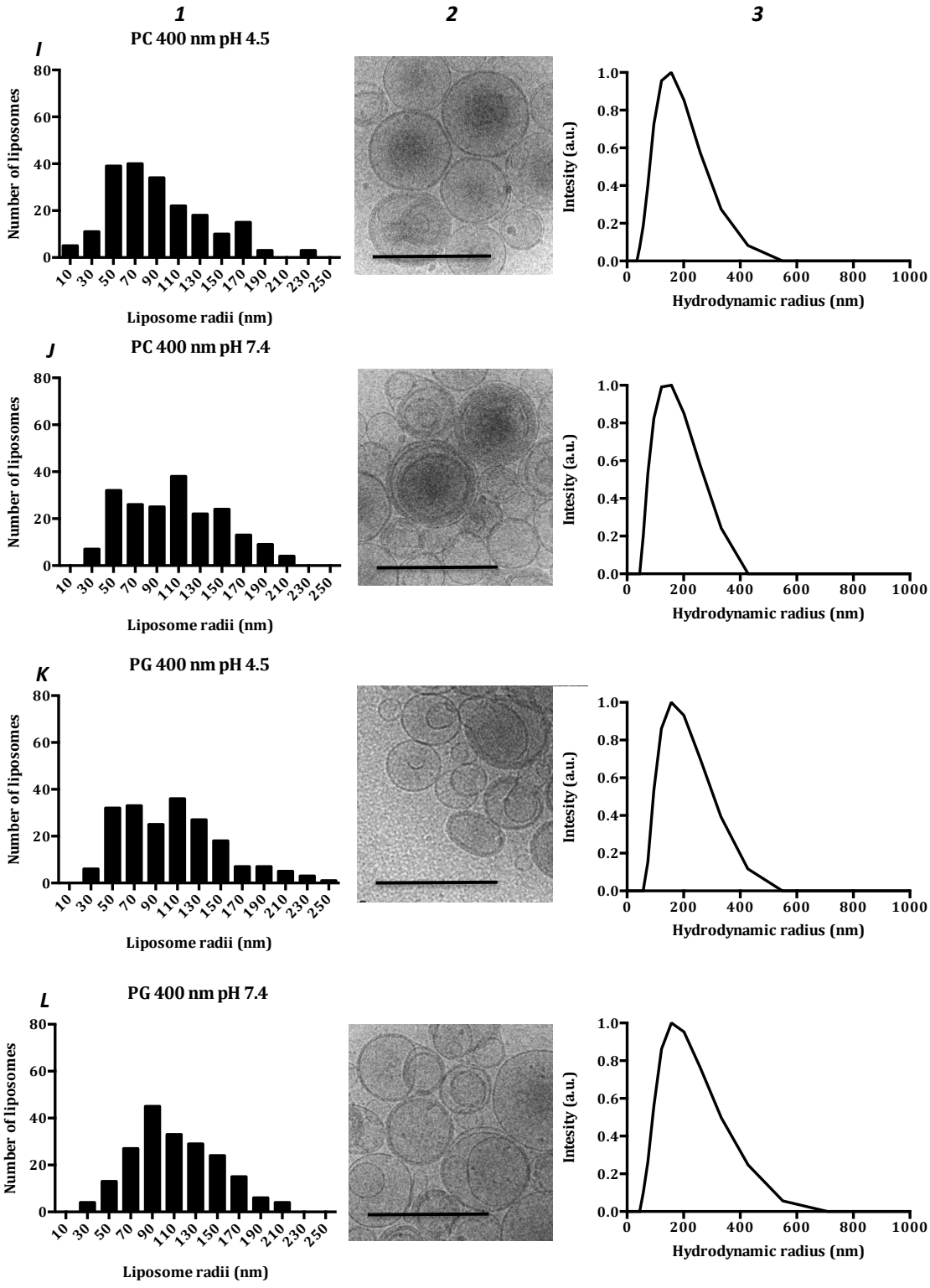
1
2
3
I
PC 400 nm pH 4.5
Number of liposomes
Liposome radii (nm)
Intesity (a.u.)
Hydrodynamic radius (nm)
J
PC 400 nm pH 7.4
K
PG 400 nm pH 4.5
L
PG 400 nm pH 7.4

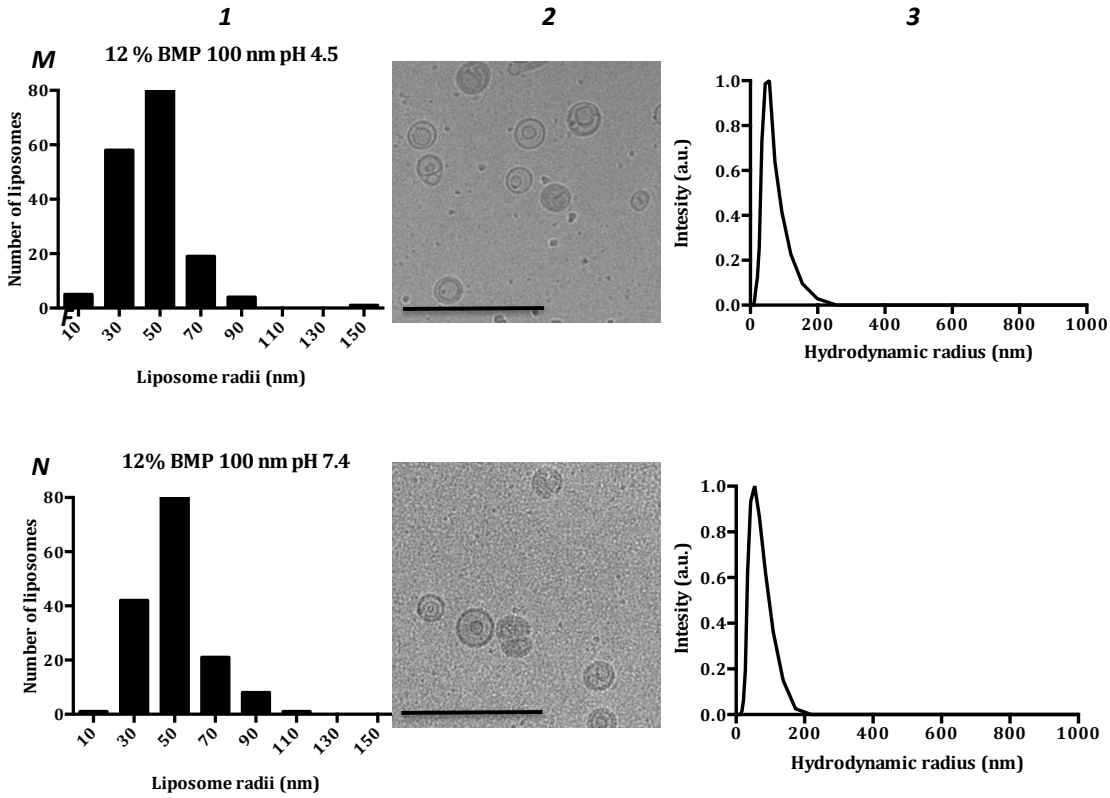

Figure 3-22 Analysis of liposome size and morphology by cryo-EM and DLS. Column one shows histogram of liposome radii as determined by measurement of liposomes imaged by cryo-EM. Column two shows representative micrograph, scale bar 500 nm. Column three shows R_h as determined by DLS, performed and analysed by Sophia Goodchild, University of Leeds. Liposome composition stated in Table 3-4. Results are summarised in Table 3-5.

Lipid Mixture (Mol %)	R_h (nm)	Median radii (nm)	Mean radii (nm)	SD (nm)	Fold change
POPC 400 nm pH 4.5	188±8	83.7	90.8	45	2.1
POPC 400 nm pH 7.4	178±7	104.8	106.4	43.2	1.7
POPG 400 nm pH 4.5	221±8	101.65	105.3	47.2	2.1
POPG 400 nm pH 7.4	229±5	107	111.1	38.5	2.1
0 % BMP 400 nm pH 4.5	186±6	73.2	78.6	37.2	2.4
0 % BMP 400 nm pH 7.4	163±8	71.6	78.4	33.6	2.1
12 % BMP 400 nm pH 4.5	168±8	89	92.3	40.4	1.8
12 % BMP 400 nm pH 7.4	160±5	81	88.7	41.9	1.8
50 % BMP 400 nm pH 4.5	131±5	68.4	75.6	36.6	1.7
50 % BMP 400 nm pH 7.4	120±5	62.8	69.9	31.1	1.7
0 % cholesterol 400 nm pH 4.5	158±6	87.2	96.7	48.3	1.6
0 % cholesterol 400 nm pH 7.4	150±9	85.6	92.7	42.7	1.6
12 % BMP 100 nm pH 4.5	56±8	44.4	45.4	15.2	1.2
12 % BMP 100 nm pH 7.4	58±5	47.3	49	14	1.2

Table 3.5 Radii of liposomes with different lipid compositions measured by DLS and cryo-EM. Hydrodynamic radii (R_h) from DLS measurements, and average radii and standard deviation by cryo-EM in grey shaded columns (n=200 liposomes for cryo-EM measurements). Fold increase in size between DLS and cryo-EM R_h and mean radii are expressed in the final column.

3.2.6 β_2m fibrils do not disrupt LUVs formed from crude lipid extract

The results presented above suggest that lipid composition and pH conditions affect the propensity of β_2m fibrils to perturb LUVs. Cellular membranes differ from LUVs formed from synthetic lipids in several key ways, including diversity of lipid composition, differential lipid composition across the two leaflets of the bilayer, and presence of integral membrane proteins. Here, the ability of amyloid fibrils to disrupt LUVs formed from heterogeneous and biologically representative lipid compositions was investigated using lipid extracts from two eukaryotic cell sources.

LUVs were extruded from L-α-Lecithin, a crude organic extract of egg yolk consisting of ~< 60% phosphatidylcholine, with the remainder consisting of phosphatidylethanolamine and other phospholipids, as well as traces of triglycerides and cholesterol. In the liposome dye release assay, at both pH 6.5 and 7.5, no detectable levels (> 5 %) of dye release were observed upon incubation with β_2m monomer, Ls or Ls-f fibrils (Figure 3-23).

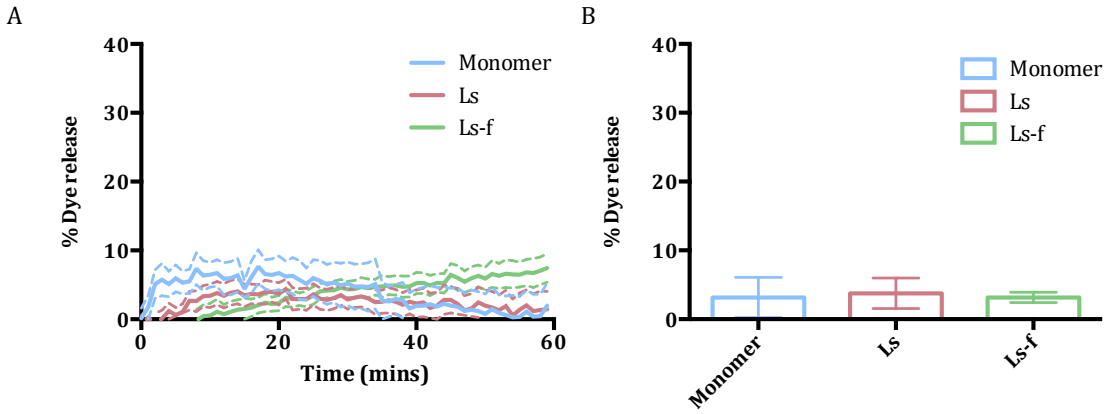

Figure 3-23 Monomeric, Ls and Ls-f β_2m fibrils do not disrupt L-α-Lecithin LUVs at pH 7.5 and 6.5. A) LUVs were incubated with 6 μM protein (monomer equivalent) and 5 μM lipid molecule for 60 mins, 37 °C at pH 7.5 and fluorescence intensity read every minute. Fluorescence was normalised to Triton X-100 treated samples (100 % dye release) and appropriate buffer treated samples (0% dye release). Error bars shown as dotted lines, and represent standard deviation of three repeats each containing three replicates. B) LUVs were incubated with 6 μM protein (monomer equivalent) and 5 μM lipid molecule for 60 mins, 37 °C, after which pH was increased to pH 7.5 and fluorescence intensity read. End point fluorescence was normalised to Triton X-100 treated samples (100 % dye release) and appropriate buffer (0 % dye release). Error bars represent standard error of three replicates, each containing three repeats.

To investigate this further, lipids were extracted from RAW 264.7 cells using organic extraction, where lipid components are separated to an upper organic phase. Proteins are denatured during the process, and protein debris separated to the lower, aqueous phase. This method is known to extract lipids cholesterol ester, free cholesterol, sphingomyelin, phosphatidylcholine, triacylglycerol, ceramide, diacylglycerol, and lyso-phospholipids with high efficiency, with the extraction of different lipids depending on their solubility (Ferraz *et al.*, 2004). The lipid composition of a cell is complex, with cells capable of synthesising thousands of different lipid types (Van Meer *et al.*, 2008). Crude lipid extraction from RAW 264.7 cells therefore contains a more heterogeneous mix of lipids compared with synthetic lipid mixes. In the liposome dye release assay with LUVs formed from crude lipid extract incubated at pH 6.5 and 7.5 show no detectable levels (> 10 %) of dye release were observed upon incubation with β_2m monomer, Ls or Ls-f fibrils (Figure 3-24).

Lipid bilayers can exist in both the liquid or gel (solid) phase, depending on the lipid composition of the membrane and temperature. Additionally, phase separation can occur,

where within the same bilayer, areas in both gel and liquid phases can exist. The transition temperature is influenced by the presence of cholesterol, the fatty acid composition and saturation of the membrane lipids (Mansilla *et al*., 2004). In order to perform extrusion, lipids must be in the liquid phase. At 37 °C, it is known cell membranes exist in both the gel (lipid rafts) and liquid phase. Therefore, extrusion of RAW 267.4 cell lipid extract at room temperature may result in poor efficiency of extrusion, depending on the proportion of lipid in the gel phase. As the transition temperature of this lipid mixture is unknown, extrusion of RAW 264.7 lipid extract, and subsequent dye release experiments, were performed at 50 °C. In the liposome dye release assay, LUVs extruded at 50 °C and incubated at 50 °C, pH 6.5 and 7.5 with protein treatment revealed no detectable levels (> 5 %) of dye release upon incubation with β_2m monomer, Ls or Ls-f fibrils (Figure 3-25).

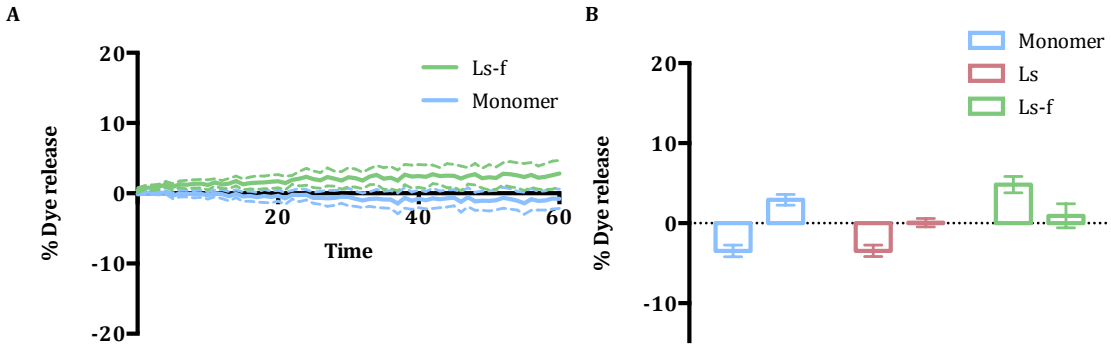

Figure 3-24 Monomeric, Ls and Ls-f β_2m fibrils no not disrupt crude biological lipid from RAW 264.7 cell LUVs at pH 7.5 and 6.5. A) LUVs were incubated with 6 μM protein (monomer equivalent) and 5 μM lipid molecule for 60 mins, 37 °C at pH 7.5 and fluorescence intensity read every minute. Fluorescence was normalised to Triton X-100 treated samples (100 % dye release) and appropriate buffer (0% dye release). Error bars show as dotted line, and represent standard deviation of 3 replicates. B) LUVs were incubated with 6 μM protein (monomer equivalent) and 5 μM lipid molecule for 60 mins, 37 °C, after which pH was increased to pH 7.5 and fluorescence intensity read. End point fluorescence was normalised to Triton X-100 (100 %) and appropriate buffer (0%). Two sets of bars represent fully independent lipid preparations. Error bars represent standard error of three replicates, each containing three repeats.

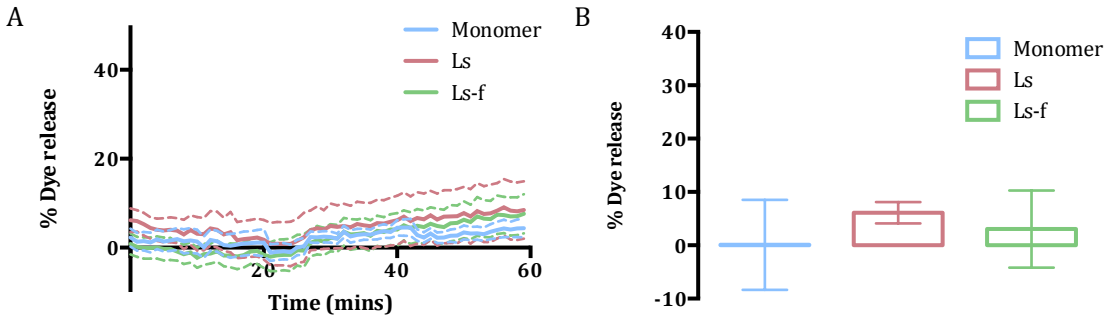

Figure 3-25 Monomeric, Ls and Ls-f β_2m fibrils no not disrupt crude biological lipid from RAW 264.7 cell LUVs extruded at 50 °C at pH 7.5 and 6.5. A) LUVs were incubated with 6 μM protein (monomer equivalent) and 5 μM lipid molecule for 60 mins, 37 °C at pH 7.5 and fluorescence intensity read every minute. Fluorescence was normalised to Triton X-100 treated samples (100 % dye release) and appropriate buffer (0% dye release). Error bars show as dotted line, and represent S.E of 9 replicates. B) LUVs were incubated with 6 μM protein (monomer equivalent) and 5 μM lipid molecule for 60 mins, 37 °C, after which pH was increased to pH 7.5 and fluorescence intensity read. End point fluorescence was normalised to Triton X-100 treated samples (100 % dye release) and appropriate buffer (0% dye release). Error bars represent standard error of three replicates, each containing three repeats.

To confirm that a control protein can disrupt the LUVs formed from L-α-Lecithin and lipid extract from RAW 264.7 cells, melittin was used as a positive. Melittin is a strongly basic peptide found in *Apis mellifica* venom (Wessman *et al.*, 2008). Its monomeric form is 2.8 kDa, although it may form higher order aggregates. At the same protein monomer concentration used to examine the effect of β_2m fibrils and monomer on LUV permeability (6 μM), within 10 minutes, at pH 6.5 and 7.5, melittin caused high levels (> 70 %) of dye release from LUVs (Figure 3-26).

To confirm the morphology of LUVs formed from a RAW 264.7 lipid extract and L-α-Lecithin, DLS was performed (Figure 3-27). DLS demonstrated that R_h of two completely independent preparations of biological lipid LUVs were not significantly different, at 151 ± 35 nm and 209 ± 89 nm. Three independent lipid preparations from RAW 264.7 cells were performed. It is likely that the overall lipid composition of each of these preparations is variable, as cellular lipid composition is known to vary depending on cell cycle and confluency (Atilla-Gokcumen *et al.*, 2014). Despite this likely variation in lipid composition, LUVs from different preparations exhibited the same behaviour in the liposome dye release assay, and had similar R_h distributions.

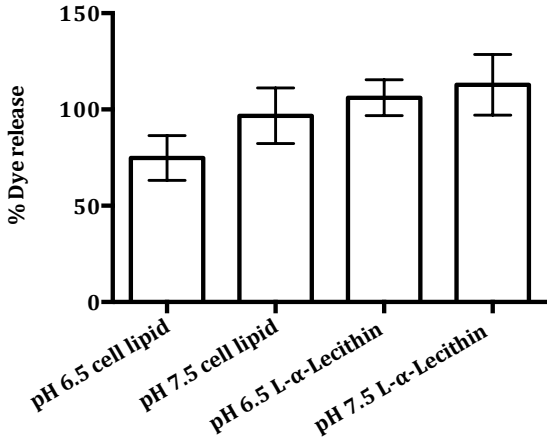

Figure 3-26 LUVs formed from L-α-Lecithin and lipid extract from RAW 264.7 cells are fully disrupted by mellittin at pH 6.5 and 7.5. LUVs at pH 7.5 or 6.5 were incubated with 6 μM protein (monomer equivalent) and 5 μM lipid molecule for 10 mins, 37 °C. For LUV preparations at pH 6.5, pH was increased to pH 7.5 to read fluorescent intensity. Fluorescence was normalised to Triton X-100 (100 %) and appropriate buffer (0%). Error bars represent S.E of nine replicates.

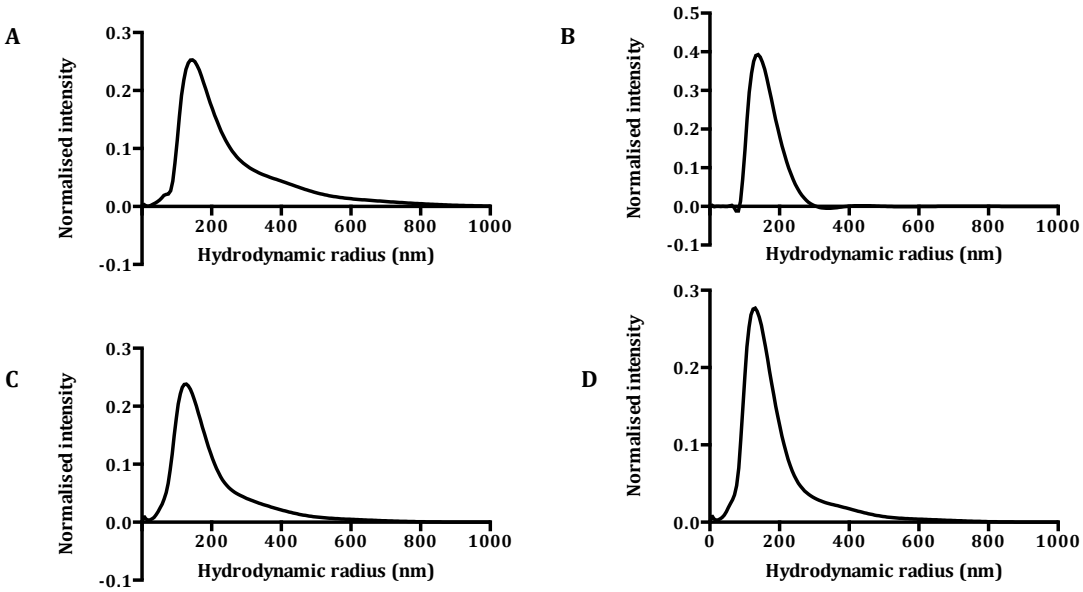

Figure 3-27 DLS of LUVs formed from crude lipid extract, extruded to 400 nm. A) Lipid extract from RAW 264.7 cells extruded at 20 °C. R_h 151 ± 35 nm. B) Lipid extract from RAW 264.7 cells extruded at 20 °C. R_h 209 ± 89 nm. C) L-α-Lecithin extruded at 20 °C. R_h 248 ± 126 nm. D) Lipid extract from RAW 264.7 cells extruded at 50 °C. R_h 272 ± 97 nm. Average of three mean readings ± 1 SD. Performed and analysed by Dr Sophia Goodchild.

3.2.7 β_2m fibrils interact with LUVs formed from crude lipid extract

To qualitatively assess whether interactions occur between LUVs formed from a crude lipid extract from RAW 264.7 cells and Ls-f fibrils, cryo-EM was performed (Figure 3-28). The LUVs displayed a similar morphology to LUVs visualised in Section 3.2.5.1, mostly unilamellar species were present, with some multilamellar species. The β_2m Ls-f fibrils adopt the expected morphology in terms of their width and length, with a clear twist. Fibrils commonly formed bundles or plaques together, with single fibrils rarely observed.

Fibril bundles were most commonly observed interacting with LUVs. As fibrils form bundles, it can be difficult to identify single fibril interactions with LUVs. However, side-on interactions appear to be the most common event. No gross perturbations of membranes by end on interactions with fibrils, as observed in work by Milanesi *et al*, were observed here (Milanesi *et al*., 2012). This work demonstrates that β_2m Ls-f fibrils interact with LUVs formed from RAW 264.7 crude lipid extract, despite no membrane disruption as measured by carboxyfluorescein dye release assay.

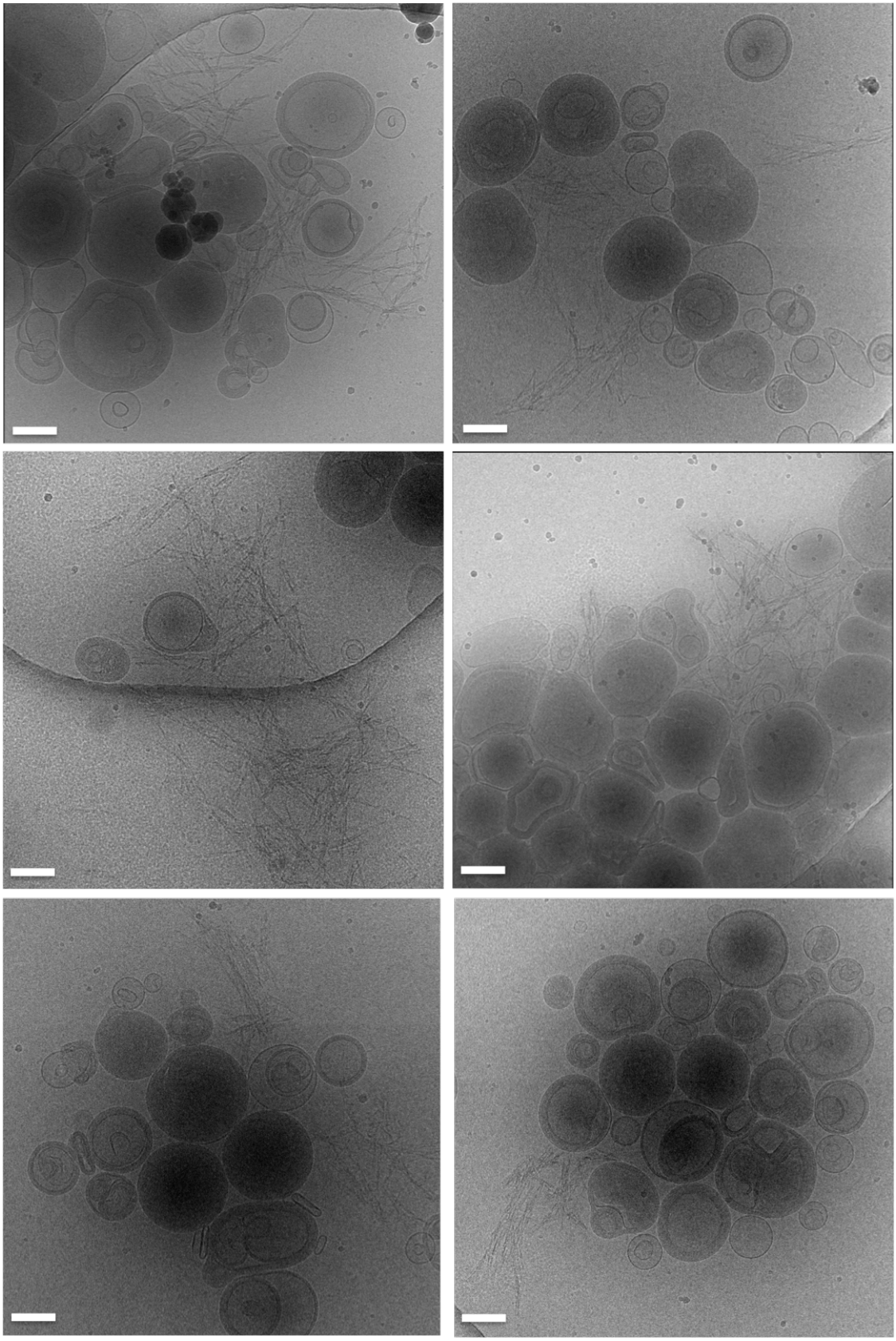

Figure 3-28 Cryo-EM of LUVs formed from lipid extract from RAW 264.7 cells interactions with β_2m Ls-f fibrils. LUVs are same population as used in liposome dye release assay, and so are loaded with carboxyfluorescein. LUVs were mixed with β_2m Ls-f fibrils at the same ratio as present in the liposome dye release assay and vitrified within 10 minutes. Scale bar 200 nm.

3.3 Discussion

Amyloid species are dynamic and heterogeneous, both *in vitro* and *in vivo.* Here, β_2m amyloid species were produced and characterised. Fragmentation of β_2m Ls fibrils produces fibrils with a lower average length distribution (Ls-f), but fragmentation does not alter immunological, dye-binding, or morphological properties as assessed by negative stain EM. However, this length reduction alters the fibrils' ability to inhibit MTT reduction and their behavior in the liposome dye release assay (Sections 3.2.3, 3.2.4, 3.2.5).

By using LUVs formed from different lipid compositions, it was demonstrated that the ability of β_2m fibrils to perturb membranes is dependent both on lipid composition and pH. LUVs formed from DMPS were perturbed by β_2m fibrils at pH 7.5 but not 6.5, whereas LUVs formed from POPG:Chol were perturbed at pH 6.5 but not 7.5. This suggests that it may be dangerous to draw conclusions from liposome dye release assays performed on a single LUV type under one set of environmental parameters.

β_2m Ls-f fibrils can disrupt synthetic lipid LUVs under conditions that mimic the cell's pH and lipid composition. By comparing the extent of dye release for LUVs enriched in different anionic lipids (BMP, POPG and POPS), it is clear that the identity of anionic lipid plays a significant role in the amount of dye release. Strikingly, β_2m Ls-f fibrils have the greatest propensity to disrupt LUVs highly enriched in BMP under acidic pH conditions. These are conditions that mimic in the late endosome and lysosome of the cell, suggesting perhaps that such membranes are more susceptible to membrane damage by β_2m amyloid fibrils.

However, liposome dye release assays performed using LUVs formed from crude biological lipid (L-α-Lecithin and RAW 264.7 lipid extract) showed that these LUVs are not perturbed by either monomeric or fibrillar amyloid β_2m. Interestingly, this discrepancy has been reported previously for amyloid species formed from different precursor proteins, but not discussed. For example, fibrillar α-synuclein has been reported to perturb LUVs formed from a variety of synthetic LUVs with one or two lipid components, but perturbation of LUVs formed from brain extract was negligible, despite interaction being demonstrated (Pieri *et al*., 2012). Liposome dye release assays are often used to demonstrate the propensity of a protein to disrupt synthetic membranes, and from this propensity, extrapolations are made about the behaviour of the protein in a cellular context. The results presented here show that extreme caution should be applied, both in choosing the lipid system to examine, and in interpreting these results in a cellular context.

Liposome dye release assays performed on LUVs formed from a crude biological lipid extract showed that no significant membrane disruption occurred (Section 3.2.6), indicating amyloid species' ability to perturb membranes is dependent on lipid composition of the membrane, and pH. β_2m fibrils may interact with biological membranes in a different manner compared with synthetic lipid LUVs. Based on this precedent, the intracellular trafficking and subsequent membrane interactions of fragmented β_2m fibrils was selected for further investigation.

It is clear from this work that variables such lipid composition and solution conditions (pH) play a significant role in the ability of amyloid fibrils to perturb LUV membranes. Here, other variables that likely also play a role in the propensity of amyloid species to perturb membranes were not explored. One interesting avenue to investigate would be the role of lipid phase. *In vivo,* lipid rafts, which are phase-separated regions of a membrane (Sengupta *et al*., 2007), may be differentially protected or susceptible to perturbation by amyloid species. Additionally, amyloid aggregates themselves may perturb phase separation in membranes, which may trigger cell death (Walsh *et al*., 2014; Sasahara *et al*., 2013). Amyloid forming proteins have been shown to modulate local lipid compositions and membrane curvature, for example IAPP has been shown to induce a charge-dependent induction of membrane curvature, leading to membrane disruption and leakage (Kegulian *et al*., 2015), and induction of membrane curvature and tubulation is well documented for α-synuclein (Varkey *et al*., 2010). In the next Chapter, interactions between β_2m amyloid fibrils and cellular membranes are explored in more detail.

4 Probing the interactions of β_2m fibrils with cellular membranes

4.1 Introduction

4.1.1 Amyloid mediated cytotoxicity

Despite many years of research showing the association between the appearance of amyloid deposits and the onset of disease *in vivo,* the specific mechanisms of amyloid pathogenicity remain unclear (Knowles *et al*., 2014). There are no consistent trends between quantity of amyloid, pathogenicity and disease progression. In systemic amyloidoses sometimes kilograms of amyloid deposits can form, with this being the probable cause of pathogenicity, whereas in some neurodegenerative disorders there is no consistent link between disease progression and the deposition of extracellular amyloid aggregates (Chiti & Dobson, 2006; Lue *et al*., 1999; Karran *et al*., 2011; Cohen *et al*., 2013; Haass & Selkoe, 2007).

4.1.2 Mechanisms of amyloid cytotoxicity

Despite years of research, precise mechanisms for amyloid-mediated cytotoxicity by both fibrils and oligomers remain unclear. However, evidence is converging on several key themes, many of which involve biological membranes.

4.1.2.1 Direct membrane disruption

Disruption of cellular membranes has been suggested as a mechanism for amyloid cytotoxicity (Stefani, 2010; Berthelot *et al*., 2013). Both monomers and higher order aggregates directly interact with membranes (Necula *et al*., 2003; Knight & Miranker, 2004; Choo-Smith *et al*., 1997; Engel *et al*., 2008). Furthermore, aggregates have been shown (in some circumstances) to permeabilise membranes, a potential mechanism of direct amyloid cytotoxicity (Stefani, 2010). There are several models for this, including carpeting effects, detergent effects, pore formation and raft-like insertion (Figure 4-1) (Lashuel & Lansbury, 2006; Luzio *et al*., 2007). In the carpeting model, aggregates carpet one leaflet of the membrane, causing asymmetric pressure and the resulting leakage of small molecules (Hebda & Miranker, 2009). The raft-like insertion model suggests amyloid forms a 'protein raft' inside the membrane (Berthelot *et al*., 2013), as has been shown for HET-s in yeast (Ta *et al*., 2012), while studies on monomeric Aβ show it inserts into membranes and then self-assembles into oligomers which may destabilise the bilayer (Zhang *et al*., 2012). Amyloid species may also have detergent-like effects. An initial electrostatic interaction allows the aggregate to bind the charged phospholipid head group, placing the hydrophobic residues of the aggregate near the membrane's hydrophobic core, causing membrane disruption (Shai, 1999). IAPP aggregates extract lipids from cellular membranes by this mechanism (Engel *et al*., 2008; Sparr *et al*., 2004).

β_2m fibrils have also been visualised using cryo-EM, interacting with synthetic liposomes, primarily by their ends, distorting the liposome and possibly extracting lipids (Figure 4-2)(Milanesi *et al*., 2012). A final mechanism by which amyloid species may disrupt liposomes is the formation of annular oligomers that may form a pore or channel across a membrane; this has been visualised in synthetic liposomes (Lashuel & Lansbury, 2006). Oligomers of this kind are known to form from many disease associated amyloidogenic proteins including huntingtin, Aβ and α-synuclein (Ding *et al*., 2002; Lashuel *et al*., 2002; Wacker *et al*., 2004).

Interestingly, the presence of lipids can directly modulate fibril formation; IAPP, Aβ peptide and α-synuclein fibril growth is accelerated in the presence of lipid (Necula *et al*., 2003; Knight & Miranker, 2004; Choo-Smith *et al*., 1997; Galvagnion *et al*., 2015). Nucleation and fibril formation of IAPP damages membranes, causing them to become permeable to small molecules, with membrane damage directly correlated with fibril growth (Engel *et al*., 2008). Lipid-induced fibrillogenesis may be an additional mechanism by which fibrils damage membranes.

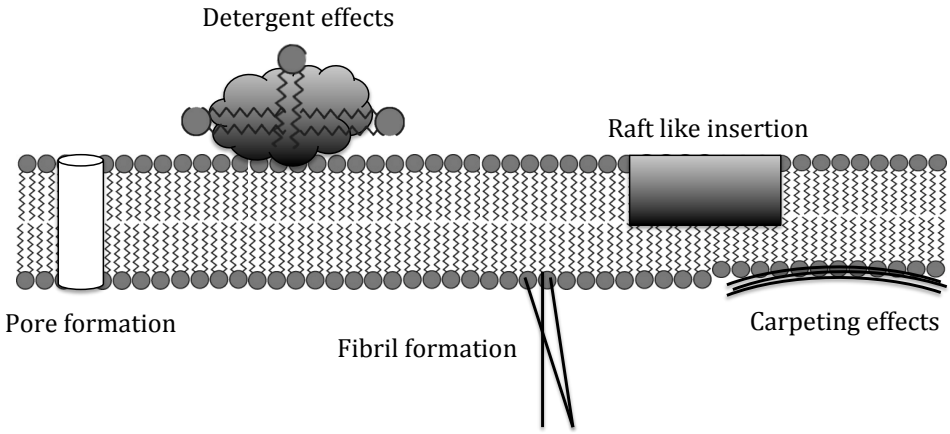

Figure 4-1 Proposed models of amyloid mediated membrane disruption.

Perturbation of normal cellular function may be caused by any combination of the mechanisms described above. The ability of amyloid to permeabilise membranes depends on the physical properties of the membrane, including lipid composition, membrane curvature, fluidity and charge density, as well as the solution conditions such as pH. This may rationalise the differential effects amyloid fibrils can have on different cellular compartments. Cell membrane disruption may trigger cell death through a variety of mechanisms. For example, lysosomal membrane permeabilisation (LMP) and the subsequent leakage of the lysosome's contents into the cytosol leads to 'lysosomal cell death', primarily by the action of lysosomal cathepsin proteases initiating necrotic or apoptotic cell death (Ono *et al*., 2003; Aits & Jäättelä, 2013). Another possible mechanism of LMP-mediated cell death is the release of Ca^{2+}, which regulates a wide range of cellular

functions and reactions (Petersen *et al.*, 2005). Disruptions to cytosolic Ca^{2+} can lead to apoptosis via caspase activation and cytochrome-c release (Glabe, 2006). Modulating the interactions of amyloid with membranes may present a novel therapeutic strategy in tackling amyloid disease. For example, Europium ions (Eu^{3+}) inhibit $A\beta_{1\text{-}42}$ membrane interactions, which may lead to membrane protection (Williams *et al.*, 2015).

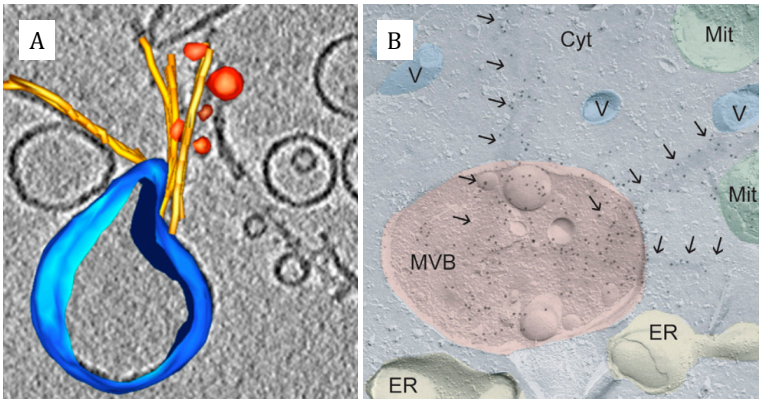

Figure 4-2 Direct perturbation of membranes by amyloid fibrils. A) Segmented cryo-electron tomogram liposome (blue) distorted by β_2m fibrils (yellow). Fibrils are associated with small vesicles (red). Adapted from Milanesi *et al.*, 2012. B) TEM images of freeze fractured J774A cells with immunogold staining of Aβ protein, which indicates fibrils penetrating membrane of multivesicular body (MVB). Adapted from Friedrich *et al.*, 2010.

4.1.2.2 Hydrophobic surfaces

Amyloid aggregates, particularly soluble oligomers, expose hydrophobic surface that is buried in globular proteins, or dispersed in disordered proteins (Chiti & Dobson, 2006; Jahn & Radford, 2008). Such a hydrophobic surface may mediate aberrant interactions between aggregates and cellular components, which may subsequently cause cytotoxicity (Campioni *et al.*, 2010; Olzscha *et al.*, 2011; Bolognesi *et al.*, 2010). The hydrophobic properties of amyloid aggregates have been shown biochemically. For example, prefibrillar aggregates of $A\beta_{1\text{–}42}$ E22G (artic variant) bind strongly to 1-anilinonaphthalene-8-sulfonate (ANS), a dye used to measure exposed hydrophobic surfaces. Changes in ANS binding to a range of amyloid fibrils correlate with cytotoxicity (Bolognesi *et al.*, 2010). These findings support the view that exposure of hydrophobic surfaces during aggregation is a common property of amyloid species (Bolognesi *et al.*, 2010). Additionally, different oligomer polymorphs assessed for hydrophobic packing and exposure demonstrated species with higher levels of exposed hydrophobic groups were more toxic than those with more hydrophobic packing into a core (Zampagni *et al.*, 2011; Campioni *et al.*, 2010).

Efforts have been made to identify interaction partners of these exposed hydrophobic patches (Virok *et al.*, 2011; Olzscha *et al.*, 2011). Olzscha *et al.,* used *de novo* designed

amyloid forming peptide expressed in the cytosol of cells, and quantitative proteomics to identify more than 2000 amyloid-aggregate binding partners (Olzscha *et al*., 2011). The binding partners were enriched with proteins containing unstructured regions, and play important roles, including proteostasis, chromatin organisation, transcription and translation, leading the authors to suggest that amyloid aggregates sequester proteins with key functions, leading to multifactorial cell dysfunction (Olzscha *et al*., 2011).

4.1.2.3 Proteostasis

All cells have tightly regulated machineries that coordinate protein homeostasis, or proteostasis (Powers *et al*., 2009). The proteostasis network includes pathways such as the ubiquitin-proteasome system (UPS), and molecular chaperones. The proteostatic capacity of cells under environmental or metabolic stress, decreases with age, as well as in various disease states (Balch *et al*., 2008). Increasingly, links are being made between disruptions of proteostasis and disease, including loss-of function disorders such as cystic fibrosis and gain-of-toxic-function disorders, which are thought to include AD, Parkinson's and Huntington's disease (Powers *et al*., 2009).

The unfolded protein response is a major mechanism by which damaged, misfolded or unassembled proteins are degraded, via ubiquitin tagging and subsequent targeting to the proteasome (Ciechanover *et al*., 2000). Polyubiquitinated proteins are usually efficiently degraded by proteasomes, but in intracellular deposits within diseased neurons ubiquitinylation is elevated, suggesting a link between UPS dysfunction and pathogenesis (Mayer *et al.*, 1988). Genetic analysis has also demonstrated a link between the UPS and several neurodegenerative diseases; for example mutations in UPS components parkin and ubiquitin carboxy-terminal hydrolase L1 are associated with PD (Cummings *et al*., 1999; Bence *et al*., 2001; Shimura *et al*., 2000). In one study, injection of adult rats with proteasome inhibitors caused PD like symptoms, including Lewy body formation (McNaught *et al*., 2004) Other studies have shown a huntingtin fragment containing a pathogenic poly-Q repeat inhibits degredation by the UPS (Bence *et al*., 2001; Park *et al*., 2013). Such evidence suggests a possible positive feedback loop in which aggregates inhibit the UPS, causing more aggregation (Bence *et al*., 2001). Molecules that modulate and regulate proteostasis, or pharmacological chaperones are being developed as potential therapeutics (Powers *et al*., 2009).

4.1.2.4 Organelle dysfunction

There is increasing evidence that amyloid aggregates perturb cellular function by causing organelle dysfunction. They induce endoplasmic reticulum stress, golgi body fragmentation and autophagy dysfunction, amongst other effects (Mercado *et al*., 2013;

Gosavi *et al*., 2002; Schon & Przedborski, 2011; Sarafian *et al*., 2013; Rugarli & Langer, 2012). In many studies, mitochondrial damage and oxidative stress have been implicated (Umeda *et al*., 2011; Schon & Przedborski, 2011; Kaminsky *et al*., 2015).

4.1.2.4.1 Mitochondrial dysfunction

Mitochondria play a vital role in energy production, as well as in calcium buffering and apoptotic signalling (MacAskill & Kittler, 2010), but their complex biosynthesis makes them particularly vulnerable to accumulation of damage over their lifetimes (Rugarli & Langer, 2012). A complex system of surveillance monitors mitochondria for damage and removes dysfunctional mitochondria, and the failure of this system is associated with cell death. Neurons are particularly susceptible to mitochondrial damage as they require high levels of ATP to transport macromolecules and organelles over long distances, perform Ca^{2+} homeostasis, and defend membrane potentials. The brain is an energetically costly organ to maintain, comprising ~2 % of body mass, but consuming 20 % of resting ATP (MacAskill & Kittler, 2010). Therefore, although all cells have similar mitochondrial quality control systems, the demands placed on a typical neuronal cell are greater than for the average non-neuronal cells (Rugarli & Langer, 2012). Many neurons are long (up to 1 m in humans), and so ATP diffusion cannot meet the energy needs of the cell (MacAskill & Kittler, 2010). Mitochondria in neurons are transported away from the cell body where mitochondrial biogenesis primarily occurs, along axons to regions with high energy and Ca^{2+} homeostasis requirements. Because of this spatial arrangement, it is energetically expensive to repair or degrade damaged mitochondria, as either the mitochondrion has to travel back to the cell body, or mitophagy machinery needs to be transported to the site of damaged mitochondria (Wang *et al*., 2006). Mitochondria have a longer half-life in neuronal cells compared with other post-mitotic cells; resulting in accumulation of damage (Rugarli & Langer, 2012). In addition, newly synthesised mitochondrial proteins are imported into the mitochondria at the cell body and therefore the mitochondria at the cell periphery may be less efficient at coping with misfolded protein or Ca^{2+} overload (Kaplan *et al*., 2009; Brown *et al*., 2006). Genetic mutations, or accumulation of amyloid aggregates that affect quality control in mitochondria, preferentially affect neurons compared with other cell types. It is therefore unsurprising that mitochondrial damage is strongly implicated in neurodegenerative diseases such as PD and AD (Alikhani *et al*., 2011; Valente *et al*., 2004; Umeda *et al*., 2011).

In PD, there is a strong correlation between and mutations in *PINK1* and *parkin* and incidence and progression of the disease, which play roles in mitophagy (Valente *et al*., 2004; Vives-Bauza & Przedborski, 2011; Pimenta de Castro *et al*., 2012). Aβ peptides have an adverse effect on mitochondria, whether they are isolated, inside cultured cells, or in

whole organisms, including decreases in mitochondrial enzymes (Complex II, III) and ATPase activity, mitochondrial Ca^{2+} overload and increased hydrogen peroxide production, all of which could contribute to amyloid mediated cytotoxicity (Kaminsky *et al*., 2015).

4.1.2.4.2 Lysosomal dysfunction

Lysosomes are a membrane-bound, acidified organelle, containing ~ 50 different hydrolases (Settembre *et al*., 2013; Lüllmann-Rauch, 2005). Lysosomes play a role in degradation of cellular components, plasma membrane repair, signalling pathways including apoptosis, energy metabolism, cholesterol homeostasis, antigen presentation and autophagy (Saftig & Klumperman, 2009; Settembre *et al*., 2013). Cell death can be initiated by lysosomal membrane permeabilisation (LMP), where lysosomal hydrolases are released from the lysosome into the cytosol (Boya & Kroemer, 2008)(Section 4.1.2.1). Proteases that are active at cytosolic pH, including cathepsins B,D and L have been implicated in triggering cell death via caspase and mitochondria-dependent pathways, depending on the cellular context (Boya & Kroemer, 2008).

Amyloid aggregates perturb cellular functions via perturbation of the lysosomal membrane and via accumulation of aggregates (Soura *et al*., 2012; Freeman *et al*., 2013; Boland & Campbell, 2004; Dehay *et al*., 2010; Ji *et al*., 2002; Ditaranto *et al*., 2001; Liu *et al*., 2010; De Kimpe *et al*., 2012). Extracellular amyloid can gain access to intracellular compartments via endocytosis, and a range of disease-associated amyloid species have been shown to be internalised, including Aβ, α-synuclein, β_2m and poly-Q (Chafekar *et al*., 2008; Zhao *et al*., 2010; Soura *et al*., 2012; H.J. Lee *et al*., 2005; Freeman *et al*., 2013; M. Porter *et al*., 2011; Morten *et al*., 2007; Ren *et al*., 2009). Increasing evidence points towards lysosomal dysfunction, and other related mechanisms such as autophagy and mitophagy, as an underlying mechanism of pathology in amyloid-associated diseases including AD, Parkinson's and Huntington's disease (Settembre *et al*., 2013). In many cases, amyloid aggregates are trafficked through, and concentrated in the endolysosomal system, making it a focus of research efforts (Soura *et al*., 2012; Dehay *et al*., 2010; Ditaranto *et al*., 2001; De Kimpe *et al*., 2012).

Perturbation of lysosomal membranes may be a key site at which amyloid species exert a cytotoxic effect. $A\beta_{1\text{-}42}$ has been shown to insert into lysosomal membranes, leading to LMP (Liu *et al*., 2010). Other mechanisms of lysosome-related Aβ cytotoxicity include the generation of free radicals which disrupt lysosomal acidification, ultimately resulting in cell death (White *et al*., 2005). LMP and consequent cell death has been observed when $A\beta_{1\text{-}42}$ oligomers are exogenously applied, while mouse models of familial AD containing

the Aβ E693Δ (Osaka) mutation, show lysosomal leakage, ER stress and mitochondrial dysfunction (Soura *et al*., 2012; Umeda *et al*., 2011). These studies suggest a central role for the lysosome in the pathogenesis of AD.

In addition to LMP, amyloid can also inhibit lysosome function. Indeed, the inhibition of lysosomal function in the absence of amyloid aggregates results in very similar effects to amyloid disease (Lee *et al*., 2011). For example, inhibition of lysosomal proteolysis results in the accumulation of lysosomes on axonal swellings, which has been observed in mouse models of AD (Lee *et al*., 2011). Another striking study demonstrated that the compound scyllo-inositol can prevent accumulation and toxicity of Aβ and Huntingtin aggregates by increasing lysosomal and proteasomal degradation (Lai *et al*., 2014; McLaurin *et al*., 2000). Lysosomal dysfunction is also proposed to play a role in non-neurodegenerative amyloid-associated diseases. IAPP disrupts lysosome-dependent degradation, which impairs autophagy in mouse models of diabetes (Rivera *et al*., 2011). β_2m amyloid fibrils accumulate in the lysosome where they inhibit the degradation of substrates, which could in turn disrupt proteostasis by inhibiting the overall degradative capacity of the cell (Jakhria *et al*., 2014).

Increasing evidence has indicated a central role for lysosomal and autophagy dysfunction in neurodegenerative diseases (Settembre *et al*., 2013). One of the first pathological features of many such diseases including AD, Parkinson's and Huntington's, is the accumulation of autophagosomes (Wong & Cuervo, 2010; Dehay *et al*., 2010; Kegel *et al*., 2000; Nixon *et al*., 2005). Autophagy is complex and dynamic, and it is extremely difficult to define the mechanisms of autophagic failure in different diseases. Different pathways of autophagic dysfunction may help to rationalise differential disease progression and pathology (Wong & Cuervo, 2010). An example of complexity in studying autophagy is that the accumulation of autophagosomes. This observation could be rationalised by both the up-regulation of autophagy, meaning more autophagosomes are formed, or by the disruption in their clearance, phenomena that are difficult to disentangle (Boland *et al*., 2008; Wong & Cuervo, 2010; Rubinsztein *et al*., 2009). Cell biological experiments are needed to tease these mechanisms apart. There is evidence for disrupted autophagic clearance via autophagosome accumulation, uncoupled with increased autophagic flux in a number of neurodegenerative diseases, which could be due to either disrupted autophagosome trafficking, decreased fusion with endosomes/lysosomes or decreased proteolysis inside lysosomes (Wong & Cuervo, 2010). A decrease in proteolysis could be due to any combination of altered lysosomal pH, accumulation of undigested substrates or impaired activity/trafficking/expression of lysosomal hydrolases. Identifying different

kinds of autophagy dysfunction may enable the development of targeted therapies for these neurodegenerative diseases (Wong & Cuervo, 2010). For example, autophagosome clearance could be increased by overexpression of transcription factor EB, up-regulating lysosomal biogenesis (Sardiello *et al*., 2009; Wong & Cuervo, 2010). The contribution of lysosomal and autophagic dysfunction in a range of neurodegerative diseases bring to mind some striking parallels between amyloid diseases and lysosomal storage disorders (Wong & Cuervo, 2010; Settembre, Fraldi, Jahreiss, *et al*., 2008).

There are over 40 metabolic disorders characterised as lysosomal storage diseases, which are caused by mutations in lysosomal hydrolases, integral lysosomal membrane proteins, and proteins involved in trafficking and post-translational modification of lysosomal proteins (Schultz *et al*., 2011; Settembre, Fraldi, Rubinsztein, *et al*., 2008). Many patients with lysosomal storage diseases display defects in the central nervous system, which can cause progressive cognitive and motor decline (Schultz *et al*., 2011). There are striking parallels between lysosomal storage disorders and neurodegenerative disease (Settembre, Fraldi, Jahreiss, *et al*., 2008; Ravikumar *et al*., 2002; Settembre *et al*., 2007). Niemann-Pick type C (NPC) disease is an autosomal recessive defect in endosomal cholesterol trafficking and shares many features with AD (Kresojević *et al*., 2014; Chang *et al*., 2005). These include endosomal abnormalities in neurones, (Nixon, 2004), accumulation of APP and Aβ, and neurofibrillary tangles of tau, but in the absence of Aβ deposition (Nixon, 2004; Yamazaki *et al*., 2001; Jin *et al*., 2004; Love *et al*., 1995). Cholesterol is a unifying theme; aberrant cholesterol trafficking is the primary factor in NPC, while high cholesterol is a risk factor in AD and aberrant cholesterol trafficking is associated with cell dysfunction (Malnar *et al*., 2014; Poirier, 2003; Nomura *et al*., 2013).

Parallels have also been shown between the lysosomal storage disorder Gaucher's disease and PD. Gaucher's disease is the most common lysosomal storage disorder, it is an autosomal recessive disease caused by loss-of-function mutations in the gene encoding glucocerebrosidase, *GBA1*, a lysosomal enzyme (Li *et al*., 2015). Gathering clinical, pathological and genetic evidence points to an association between Gaucher's and PD (Li *et al*., 2015; Stern, 2014). Type 1 Gaucher's disease patients clinically present Parkinsonism, with genetic evidence further supporting a strong link (Mao *et al*., 2010; McNeill *et al*., 2012; Sidransky & Lopez, 2012). Mutations in *GBA1* is the most common genetic risk factor for PD known to date (Mazzulli *et al*., 2011; Sidransky *et al*., 2009). The aggregation of α-synuclein has been implicated in the progression of Gaucher's disease, as α-synuclein positive Lewy bodies are found in the brains of Gaucher's disease patients (Wong *et al*., 2004) One interesting observation potentially links these diseases

mechanistically; the accumulation of α-synuclein species depletes lysosomal glucocerebrosidase, leading to a build up of glucocerebroside inside cells, which in turn stabilises α-synuclein aggregates in a positive feedback loop (Mazzulli *et al*., 2011). These parallels, as well as evidence that amyloid species perturb lysosomal membranes, indicate the lysosome is an interesting subject for investigating amyloid-membrane interactions.

4.2 Results

In the previous Chapter, the ability of β_2m amyloid fibrils to perturb synthetic liposomes enriched in the lipid BMP indicted the lysosome may be an important site at which amyloid species exert toxic effects. Liposome dye release experiments in Chapter three suggest that there may be significant differences in the ability of β_2m amyloid fibrils to perturb synthetic liposomes and LUVs formed from crude eukaryotic lipids. In this Chapter, the intracellular trafficking of β_2m amyloid fibrils and interactions with cellular membranes were investigated.

4.2.1 Intracellular trafficking of amyloid

It has been demonstrated that amyloid species formed from a variety of different precursor proteins can be internalised in cells (Section 4.1.2). Here, the intracellular trafficking of Ls-f β_2m amyloid fibrils in the cell line RAW 264.7 cells was assessed.

4.2.1.1 Fluorescent labelling and characterisation of β_2m amyloid fibrils

To generate fluorescently labelled amyloid fibrils for confocal imaging, monomeric β_2m was labelled with Alexa Fluor® 647 (AF647) succinimidyl ester, which reacts with primary amines (Section 2.3.7). Labelled protein exhibited the predicted absorbance profile, with a peak at 280 nm corresponding to tryptophan and tyrosine of the protein and 647 nm, corresponding to AF647 (Figure 4-3A). The absorbance profile of AF647 succinimidyl ester alone, and conjugated to protein, was the same as expected (Figure 4-3 B). ESI mass spectrometry was used to confirm labelling. The major peak corresponds to the predicted mass of unlabelled protein (11858 ± 0.97 Da), the minor to labeled protein (12701 ± 0.44 Da) (Figure 4-3 C). The ratio between the peaks suggests that approximately a third of monomeric protein was labeled with a single AF647 molecule.

To generate labelled amyloid fibrils, AF647 labelled β_2m was introduced into seeded fibril formation reaction as described (Section 2.3.8) in a ratio of 1:9 labelled to unlabelled β_2m monomer. Fibrils with Ls morphology were produced, and fragmented to produce AF647 Ls-f fibrils. In order to confirm fibril morphology was not altered in a gross fashion by incorporation of AF647, negative stain EM was performed. No gross morphological differences were observed between AF647 Ls and Ls-f fibrils compared with non-labelled fibrils (Figure 4-4).

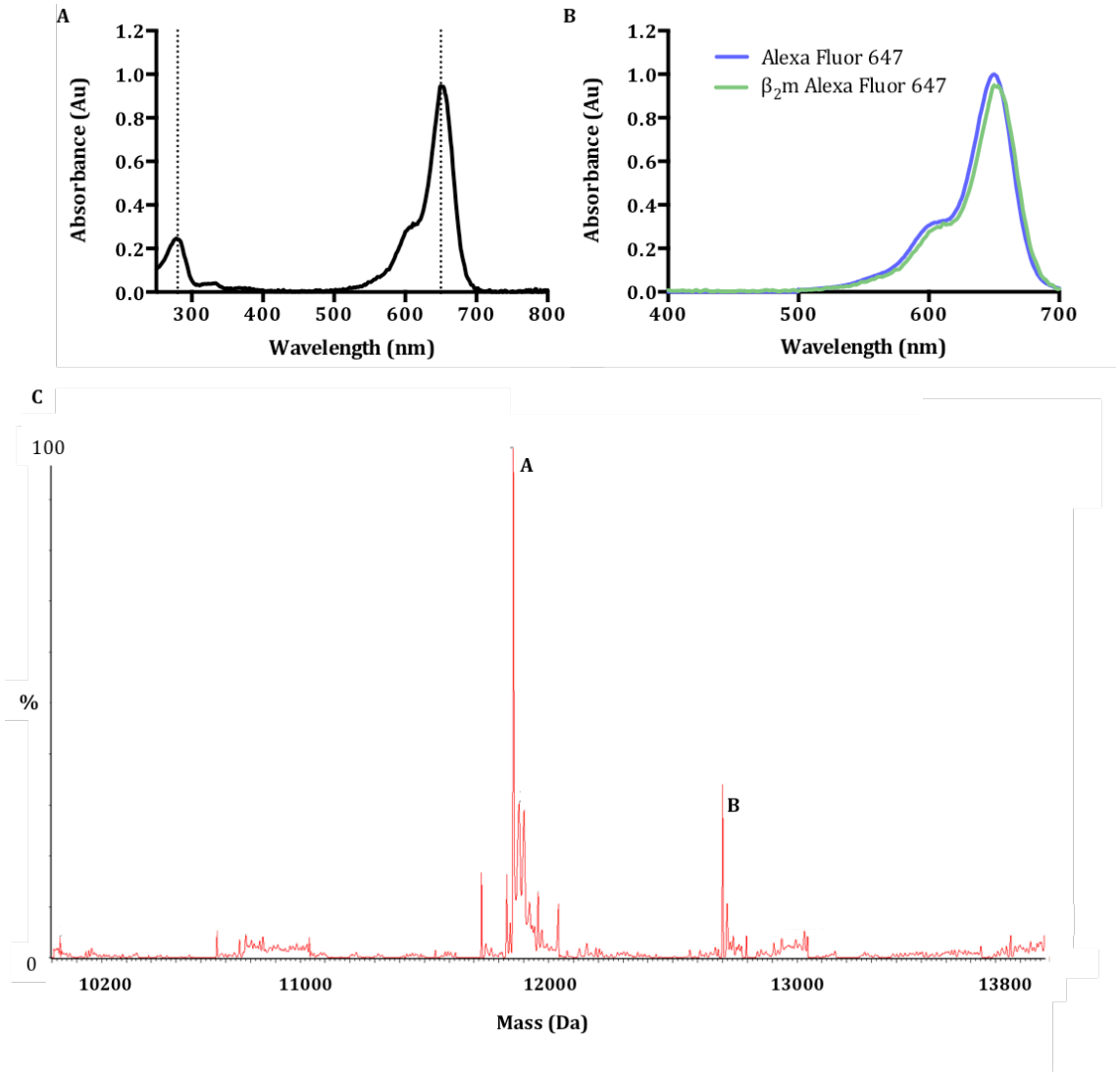

Figure 4-3 Labelling of monomeric β_2m 1° amines with AlexaFluor647. A) Absorbance of AF647 β_2m monomer, showing expected absorbance peaks at 280 nm (tryptophan) and 647 nm (fluorophore). B) Unbound AF647 and AF647 β_2m monomer form show same absorbance peak at 647 nm. C) The AF647 β_2m protein was analysed by ESI-MS. The major peak (peak A) corresponds to 11858 ± 0.97 Da, and represents unlabelled β_2m (expected mass 11860 Da). The minor peak (peak B) corresponds to 12701 ± 0.44 Da and represents β_2m singly labelled with AF647. Other peaks are potassium and phosphate adducts. Sample analysis was performed by James Ault, Mass Spectrometry Facility, University of Leeds.

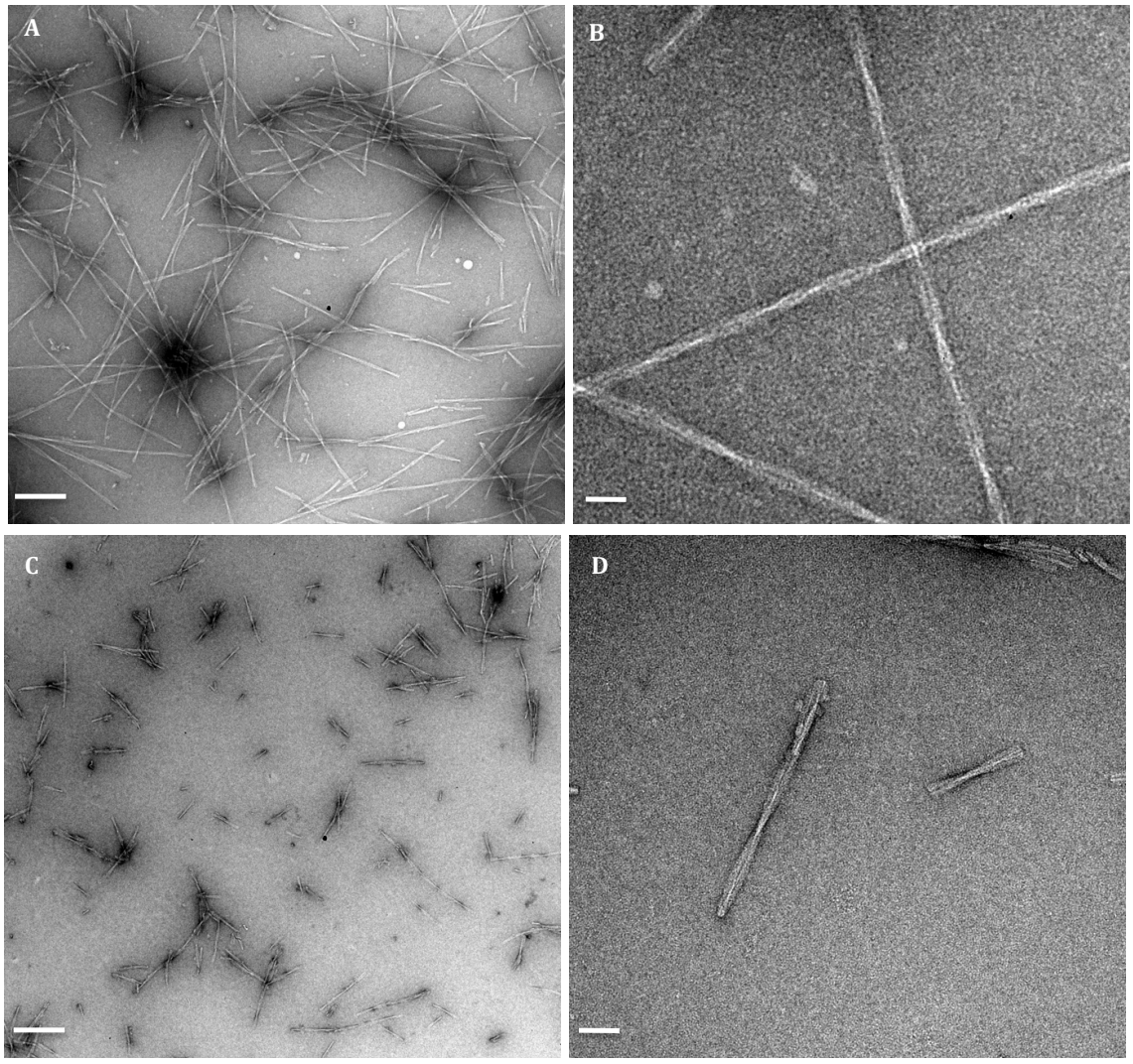

Figure 4-4 Structural characterisation of AF647 β_2m fibrils. AF647 β_2m Ls (A,B) and AF647 β_2m Ls-f fibrils (C,D) were visualised using negative stain EM. No gross morphological changes were observed compared with unlabelled fibrils (Figure 3-9). Scale bar 200 nm (A,C) or 50 nm (B,D).

4.2.1.2 β_2m amyloid fibrils are trafficked to the lysosome

In many amyloid-associated disease states, aggregates are present in the extracellular environment, and fibrillar or oligomeric species are endocytosed by neighbouring cells. In DRA, macrophages infiltrate the joints where they endocytose β_2m aggregates (Argiles *et al*., 2002; Porter *et al*., 2011; Morten *et al*., 2007). Therefore RAW 264.7 cells, a mouse macrophage cell line, is a physiologically appropriate cell type for studies on intracellular amyloid trafficking.

Live cell confocal imaging was used to investigate the time-scales over which β_2m Ls-f fibrils were endocytosed, and their intracellular location. Fluorescently labelled amyloid species (Section 4.2.1.1) can be used to track the intracellular location of the fluorophore conjugated to monomeric protein, which may be part of a higher order aggregate. Confocal

imaging of cells labelled with the lysosomal marker lysotracker and AF647 labelled β_2m species revealed that both AF647 labelled β_2m monomer and Ls-f, AF647 labelled β_2m Ls-f fibrils were trafficked to the lysosome within 4 h, and were still present at 24 h (Section 2.8)(Figure 4-5).

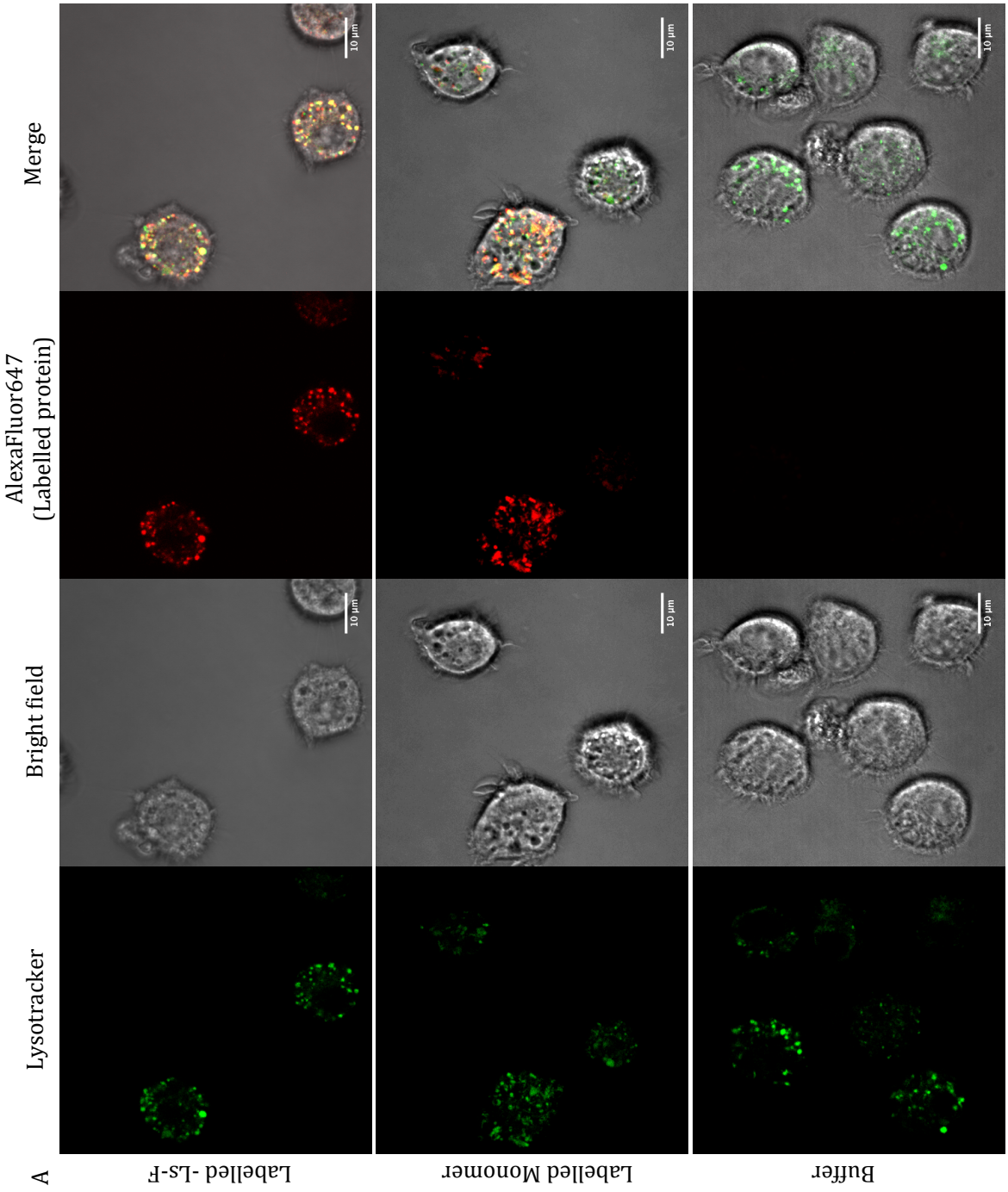
A
Lysotracker
Bright field
AlexaFluor647
(Labelled protein)
Merge
Labelled -Ls-F
Labelled Monomer
Buffer
10 µm

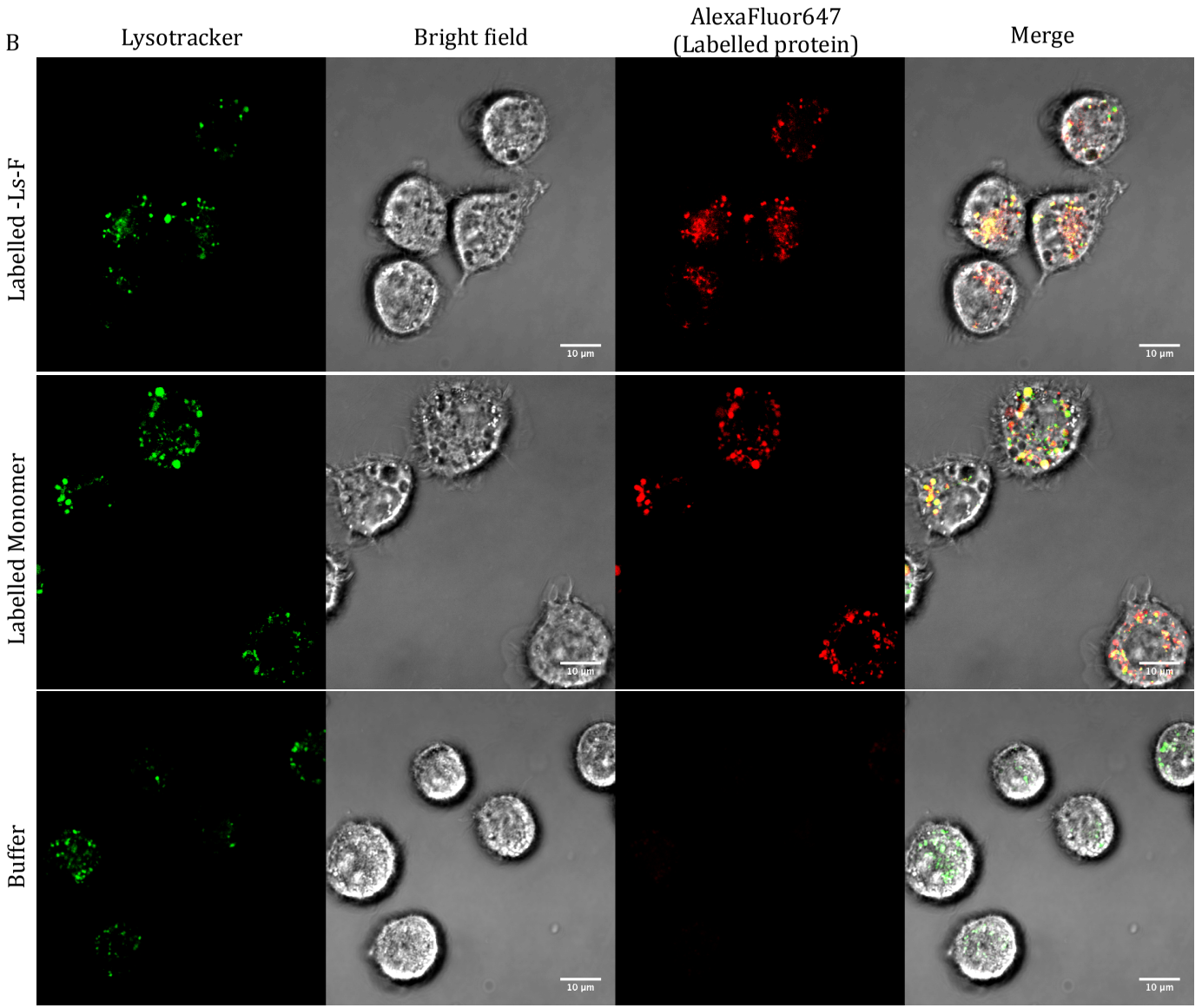

Figure 4-5 β_2m Ls-f and monomer is trafficked to lysosomes by 4 h (A) and persists at 24 h (B). RAW 264.7 cells were incubated with 1.2 µM (monomer equivalent) AF647 labelled β_2m Ls-f, AF647 labelled β_2m monomer, or pH 2.0 fibril buffer for 4 h or 24 h and imaged immediately (A,B) Lysotracker green was added 30 minutes before imaging. Cells were washed prior to live cell imaging with the Zeiss LSM 700 Meta laser scanning confocal microscope (63X objective). Representative confocal images for each condition are shown. Scale bar represents 10 µm

4.2.1.3 Probing intracellular amyloid formation using NIAD-4

While using fibrillar species formed from fluorescently labelled monomeric protein provides information about the location of the protein monomer, it does not provide any information about the higher order state that the fluorescently-labelled monomeric protein may be a part of. For example, fibrillar species could depolymerise into oligomeric or monomeric species before, or upon, entry to the cell (Tipping, Karamanos, *et al*., 2015). NIAD-4 has been shown to exhibit a large increase in fluorescence upon binding to β_2m amyloid fibrils at pH 2.0, 4.4 and 7.4 *in vitro,* which covers the range of pH conditions in cellular compartments, and therefore can act as a tool for probing intracellular amyloid conformation (Section 3.2.2). However, *in vitro* fluorescence revealed NIAD-4 displays different emission maxima with Ls β_2m fibrils, as well as reduced fluorescence intensity at acidic pH, indicating NIAD-4 is not a suitable fluorophore for quantitative analysis, as fluorescence would vary across different intracellular compartments, but it is suitable for performing qualitative analysis as it fluoresces across a broad range of physiological pH conditions.

Compatible fluorophores to perform dual colour confocal microscopy with NIAD-4 were determined by measuring the emission spectra of NIAD-4 in the presence and absence of Ls β_2m fibrils at a variety of commonly used wavelengths to excite samples in confocal microscopy (Figure 4-6). 488 nm was determined to be a suitable wavelength for excitation of NIAD-4 owing to the low fluorescence in the absence of Ls fibrils, and the strong fluorescence when they are present. At 639 nm, low levels of NIAD-4 fluorescence are seen in the presence and absence of fibrils indicating this is a suitable excitation wavelength for a fluorescent dye to complement NIAD-4 staining.

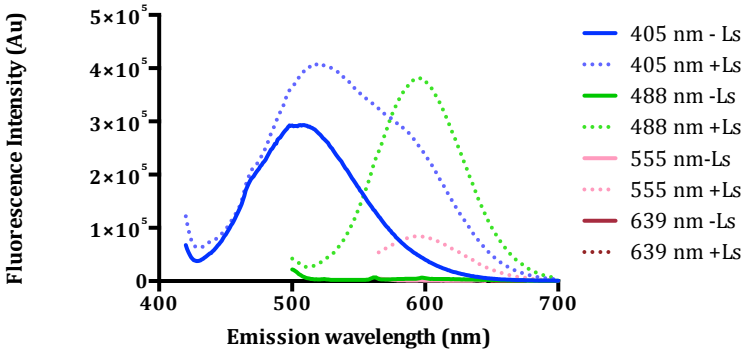

Figure 4-6 Emission spectra of NIAD-4 in the presence and absence of Ls β_2m fibrils. 7.5 µM NIAD-4 +/- 12 µM monomer equivalent excited at 405, 488, 555 and 639 nm to correspond with common lasers fitted to confocal microscopes. Samples were incubated at pH 6.4 for 10 minutes before a fluorescence emission spectra was collected at variable excitation wavelengths using at PTI Quantmaster fluorescence spectrometer. Lines for samples 555 nm – Ls, and 639 nm +/- Ls cannot be seen as they sit very close to the baseline.

In Section 4.2.1.2 it was demonstrated that β_2m Ls-f fibrils are trafficked to the lysosome within 4 hours, but this does not provide any information about the fibril's intracellular conformation. NIAD-4 was shown to be suitable as a tool for probing intracellular amyloid conformation, and so was used here in conjunction with lysotracker lysosome stain and AF647 β_2m monomer and fibrils to investigate intracellular conformation of amyloid species. NIAD-4 staining with cells exposed to AF647 labelled β_2m species demonstrated AF647 labelled β_2m Ls-f puncta colocalise with NIAD-4 staining, indicating the AF647 Ls-f retains an amyloid conformation (Figure 4-7A, C). Cells exposed to AF647 labelled β_2m monomer do not show any NIAD-4 staining, indicating no detectable NIAD-4 species are forming over the time-course of the experiment (Figure 4-7 A, C). In line with the observation that fluorescently labelled species reach the lysosome by 4 hours, colocalisation of NIAD-4 staining with Alexafluor647 labelled β_2m Ls-f was observed at 4 hours and 24 hours.

It may be possible that fibrils are degraded upon entry to the lysosome, and fluorescence at 24 h is a result of β_2m species being continually internalised. To investigate this, cells were exposed to AF647 β_2m monomer or Ls-f for 4 h or 24 h, washed, and incubated in fresh cell culture medium for a further 2 h before imaging. Colocalisation of AF647 β_2m Ls-f with NIAD-4 was observed at both 4+2 h and 24+2 h was seen, indicating Ls-f species persist in a NIAD-4 positive state over this time period.

To confirm that NIAD-4 positive species are trafficked to the lysosome, live cell confocal imaging was used to image cells stained with the lysosomal marker lysotracker and NIAD-4. Imaging demonstrated that NIAD-4 positive species colocalise with the lysosome at 4 h and 24 h (Figure 4-8).

Throughout live cell imaging, fluorescence associated with β_2m species was primarily observed as intracellular puncta. However, in some samples exposed to Ls-f species, extracellular aggregates were seen, including in cells that were washed and incubated for a further 2 h (Figure 4-7 B, Figure 4-8). This indicates Ls-f amyloid fibrils may associate with the plasma membrane and not become internalised in some cases. It is also interesting to note NIAD-4 puncta are occasionally not associated with labelled Ls-f species, the origin of this is unclear (Figure 4-7 D).

A
Labelled -Ls-F
Labelled Monomer
Buffer
NIAD-4
(Amyloid conformation)
Bright field
AlexaFluor647
(Labelled protein)
Merge
10 µm

B
Labelled -Ls-F
Labelled Monomer
Buffer
NIAD-4
(Amyloid conformation)
Bright field
AlexaFluor647
(Labelled protein)
Merge
10 µm

C
Labelled -Ls-F
Labelled Monomer
Buffer
NIAD-4
(Amyloid conformation)
Bright field
AlexaFluor647
(Labelled protein)
Merge
10 µm

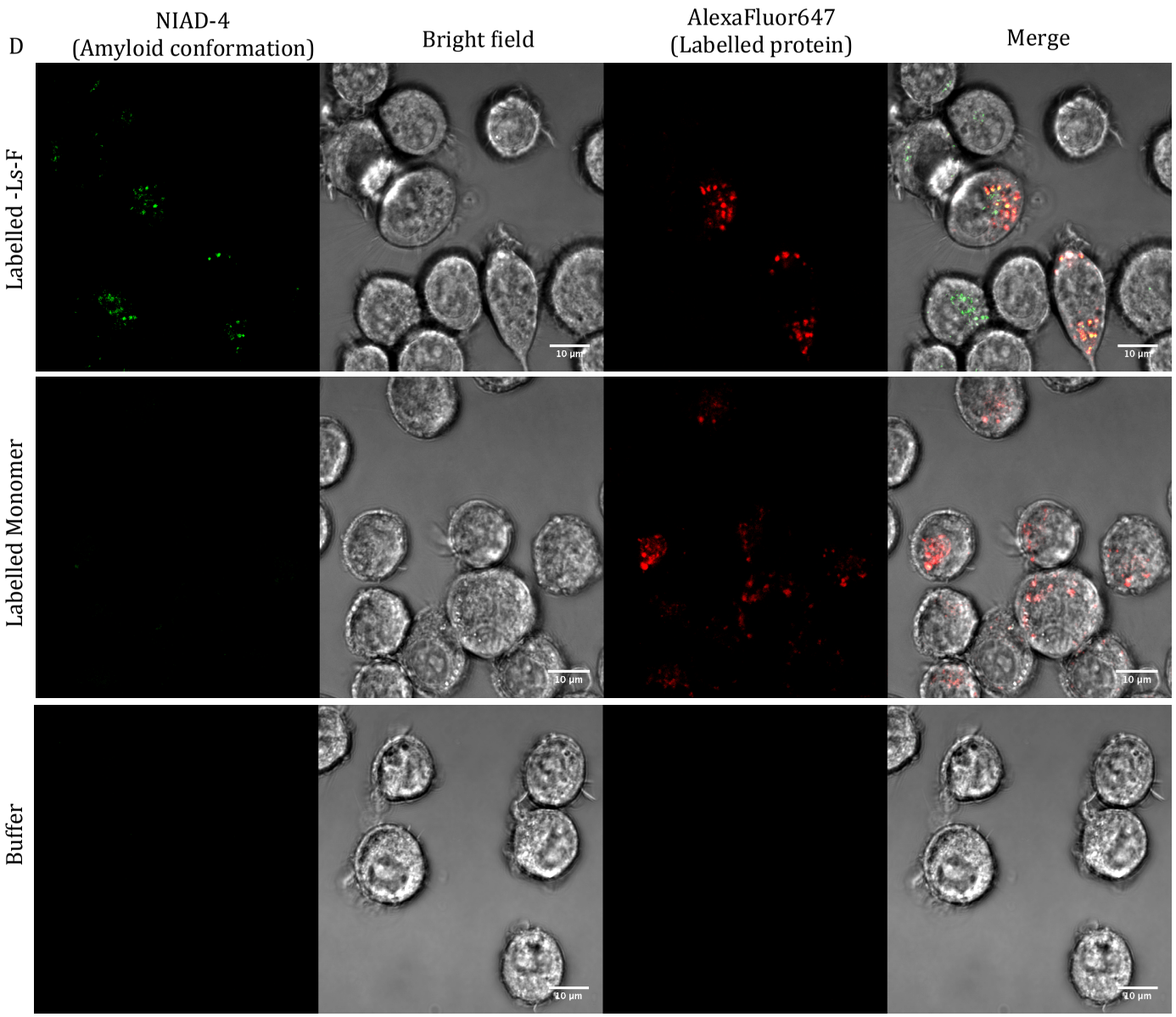

Figure 4-7 β_2m Ls-f fibrils, but not β_2m monomeric protein, is NIAD-4 positive after 4 h and 24 h incubation with treatment, and remain NIAD-4 positive when cells are washed and imaged 2 hours after fibrils have been removed from the cell media. RAW 264.7 cells were incubated with 1.2 µM (monomer equivalent) AF647 labelled β_2m Ls-f, AF647 labelled β_2m monomer, or pH 2.0 fibril buffer for 4 h or 24 h and imaged immediately (A,C) or thoroughly washed and media changed before a further 2 h incubation (B 4+2 h, D 24 + 2 h). NIAD-4 was added 30 minutes before imaging. Cells were washed prior to live cell imaging with the Zeiss LSM 700 Meta laser scanning confocal microscope, 63X objective. Representative confocal images for

A
Ls-F
Monomer
Buffer
NIAD-4
(Amyloid conformation)
Bright field
Lysotracker
Merge
10 µm

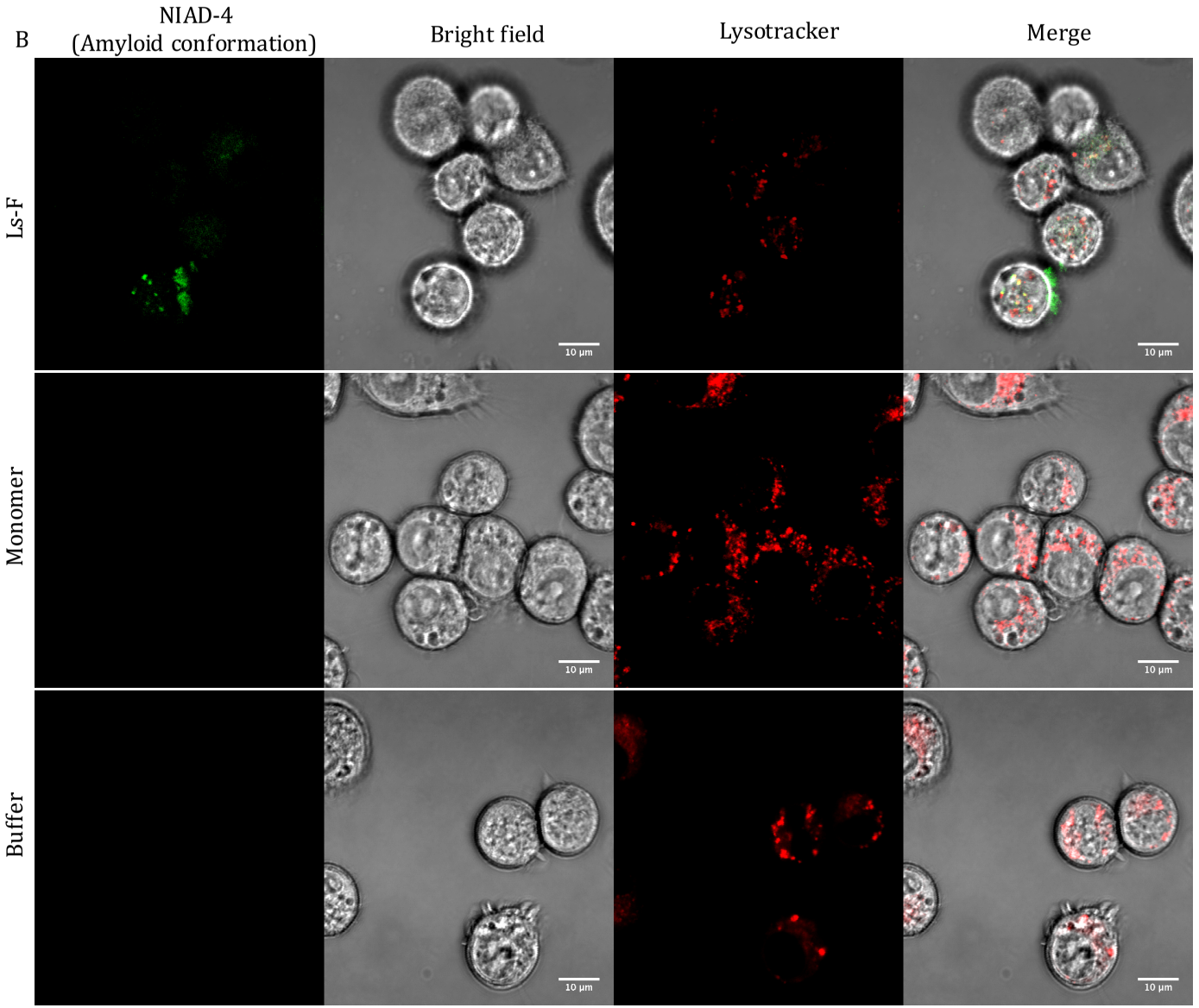

Figure 4-8 β_2m Ls-f maintains NIAD-4 binding conformation inside lysosomes at 4 h (A) and 24 h (B). RAW 264.7 cells were incubated with 1.2 µM (monomer equivalent) β_2m Ls-f, β_2m monomer, or pH 2.0 fibril buffer for 4 h or 24 h and imaged immediately. Lysotracker deep red and NIAD-4 was added 30 minutes before imaging. Cells were washed prior to live cell imaging with the Zeiss LSM 700 Meta laser scanning confocal microscope, 63X objective. Representative confocal images for each condition are shown. Scale bar represents 10 µm.

4.2.2 β_2m fibrils are stabilised by cell culture growth medium

The results presented in Section 4.2.1.3 demonstrate that β_2m Ls-f fibrils are trafficked to lysosomes within ~4 hours, where they retain an amyloid (i.e. NIAD-4 positive) state. It has been shown previously that β_2m fibrils formed *in vitro* at pH 2.0 rapidly depolymerise (within 30 minutes) into monomeric β_2m when incubated at pH 7.4 (Tipping *et al*., 2015). Here, negative stain EM was used to investigate the state of β_2m amyloid species formed *in vitro* at pH 2.0 upon exposure to cell culture medium, as occurs during cell-based assays. β_2m Ls fibrils were incubated at a final monomer equivalent concentration of 1.2 μM in cell culture medium (Section 2.5) and imaged using negative stain EM (Figure 4-9). Negative stain EM provides a qualitative view of morphological changes to fibril samples. Upon dilution of Ls fibrils into cell medium, the fibrils appear to bind components of the medium, a trend which continues over the course of the time series. Over time, the twist of the fibril becomes less visible. This could be the binding of protein obscuring the twist, a morphological change in fibril structure, or a combination of the two. There also appeared to be a progressive increase in fibril bundling, in contrast to pH 2.0 fibrils. After 24 hours, fibrils are still clearly visible, although they look different to their pH 2.0 counterparts, as they appear to be coated with additional material (Figure 4-9 A,B,O,P).

While negative stain EM is a useful tool for assessing morphology changes, it is hard to assess changes in length distribution, formation of other species through depolymerisation, alterations to fine fibril structure such as twist crossover length, or other subtle structural changes. Both the morphological changes observed, such as the bundling, binding to FCS components, as well as other structural changes that may have occurred, may alter the behaviour of amyloid species in cell-based assays compared with *in vitro* experiments. Fundamentally, the amyloid species interacting with the cell are different to the amyloid species formed and assayed *in vitro*, such as the liposome dye release experiments performed in Chapter three, an important consideration when comparing results from cell based and *in vitro* assays.

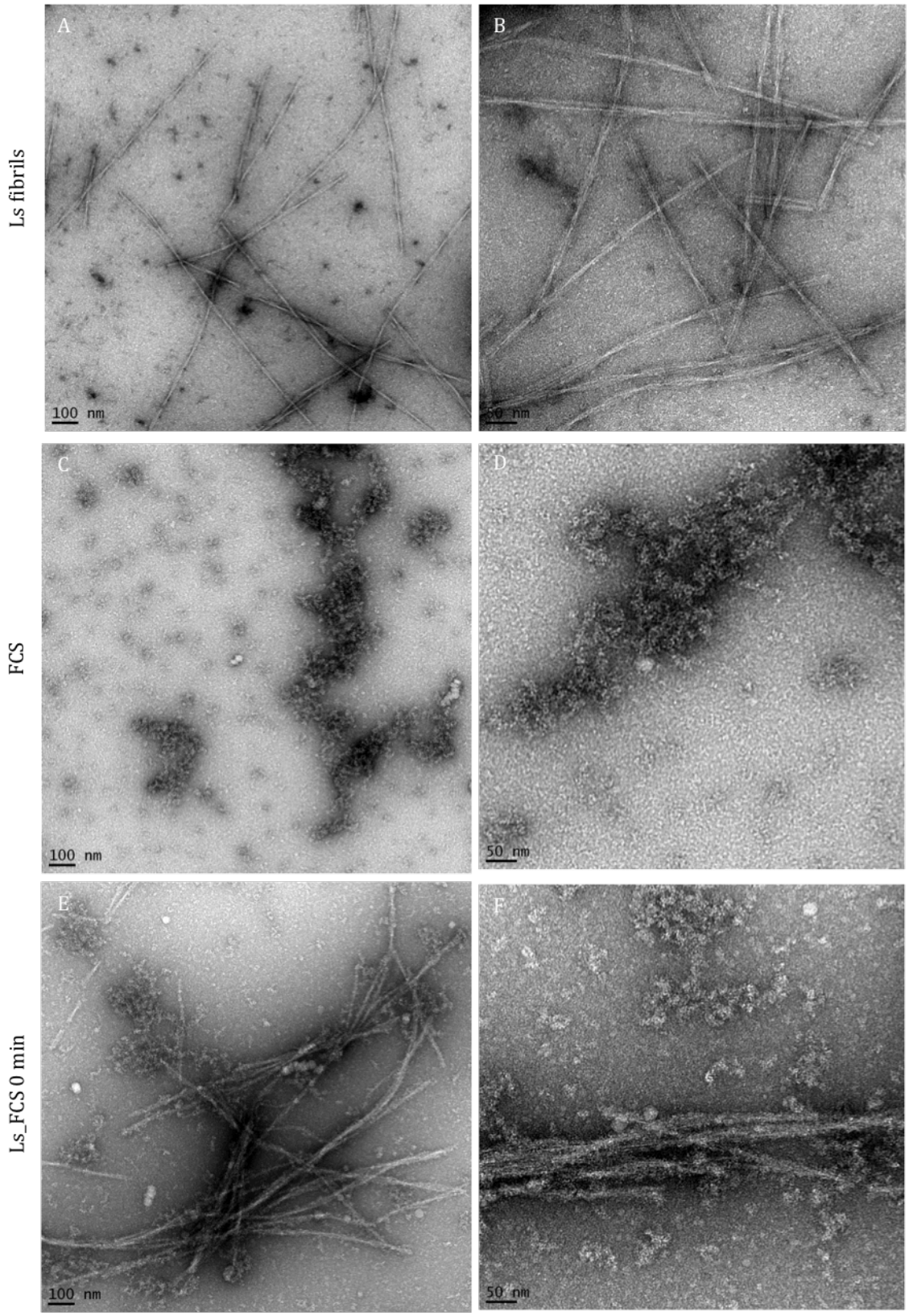
Ls fibrils
FCS
Ls_FCS 0 min
A
B
C
D
E
F
100 nm
50 nm
100 nm
50 nm
100 nm
50 nm

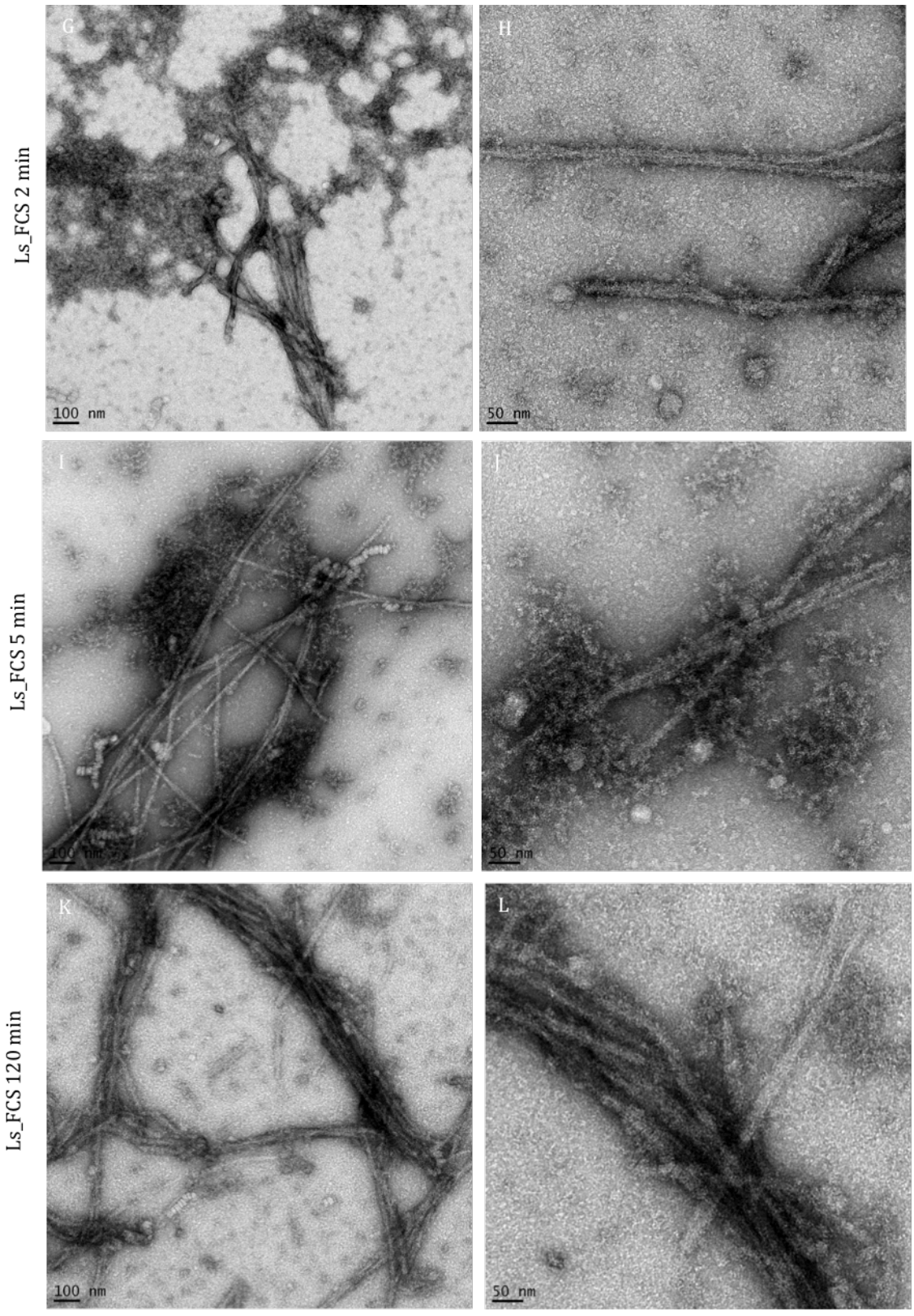
Ls_FCS 2 min
G
100 nm
H
50 nm
Ls_FCS 5 min
I
100 nm
J
50 nm
Ls_FCS 120 min
K
100 nm
L
50 nm

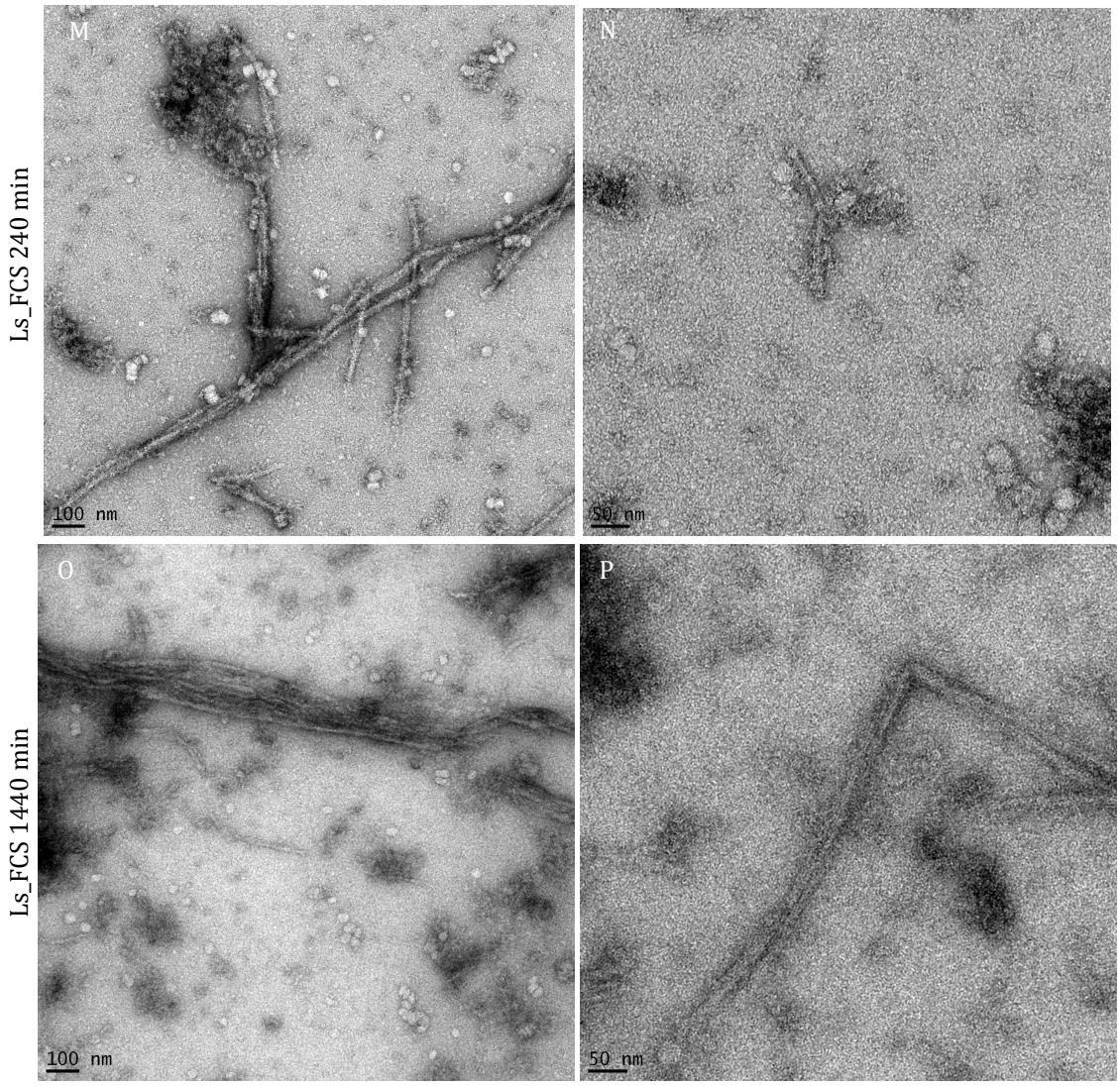

Figure 4-9 β_2m fibrils persist in cell culture media. β_2m Ls fibrils were diluted to a final concentration of 1.2 μM monomer equivalent in pH 2.0 fibril buffer (A,B), or DMEM supplemented with 10 % (v/v) foetal calf serum (FCS), 2 mM L- glutamine, 100 IU/ml penicillin and 100 μg/ml streptomycin (E-P) for the stated time period. After 24 hours, structures with fibrillar morphology were still clearly visible (O,P). For comparison, FCS alone was imaged (C,D). Representative micrographs shown for each condition. Scale bar left column, 100 nm; right column 50 nm.

4.2.2.1 Assessing perturbation of isolated cellular membranes with β_2m fibrils

In Chapter three, it was demonstrated that β_2m amyloid fibrils disrupt LUVs formed from some synthetic lipid mixes (Section 3.2.4, 3.2.5) but do not appear to disrupt LUVs formed from crude lipid extract from RAW 264.7 cells or L-α-Lecithin (Section 3.2.6). Cellular membranes differ from both of these LUV types in several ways, including membrane curvature, the presence of integral and peripheral membrane proteins and in lipid composition. There is increasing evidence that the lysosome may be a site at which amyloid species exert their cytotoxic effects, which includes possible direct membrane

perturbations (Section 4.1.2). To assess the propensity of β_2m species to perturb lysosomal membranes, a crude lysosomal pellet (CLP) fraction enriched in lysosomes, mitochondria and endoplasmic reticulum was extracted from RAW 264.7 cells (2.7.6.2). CLP was incubated with β_2m monomer, Ls-f, Ls buffer or detergent, and incubated at 37 °C for one hour. These were then centrifuged to separate membrane bound (pellet) and soluble fractions, and the NAGA (soluble lysosomal enzyme, (Sellinger *et al.*, 1960)) activity of each fraction assessed. If the lysosomal membranes remain intact, NAGA activity would localise primarily to the pellet. Upon perturbation, NAGA activity would localise to the soluble fraction. At both pH 7.5 and 6.5, monomeric, Ls and Ls-f β_2m species do not appear to perturb lysosomal membranes, as NAGA activity primarily localises to the pellet fraction. NAGA is 45 kDa, and so it is possible that membrane disruption does occur, but not to the extent that NAGA is liberated from the lumen of the lysosome. Additionally, the assay may not be sensitive enough to detect low levels of membrane perturbation (~ < 5-10 %). However, this assay suggests that β_2m species are unable to perturb isolated lysosomal membranes under these conditions.

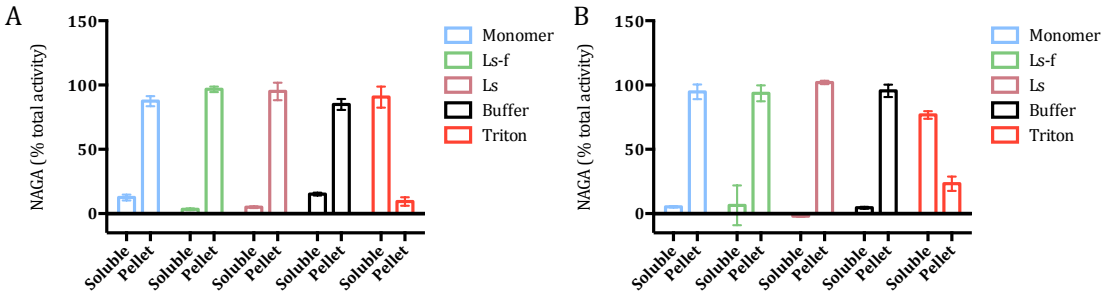

Figure 4-10 Isolated cellular membranes are not perturbed by β_2m amyloid or monomer. CLP from RAW 264.7 cells were incubated with a final concentration of 6 μM β_2m monomer, Ls, Ls-f, Optiprep™ homogenisation buffer or 0.5 % (v/v) Triton X-100 for 1 hour at 37 °C at pH 7.5 (A) or 6.5 (B), centrifuged, and NAGA activity in the soluble and pellet fractions assessed. Data for each treatment (sum of soluble and pellet NAGA fraction) normalised to 100 % NAGA activity (Soluble + pellet fraction). Error bars represent standard deviation of 3 replicates.

4.2.3 Subcellular fractionation

Biochemical assays did not demonstrate lysosomal membrane perturbations by β_2m amyloid fibrils, and so to investigate the nature of cellular membrane-amyloid interactions further, subcellular fractionation was used to isolate an enriched fraction of lysosomal membranes for further experimentation. To isolate an enriched lysosomal population, gradient-based subcellular fractionation was performed. The density-gradient centrifugation method used separates organelles and other cellular components on continuous or discontinuous gradients formed from various media including sucrose,

Ficoll, Percoll, Nycodenz and Iodixanol (Lee *et al*., 2010). In density-gradient centrifugation, the sedimentation rate of an organelle is dependent on its density relative to medium, which in turn is determined by the organelle's contents, lipid/protein ratio, size and shape (Lee *et al*., 2010). Firstly, the utility of two density gradient media to generate fractions for imaging by cryo-EM was assessed.

4.2.3.1 Subcellular fractionation using a percoll gradient

It has been demonstrated previously that lysosomes can be enriched using gradient centrifugation with percoll (Casey *et al*., 2007; Morten *et al*., 2007). Percoll is a sodium-stabilized colloid particle coated with polyvinylpyrrolidone, with an average diameter of 15-35 nm (Pertoft, 2000). Percol gradients are iso-osmotic, making it an attractive gradient density medium.

An enriched lysosomal population from RAW 264.7 cells was generated by performing subcellular fractionation of the post nuclear supernatant (PNS) on a percoll gradient (Section 2.7.4). To determine the location of organelles, fractions were assayed for the enzymatic activity of alkaline phosphatase (a plasma membrane marker), NAGA and acid phosphatase (lysosomal markers)(Figure 4-11)(Sellinger *et al*., 1960; Emmelot *et al*., 1964; Bull *et al*., 2002). Fraction nine contained a peak in NAGA and acid phosphatase enzyme activity, and a de-enrichment in alkaline phosphatase activity, indicating lysosomes were enriched in this fraction and plasma membrane was depleted. This was confirmed by western blotting with primary antibodies directed against cathepsin D, a luminal lysosomal marker (Sardiello *et al*., 2009). Fraction nine was depleted in contaminating membranes such as the plasma membrane, as assessed by alkaline phosphatase enzyme activity and immunoblotting against calreticulin (soluble endoplasmic reticulum marker)(Müller-Taubenberger *et al*., 2001). Membranes from fraction nine were subject to an additional centrifugation step to attempt to remove percoll, then imaged using cryo-EM.

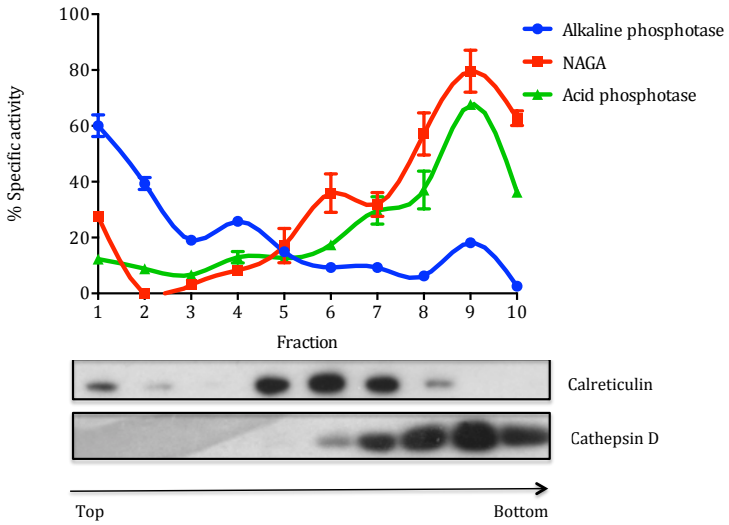

Figure 4-11 Subcellular fractionation of RAW 264.7 cells PNS on a percoll gradient. Subcellular fractions of RAW 264.7 cells were obtained by centrifugation on a 27 % (v/v) percoll gradient. 10 x 1 ml fractions were collected from the top and assayed for NAGA (lysosome marker), acid phosphatase (lysosome marker) and alkaline phosphatase (plasma membrane marker). Fractions were immunoblotted with antibodies specific for calreticulin (endoplasmic reticulum marker) and cathepsin D (lysosome marker). Error bars represent standard deviation of 3 replicates, which in some cases are smaller than the marker. Fraction 1 represents the top of the gradient (least dense), fraction 10 the bottom of the gradient.

4.2.3.2 Imaging of the enriched lysosomal fraction by cryo-EM

To assess the morphology of membranes isolated by the percoll gradient, and their compatibility for imaging by cryo-EM, membranes from fraction nine (Figure 4-11) were immobilised in vitreous ice and imaged by cryo-EM. A wide variety of membrane morphologies were observed, many consistent with known lysosomal morphologies. The most common species observed possessed a single membrane bilayer that appeared dark, indicating it contained more electron scattering material than the solute. Other species observed include tubular shaped membranes with striations in, multilamellar membranes, single membrane organelles containing granular material, and hybrid organelles (Figure 4-12). A large amount of particulate material was observed in the background that corresponds to the dimensions of percoll. Despite a centrifugation step after subcellular fractionation designed to separate membranes from percoll, high levels of residual percoll remain.

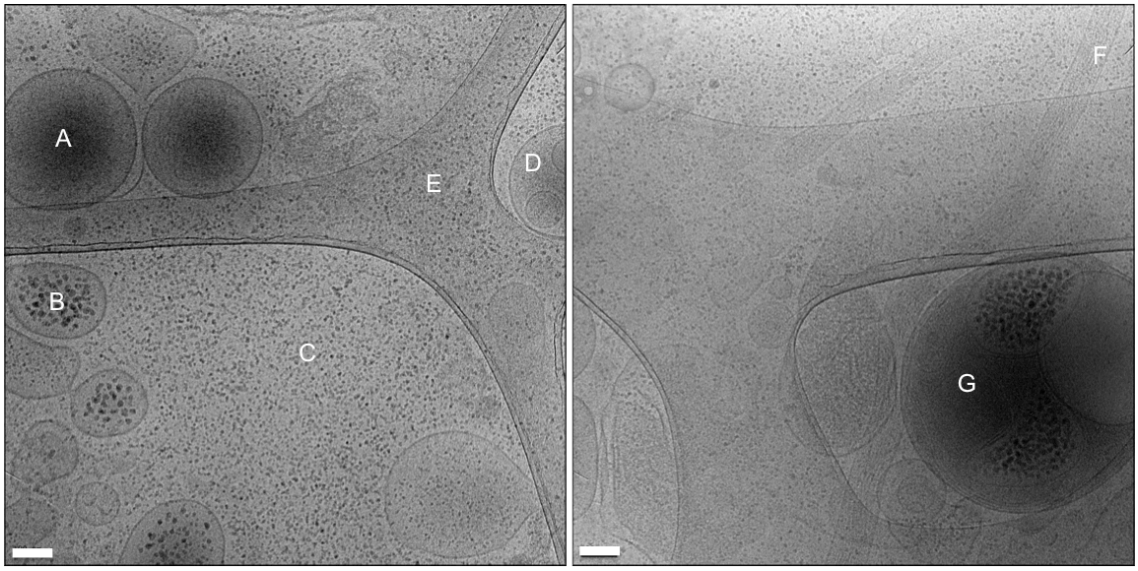

Figure 4-12 Membranes isolated from percoll gradient. Images are representative examples of membranes isolated from fraction 9 of a percoll gradient. A) Dense core lysosome. B) Granular lysosome. C) Percoll background D) Multivesicular body. E) Carbon support film. F) Tubular structure. G) Hybrid organelle. Scale bar 100 nm

4.2.3.3 Imaging in 3D by cryo-ET

To assess the feasibility of imaging the enriched lysosomal population cryo-ET was performed. Tomograms generated from these tilt series resolved membrane bilayers, and the contents of organelles, such as the multi-lamellar nature of some organelles, as well as the granular contents of others (Figure 4-13). However, the tomograms revealed high levels of percoll throughout the ice layer. Owing to the particulate nature of percoll, this is a prominent feature in the tomograms. Attempts to remove percoll through additional centrifugation techniques were made, however with each additional step to sediment percoll, a large proportion of membranes are sequestered into the percoll fraction. As a result, subcellular fractionation using percoll was deemed unfeasable when the downstream use of membranes by cryo-EM, and alternative subcellular fractionation techniques were explored.

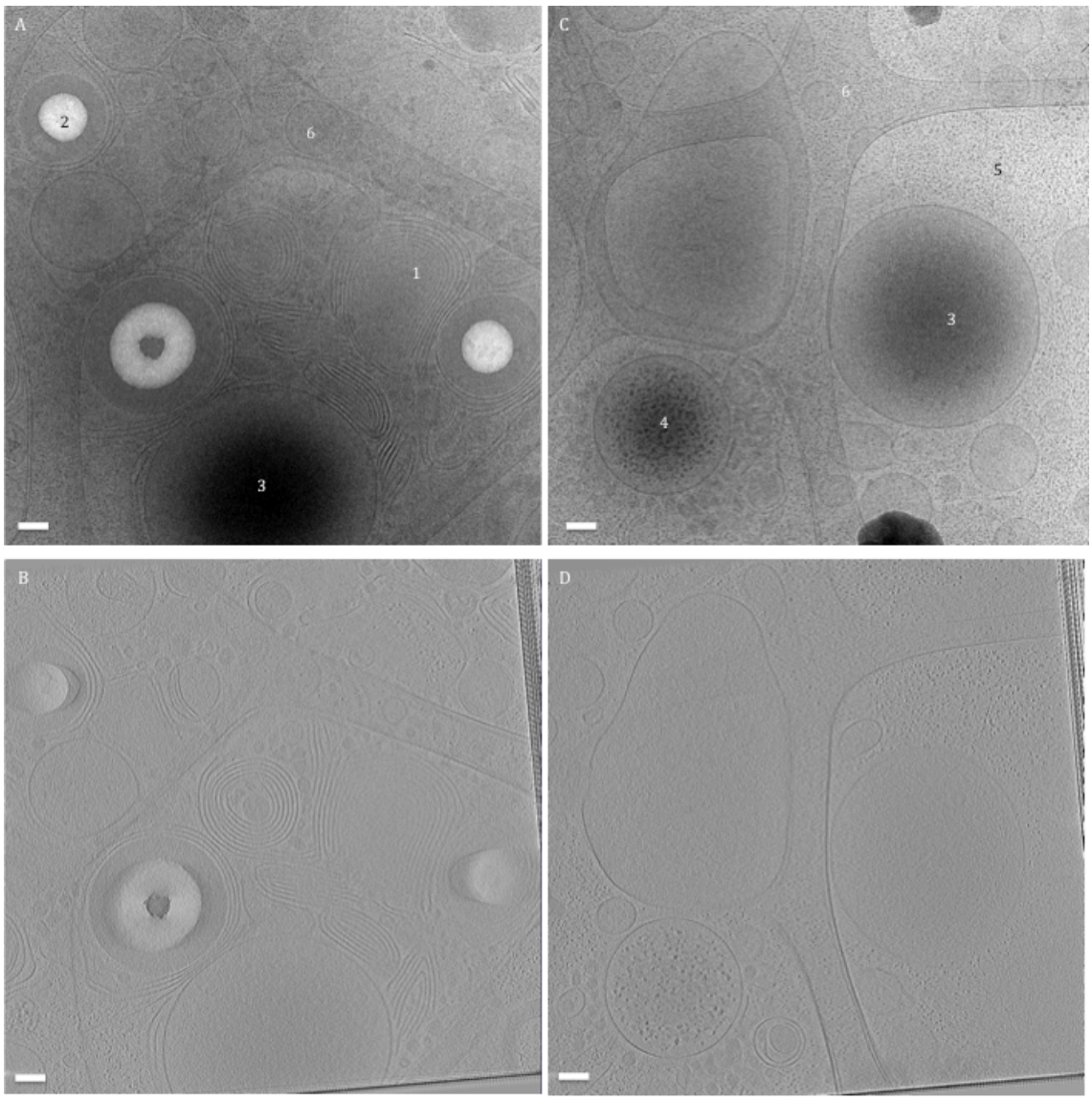

Figure 4-13 Cryo-ET of membranes from a percoll gradient A) -1° tilt image (Tilt series 'Percoll-tilt1.mov, Appendix B. B) Section of z stack of the tomogram generated from image stack A is taken from image (Tomogram 'Percoll-tomo1.mov, Appendix B) C) -1° tilt image (Tilt series 'Percoll-tilt2.mov, Appendix B) D) Section of z stack of the tomogram generated from image stack C is taken from image (Tomogram 'Percoll-tomo2.mov, Appendix B). Lines on the edges of B and D are artefacts from tomogram generation. Features indicated by numbers in A and C are multilamellar membranes (1), electron lucent structures (2), lysosomes (3), structures containing granular material (4) percoll packground (5), lacy carbon support film (6). Scale bar 100 nm.

4.2.4 Subcellular fractionation using an Optiprep™ gradient

To circumvent difficulties with residual percoll in the enriched lysosomal membranes, alternative subcellular fractionation procedures were investigated. Optiprep™, a solution of 60% (v/v) iodixanol can form iso-osmotic solutions at densities up to 1.32 g/ml (Ford *et al.*, 1994), and so is also suitable for separations of biological organelles (Figure 4-14).

Subcellular fractionation was performed using a modified version of a published protocol (Section 2.7.5)(Schmidt *et al*., 2009). Firstly, primary organelle enrichment was performed by differential centrifugation to obtain a fraction enriched in lysosomes, mitochondria and endoplasmic reticulum, known as the crude lysosomal pellet (CLP). These were then separated on a discontinuous Optiprep™ gradient. Six fractions were collected at the individual interphases between different densities of Optiprep™. These were concentrated by centrifugation, and used for subsequent analysis (Figure 4-14). Enzymatic activity of NAGA enzyme was assessed in each fraction, and demonstrated that fraction two was most highly enriched in NAGA activity, indicating this fraction is most highly enriched in lysosomes. This was corroborated by western blotting against the lysosomal marker cathepsin D. Complex 1, a mitochondrial marker, localised to fraction five on the gradient, indicating this Optiprep™ gradient was able to separate lysosomes from contaminants.

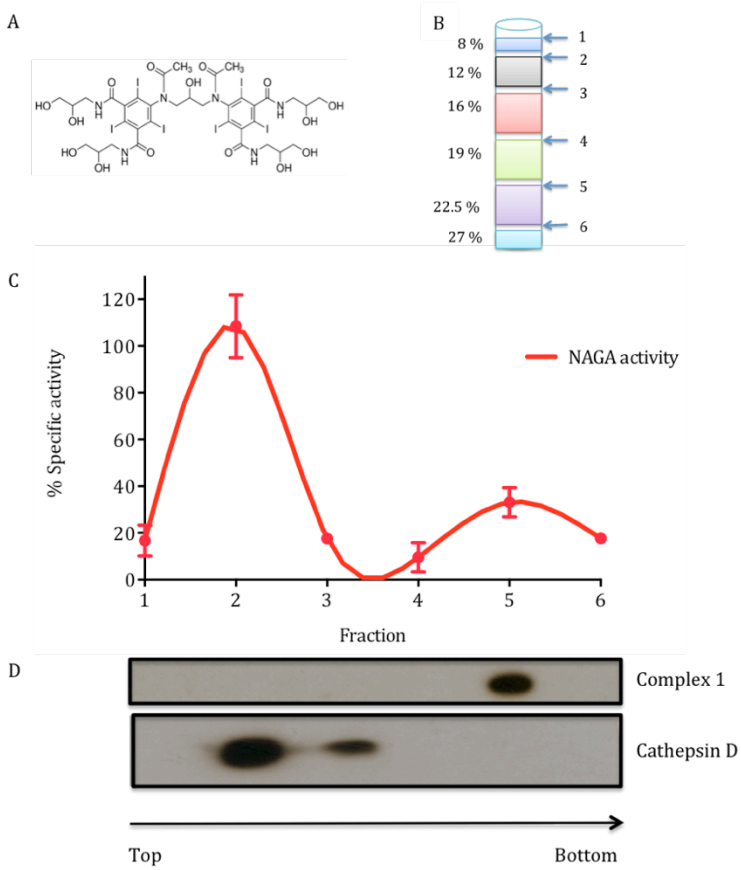

Figure 4-14 Subcellular fractionation of RAW 264.7 cells PNS on an Optiprep™ gradient. A) Structure of iodixanol. Optiprep™ is formed from a 60 % (v/v) iodixanol. B) Schematic of discontinuous Optiprep™ gradient. CLP was resuspended to 19 % (v/v) Optiprep™ and loaded between 22.5 and 16% layers into a discontinuous gradient of 27,22.5,16,12,8 % (v/v) Optiprep™, with the densest fractions at the bottom of the ultracentrifuge tube. 6 x 200 µl fractions were collected as indicated. Fraction 1 represents the top of the gradient (least dense), fraction 6 the bottom of the gradient. C) Activity of NAGA across fractions. Error bars represent standard deviation of 3 replicates, which in some cases are smaller than the marker. D) Fractions were immunoblotted with antibodies specific for cathepsin D (lysosomal marker) and Complex I (mitochondrial marker).

4.2.4.1 Morphological characterisation of membranes from Optiprep™ gradient

Cryo-EM was used to image fractions from the Optiprep™ gradient. Unlike fractionation on a percoll gradient, 2D images of all fractions from an Optiprep™ gradient had no obvious background contamination, enabling some organelles and cellular components such as cytoskeleton to be morphologically identified through 2D cryo-EM images (Figure 4-15, Figure 4-16). Multivesicular bodies are single membrane bound organelles that contain intraluminal vesicles of varying sizes, a feature which is clearly identifiable in the EM (Figure 4-15, 1)(Piper, 2007). During ball bearing homogenisation and centrifugation, the endoplasmic reticulum vesiculates, producing artificial structures known as microsomes. Where these are formed from rough endoplasmic reticulum, the resulting membranes are studded with ribosomes (Figure 4-15, 2). Some structures are regularly observed but are not clearly identifiable from their morphology. One such structure is bound by a single membrane, with an often-elongated appearance, containing material that gives a striated appearance, highly similar to structures seen in the percoll gradient (Figure 4-12, Figure 4-15, 3). These structures could be products of the homogenisation and centrifugation processes, such as microsomes. Their identity will be discussed further in Section 4.2.4.4. Mitochondria are easily identified by their double membrane and cristae (Figure 4-15, 4). Lysosomes are morphologically heterogeneous and resemble other organelles on the endocytic pathway, and as a result are often functionally rather than morphologically defined. Functionally, lysosomes are acidic organelles that contain mature acid-dependent hydrolases and lysosome-associated membrane glycoproteins (LAMPs) but lack mannose 6-phosphate receptors (MPRs) (Dell'Angelica *et al*., 2000). The organelles shown in Figure 4-15, 5 are consistent with previously described lysosome morphologies, and are enriched in lysosomal markers. Non-membrane bound cellular components can also be morphologically identified, such as cytoskeletal filaments including actin and microtubules (Figure 4-16, A,B). When imaging of cruder cell fractions, a background of macromolecular complexes was seen (Figure 4-16, C),

As many different cellular components can be identified by their morphology, fractions were imaged using cryo-EM. Fraction numbers correspond to those in Figure 4-14. Imaging by cryo-EM provides a qualitative indication of the success of the fractionation process, to complement biochemical analysis. Imaging of whole cell lysate and PNS revealed the expected diverse range of organelles and cellular components, including mitochondria, microsomes and cytoskeleton (Figure 4-17, 4-18). The CLP is generated by centrifugation of the PNS, separating denser organelles including lysosomes and mitochondria, from lighter membranes such as the plasma membrane and soluble

macromolecular complexes (Section 2.7.3). Therefore, as expected, the supernatant from this process contained free cytoskeleton, microsomes and other small membranes, on a background of macromolecular complexes (Figure 4-19). By contrast, the CLP contained an enrichment of microsomes with a larger diameter, mitochondria, and lysosomes, but still contained some macromolecular complexes and smaller membranes of an unclear origin. Fractionation on a discontinuous Optiprep™ gradient yielded fractions enriched with specific membranes (Figure 4-14). Fraction two, biochemically shown to be enriched in the lysosomal marker cathepsin D and lysosomal enzyme NAGA, was enriched in membranes consistent with a lysosomal morphology, along with a depletion of smaller membranes and soluble complexes compared with more crude preparations (Figure 4-21). By comparison, fraction 5, biochemically enriched with the mitochondrial marker fraction Complex I, was shown to contain a large number of mitochondria, accompanied by some small (< 200 nm), unidentifiable membranes.

Visually confirming the products of subcellular fractionation has two benefits. Firstly, biochemical analysis of the products of subcellular fractionation enable us to locate specific cellular markers, for example Complex I or cathepsin D, but does not confirm that the organelle is intact after cell homogenisation and centrifugation. Visual inspection of the gradient fractions enables us to confirm organelles still adopt the expected morphologies. Additionally, imaging fractions from the Optiprep™ gradient demonstrates these are suitable for further investigations examining the interactions of amyloid fibrils with biological membranes using cryo-EM.

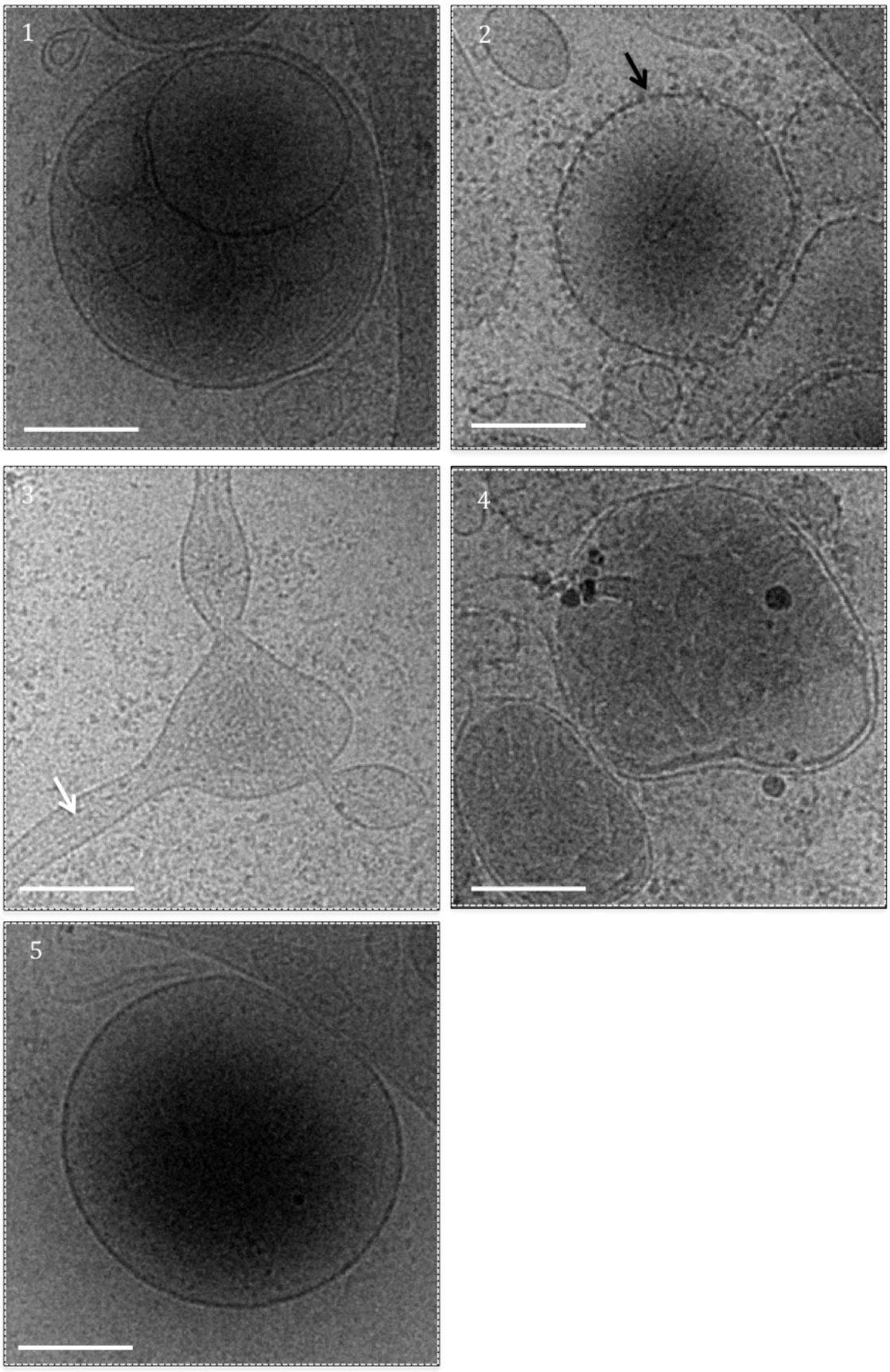

Figure 4-15 Range of organelles in subcellular fractions, observed by cryo-EM. MVB (1), rough microsome. Ribosomes indicated by black arrow (2), unknown structure containing striations, indicated by white arrow (3), mitochondria (4), lysosome (5). Scale bar 250 nm.

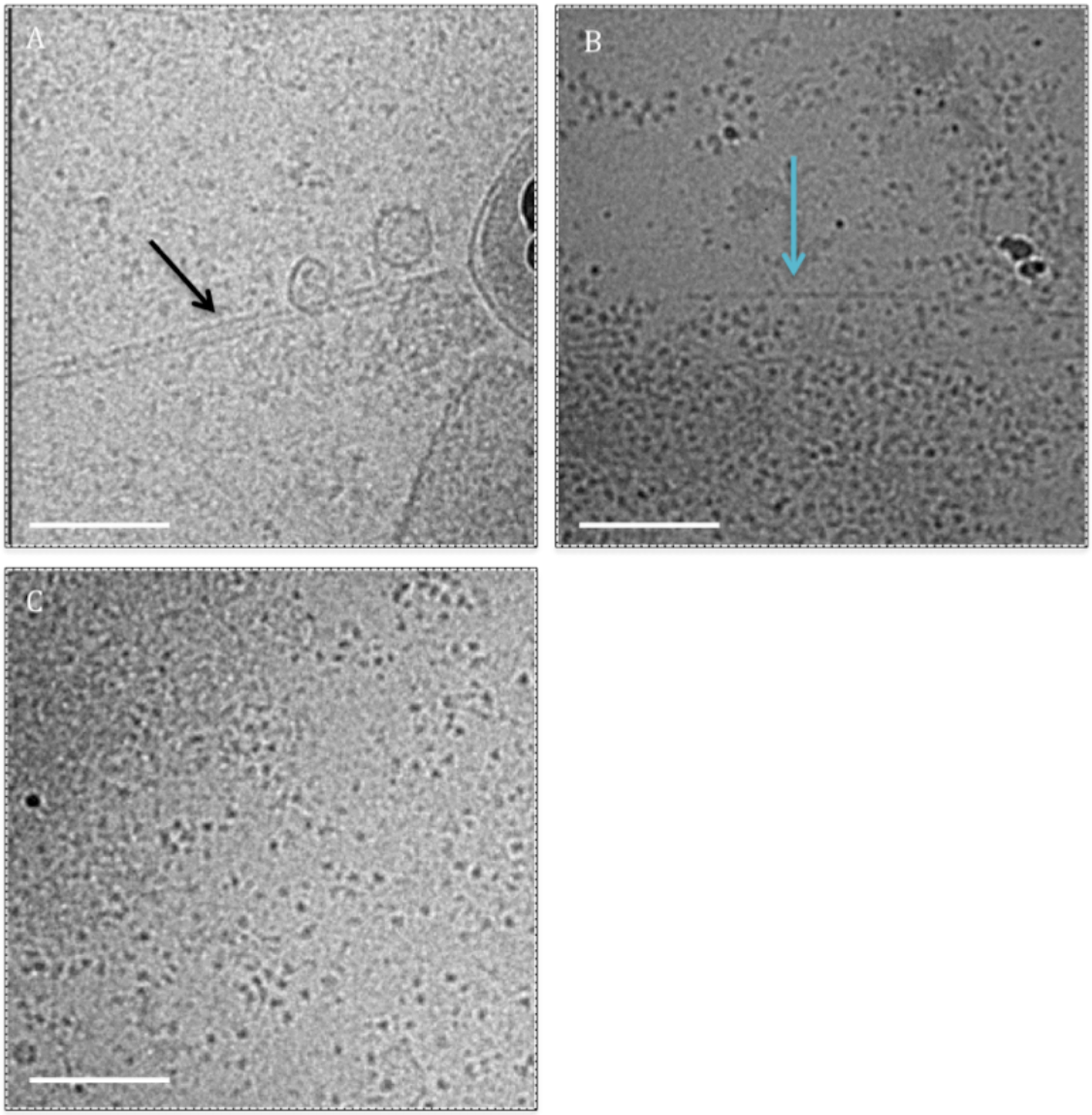

Figure 4-16 Range of cytosketeton and soluble material observed by cryo-EM. A) microtubule indicated by black arrow. B) Actin indicated by blue arrow. C) Soluble macromolecules. Scale bar 250 nm.

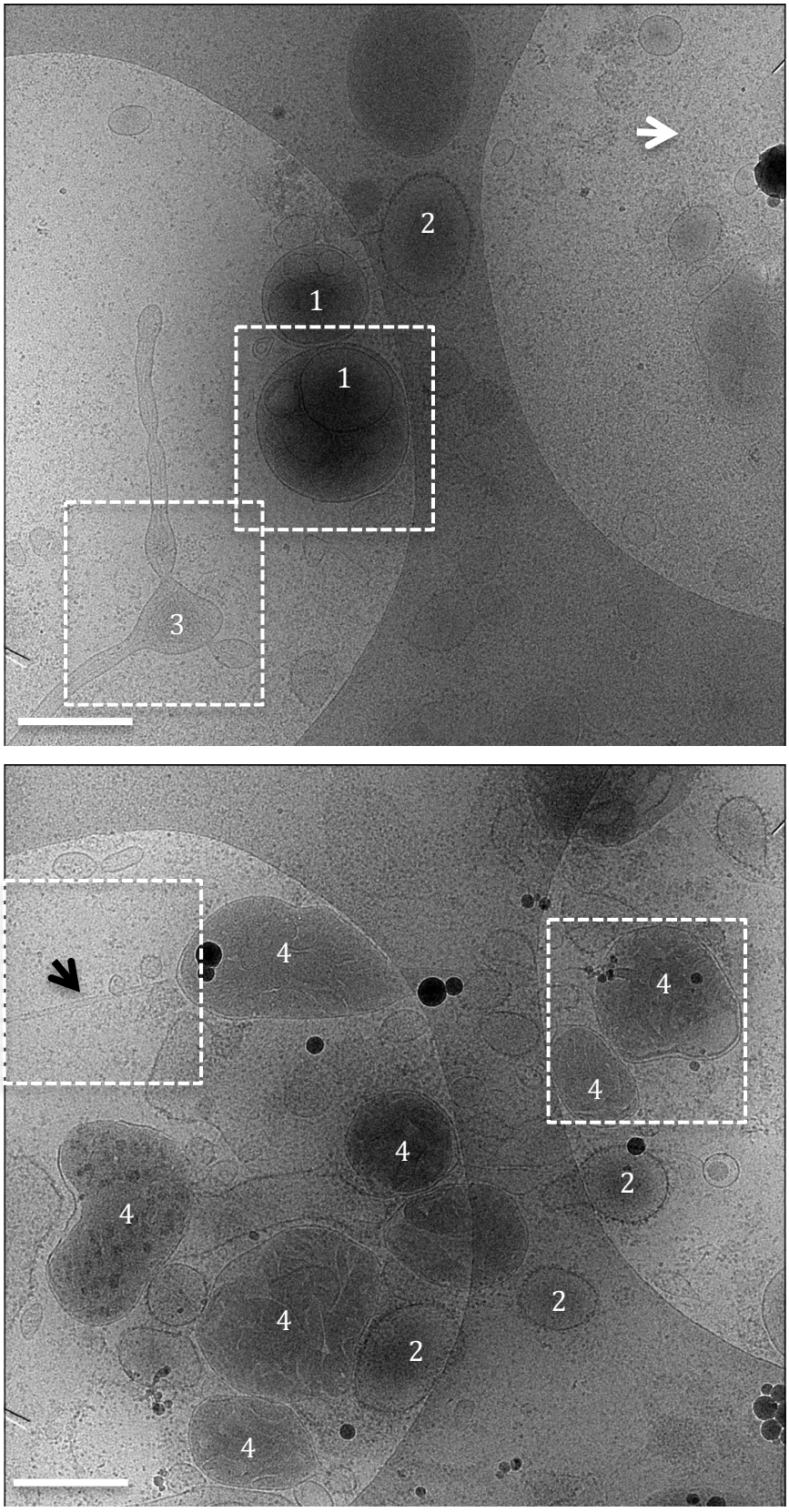

Figure 4-17 Cryo-EM of whole cell lysate. Two representative micrographs with a range of organelles present, including MVBs (1), rough microsomes (2), unknown tubular structures (3), mitochondria (4), cytoskeleton including microtubules (black arrow) and soluble macromolecular complexes (white arrow indicates sample area). White dashed boxes indicate area shown in Figure 4-15 and Figure 4-16. Scale bar 500 nm.

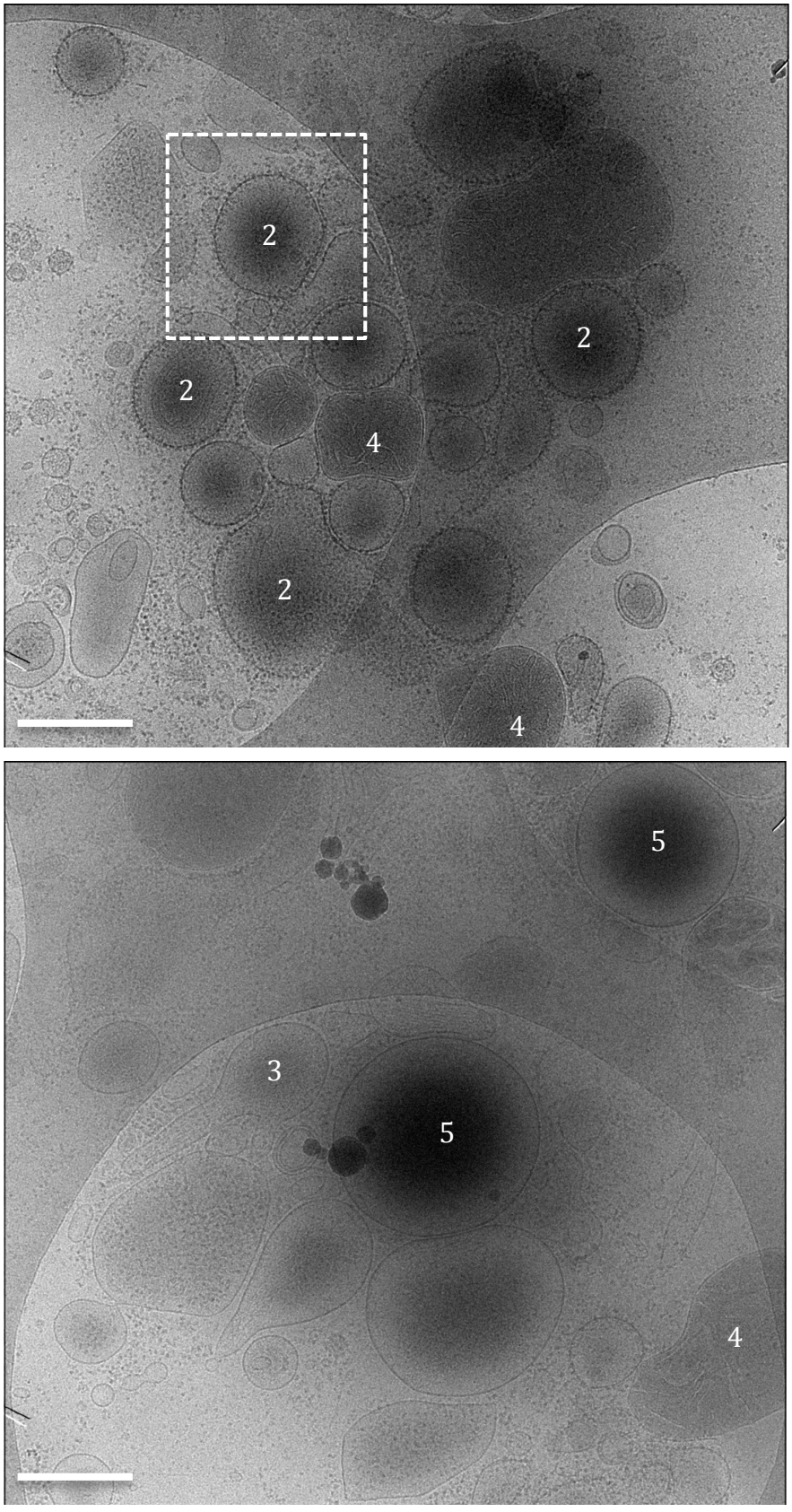

Figure 4-18 Cryo-EM of post-nuclear supernatant. Two representative micrographs with a range of organelles present, including rough microsomes (2), unknown tubular structures (3), mitochondria (4), lysosomes (5). White dashed boxes indicate area shown in Figure 4-15. Scale bar 250 nm.

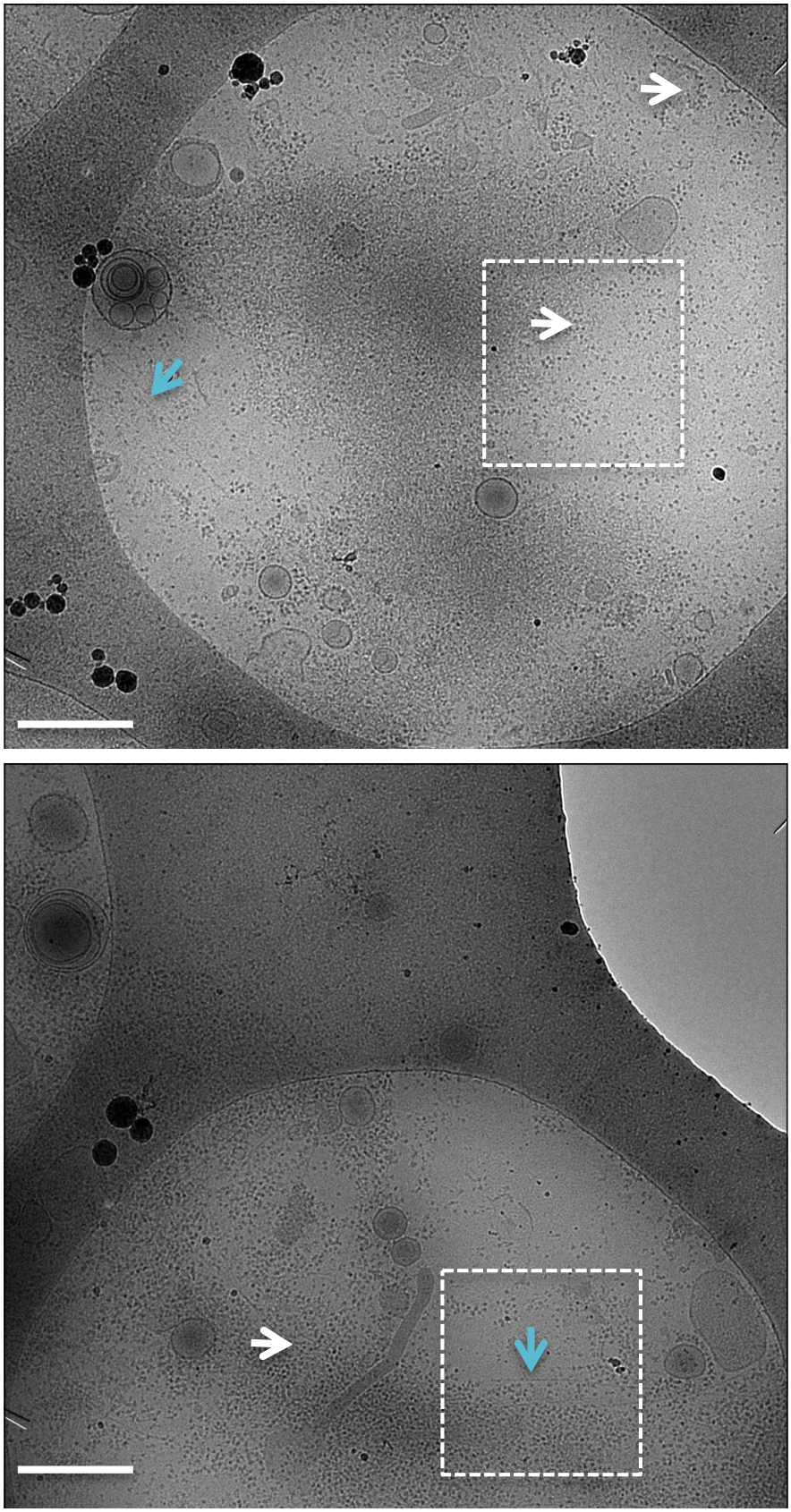

Figure 4-19 Cryo-EM of post-20,000 x g supernatant. Two representative micrographs with a number of small membranes, soluble macromolecular complexes (white arrow) actin cytoskeleton (blue arrow). White dashed boxes indicate area shown in Figure 4-15 and Figure 4-16. Scale bar 500 nm.

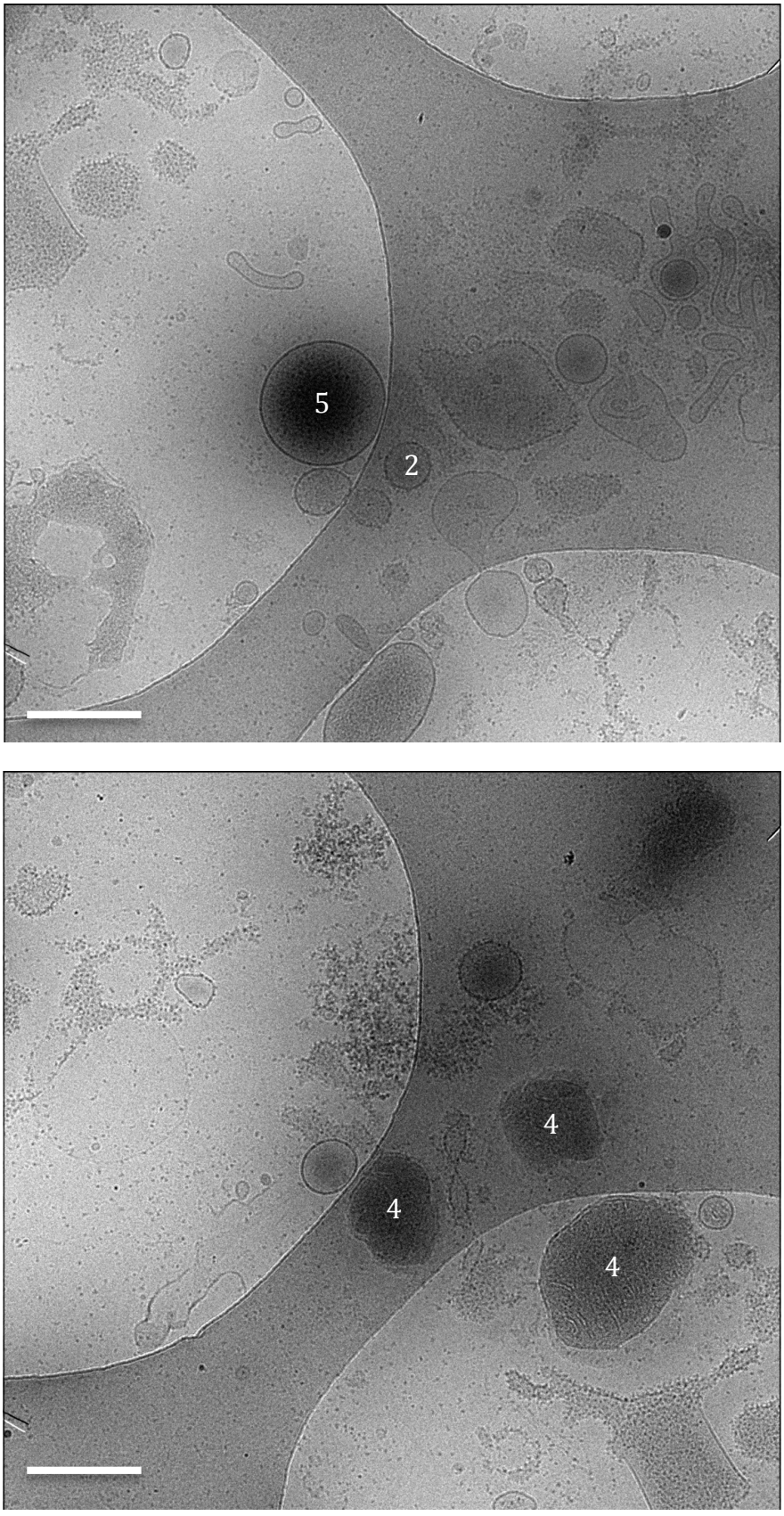

Figure 4-20 Cryo-EM of crude lysosomal pellet. Two representative micrographs with a range of organelles present, including rough microsomes (2), mitochondria (4), lysosomes (5). Scale bar 500 nm.

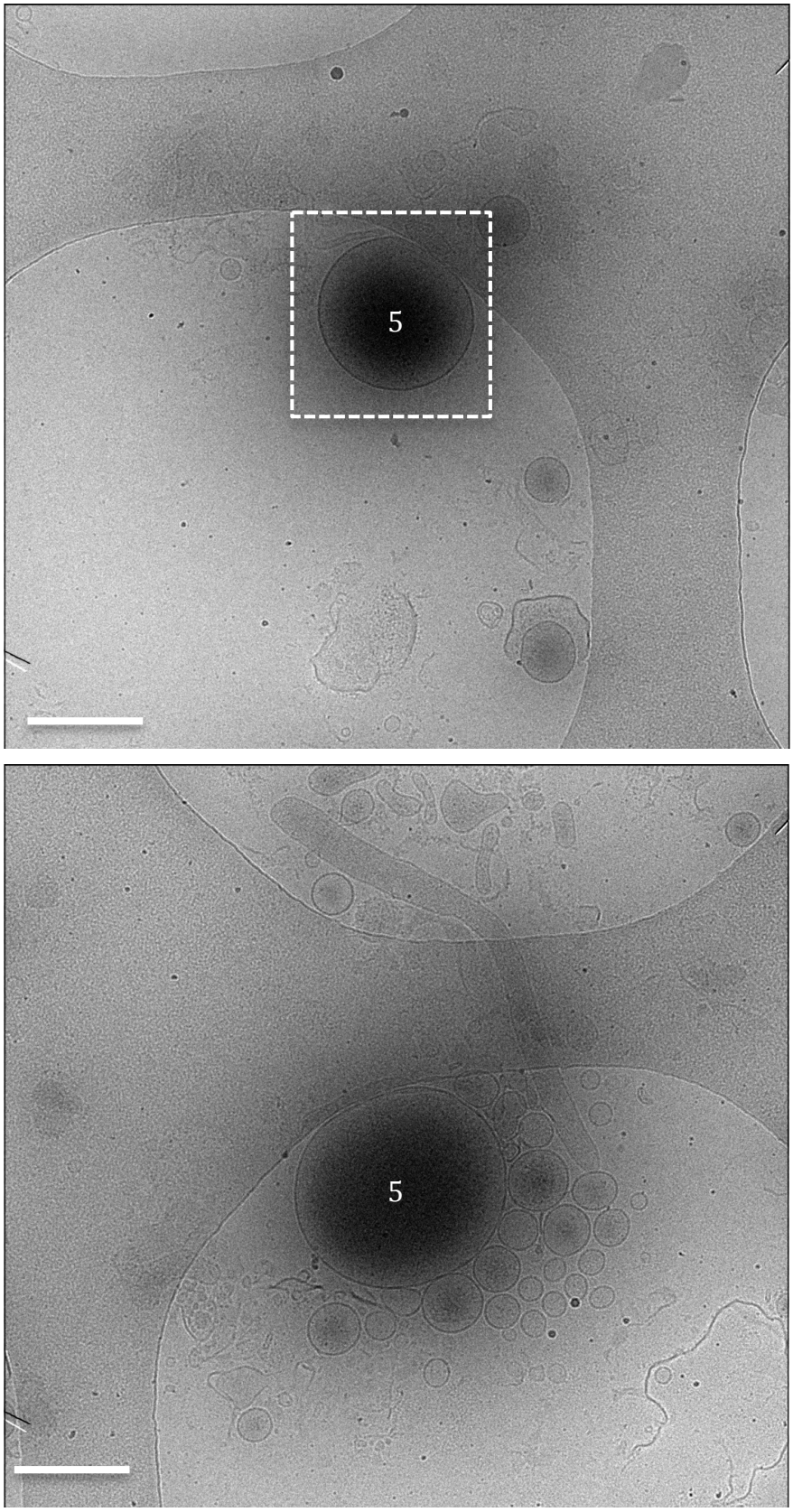

Figure 4-21 Cryo-EM of fraction two. Fractions defined in Figure 4-14. Two representative micrographs showing lysosomes (5), and a range of smaller membranes. White dashed boxes indicate area shown in Figure 4-15. Scale bar 500 nm.

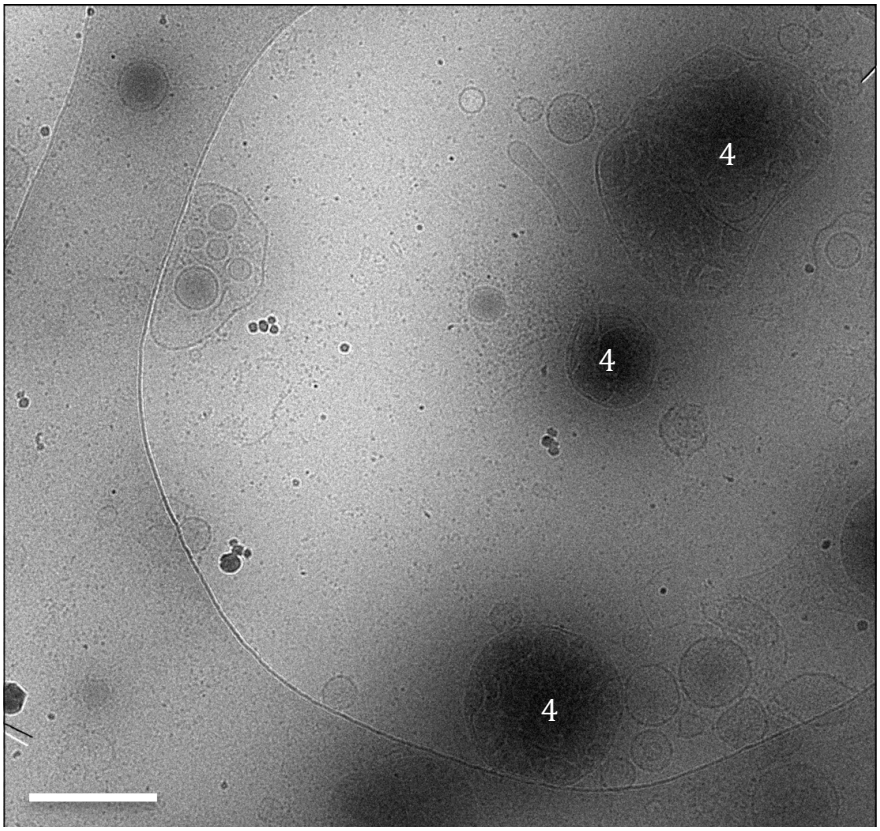

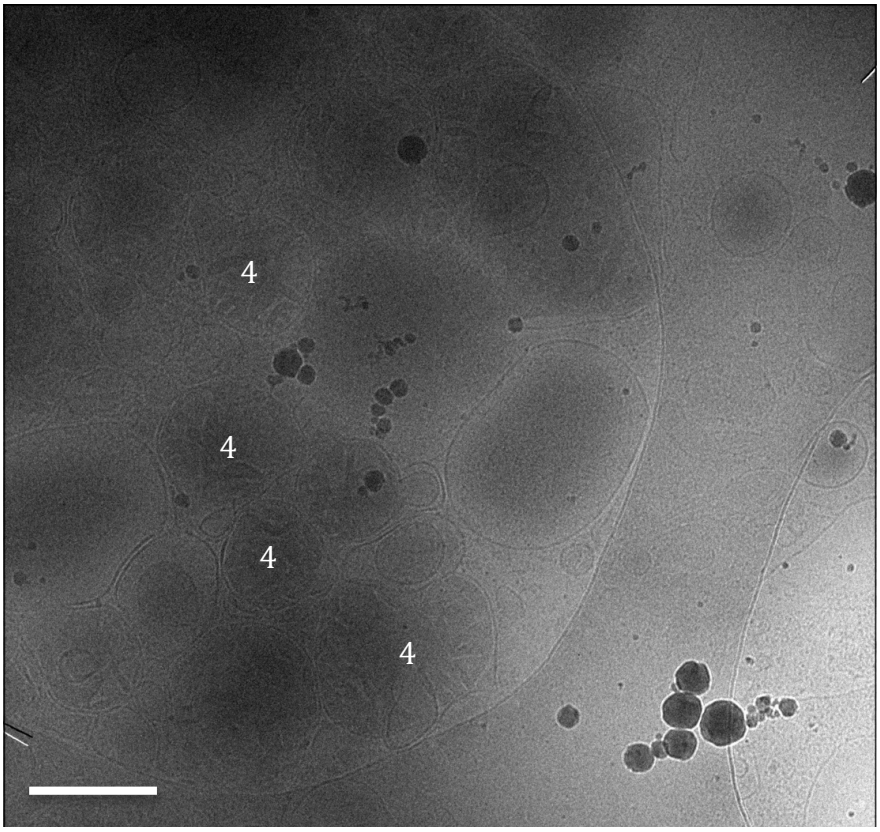

Figure 4-22 Cryo-EM of fraction five. Fractions defined in Figure 4-14. Two representative micrographs showing mitochondria (4), and a range of smaller membranes. Scale bar 500 nm.

4.2.4.2 *Subcellular fractionation of cells exposed to* β_2m Ls-f

It has been shown previously that β_2m amyloid fibrils are endocytosed by RAW 264.7 cells, and trafficked to the lysosome, where they retain an amyloid conformation as judged by their ability to bind NIAD-4 (Section 4.2.1). To investigate the interactions between amyloid fibrils and lysosomal membranes, cells were incubated with Ls-f β_2m fibrils (fibril fed), or pH 2.0 fibril growth buffer (control) for 24 h before cell harvesting. Subcellular fractionation was performed on a discontinuous Optiprep™ gradient as in Section 4.2.4.

The control fractionation displayed a similar distribution of subcellular components as previously presented (Figure 4-14), with fraction two most highly enriched in the lysosomal markers cathepsin D and NAGA enzyme, while fraction 5 is highly enriched in mitochondrial marker Complex I. However, upon exposure of cells to Ls-f β_2m fibrils, biochemical markers migrated differently within the gradient. Lysosomal markers (Cathepsin D and NAGA enzyme) were both present fraction one, two and three, compared with the control gradient, while lysosomal markers were almost exclusively present in fractions one and two. Both NAGA and cathepsin D are soluble lysosomal proteins, and so their presence in fraction one may be due to a proportion of lysosomes becoming structurally compromised, and leaking, which then localise to the top the gradient due to their low density. However, it was demonstrated in Section 4.2.1 that Ls-f β_2m fibrils trafficked to the lysosome, so the fibrillar amyloid cargo may change the density of the lysosomes, altering their position in the gradient. To monitor the location of Ls-f β_2m fibrils across the gradient, western blotting with an anti-β_2m antibody was performed. In control samples, no bands were observed; indicating endogenous expression of β_2m is undetectable at the concentrations isolated from the gradient. In the sample exposed to Ls-f fibrils, β_2m was shown primarily to localise to fractions three, five and six. Fibrils localised to fraction three may thus be associated with, or internalised within, lysosomes.

Interestingly, in fibril fed samples, Complex I also changed its distribution in the gradient. While the highest levels of enrichment were observed in fraction five, as seen in the control sample, an additional small band was observed in fraction three. There are several explanations for this. Firstly, that a small population of mitochondria have changed density, altering their position in the gradient. Secondly, the turnover/degradation of mitochondria in the cell could be affected, a process known as mitophagy. The removal of mitochondria requires two steps; firstly, induction of general autophagy and secondly, marking of mitochondria for selective autophagic recognition. Degradation by mitophagy relies on autophagosomes fusing with lysosomes. Complex I, present in fraction three, could be due to β_2m amyloid fibrils inhibiting the function of lysosomal hydrolases,

leading to Complex I remaining in this fraction. This is consistent with the previous observation that β_2m amyloid fibrils inhibit the ability of the lysosome to degrade protein substrates (Jakhria *et al.*, 2014).

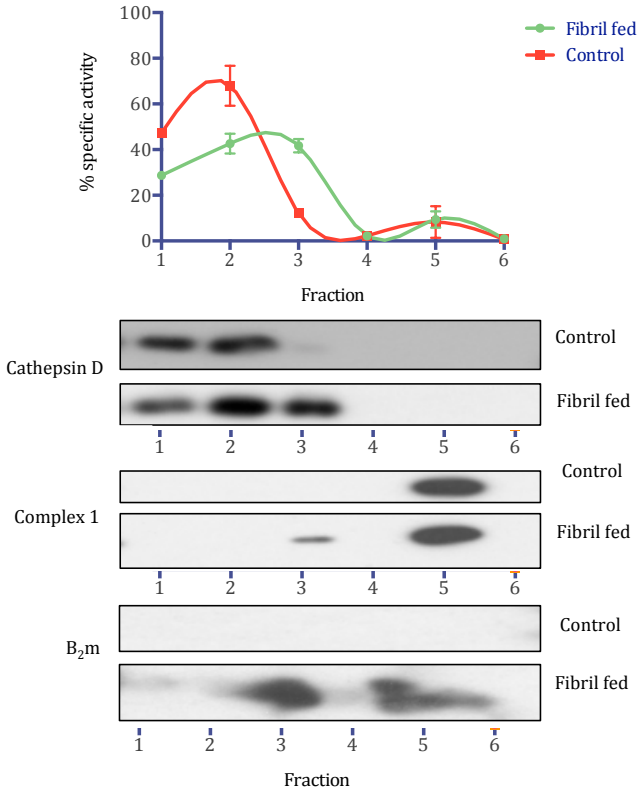

Figure 4-23 Subcellular fractionation of RAW 264.7 cells on an Optiprep™ gradient. Cells were either incubated with 1.2 µM final concentration Ls-f β_2m fibrils (fibril fed) or equivalent volume of pH 2.0 fibril buffer (control). CLP was resuspended to 19 % (v/v) Optiprep™ and loaded between 22.5 and 16% layers into a discontinuous gradient of 27,22.5,16,12,6 % (v/v) Optiprep™, with the densest fractions at the bottom of the ultracentrifuge tube. 6 x 200 µl fractions were collected from each gradient and assayed for NAGA activity (lysosomal marker). Fractions were immunoblotted with antibodies specific for cathepsin D (lysosomal marker) and Complex I (mitochondrial marker) and β_2m, to follow the presence of β_2m species in the gradient. Error bars represent standard deviation of 3 replicates, which in some cases are smaller than the marker. Fraction 1 represents the top of the gradient (least dense), fraction 6 the bottom of the gradient.

4.2.4.3 2D imaging of Optiprep™ fractions exposed to β2m fibrils

As shown in Section 4.2.4.1, enrichment of membranes on an Optiprep™ gradient is compatible with imaging by cryo-EM. To investigate β_2m Ls-f fibril interactions with membranes, the CLP and fraction three from an Optiprep™ gradient was imaged by cryo-EM (Figure 4-23, Figure 4-24). In both, membranes were seen which appeared to contain fibrillar material (Figure 4-24, A,B). To confirm that such structures were not a consequence of cells' exposure to a protein substrate, a CLP was generated from cells exposed to 1.2 μM β_2m monomer for 24 h before cell harvesting. Images of this CLP revealed the usual range of organelles present, including multivesicular bodies and lysosomes, but no structures resembling β_2m Ls-f fibrils (Figure 4-25).

Interestingly, in both the CLP and fraction three, β_2m amyloid fibrils not confined by a membrane were identified. These fibrils are morphologically consistent with β_2m Ls-f fibrils, and their presence outside of membranes may be due to fibrils escaping the endocytic pathway inside cells before homogenisation and/or subcellular fractionation. Alternatively, it could be an artefact of homogenisation and/or centrifugation, which is know to perturb cellular membranes and can generate structures not present inside cells, such as microsomes. Finally, it could be a result of fibril clumps associating with the plasma membrane. Although the cells are washed thoroughly before homogenisation, confocal imaging shows some fibrils remain associated (Section 4.2.1). Consistent with imaging of β_2m in cell culture medium (Section 4.2.2), fibrils outside of membranes were bundled, and were always seen in association with membranes. Some of these interactions, such as in Figure 4-24 C, are reminiscent of side-on interactions seen by Milanesi *et al* when imaging synthetic liposomes interacting with β_2m fibrils (Milanesi *et al*., 2012). In 2D however, it is challenging to fully interpret these interactions. As 3D spatial information is required for such interpretation, cryo-ET was performed.

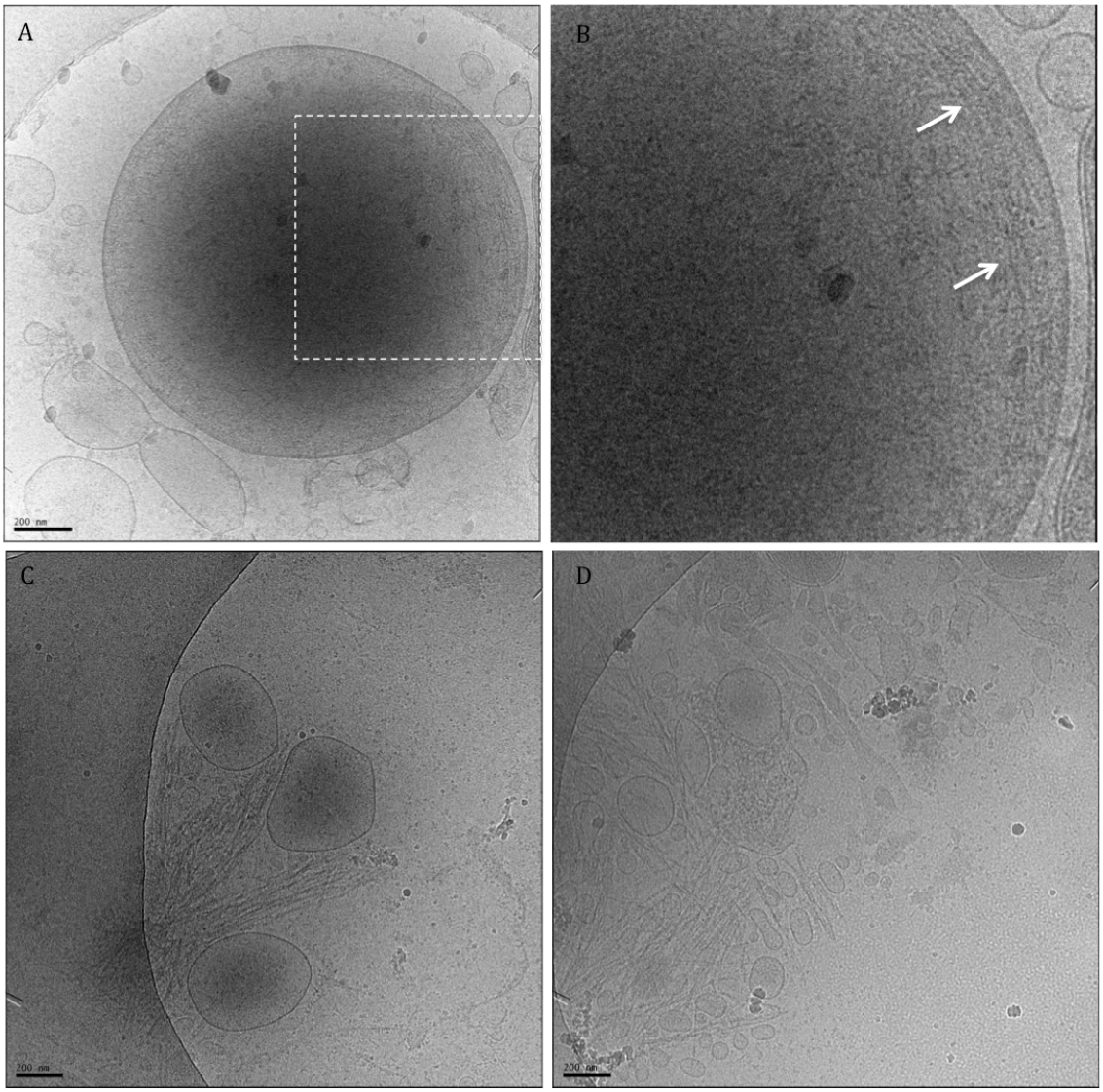

Figure 4-24 2D cryo-EM images of fractionated RAW 264.7 cells exposed to 1.2 μM monomer equivalent Ls-f β_2m fibrils 24 h before cell harvesting and fractionation. A) Fraction three, enriched in lysosomes as judged by NAGA enzyme activity and cathepsin D immunoblotting. White dotted box shows area magnified in B. C, D) CLP showing β_2m Ls-f fibril bundles interacting with biological membranes. Scale bar 200 nm.

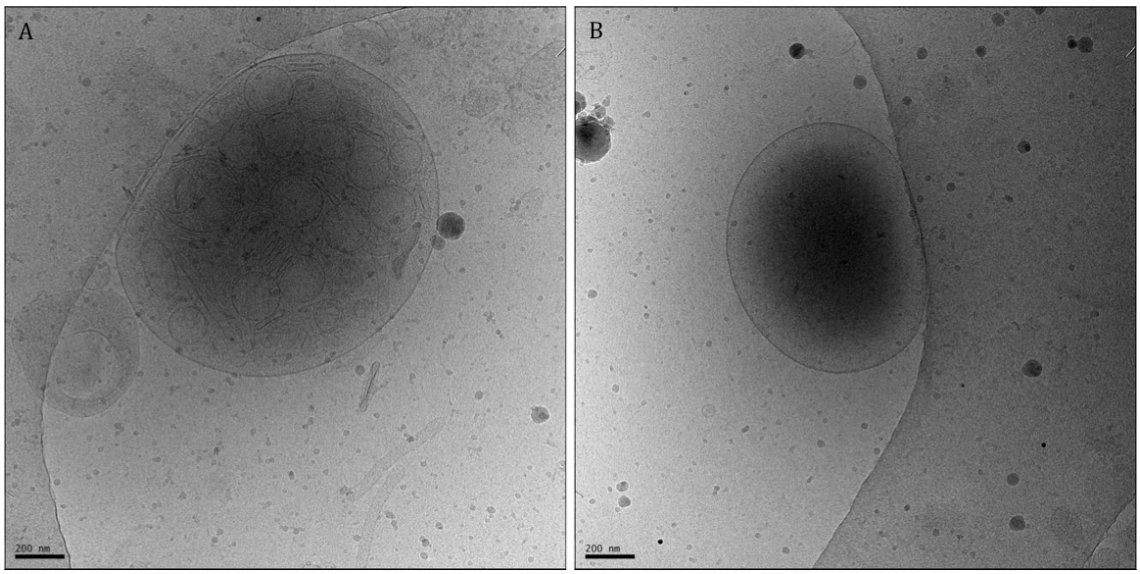

Figure 4-25 Imaging of membranes form CLP of RAW 264.7 cells exposed to 1.2 μM β_2m monomer for 24 h before cell harvesting and processing. A) Multivesicular body B) Lysosome. Scale bar 200 nm.

4.2.4.4 Imaging Optiprep™ fractions in 3D

CLP enriched fraction from RAW 264.7 cells exposed to 1.2 μM β_2m Ls-f for 24 h before cell harvesting and processing was imaged by cryo-ET. ET was performed at Birkbeck College on an FEI Polara microscope equipped with an energy-filtered K2 DED with tilt series collected at ±60°, and processed into tomograms using Imod (Section 2.14.2).

To visualise interactions more clearly (Figure 4-26), tomograms were segmented in a semi-automated fashion using Amira (Section 2.14.3). Tomograms were first filtered (Figure 4-26 B), and then the interactive thresholding tool was used to select density in each 2D Section through the tomogram (Figure 4-26 C). In 2D projection images, features can overlap and interpretation can be impossible, but such difficulties are much reduced in 3D (Figure 4-26 B). To aid interpretation of the 3D volumes, voxels of interest can be assigned as specific materials, such as membranes or amyloid fibrils and displayed separately. In the tomogram in Figure 4-26, voxels were either assigned to membrane (blue) or fibril (green). The β_2m amyloid fibril shown is morphologically consistent with previous reports of fibril dimensions, including a visible twist. The fibril is seen interacting in an end-on fashion with the biological membrane. A reduction in density associated with the membrane is observed at the point where the fibril meets the membrane. Within the membrane, integral membrane proteins are also observed (Figure 4-27).

In 2D, imaging of enriched lysosomal populations from both percoll and Optiprep™ gradients, and imaging of the CLP, revealed membrane compartments containing striated material (Figure 4-12,Figure 4-15). The morphology of these structures does not resemble

any known organelle, and so it was hypothesised that they were a product of cellular homogenisation and/or the centrifugation process. Cryo-ET of these structures revealed that the dimensions of this striated material within these structures is consistent with actin, with a diameter of ~ 7 nm (Figure 4-28). RAW 267.4 cells are a motile cell line that uses actin to generate lamellipodia and other structures during cell motility (S. Müller *et al.*, 2013). A range of crossovers were observed, from ~25 nm to ~35 nm. Actin is commonly observed to have a crossover of (35-38 nm), but actin binding partners such as cofilin are known to shorten the observed crossover length to ~ 27 nm (McGough *et al.*, 1997). The membrane-bound structures therefore could be a product of the homogenisation process, where actin becomes encapsulated within membranes. If this is correct, these artificial structures have not been reported in the literature to our knowledge, but there is a precedent for homogenisation and centrifugation to create non-native structures (e.g. microsomes).

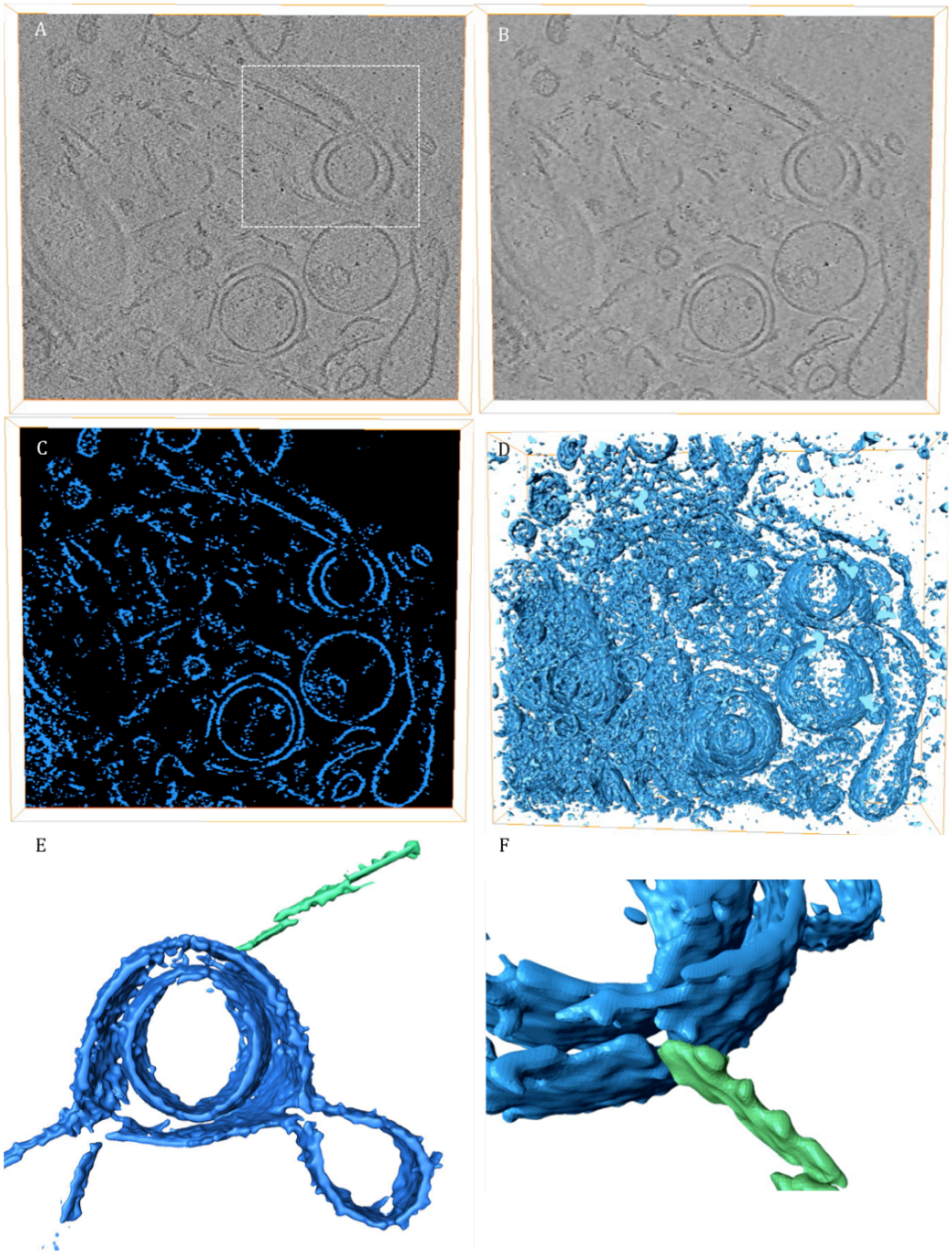

Figure 4-26 Cryo-ET and tomogram segmentation of CLP from RAW 264.7 cells exposed to 1.2 µM monomer equivalent Ls-f β_2m fibrils 24 h before cell harvesting and fractionation. A) Section through the z-stack of a tomogram. Membranes and amyloid fibrils are observed. The same z-stack slice is viewed in B and C. B) Tomogram filtered using X in Amira software to improve SNR and aid segmentation. C) Interactive thresholding tool in Amira was used to identify density in each 2D slice of the z-stack. D) Segmentation can be visualised in 3D. E) Voxels associated with the membrane (blue) and β_2m fibril (green) were selected to aid interpretation of the 3D volume. F) β_2m fibril is visualised directly interacting with the membrane in an end-on fashion. Tomogram segmentation performed in Amira. Movie of segmentation Amira.mpg (Appendix B). Data collected at Birkbeck, London (Section 2.12.1).

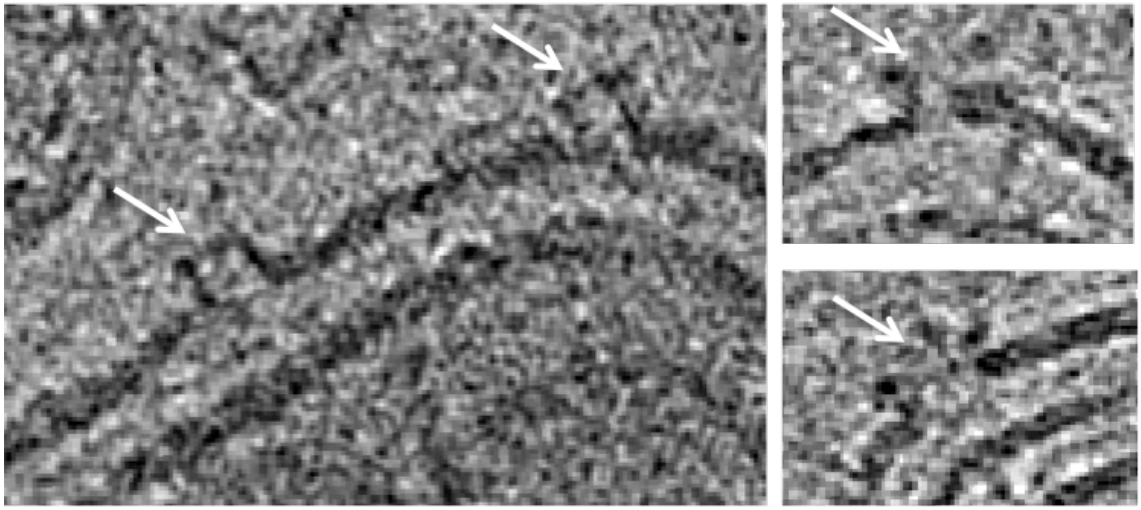

Figure 4-27 Integral membrane proteins observed in tomogram visualised in Figure 4-26. Square shaped membrane proteins indicated by white arrows.

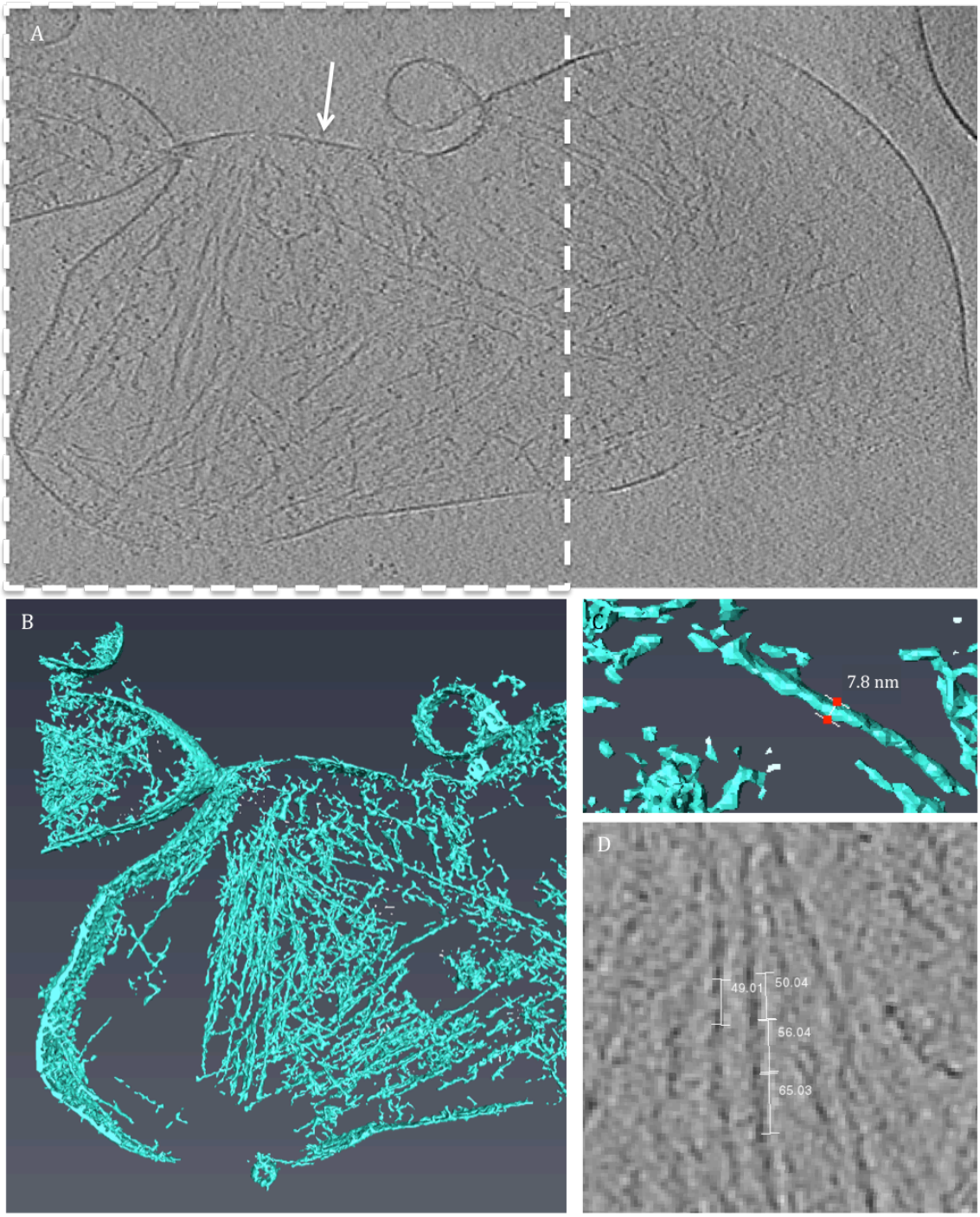

Figure 4-28 Tomogram with actin. Section through the tomogram (A). White arrow delineates the membrane. Dotted white box shows area where volume is segmented, shown in B. Approximate width of filaments (C) and crossover lengths (D). Crossover lengths are shown in pixels, and range from 26 nm to 34.5 nm (0.53 nm/pixel). Data collected at Birkbeck, London (Section 2.12.1).

4.2.5 Methods for investigating amyloid membrane interactions in cells

As discussed above, ball-bearing homogenisation and subcellular fractionation may cause non-native species to form, and existing membrane species to break open or fuse in a non-native manner. As a result, interpretation of images from these fractions must always reflect the fact that the membranes may not be in their native state. As a result, imaging of these interactions inside cells would be preferable. Here two methods to image membranes inside cells are discussed.

4.2.5.1 CLEM

CLEM is a method that combines the benefits of two complementary imaging techniques. A combination of cryo-fluorescence microscopy and cryo-electron microscopy at the thin edge of vitrified cells may be particularly appropriate for imaging in membrane structures. Areas of interest could be fluorescently labelled before cell vitrification, and identified during cryo-fluorescence or confocal microscopy. In the first steps to achieve this, a range of different cell lines, including HeLa, RAW 264.7 and SH-SY5Y have been grown on unmodified, carbon-coated, gold EM grids (Figure 4-29). These live cells can be stained to reveal the location of subcellular structures, such as Hoechst nuclear stain or lysotracker lysosome stain. Cells remain adhered to the carbon surface during staining, and fluorescence is maintained during and after vitrification, as shown by cryo-fluorescence imaging of cells stained with lysotracker red (Figure 4-30). By use of a specialist stage that is fitted onto a confocal microscope, cryogenically-fixed cells can be imaged. Here, a Linkam instruments cryo-stage was used

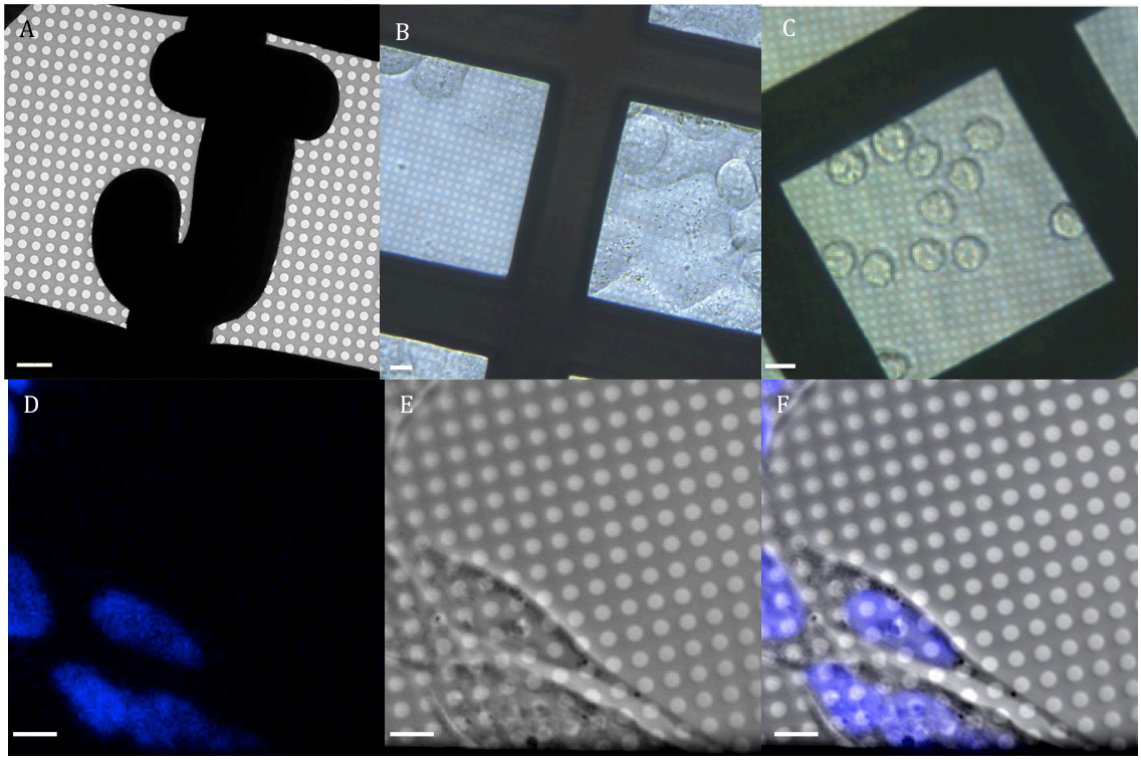

Figure 4-29 A range of cell lines can be grown on electron microscopy grids. A) Gold finder grid R2/2 B) HeLa cells grown on Quantifoil gold, 200 mesh R2/2 grids D) RAW 264.7 cells grown on Quantifoil gold, 200 mesh R2/2 grids. D-F) SH-SY5Y cells grown on Quantifoil gold R2/2 grids and labelled with Hoechst nuclear stain. Hoechst fluorescence (D), brightfield (E) and merge (F) images shown. Scale bar A-C, 10 µm. Scale bar D-F, 6 µm.

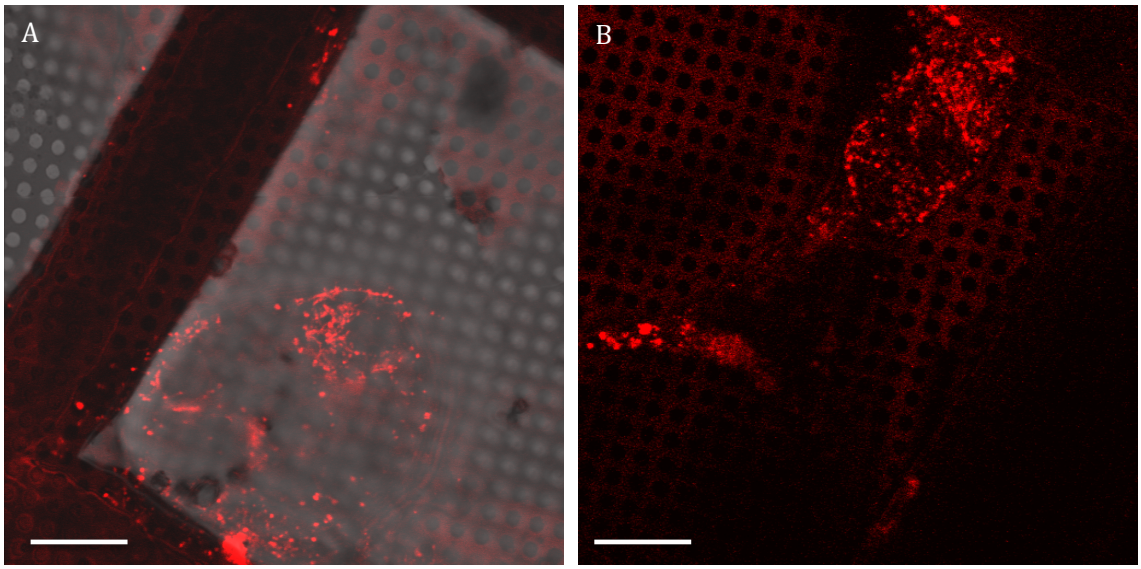

Figure 4-30 Cryo-confocal microscopy of RAW 264.7 cells labelled with lysotracker red. A) Merge of RAW 264.7 cells imaged by brightfield and lysotracker red fluorescence channel. B) RAW 264.7 cells stained with lysotracker red. Scale bar 10 µm.

Cryo-fluorescence microscopy enables an area of interest to be identified, for example a lysosome at the cell periphery. With great care to maintain grid integrity and low temperature, it can then be transferred into the EM. Many cells, including RAW 264.7 cells, adopt a 'fried egg' shape, where the nuclear region is thick, and so prevents electrons from fully penetrating (Figure 4-31). Towards the cell periphery, the cell is much thinner. Imaging cells in 2D enables the plasma membrane to be identified, along with some internal vesicles. However, because 2D images are a projection of the whole contents of the cell, they can be difficult to interpret and obviously do not provide any 3D information. Cryo-electron tomography can be used to generate this third dimension, and using this approach, details such as cytoskeleton and membranes can be visualised. Figure 4-32 shows a section through a tomogram of SH-SY5Y cell line, in which a microtubule and the double membrane and cristae of a mitochondria are resolved.

This type of CLEM at the edge of a cell is technically challenging. During the transfer of the grids between the imaging systems, damage and contamination may occur, and navigation back to the area imaged in the first imaging modality is a challenge. Theoretically, accuracy of navigation by using grid letters on finder grids to locate the square of interest, and the regular pattern of holes on a quanitfoil grid can be used to navigate to a region with better than 2 μm accuracy, but this represents a formidable technical challenge. Due to the time consuming nature of performing imaging in each mode, and the time taken to transfer specimen between microscopes and perform correlations, CLEM of this nature is a very low throughput imaging technique.

This work demonstrates that cryo-ET is a powerful approach to examine amyloid-membrane interactions at nm scale resolution, in a cellular setting. Fluorescently labelled amyloid fibrils, with complementary labelling of lysosomal compartments with lysotracker, would enable areas of interest to be identified using cryo-confocal imaging, and then re-imaged using cryo-ET, and would be able to answer question including the nature of any amyloid-membrane interactions in a cellular setting, if fibrils remain encased within the membrane, and possibly information about the structure amyloid fibrils adopt upon internalisation.

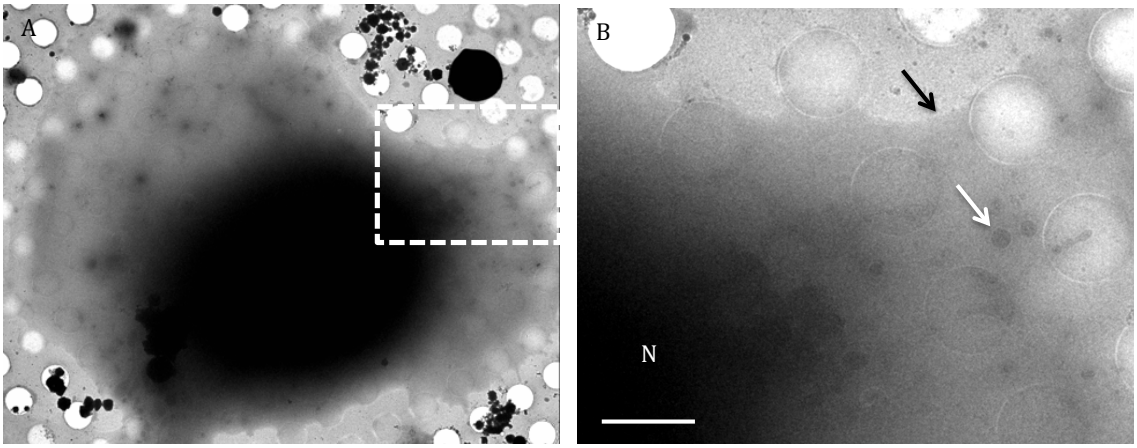

Figure 4-31 Cryo-EM of RAW 264.7 cell (A). Cell adopts 'fried egg' shape, where thick nuclear region of the cell is too thick for electrons to penetrate, while cytoplasm extends outwards. White box indicates area shown at increased magnification in B. Plasma membrane indicated by black arrow, internal vesicles indicated by white arrow and nulceus/thick perinuclear region by N. Scale bar 2 μm.

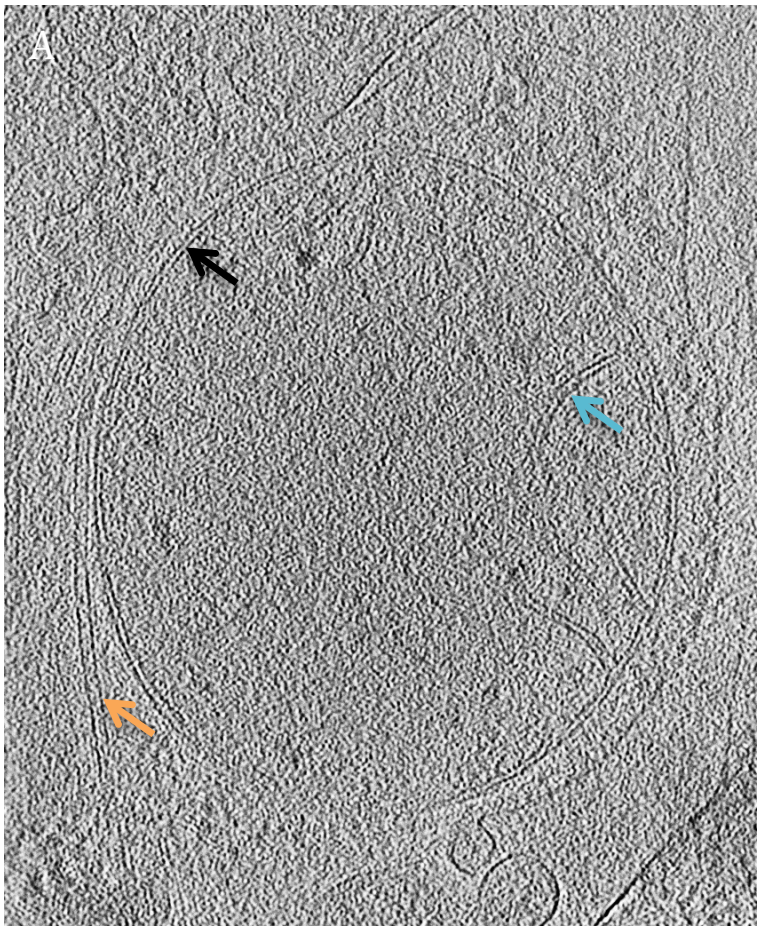

Figure 4-32 Cryo-electron tomography of a whole, vitrified SH-SY5Y neuroblastoma cell line. Mitochondrion is shown, with the double membrane (black arrow) and cristae (blue arrow) clearly visible. A microtubule can also be seen (orange arrow). Full tomogram movie can be seen in Full tomogram cell.mov, Appendix B.

4.2.5.2 Soft X-ray microscopy

While cryo-ET can provide high-resolution (better than 10 nm) information, at the magnification used to achieve these resolutions, the field of view is limited. Additionally, the nuclear and perinuclear regions of eukaryotic cells are too thick for electrons pass through, and so are not suitable for cryo-ET. Cryo-XM is an alternative imaging technique that may be useful for investigating gross changes to membranes in cells upon exposure to amyloid fibrils.

The B24 beamline facility at Diamond Light Source was used to collect cryo-XM data (Section 2.13), where collection of a tilt series takes 24 h, and resolutions of better than 70 nm can be achieved. Sufficient time was available to collect a single tilt series and some 2D images, as a proof of principle. RAW 264.7 cells were exposed to Ls-f fibrils for 24 h before vitrification. 2D imaging of the cells shows they adopt the same 'fried egg' morphology that was observed in cryo-EM, but X-rays at these wavelengths can pass through the cell, allowing visualisation of nuclear and perinuclear regions (Figure 4-33). An interesting feature of these cells are large, lucent structures, which have been previously identified as endosomes by correlative fluorescence and cryo-XM (Duke *et al*., 2014). In the cryo-XM tomogram, the nuclear envelope, and several lucent structures were identified. Unfortunately, we were unable to collect images of cells not exposed to amyloid fibrils, and therefore cannot say if these unusual lucent structures form as a result of exposure to amyloid fibrils, or if they are simply a feature of this cell line. These images do, however, suggest that cryo-XM may be a powerful and useful tool for assessing gross cellular response to amyloid fibrils.

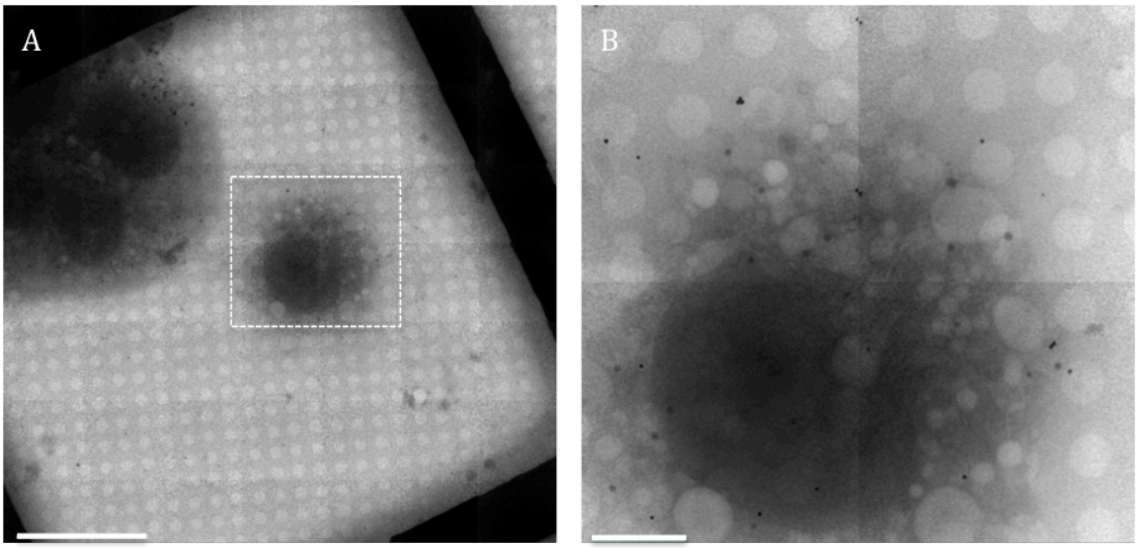

Figure 4-33 Soft X-ray microscopy of RAW 264.7 cells exposed to Ls-f fibrils for 24 h. View of a grid square (A), white dashed box is seen at higher magnification in B. Scale bar A- 25 μm B- 5 μm.

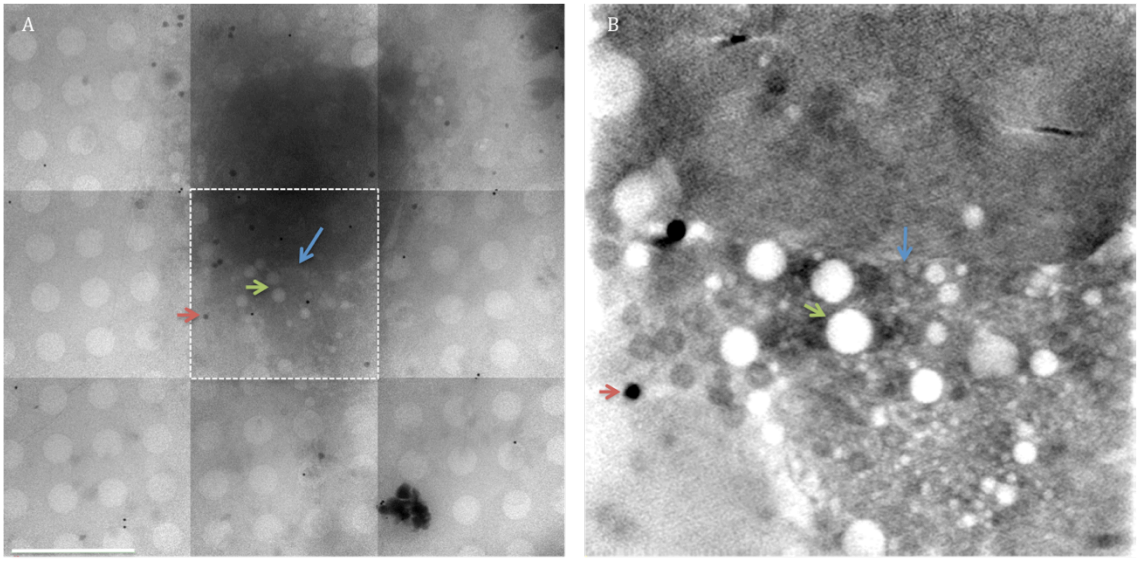

Figure 4-34 Soft X-ray tomography of RAW 264.7 cell exposed to Ls-f β_2m fibrils for 24 h. 2D image of cell (A), white dashed box is area where tomogram was performed. Section through tomogram is shown in B (Full tomogram 'X-ray.mov', Appendix B) Features of interest are indicated, including fiducial marker (red arrow), nuclear envelope (blue arrow) and lucent structures (green arrow). Scale bar A, 10 μm.

4.3 Discussion

While the link between amyloid deposition and disease has been known for many years, the mechanisms of cytotoxicity remain unclear (Knowles *et al.*, 2014). Accumulating evidence suggests that amyloid fibrils, alongside oligomeric species, exert toxic cellular effects (Gharibyan *et al.*, 2007; Anderluh *et al.*, 2005; Mossuto *et al.*, 2011; Novitskaya *et al.*, 2006). The experiments described in Chapters three and four have probed the interactions between amyloid fibrils and membranes of various compositions.

4.3.1 Intracellular trafficking of β_2m amyloid fibrils

Amyloid species formed from a variety of different precursor proteins applied to cells exogenously can gain access to endocytic compartments (4.1.2). In a disease context, many amyloid aggregates form in the extracellular environment, including Aβ, IAPP and β2m. Disease-associated amyloid proteins that form intracellular inclusions *in vivo,* such as α-synuclein, may also become internalised, altering disease progression. α-synuclein is thought to be secreted into cerebrospinal fluid where it may aggregate prior to internalisation (Borghi *et al.*, 2000). Intracellular α-synuclein amyloid aggregates may also access the extracellular environment during neuronal cell death, where membranes become destabilised and cytosolic components leak from the cell. At this point, neighbouring cells may internalise these amyloid aggregates, allowing access to endocytic compartments (Mougenot *et al.*, 2011; Angot *et al.*, 2010; Visanji *et al.*, 2013).

With amyloid aggregates formed outside the cell (Aβ, IAPP and β_2m) and those formed inside but can escape to the extracellular environment (α-synuclein), endocytosis can lead to amyloid accumulating in the lysosome. Much evidence points towards lysosomal dysfunction in amyloid disease (Section 4.1.2.4). In this Chapter, it has been demonstrated that β2m Ls-f species are endocytosed and trafficked to lysosomes, where they retain a NIAD-4 binding state for at least 24 h, indicating retention of at least elements of amyloid structure (Section 4.2.1).

An interesting aspect of intracellular trafficking that may play a role in the transmission of toxic amyloid species *in vivo* are exosomes (Bellingham *et al*., 2012). Exosomes are formed upon the exocytosis of late endosomes (also known as multivesicular bodies) that contain small (< 100 nm) intraluminal vesicles, which can contain protein and nucleic acid cargo. Upon exocytosis, these intraluminal vesicles are known as exosomes. Aβ-containing exosomes may fuse with the plasma membranes of recipient cells, causing the release of potentially toxic cargo into the cytoplasm (Bellingham *et al*., 2012). Aβ-containing exosomes may also play a role in plaque formation, exosomal proteins including Alix and Flotillin-1 have been found in plaques isolated from the brains of AD patients, suggesting exosomes may traffic Aβ (Rajendran *et al*., 2006). As β_2m fibrils are known to be trafficked along the endocytic pathway, it may be interesting to investigate the potential role of exosomes in trafficking of β_2m amyloid species.

4.3.2 Different membrane species enriched by percoll and Optiprep™ gradients

Here, subcellular fractionation of homogenised RAW 264.7 on percoll and Optiprep™ gradients was performed. Biochemical assays (both enzyme assays and immunoblotting), enabled fractions to be identified as enriched for lysosomes, and depleted in other cellular membranes. Interestingly, cryo-EM of these enriched lysosomal fractions from different gradient systems showed differences in the morphology of species present. Enriched lysosomal fractions from a percoll gradient possessed many multilamellar species, and membranes containing granular material, which were absent from equivalent fractions from an Optiprep™ gradient, or the CLP. One challenge with subcellular fractionation is that biochemical assessment of membrane preparations only gives a global indication of the cellular markers present. Even where high levels of enrichment in a particular membrane are seen, unambiguous identification of a particular structure as a particular organelle can be impossible by cryo-EM, unless a distinctive morphology is observed (as for mitochondria). Lysosomes are traditionally defined functionally, can exhibit a broad range of morphologies, and are potentially difficult to separate from other membranes in the endocytic pathway such as early endosomes and multivesicular bodies (late

endosomes). Here, relatively few cellular markers were used to characterise membrane separation on gradients. Differences in the membranes isolated from the two gradient systems could be due to the range of organelle morphologies present in the cell displaying different buoyancies in percoll and Optiprep™, leading to poor separation. Given that lysosomes sediment towards the bottom of percoll gradients, and towards the top of Optiprep™ gradients, it is likely that this rationalises at least some of the differences seen between the two gradient systems. As a subset of morphologies are conserved in the enriched lysosomal fraction from both gradient systems, this increases confidence that the qualitatively assessed most commonly observed species in both gradients, single membrane bound organelles with dark interior, are lysosomal species.

4.3.3 Creation of non-native membranes through homogenisation and centrifugation

As discussed in Section 4.2.4.4, some structures observed by cryo-ET do not conform to known cellular organelle morphologies. It is known that ball bearing cell homogenisation, as well as centrifugation, can cause organelles such as the ER to undergo vesiculation into non-native structures. The membrane leaflet of the resulting microsomes may be orientated the same as in the cellular environment, be inside out, or a chimera of different membranes (Stillwell, 2013). Here, membrane-bound structures that most likely contain actin may be a product of homogenising cells that contain an extensive network of cytoskeletal actin filaments. The identity of the striated cargo could be made as fractions were imaged using cryo-EM, which provided sufficient resolution to characterise the cargo. This is the first time structures such as these have been described. Biochemical characterisation of the gradient would not have revealed the identity of these non-native structures, illustrating the power of using cryo-EM to characterise subcellular fractions. Additionally, this shows clearly that great care should be taken when performing cell homogenisation and subcellular fractionation to minimise the formation of non-native species, although it is likely that procedures to disrupt cells will result in some non-native structures forming. Cryo-EM can be a valuable tool for assessing the morphology of species present in sub-cellular fractions.

4.3.4 Propensity of amyloid fibrils to disrupt synthetic vs biological membranes

In Chapter three, the liposome dye release assay was used to assess the propensity of β_2m amyloid fibrils to disrupt synthetic liposomes. This revealed that LUVs formed from lipids more accurately reflecting average biological membranes are not perturbed by β_2m amyloid fibrils, while synthetic LUVs enriched in BMP are highly susceptible to perturbation under the same conditions. In this Chapter, biochemical assays to detect the

location of soluble lysosomal proteins, alongside visualisation of fibril interactions with biological membranes showed that fibrils interact with biological membranes. Both end-on and side-on interactions were observed, as previously described for synthetic liposomes (Milanesi *et al.*, 2012). These observations could help rationalise discrepancies between liposome dye release data and cell-based experiments using β_2m fibrils. *In vitro* liposome dye release assays performed in Chapter three demonstrate that β_2m fibrils perturb synthetic LUVs enriched in the anionic lipid BMP under acidic conditions, reflecting conditions found in late endosomes and lysosomes of cells. However, in cell-based assays on SH-SY5Y cells treated with β_2m fibrils, no detectable increases in lysosomal membrane permeability were seen, indicating gross membrane perturbation is not occurring (Jakhria *et al.*, 2014). These results demonstrate that extreme caution should be applied, both in choosing an appropriate model lipid system to study amyloid-lipid interactions, and in interpreting these results in a cellular context.

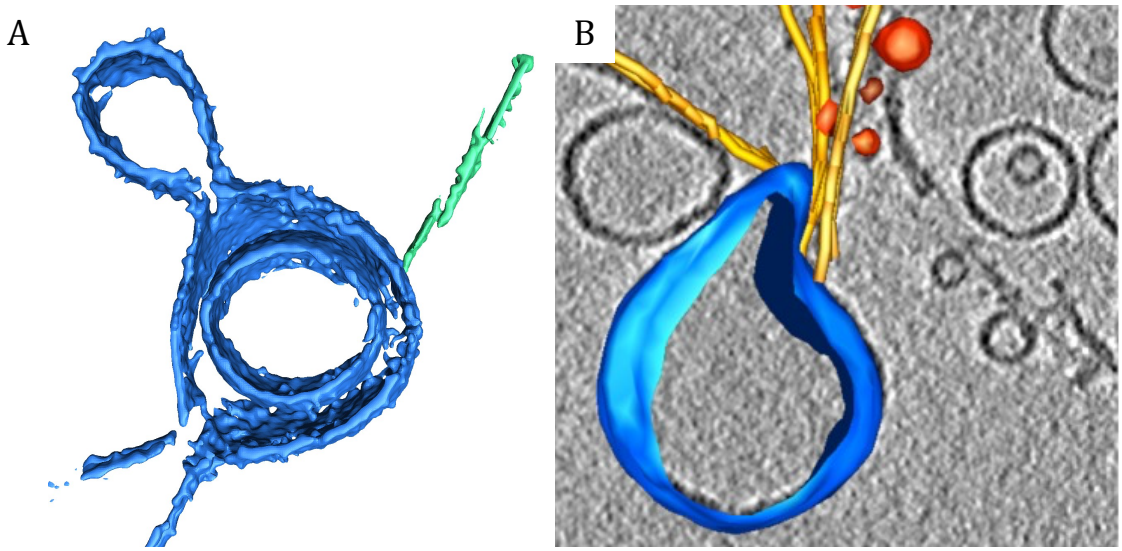

Figure 4-35 β_2m Ls-f amyloid fibrils interacting with membranes. A) Biological lipid from CLP (blue) interacting with β_2m Ls-f fibril (green) fromFigure 4-26. B) 4:1 mol ration PC:PG LUV (blue) interacting with yellow β_2m Ls-f fibril. Adapted from Milanesi *et al.*, 2012.

4.3.5 Summary and future perspectives

In summary, work in Chapters three and four demonstrates that the interactions between β_2m amyloid fibrils and synthetic liposomes or biological membranes are profoundly different. Biological membranes appear to be more resistant to perturbation by β_2m amyloid fibrils than their synthetic membrane counterparts. These findings rationalise previous studies which have found that synthetic LUVs resembling lysosomal membranes are perturbed by Ls-f β_2m fibrils, while no disruption of lysosomal membranes is detected in cells (Goodchild *et al*., 2014; Jakhria *et al*., 2014).

Over the period of this project, imaging technologies have developed rapidly. This chapter describes progress towards understanding the nature of amyloid fibril-biological membrane interactions, but this does not y*et al*low us to draw extensive conclusions about their behaviour in cells. However, the new technologies described above, such as CLEM, cryo-ET at the thin edge of cells, and cryo-XM, would be powerful tools to investigate the nature of membrane-fibril interactions inside cells (Section 4.2.5). Fluorescent co-labelling of lysosomal compartments and amyloid fibrils would enable lysosomes containing material of interest to be identified unambiguously, and in a cellular setting. Beyond imaging the thin edge of the cell, FIB milling could be used to generate a thin section through a vitrified cell for cryo-ET, allowing 3D structure determination in the nuclear and perinuclear regions. Future work seems almost certain to make use of these emerging imaging technologies to offer exciting opportunities to extend the work carried out in this thesis.

5 Structural properties of the *Leviviridae*

5.1 Introduction

Viruses are fascinating, dynamic, metastable macromolecular assemblies, which are minimally comprised of a protective capsid made from proteins, and the nucleic acid that constitutes their genome. Some viruses also encompass a lipid bilayer envelope. EM has greatly contributed to the field of virology, and equally viruses as test subjects have contributed to the development of EM.

EM has long been used for imaging viruses. EM was used to image Tobacco mosaic virus as early as 1939 (Kausche *et al*., 1939), and in 1948 it was used to differentiate between smallpox and chickenpox infections (Nagler & Rake, 1948). Even today where molecular diagnostics tools can detect pathogens during viral outbreaks, EM is still widely used for viral diagnostics, especially for emerging viral pathogens, suspected bioterrorism, or where biological information may be lacking (Goldsmith & Miller, 2009). Although it is not a high-throughput technique, EM can rapidly offer morphological information on a virus, and a preliminary diagnosis (Hazelton & Gelderblom, 2003). Negative staining was introduced in the 1950's, and viruses were amongst the first samples imaged (Brenner & Horne, 1959; Hall, 1955). By enabling their direct visualisation, EM has provided morphological information that can be used to elucidate evolutionary viral relationships, and then used for classification purposes. While even low-resolution structural information can be sufficient for gross morphological characterisation, the introduction of averaging techniques and cryo-EM now provides 3D structural information and increased resolution (Adrian *et al*., 1984; Crowther *et al*., 1970). The first 3D reconstruction of a virus was carried out in 1968 in pioneering work by David de Rosier and Aaron Klug, and in subsequent years a great many 3D structure of viruses have been determined by EM (Haguenau *et al*., 2003). While this has provided valuable biological insight, historically the resolution of EM structures was poor (typically ~10 Å) compared with X-ray crystallographic structures (routinely > 3 Å). However, in recent years technical advances in microscope and detector hardware, and in image processing, have to lead to what some have termed the 'resolution revolution' (Section 1.6) (Kuehlbrandt, 2014). For viruses with ordered, symmetric capsids, it is now relatively common to obtain < 5 Å structures.

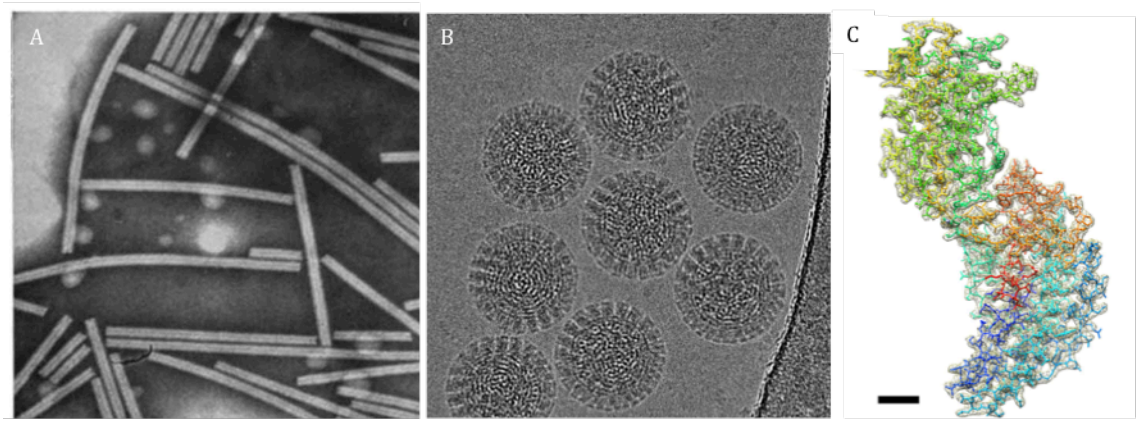

Figure 5-1 History of virus structure determination by EM. Early example of negative staining (A) TMV embedded in phosphotungstic acid, adapted from (Brenner & Horne, 1959). 3D reconstruction of rotavirus (shown in B) VP6 to 2.6 Å, with the docked atomic model (C). B,C adapted from Grant & Grigorieff, 2015.

5.1.1 The life of an obligate, intracellular parasite

Viruses survive and replicate by subverting their host cells' machinery to produce new viral particles that are capable of infecting another host cell. Viruses are ubiquitous, infecting all Kingdoms of life. Metagenomic analysis of environments from pristine artic lakes, to fecal samples and sewage shows that many viruses persist in an extracellular environment, and there are likely a vast number of uncharacterised viruses (Cantalupo *et al.*, 2011). The study of viruses is important for human health, and because of their impacts on animal and plant health, which have huge in implications for food security and the agriculture economy.

5.1.2 Virus classification

The most common scheme for virus classification is from the International Committee on Taxonomy of Viruses (ICTV), which uses genome sequence, biochemistry, structural biology and host to classify viruses. ICTV defines orders, families, subfamilies, genra and species. Order principally describes the genome type and particle morphology. Nucleic acid sequence is generally only useful within families due to high rates of genome change. Virus evolution at both the protein or nucleic acid sequence level may be very high; especially within viruses with RNA genomes, as RNA polymerases lack proofreading mechanisms (Holmes, 2003).

Schemes for classification have also been suggested that are based on the structure of the capsid used to package the genome. The rationale is that as there is a high level of redundancy in sequence-structure space, it is the structure of the capsid that is the most persistent feature of a particular virus. The authors claim to identify more distant evolutionary relationships than is possible via sequence-based methods alone. Using this

approach, four major evolutionary lineages were defined; Blue Tongue Virus-like, PRD1 or adenovirus like, HK97-like, and Picorna-like lineages (Butcher *et al*., 2011; Abrescia *et al*., 2012).

5.1.3 Virus morphology

A range of viral morphologies exist, broadly split into isometric or spherical, such as Poliovirus; filamentous or rod-shaped such as tobacco mosaic virus; or pleomorphic such as HIV and influenza. The protein assemblies of each morphology protect the genome, and are composed from multiple copies of a single, or small number of different, protein subunits. This is an elegant solution to the problem of 'genetic economy' that faces most viruses. A single (or small number of) protein(s), that has the capacity to self-interact means that large, highly symmetric capsids can be built from a simple building block. Utilisation of symmetry means that only a few simple, local rules of association are required, and these can be encoded in a single protein. The icosahedron has the highest closed point group symmetry of all shapes, allowing the highest internal volume for a given subunit size (Figure 5.2).

Only a small number of protein folds are currently known to form viral capsids. This includes the jelly-roll β barrel (e.g. tomato bushy stunt virus (TBSV)) and the four-helix bundle (e.g. tobacco mosaic virus) (Chapman & Liljas, 2003). These units can interact to self-assemble into symmetrical structures based on the structural and energetic complementarity of their surfaces. The most common fold found in virus capsid is the β-sandwich fold (Harrison *et al*., 1978). At the core of this fold are eight antiparallel β-strands, arranged into two sheets that associate via hydrophobic residues to form the barrel. Outside of this core region, N- and C-termini and loop regions between the β-strands are highly variable from virus to virus, but often have specific functional roles (Liljas, 2004). Because of sequence-structure redundancy, two viruses that have high levels of structural homology, may be not appear to be related at the sequence level, highlighting the need for structural studies on viruses.

Around half of characterised virus families have capsids with icosahedral symmetry (Zlotnick *et al*., 2000). Icosahedrons can be simply built from protein subunits if three identical subunits are placed in symmetry-related positions in each triangular face. They are thus minimally composed of 60 equivalent (or asymmetric) units, with 5:3:2 symmetry. The simplest viruses follow precisely this arrangement, such as seen in the X-ray crystallography structure of satellite tobacco necrosis virus (Larson *et al*., 1998).

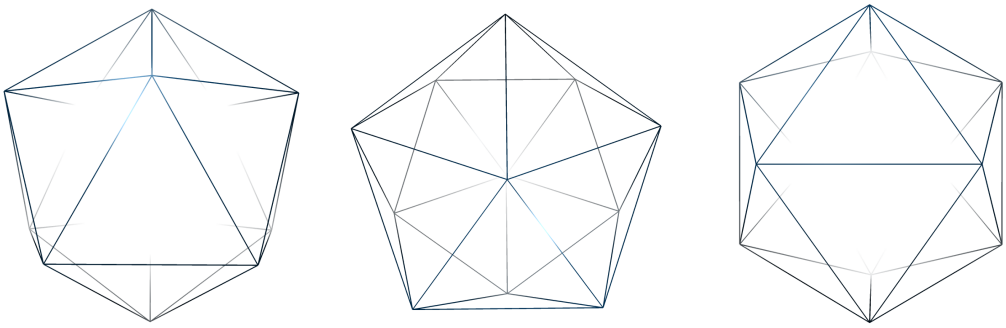

3-fold 5-fold 2-fold

Figure 5-2 Schematic of a platonic icosohedron. An icosohedron has 20 identical triangular faces, 12 vertices and 30 edges. The resulting particle has 12 x 5-fold symmetric vertices.

However, a strict icosohedral arrangement imposes severe constraints on the size of the viral genome that can be encapsidated. To create larger capsids by encoding more coat protein subunits is not a feasible solution, as the genome increases in size more quickly than the encoded protein, owing to the triplet genetic code and the size of individual bases in nucleic acid. However, many viruses have hit upon quasi-equivalence to solve this problem.

An icosohedron is constrained by its overall geometry, but more than 60 subunits can be incorporated. We can understand how different numbers of subunits give rise to differently-sized icosahedrons using the concept of triangulation. An icosohedron has 12 vertices with 5-fold rotational symmetry, necessary to form a closed structure. To increase the icosohedron's size, the number of units in each triangular face can be increased. This controls the spacing between the 5-fold vertices and therefore the size of the capsid. This can be described by;

$$T = \mathrm{h}^2 + \mathrm{hk} + \mathrm{k}^2$$

Where T is the triangulation number. It describes the distance along a hexagonal net between 5 fold vertices. In a T = 1 capsid, pentamers are immediately adjacent to each another. For T = 3, the triangular faces of the icosahedron are constructed from larger triangles which themselves constructed from equilateral triangles, meaning hexamers with quasi-6-fold symmetry separate the 5-fold vertices. The T number, as calculated using the equation above, is a useful means of characterising features of an icosahedral virus assembly.

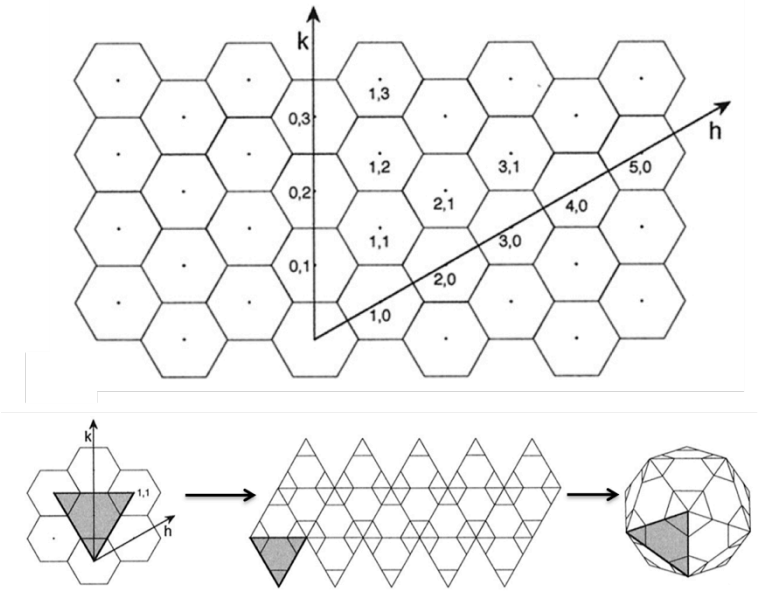

Figure 5-3 Formation of a *T*=3 (h,k=1,1) icosohedron from a hexagonal lattice. A hexagonal lattice (top) has two vectors termed h and k separated by 60° from an arbitrary origin. An equilateral triangle is defined in grey on the hexagonal lattice with one of its vertices at the point of origin of one of the vectors. This initial triangle placement seeds how the next 19 triangles lie. This triangular pattern can then be folded to form the icosohedron. Adapted from Baker *et al*., 1999.

The ability of viral coat proteins to adopt quasi-equivalent positions in a lattice that tessellates the surface of a spherical capsid is fundamental to the diversity of size and architectures found in the virosphere. Subtle differences in bonding between the capsid subunits allow triangulation to occur. Conformational switching determines the role each subunit plays within the lattice. In *T*=3 viruses, flexible loop regions may control interactions between quasi-equivalent subunits. For example, the N-terminal arms of TBSV are either ordered or disordered, defining the nature of subunit interactions (Harrison *et al*., 1978).

5.1.4 Bacteriophages

Bacteriophages are viruses that infect bacteria or archaea, and their study has played a major role in expanding our knowledge of basic molecular biology and virology (Friedman *et al*., 2012). Bacteriophages are classified into 19 families, with all genome types represented (Ackermann, 2009). Tailed dsDNA viruses represent ~ 96 % of known phages, with the remaining 4% consisting of a range of viruses such as the ssDNA *Microviridae* and ssRNA viruses such as *Leviviridae* (Fokine & Rossmann, 2014). They may be as much as 10x more abundant than bacterial cells, and so are easily the most abundant entities in the biosphere (Fokine & Rossmann, 2014).

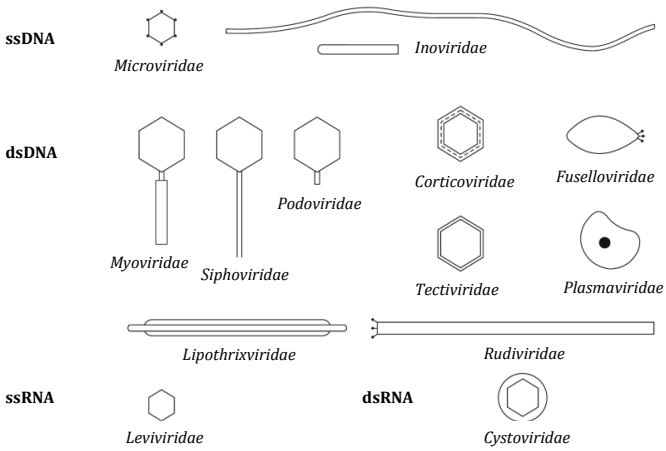

Figure 5-4 Genomic and structural diversity of the bacteriophages. Adapted from Ackermann, 2009.

Bacteriophages have several commercial uses, such as phage display which is used to study protein interactions (Sidhu *et al*., 2000). In the food industry, LMP-102 (Intralytix) is an FDA approved cocktail of bacteriophages designed to prevent *Listeria* contamination in meat products (Sulakvelidze, 2013). For *in vitro* diagnostics, KeyPath MRSA/MSSA Blood Culture Test detects *Staphylococcus aureus* using bacteriophages, and determines antibiotic resistance or susceptibility (Sullivan *et al*., 2013). Bacteriophages may also have potential use as therapeutics, particularly where antibiotic resistance has arisen. In one study, bacteriophage therapy was effective in the treatment of antibiotic-resistant *Pseudomonas aeruginosa* (Wright *et al*., 2009), although no treatments are currently approved for use.

5.1.5 Leviviridae

Originally isolated from the New York sewerage system, the *Leviviridae* are icosahedral, non-enveloped ssRNA(+) viruses comprising of two genera, Allolevivirus and Levivirus, of which the best characterised are Qβ and MS2 respectively (Bollback & Huelsenbeck, 2001). 'Levi' is translated as 'light' as these viruses have very small genome sizes. The two genera are divided on serological properties and genome organisation. The genome of Leviviruses is smaller than Allolevivirus, ~3500 nucleotides vs ~4200 respectivley (Olsthoorn & Duin, 2011). The *Leviviridae* specifically infect host bacteria via their pili, including F-pili expressing members of the Enterobacteria, and polar pili expressing *Caulobacter* and *Pseudomonas*. As a result the *Leviviridae* are sometimes described as plasmid-specific coliphages (Ackermann, 2009). Enterobacteria including *Shigella*, *Proteus* and *Salmonella*, can be rendered sensitive to coliphages by expression of F^+, F' or HFr pili (Olsthoorn & Duin, 2011). *Leviviridae* are typically present at extremely high titres in faeces (10^2-10^7 plaque forming units per ml)(Long *et al*., 2005). Members of the *Leviviridae* are being identified on an on-going basis from metagenomic sequencing,

for example recently from the San Francisco wastewater system (Greninger & DeRisi, 2015).

The *Leviviridae* have a long history as model systems for the study of ssRNA viruses, one of the largest classes of viral pathogens. Positive sense ssRNA viruses infect all kingdoms of life, and include pathogens in the *Picornaviridae, Flaviviridae* and *Togaviridae* families that each contain viruses that have major impacts on human health. RNA phages have the same morphology and chemical properties as many of these (Duin, 2006). The *Leviviridae* can be safely and easily grown, allowing their structural and functional states to be studied. While there has been some interest in bacteriophages as therapeutics, it is unlikely coliphages will be effective as bacteria adapt by loosing their pili (Duin, 2006).

Host	Genus	Species	Example members	Sequence
Escherichia	Levivirus	I	**MS2** Fr	Fully sequenced Fully sequenced
		II	**GA** JP34	Fully sequenced Partially sequenced
	Allolevivirus	III	**Qβ** M11	Fully sequenced Fully sequenced
		IV	**SP** NL95	Fully sequenced Fully sequenced
Acinetobacter	Levivirus (AP205)	Unknown	AP205	Fully sequenced
Caulobacter	Unknown	Unknown	ØCb5	None
Pseudomonas	Levivirus (PP7)	Unknown	PP7	Fully sequenced
Polyvalent	Unknown	Unknown	PRR1	None

Table 5.1 Example members of the *Leviviridae* family. Adapted from Olsthoorn & Duin, 2011. Best characterised members shown in bold. Group I and II viruses are sometimes grouped into group A and III and IV into group B.

5.1.5.1 Genome

MS2 was the first genome of an organism to be fully sequenced at 3569 nucleotides (Fiers *et al*., 1976). Biochemical experiments indicate that the genomes of the *Leviviridae* have extensive secondary structure, which is implicated in the regulation of the expression of viral proteins. The 5' and 3' ends of the genome have untranslated regions which form ~ 10 % of the genome. All known ssRNA phages start with 5' pppGG and end with CCA_{OH}, where the terminal A is a non-coded base added by the terminating replicase (Duin, 2006). The four bases occur at roughly equal ratios in the *Leviviridae* (Duin, 2006). Alloleviviruses and Leviviruses each have coat protein, maturation protein and subunit II of replicase, but Alloleviviruses' genome is ~700 nucleotides longer and has a read-through frame, while Leviviruses have a separate lysis gene, an out-of-frame overlapping gene encoding a ~70 amino acid hydrophobic peptide (Figure 5-5). In Alloleviviruses, the

maturation protein is thought to trigger cell lysis (Duin, 2006). In Alloleviviruses the coat protein ends in a leaky stop codon (UGA) that is read as a tryptophan with a probability of 5 %, creating a C-terminal extended coat protein, sometimes termed A1. The extended coat protein is required for infectivity, and a crystal structure is available for this protein (Figure 5-8)(Rumnieks & Tars, 2014).

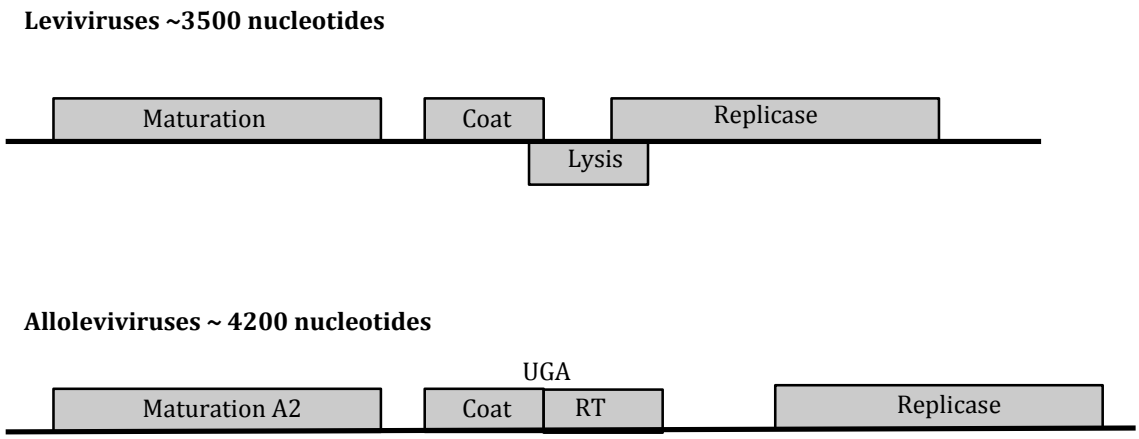

Figure 5-5 Genome structure of Alloleviviruses and Leviviruses. Adapted from Duin, 2006.

Genome replication is inaccurate, but despite this, there is little evidence for rapid evolution or sequence drift in *Leviviridae*. Despite many years of cultivation in the lab, Qβ and MS2 sequences have not changed significantly. In nature, phage sequences have not diverged substantially from the subgroup prototype. For example, group I MS2, f2, R17, M12 and JP501, isolated from across the globe show more than 95% sequence identity, indicating there must be strong selective pressure limiting drift rate (Friedman *et al*., 2009).

5.1.6 Leviviridae *lifecycle*

Leviviridae infect bacteria by introducing a maturation protein (MP)-genome complex into the host cell cytoplasm. *Leviviridae* attach to pili or filaments, depending on their host, and use this to gain entry to the cell. F-pili are used by bacteria such as *E.coli* to aid bacterial conjugation, and are involved in horizontal gene transfer between F-plasmid carrying bacteria, and F^- bacteria. The F-pili is a retractable structure, formed from subunits of a 70 amino acid Pilin protein. Pili are 85-95 Å in diameter, with a 20-30 Å wide lumen (Wang *et al*., 2009). F-pili can extend from a cell at a rate of 40 nm/sec, allowing a pilus >10 μm long to be assembled in < 5 minutes (Clarke *et al*., 2008). The trigger for pili retraction is unknown, but once started continues until its full length is withdrawn, rotating as it is withdrawn presumably owing to the helical symmetry of the pilus as it is disassembled (Clarke *et al*., 2008). Heavy decoration of the pili with bacteriophage such as R17 seems to

slow retraction (Clarke *et al*., 2008). Multiple F-pili can be present on a single cell, with extension and retraction of these independent from each other. The attachment of the phage to the sides of the pili requires the maturation protein (Dent *et al*., 2013). The coat protein is not needed for pili adhesion, but in Alloleviviruses the minimal infection set does requires the additional presence of the coat read-through protein (Olsthoorn & Duin, 2011).

Phage binding to the pilus results in cleavage of its MP into two fragments (Krahn *et al*., 1972). It is hypothesised this cleavage triggers the ordered ejection of the RNA from the virus capsid. The two MP fragments remain associated with the genome during penetration of the cell envelope, but it is unlikely they play any further role in infection, as naked RNA in a spheroplast can generate infectious progeny (Olsthoorn & Duin, 2011).

The positive sense, ssRNA genome that enters the cell acts directly as the message for viral protein synthesis, including the viral replicase. The replicase holoenzyme contains four different proteins (Olsthoorn & Duin, 2011), three of which are host proteins that are recruited to allow RNA synthesis. Subunit I is ribosomal protein S1, and subunits III and IV are the translation elongation factors EF-Tu and EF-Ts respectively (Olsthoorn & Duin, 2011). The virally encoded subunit II has RNA polymerisation activity. To copy the negative strand, only subunits II, III and IV are required, whereas copying the positive strand also needs subunit I.

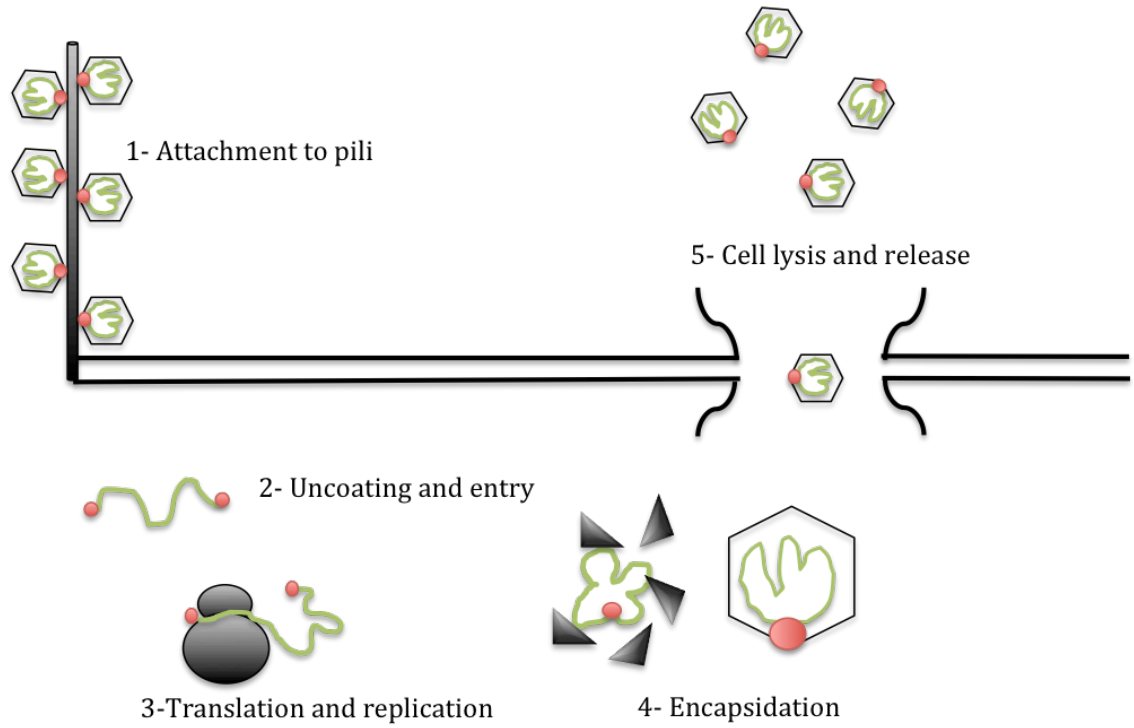

Figure 5-6 Life cycle of *Leviviridae.* Virions attach to the bacteria pili (1). The viral genome enters the cell (2) where it is translated and replicated (3). The newly synthesised viral components, including ssRNA genome (green), maturation protein (red) and coat protein dimers (black) are assembled (4). Cell lysis then occurs by the lysis protein in Leviviruses and C-terminally extended coat protein in Alloleviviruses.

Expression of phage-encoded proteins is temporally controlled. Small quantities of replicase are expressed early in infection, while very large amounts of coat protein are expressed later on. RNA secondary structure is thought to play a key role regulating access of the ribosome to initiation regions.

Once translated, viral components can assemble in the cytoplasm. In principle, capsid formation can occur without viral RNA present, but in the presence of viral RNA much lower coat protein concentrations are sufficient to form capsids. The RNA directs the assembly of the *T*=3 capsid (Basnak *et al.*, 2010) It is thought that the binding of MP to RNA is an early assembly event, preceding capsid formation. Cell lysis and release of virions occurs via the action of the lysis protein in Leviviruses and the MP in Alloleviviruses. A single copy of the genomic RNA is sufficient to infect a cell. Several thousands of phage can be produced within a few hours from a single parent virus particle

5.1.6.1 Structure

The *Leviviridae* form spherical capsid shells 260-300 Å in diameter with a ~ 2 nm thick protein shell that has *T*=3 quasi-icosahedral symmetry, and containing one molecule of

positive-strand genomic RNA. In addition, *Leviviridae* are thought to contain one copy of the maturation protein. The protein shell is composed of 90 dimers of coat protein subunits, and maturation/read-through protein(s), which encapsidates the ssRNA genome. X-ray crystallography has been used to solve the structure of several *Leviviridae* including phages MS2, GA, fr, Qβ, PP7 and PRR1 (van den Worm *et al*., 1998; Tars *et al*., 1997; Liljas *et al*., 1994; Golmohammadi *et al*., 1996; Tars *et al*., 2000; Persson *et al*., 2008). 16-17 Å pores can be seen at the 3-fold and 5-fold axes, which have been suggested as exit sites for the viral genome (Stockley *et al*., 1993).

The asymmetric unit of the capsid is formed by coat protein forming stable dimers via hydrophobic interactions, which then associate by hydrophilic interactions to form the capsid (Valegard *et al*., 1990). The dimer interface between coat proteins is stabilized by inter-digitation of the C-terminal α-helices. Asymmetric and symmetric dimers form; symmetric dimers (C/C dimers) are found at the 2-fold symmetry axes of the capsid, while asymmetric (A/B) dimers are organized around 5-fold axes, and alternately with the C/C around the 3-fold vertices. The coat protein fold is an α/β 2-layer-sandwich consisting of seven β-strands and two α-helices, a fold only observed in this viral family (Valegard *et al*., 1990). Helices from two coat protein units interlock to form dimers with a continuous ten-stranded β sheet that lines the interior of the capsid and forms the genome binding surface. It has been suggested that the formation of A/B or C/C dimer conformers is dependant on interactions with RNA in a phenomenon known as 'dimer switching' (Stock-Ley *et al*., 1994; Dykeman *et al*., 2013; Stockley *et al*., 2013). Dimer switching may play a role in the initiation of assembly, but also in building a capsid of the correct size and symmetry by specifying the local rules for protein conformation.

In Alloleviviruses, the C-terminally extended coat protein is thought to incorporated 3-10 times per virion, based on biochemical studies from the 1970's (Hofstetter *et al*., 1974; Weiner & Weber, 1973). This read-through extension is not visible in the crystal structure of Qβ. A crystal structure is available for residues 144–328 of full-length A1 protein, although this has not shed light on its function (Rumnieks & Tars, 2011).

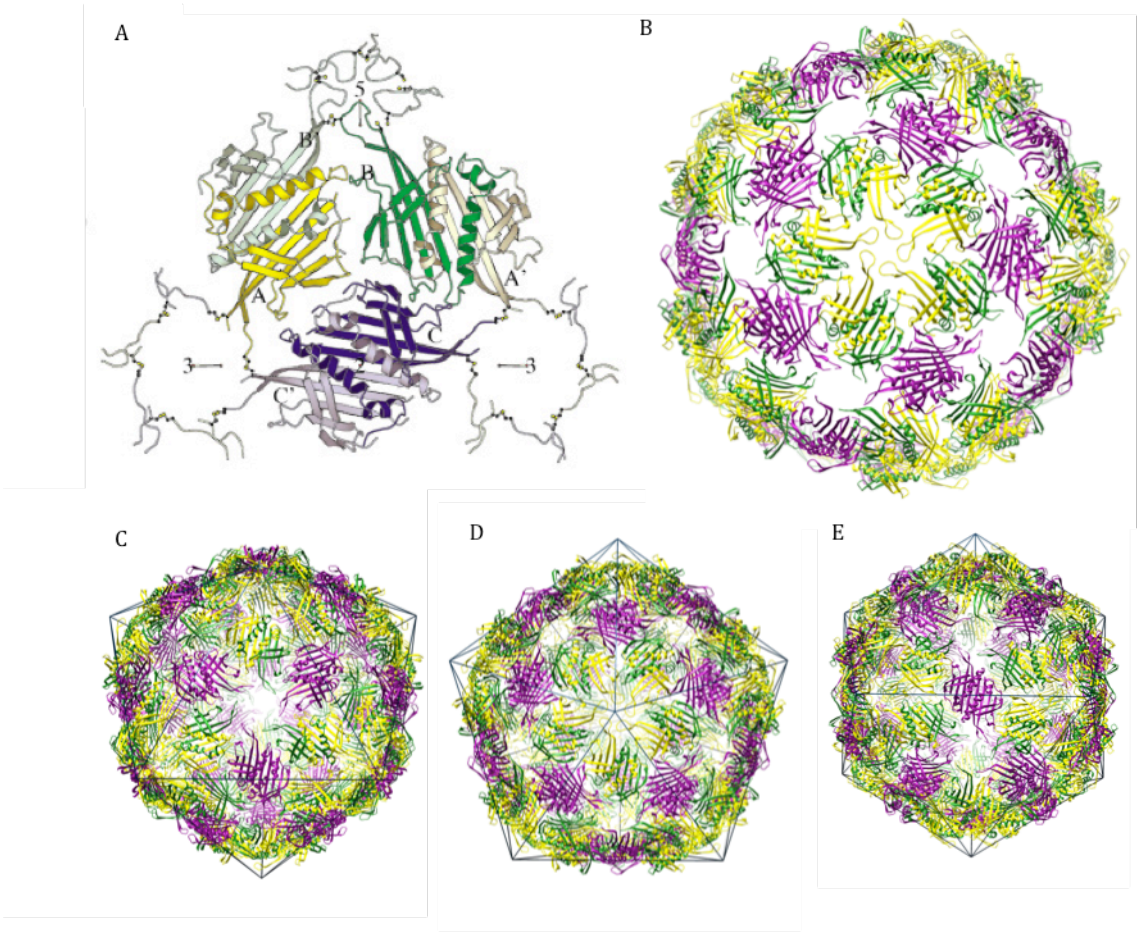

Figure 5-7 Crystal structure of Qβ bacteriophage. A) Schematic drawing of the subunit arrangement in Qβ as seen from the outside of the capsid down a twofold axis. The three subunits are shown; A (yellow), B (green), and C (purple), representing the icosahedral asymmetric unit are shown in colours, and the three symmetry-related subunits completing the dimers are shown in light colours. The loops forming the interactions at the five-fold and three-fold axes are shown. (Adapted from Golmohammadi *et al.*, 1996. B) Biological unit capsid structure of Qβ CE) Icosohedral structure of capsid facing 3-fold (C), 5-fold (D) and 2 fold (E) axes. B-E from PDB 1QBE visualised in Chimera.

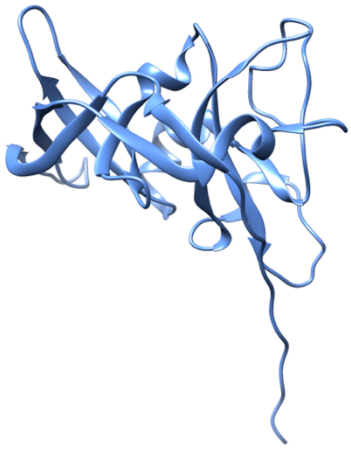

Figure 5-8 X-ray crystal structure of residues 144–328 of full-length A1 protein, representing part of the C-terminal extension to the coat protein. PDB accession codes 3RLK.

5.1.7 Coat protein-RNA interactions

Leviviridae coat protein dimers recognize and bind to stem loop structures in their genomes that incorporate the start codons of their replicase genes. This well known, single-copy, high affinity coat protein binding side (TR) acts as a translational operator, directly linking expression of the replicase to coat protein dimer concentration, and acting as a trigger for genome assembly (although additional sites within *Leviviridae* genome also promote assembly)(Dykeman *et al*., 2013). The interaction between TR and coat protein is thought to contribute to the specificity of encapsidation of genomic rather than host RNA. Upon binding to RNA stem-loop structures such as the TR sequence, and other weaker packaging signal, coat protein dimers switch from the symmetric C/C-like dimer to an asymmetric A/B conformation, with this dimer switching coordinating the assembly of the T= 3 capsid (Dykeman *et al*., 2010; Stockley *et al*., 2007).

A crystal structure has been solved for Qβ coat protein bound to its cognate translational operator (Rumnieks & Tars, 2014). The structure shows that a single nucleotide base in the hairpin loop makes sequence-specific contacts with the coat protein. Some *Leviviridae* including MS2 use an adenine-recognition pocket for binding a bulged adenine base in the hairpin stem, but Qβ uses a stacking interaction with a tyrosine side chain to accommodate the base instead. The extended loop between the E and F β-strands of the Qβ coat protein makes contacts with the lower part of the RNA stem. Despite Qβ requiring a smaller amount of sequence specific information, the coat protein is still able to discriminate its cognate operator from host RNA, which suggests the protein and RNA have co-evolved (Rumnieks & Tars, 2014). Crystal structures of the coat protein-operator complex are known for several members of the *Leviviridae*, and the overall binding mode is similar in each of these structures.

Cryo-EM has been used to probe the structure of the packaged genome in MS2 to sub-nanometer resolution (Toropova *et al*., 2008). The icosahedrally-averaged genome is organised into two concentric shells of density. The outer shell contains approximately two thirds of the genome and is associated with the coat protein shell. An inner shell contains the remained of the genome. Structures of recombinant MS2 virus-like particles (VLPs) packaging a range of different sub-genomic RNAs demonstrate that particles that have packaged shorter RNAs maintain the outer shell but not the inner.

5.2 Results

X-ray crystallography has provided high-resolution information about the structure of *Leviviridae* members. However, crystal structures are a representation of the virus packed in a crystal, which may not always be representative of the solution structure. Additionally, information about the genome and its interactions with the capsid is frequently lost in X-ray structures (Section 1.1.3). Here, cryo-EM was used to investigate structural properties of MS2 and Qβ bacteriophage.

5.2.1 Maturation protein mediates binding to F-pili

As discussed in Section 5.1.6, at least one copy of MP is present in Leviviruses and is thought to be required for infectivity. (Krahn *et al*., 1972; J.W. Roberts & Steitz, 1967). To test this hypothesis, isolated F-pili were incubated with either recombinant MS2 virus-like particles (VLPs), which lack MP, or wt MS2 virions, most of which contain it (Roberts and Steitz, 1967)(Section 2.10). Cryo-EM was then used to image these preparations. Both experiments were performed on the same preparation of F-pili, and under identical solution conditions. In the wt MS2-F-pili preparation, virus particles were seen binding the F-pili readily (Figure 5-9 A,B). By contrast, in the VLP-F-pili sample, it was extremely difficult to image F-pili in the presence of VLPs, as the F-pili aggregate into bundles. The VLPs are not seen binding (Figure 5-9 D,E). In fact, the binding of virus particles to the F-pili therefore appears to help solubilise them. This work reinforces the key role of the maturation protein in receptor (F-pili) recognition (Dent *et al*., 2013).

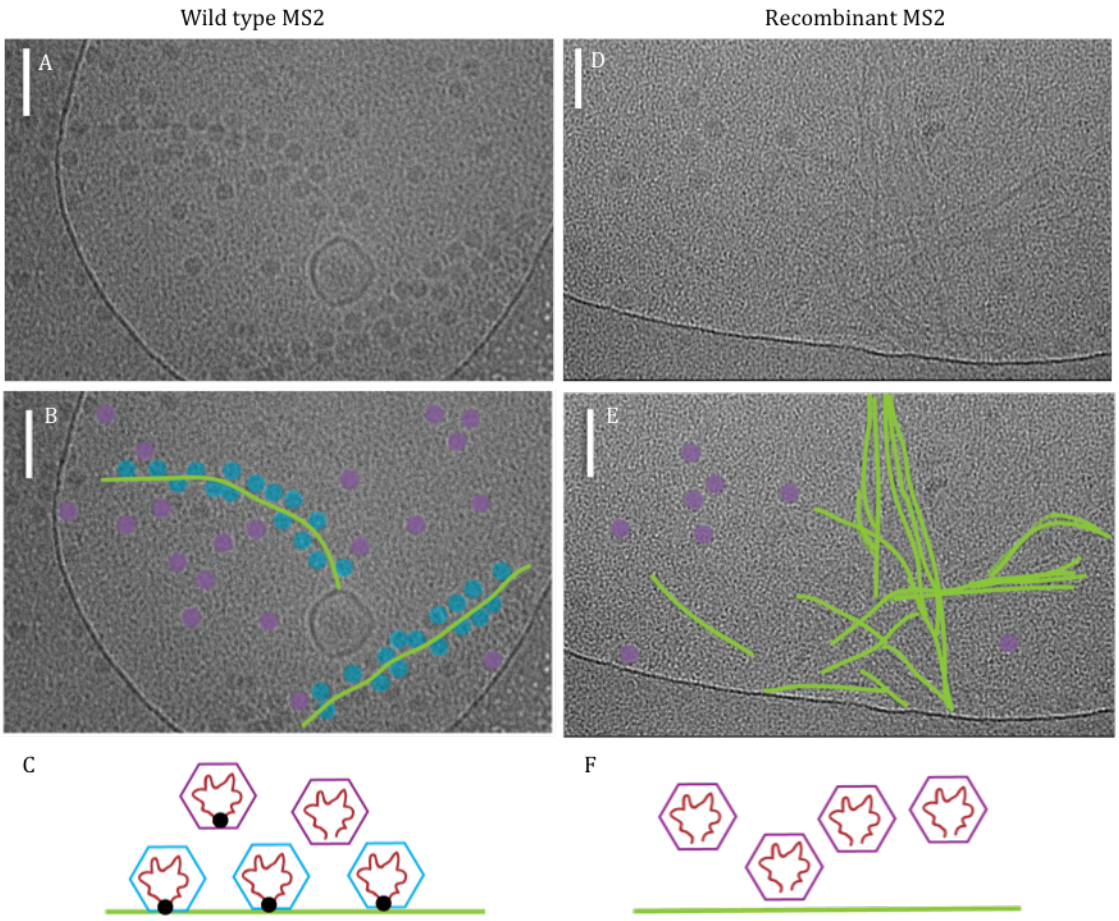

Figure 5-9 Binding of MS2 to F-pili is mediated by the maturation protein. Cryo-EM of wild-type MS2 (A) or recombinant MS2 lacking maturation protein (C). For clarity, pili (green), bound (blue) and unbound (purple) particles are highlighted in B,E. Schematic (C,F) shows particles containing maturation protein (black) are bound (blue capsid) to the pili (green). Unbound particles in C may either not contain maturation protein. Particles in F do not contain maturation protein, and so do not bind. Scale bar 100 nm.

5.2.2 Structure of Qβ bacteriophage

Owing to improvements in EM detectors, microscope hardware and image processing algorithms, achieving high-resolution (better than 5 Å) structures by SPA cryo-EM is becoming possible. Here, we used cryo-EM and SPA to generate a high-resolution structure of Qβ, in order to investigate properties of the protein capsid in solution, and investigate asymmetric properties of the virus such as the genome.

5.2.2.1 Cryo-EM of Qβ

Cryo-EM grids of Qβ were prepared, and particle distribution and ice thickness optimised at the University of Leeds on an FEI F20 microscope (Section 2.11.3, 2.12.1). Optimised grids were imaged at the MRC LMB using an FEI Titan Krios microscope with a Falcon II detector at a magnification of 103,704 x, resulting in a sampling of 1.35 Å per pixel and a

total dose of ~50 $e^-/Å^2$. Dose was fractionated across 34 frames during a 2 s exposure (Figure 5-10). A total of 1206 micrograph 'movies' were recorded. Micrographs and their power spectra were manually inspected, and any showing significant drift or charging were removed, yielding 1170 micrographs which were taken forward to further image processing steps.

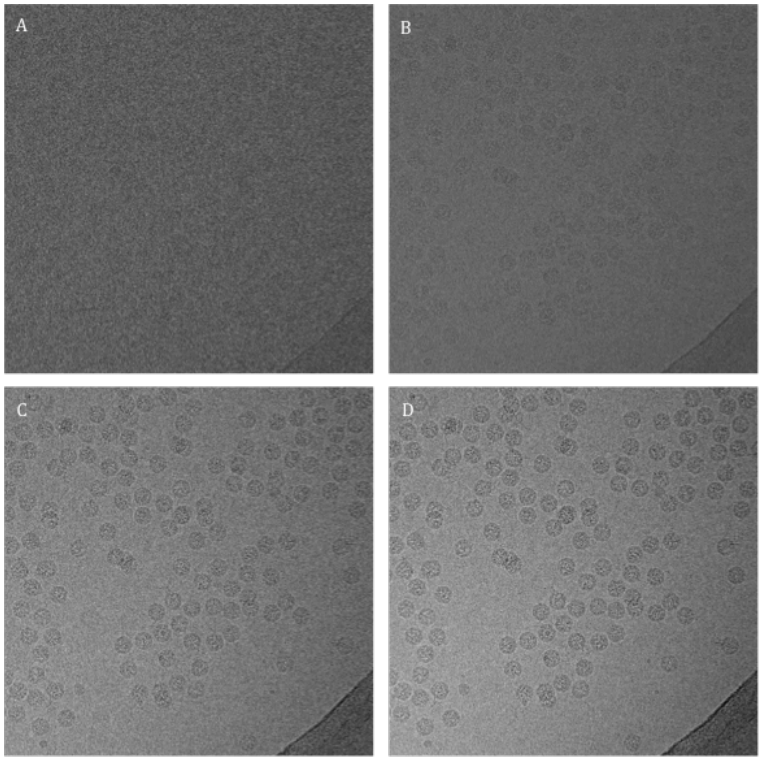

Figure 5-10 Collection of data on a direct electron detector. A) One frame. B) Sum of frames 1-8. C) Sum of frames 1-17. D) Sum of frames 1-34.

5.2.2.2 Initial processing

Initial processing of the micrographs was performed to produce a stack of particles that could be taken forward for high-resolution 3D structure determination. All data processing was carried out using RELION 1.3 unless otherwise specified. EM micrographs are distorted by a point spread function that is introduced by the defocus used to generate phase contrast, and aberrations resulting from imperfections in the optics of the microscope (Section 1.3.8). To correct for this, defocus parameters were determined using CTFFIND4 (Rohou & Grigorieff, 2015). Micrographs had a defocus range of – 0.8 µm to – 3.8 µm. Example micrographs and power spectrum fitting are shown in Figure 5-11.

2000 particles were picked manually and subject to reference-free, 2D class averaging. For all processing, a box size of 288 pixels (388.9 Å) and a mask with a diameter of 300 Å was used. These particles were then used as templates for automatic picking of particles in RELION 1.3 (Scheres, 2015). 28,156 total particles were then picked automatically. These were subject to reference free 2D classification into 50 classes over 25 iterations. 2D classification allows the removal of particles erroneously picked during automated

particle picking, and also for the quality of the data to be assessed. 2D class averages revealed most particles (24,109) contributed to classes that clearly resembled Qβ bacteriophage, with the remaining classes resembling the edge of carbon film or contaminant (Figure 5-12). Particle sorting by Z-score and log-likelihood was used to remove particles not resembling Qβ bacteriophage. This yielded a final particle stack of 21,767 that was taken forward for 3D structure determination.

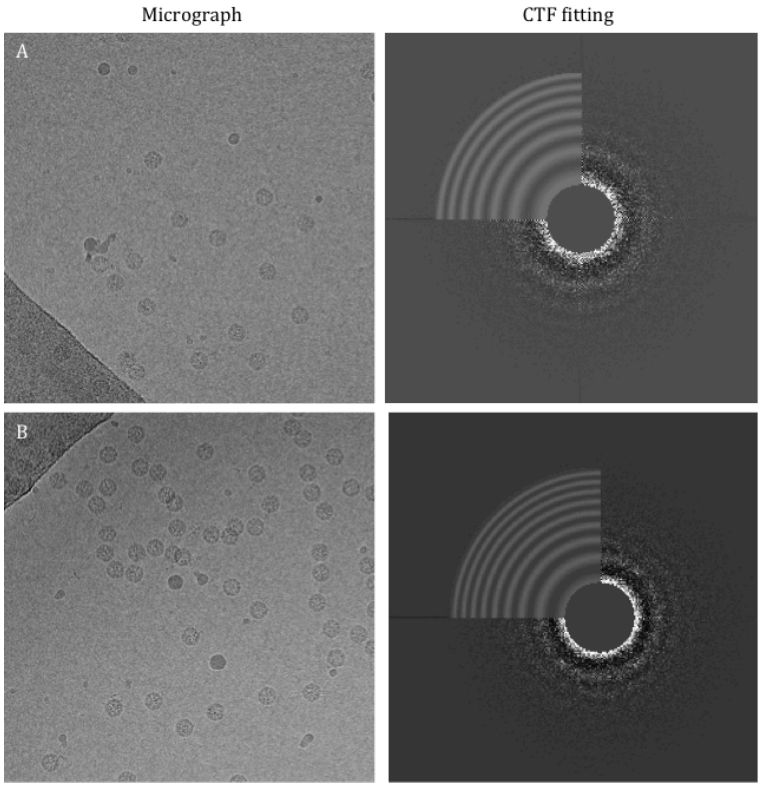

Figure 5-11 CTF and defocus determination by CTFFIND4. Two representative micrographs at -1.7 (A) -2.2 (B) microns defocus, as determined by CTFFIND4. ¾ of micrograph FFT is shown, with ¼ CTFFIND4 fitting.

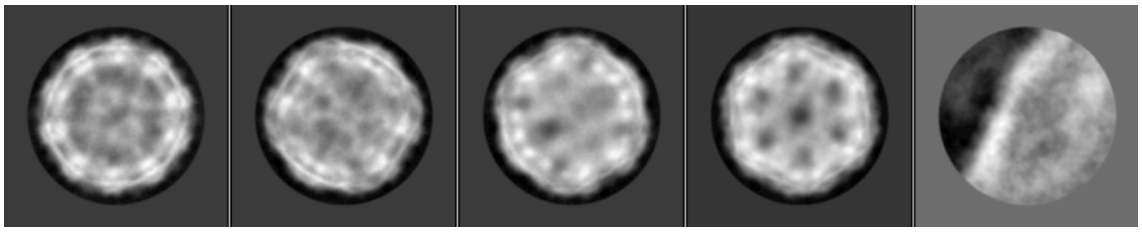

Figure 5-12 Representative 2D class averages of Qβ bacteriophage. First four classes show Qβ bacteriophage, fifth class shows carbon film.

5.2.2.3 3D structure determination of Qβ bacteriophage

Unsupervised 3D classification with icosahedral symmetry imposed, into two classes was performed in RELION to assess dataset heterogeneity. A sphere with a radius of 26 nm was used as a starting model. One 3D class was selected from this was Fourier filtered to 50 Å to aid prevention of model bias, then used as the starting model for a second round of 3D structure determination. The full particle stack split roughly evenly between two classes during 3D classification, and the resulting 3D structures converged to a marginally

worse resolution when compared to 3D structure containing all the particles. Therefore, the full particle stack was used for high-resolution 3D refinement.

For high-resolution 3D structure refinement, previous 3D structure determination filtered to 50 Å was used as a starting model. Using the autorefine procedure, refinement had converged after 21 iterations. The unsharpened and unmasked map was calculated to be 4.8 Å resolution. At this point, processing involved particles from the sum of the 34 movie frames collected for each micrograph. Over the course of sample exposure to the electron beam, the particle may move, the physical stage of the microscope may not be stable (mechanical drift), or we may observe a charging effect. By looking at individual frames, and particle movements between each frame, we can correct these effects. Particle polishing was performed using a running average of 3 frames, and each particle trajectory was fitted individually. RELION's polishing algorithm estimates a *B*-factor and a linear intensity factor that describes the resolution-dependent power of the signal in each frame of the movie. In this way, radiation-induced damage is modelled by performing a weighted average of all aligned movie frames for each particle. The *B*-factors were calculated for each frame, and they showed a distinct pattern (Figure 5-13). In the first few frames, beam-induced movement of particles is very significant. The *B*-factor improves after frame 5, until total electron dose causes radiation damage, and *B*-factor starts to fall again, around frame 25. Therefore, only information from frames 5-25 was used in the final reconstruction. Particles from the polishing process were re-refined, giving an estimated accuracy of angular assignments of 0.556° and RELION calculated the refinement had converged after 24 iterations. The unsharpened, unmasked map was calculated to be 4.32 Å.

The 3D map was then sharpened and masked to make high-resolution features clearer. Auto-masking was performed using an initial binarisation threshold of 0.01, a hard mask of 2 pixels and a soft edge of 7 pixels. The modulation transfer function (MTF) of the detector was accounted for at this stage. *B*-factor calculation was performed automatically, with the 10 Å lowest resolution for auto-B fitting. This yielded a map at 4.22 Å resolution as judged by gold standard FSC at a threshold of 0.143 (Figure 5-13 B, Figure 5-14).

To compare EM density with previous structural information, the crystal structure (1QEB) was fitted into the EM-derived density map using the 'fit in map' tool in Chimera. The model obtained by X-ray crystallography agrees very well with the density map generated by SPA (Figure 5-15 A). At this resolution, we clearly resolve alpha helices, the separation of beta strands, and see density for some of the larger side chains (Figure 5-15 B, C).

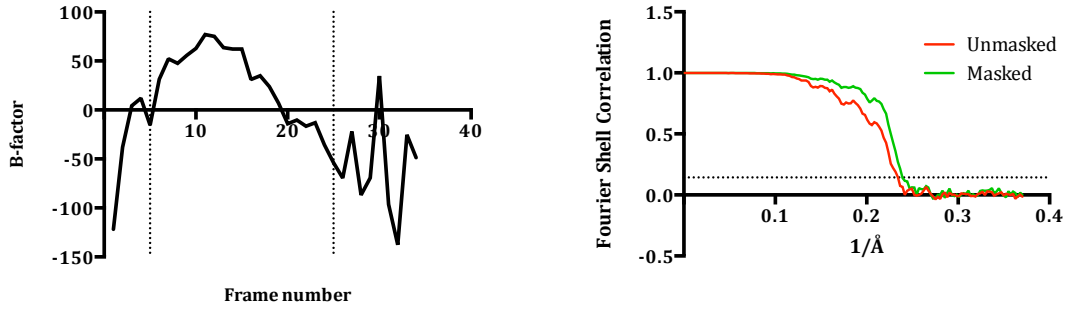

Figure 5-13 Descriptive statistics during refinement of Qβ bacteriophage. A) Calculated B-factors across movie frames. B) Gold standard FSC resolution estimation of unmasked (red) and masked (green) structures, the FSC cut-off of at 0.143 is shown as a dotted line.

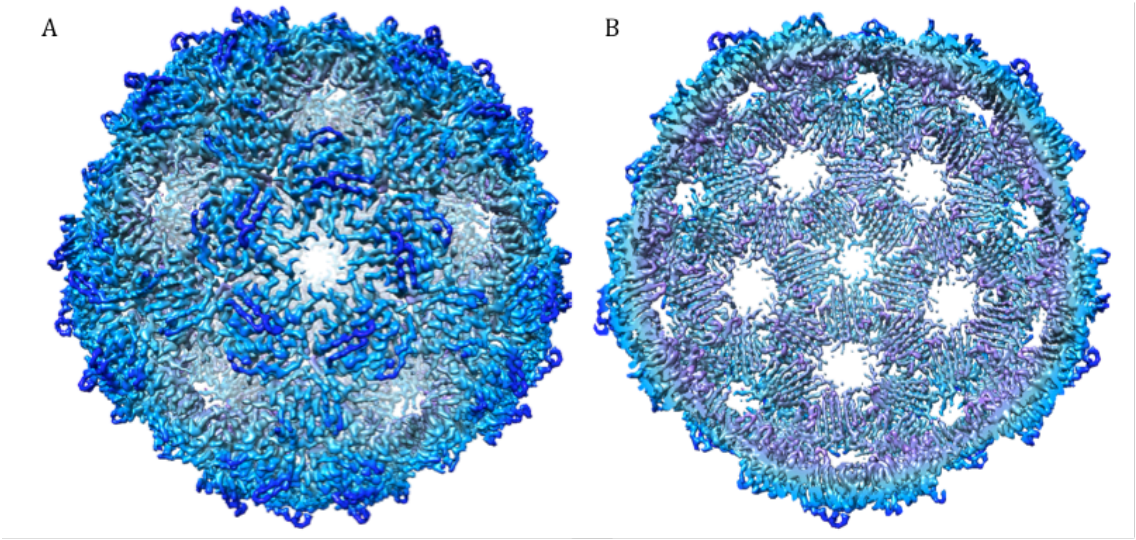

Figure 5-14 Structure of Qβ bacteriophage. Capsid exterior (A) and slice through into interior (B). Structure radially coloured and visualised at 0.1 threshold in Chimera.

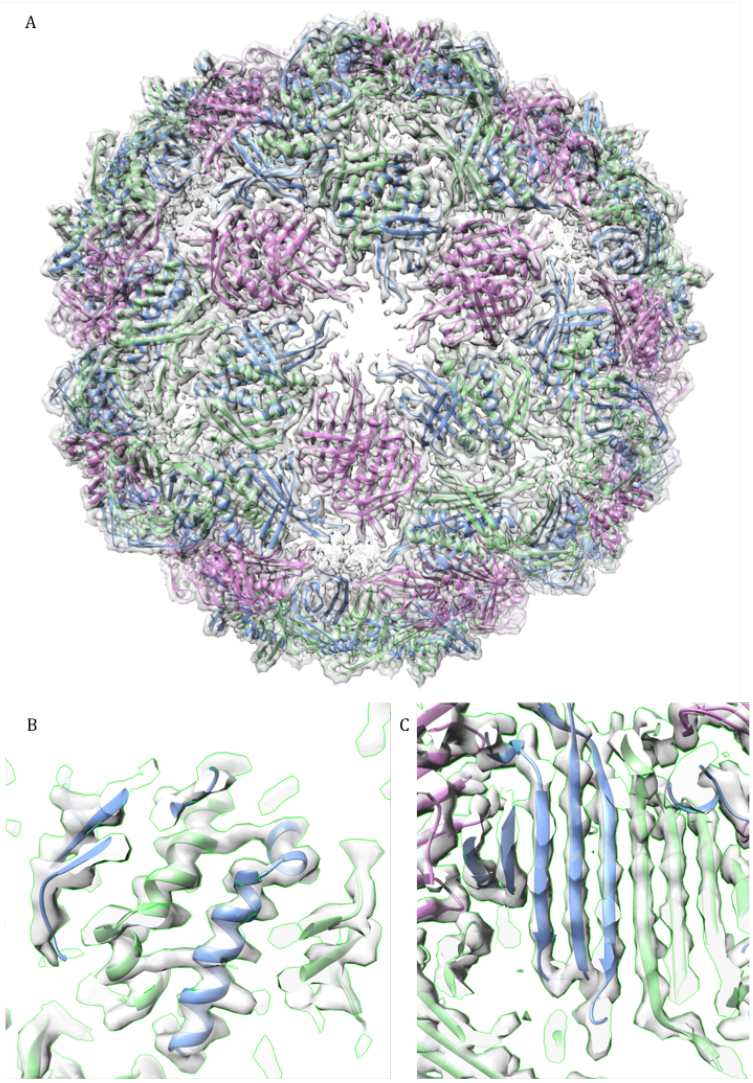

Figure 5-15 Fitting of crystal structure into electron density map. Electron density map with crystal structure (1QBE) fitted (A). EM density map visualised at 0.1 threshold. Chain A shown in blue, chain B in green and chain C in purple. Examples of α-helical (C) and β-sheet density with crystal structure fitted.

5.2.2.4 Local resolution determination

While a global resolution estimation, such as that obtained by the 'gold-standard' FSC, can be very useful, there can be significant differences in resolution across the map. Local resolution estimations can be performed to estimate the resolution variations throughout a map. Local resolution estimations were performed using ResMap software (Kucukelbir *et al.*, 2014)(2.14.1). Resolution was assessed between 3 and 9 Å with a step size of 0.5 Å. This shows that much of the protein capsid is at 3 Å (Figure 5-16 A). When the density map is contoured to show genome density on the interior of the map, this is a significantly poorer resolution compared with the protein capsid density. Therefore, while the global resolution value reports resolution as 4.2 Å, much of the protein capsid is of significantly better resolution, while the genome is significantly poorer. In the global FSC resolution estimates, this evens out at an intermediate resolution that underrepresents the quality of

parts of the map. This highlights the value of performing local resolution estimates to assess resolution.

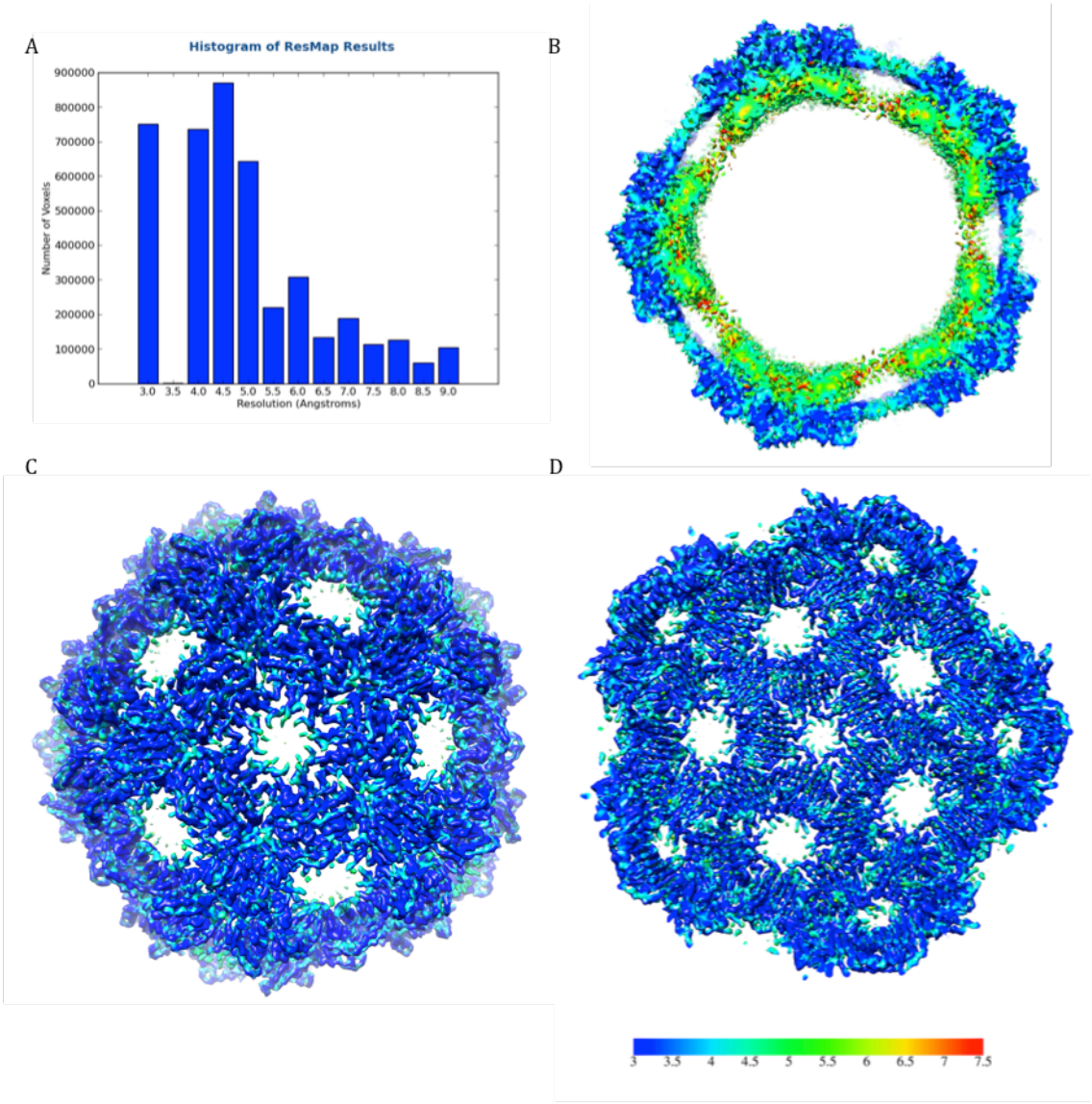

Figure 5-16 Local resolution estimation of Qβ bacteriophage electron density map. Histogram output from ResMap software, showing number of voxels in different resolution bins (A). B) Slice through density map showing capsid and shell of density attributed to genome. C) View of the outside of the capsid. D) View of the inside of capsid. Electron density maps shown are coloured by local resolution at 0.04 threshold (B) or 0.1 threshold (C,D). Key for local resolution shown bottom right (Å.).

5.2.3 Refining the crystal structure of Qβ bacteriophage

As discussed in Section 5.1.6.1, the $T = 3$ capsid is formed from a single coat protein which is found in three distinct qausi-equivalent conformations, termed A, B and C. The capsid contains two types of dimer, A/B and C/C; formation of the 3-fold axis occurs by the interdigitation of A/B and C/C coat protein dimers. To better understand the detailed structure of Qβ, density corresponding to the A/B and C/C dimers was segmented out

using Chimera. The corresponding dimers from the X-ray crystal structure were refined into the EM-derived electron density using Rosetta (DiMaio *et al.*, 2015). The crystal structure of Qβ bacteriophage is at 3.5 Å, and significant portions of the density were disordered. 18 amino acids per coat protein subunit could not be modelled at all, and six residues were not modelled beyond their Cβ (Lys16, Ser56, Arg57, Asn58, Arg59, Lys60).

Regions in both the A/B and C/C dimer could not be modelled using data from the X-ray crystal structure (Residues 76-79 and 56-60). The electron density map for the A/B and C/C dimers was visualised at different contour levels to see if any density for these regions was present. At high contour there is no evidence for density relating to the extra residues. In all cases, even at low contour level, no additional density that could correspond to the missing residues is present. One region with missing residues 75-79 from the A/B dimer is shown in Figure 5-17 to illustrate this. This lack of density indicates these residues must be extremely flexible or missing. There is no evidence for cleavage at present, and further mass spectrometry studies would be needed to test this idea.

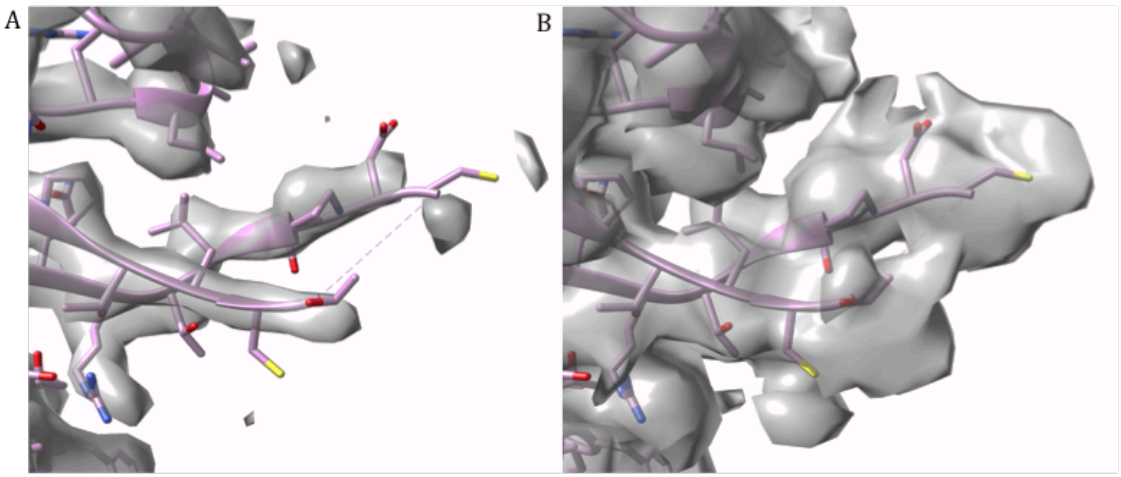

Figure 5-17 Electron density map and crystal structure (1QBE) for the A/B dimer. Dotted line illustrates missing residues 76-79. EM density map shown at 0.1 (A) and 0.011 (B).

Atomic refinement in Rosetta is based on the 'relax' protocol with an additional tool to assess agreement with the density (DiMaio *et al.*, 2015). For both the A/B and C/C dimer structures, refinement in Rosetta only resulted in subtle changes to backbone alignment. However, Rosetta was able to build in residues that were only modelled to the Cβ in the original X-ray crystal structure (Figure 5-18). Statistical analysis was performed to assess the quality of refinement in Rosetta. The 'Rosetta total score', which represents the total energy of the conformation, improves for both the A/B and C/C dimers. The MolProbity score is a log-weighted combination of the clashscore, percentage of unfavoured

Ramachandran residues and percentage of bad side-chain rotamers. It is a standard validation tool for crystallographic structures, and is calculated using the MolProbity server (Chen *et al.*, 2010). As Rosetta uses a rotamer library to introduce idealised rotamers, we would expect this number to improve for the Rosetta structures, which it does. The Clashscore is the number of 'serious' (non-donor–acceptor atoms overlap by more than 0.4 Å) clashes per 1000 atoms. This score significantly improves in the Rosetta refined structures compared with the X-ray crystal structure derived model. The total number of favoured residues on a Ramachandran plot also improves for the refined Rosetta structures compared with X-ray crystal derived structures.

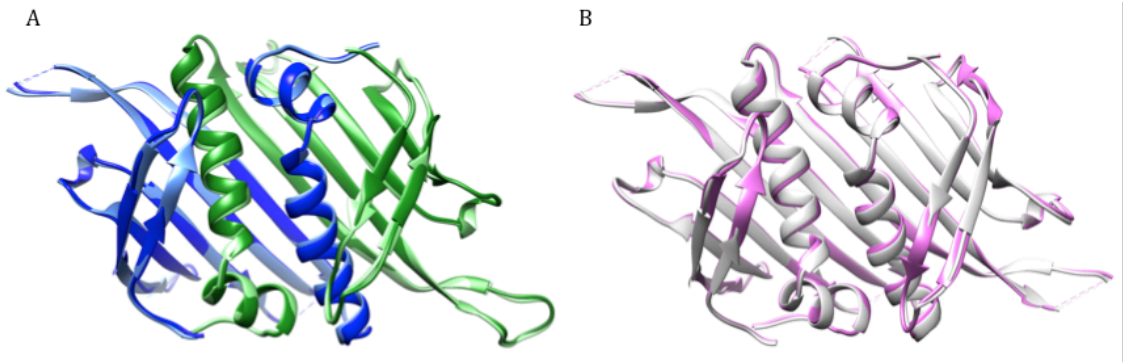

Figure 5-18 Refining crystal structure of A/B and C/C dimers into corresponding electron density. A) A/B dimer crystal structure shown in light blue (A subunit) and light green (B subunit) (1QBE), Rosetta structure shown in dark green and dark blue. B) C/C dimer crystal structure shown in pink (1QBE), Rosetta structure show in white. In both the A/B and C/C dimer, there is close agreement between the backbone traces.

	Rosetta total score	MolProbity score	Clashscore	Ramachandran favoured (%)
A/B PDB	-2274.642	2.81	18.32	93.12
A/B Rosetta	-3095.716	1.1	1.55	96.76
C/C PDB	-2355.823	2.63	13.54	94.02
C/C Rosetta	-3022.104	0.97	0.81	96.58

Table 5.2 Statistical analysis of atomic model refinement. Rosetta total score is a measure of total energy, calculated in Rosetta (DiMaio *et al.*, 2015). MolProbity, Clashscore and Ramachandran favoured residues (%) calculated in MolProbity (Chen *et al.*, 2010).

5.2.4 Genome organisation

In the X-ray structure of Qβ, no information about the encapsidared 4.2 kb genome was revealed (Rumnieks & Tars, 2014). Icosohedrally-averaged EM-dreived density maps generated in Section 5.2.2.3 retain some information about the genome. The challenge of interpreting density within the capsid is that icosahedral symmetry is imposed during refinement, meaning that the genome, which is an asymmetric RNA molecule, is inappropriately icosahedral averaged. An asymmetric reconstruction of Qβ was also

therefore generated to 7.7 Å (Section 2.14.1)(Figure 5-19). Even in this asymmetric reconstruction, the refinement process is dominated by the strong icosahedral symmetry of the capsid. Despite this, interesting information regarding the genome can still be extracted from these models.

Electron density maps generated and shown in Section 5.2.2.3 as well as Figure 5-19 were subjected to masking and *B*-factor sharpening to calculate resolution and more easily visualise features of the protein capsid. However, in this process, many lower resolution features including part of the internal density attributed to the genome is masked out. In this section, only the unmasked density will be assessed.

In the unmasked density for both asymmetric and icosahedral structures, within the capsid two concentric shells of density are observed (Figure 5-20). The outer shell lies directly under the protein capsid (Figure 5-20, yellow density), and consists of a regular, connected network of density with discrete 'packets' of density, and appears similar in the asymmetric and icosahedral averaged structures. The positions of the RNA in this layer precisely map to the lattice of RNA binding sites on the inner surface of the capsid. The density appears to be different beneath each type of quasi-equivalent coat protein dimer, and this difference is more pronounced in the asymmetric structure (Figure 5-20 D) than the icosohedrally-averaged structure (Figure 5-20 B). The second density shell is at lower radius; maps must be visualised at a lower threshold to show this density (Figure 5-20 A, C, orange). The central density appears very different in the icosahedral and asymmetric structures.

Crystal structures are available for *Leviviridae* in complex with various RNA oligonucleotides (Rumnieks & Tars, 2014; Persson *et al*., 2013; van den Worm *et al*., 1998). Here, in order to guide interpretation of the genome-associated density observed in the outermost ring, the crystal structure of MS2 complexed with the wild-type TR stem loop (1AQ3) was fitted into the EM-derived density map. The structures of coat protein from MS2 and Qβ overlay closely and both fit into the Qβ map (Figure 5-21 A). The TR RNA is a type A helical structure, and fits well into the density immediately beneath each coat protein dimer (Figure 5-21 B, C). Dimers in the A/B conformation display RNA associated density directly beneath the dimer interface, extending towards the icosahedral 5-fold axes. A connected ring of density is therefore formed around the 5-fold axes. Close inspection of the density beneath A/B and C/C dimers in both the icosahedral and asymmetric averaged structures shows slightly different density beneath each quasi-equivalent coat protein dimer, with a larger density beneath C/C dimer compared with the

A/B dimer (Figure 5-21 D, F). This is expected as RNA binds in two, symmetry related orientations at the C/C dimer, but only in one conformation to the A/B dimer. This is due to the conformation of the FG loop in the B subunit of the A/B dimer appears to restrict the binding of the RNA. Therefore, in the averaged structures, an averaging of the two conformations occurs, leading to a larger density beneath the C/C dimer compared to that found bound to A/B dimers. This suggests that, on average, there is a different interaction between RNA and each type of quasi-equivalent coat protein dimer. This feature has been observed at lower resolution using cryo-EM in the related virus MS2.

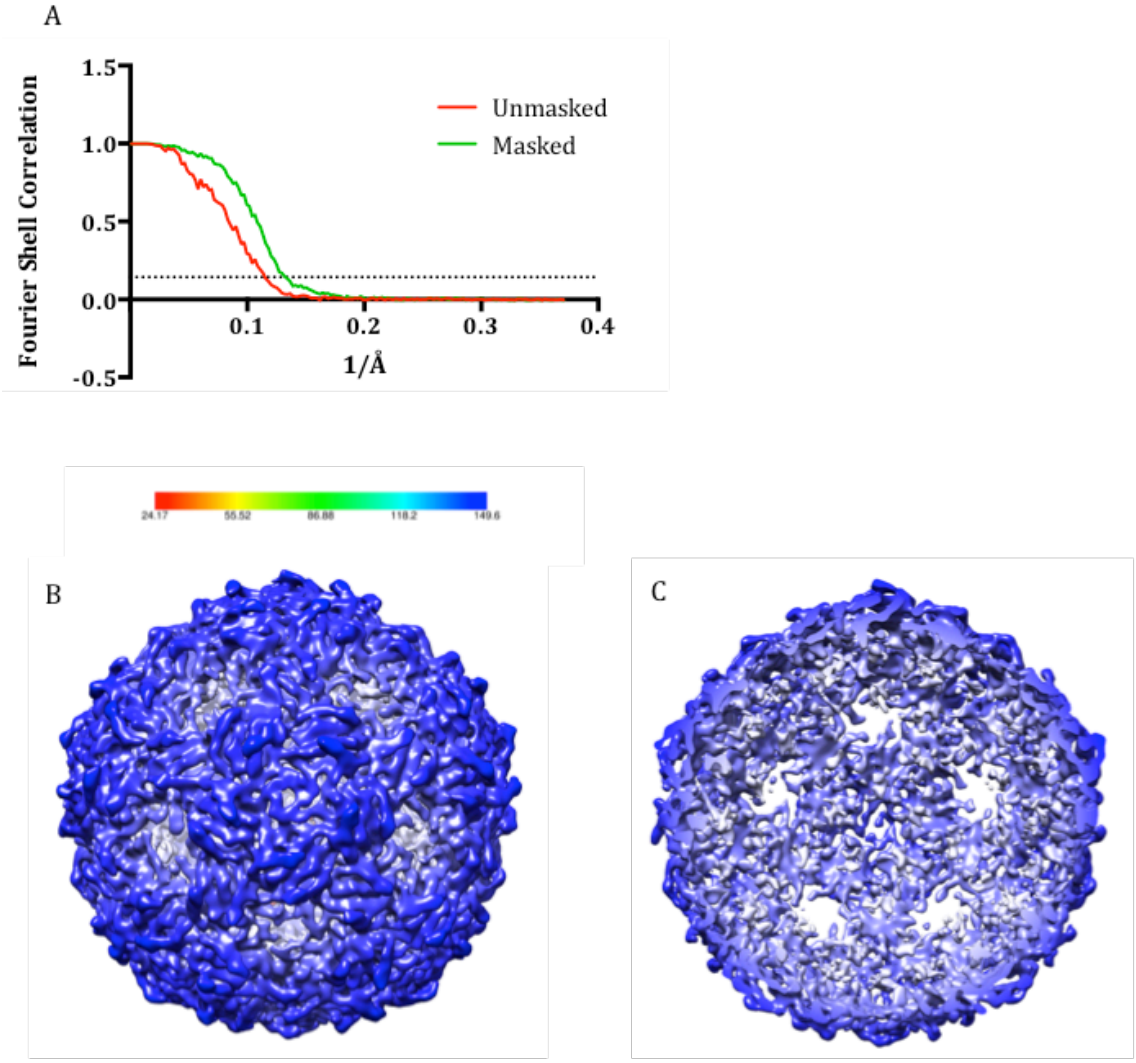

Figure 5-19 Asymmetric reconstruction of Qβ to 7.7 Å. A) Gold standard FSC resolution estimation of unmasked (red) and masked (green) structures, the FSC cut-off of at 0.143 is shown as a dotted line. Asymmetric structure of Qβ radially coloured according to the key (Å from centre of capsid) showing capsid exterior (B) and interior (C) at 0.985 threshold.

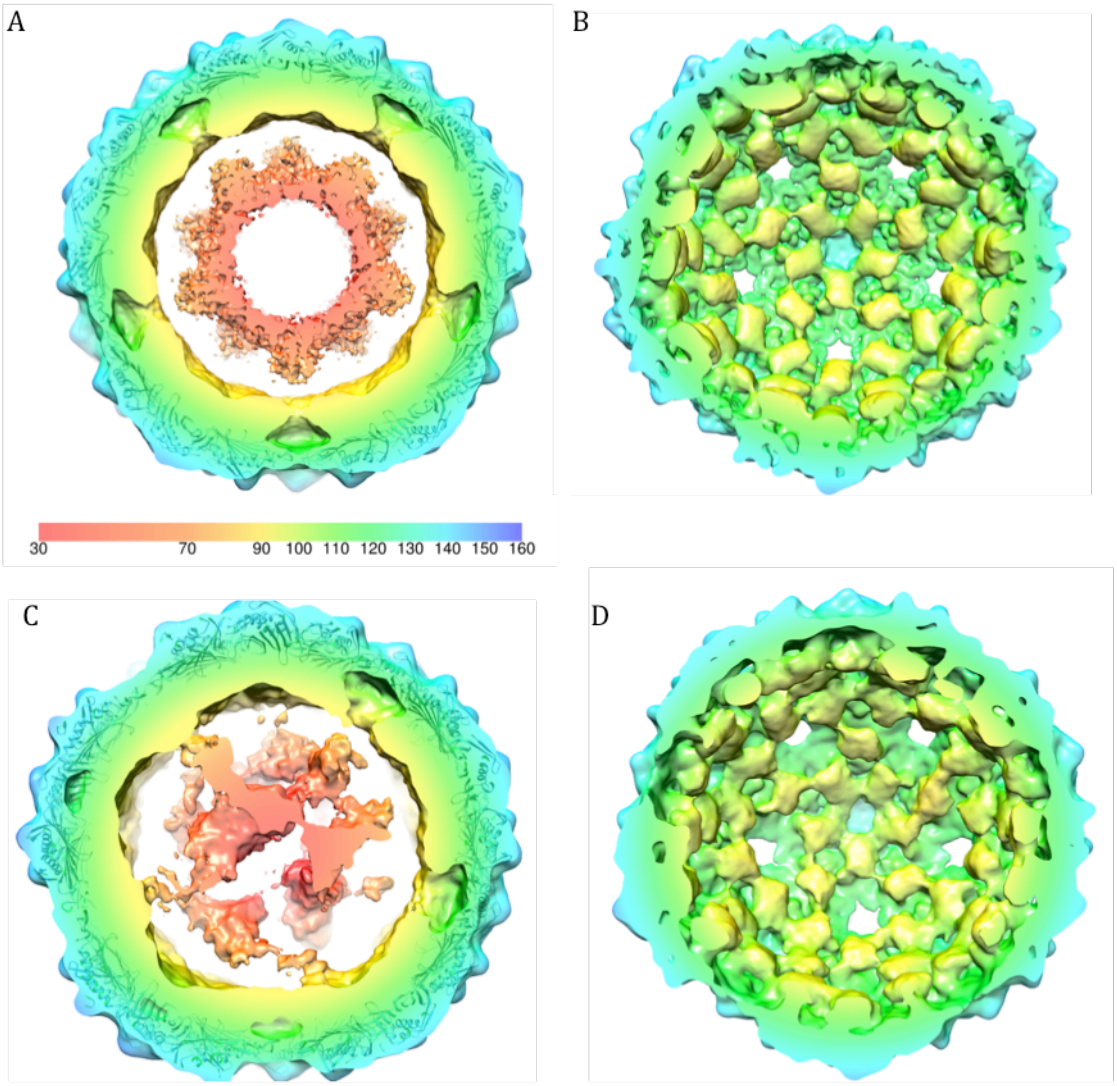

Figure 5-20 Genome organisation in Qβ. Icosohedrally averaged (A,B) and asymmetric (C,D) structures of Qβ, coloured by radius according to the key (distance from capsid centre, Å). A, C visualised at 0.003. B,D visualised at 0.016 threshold.

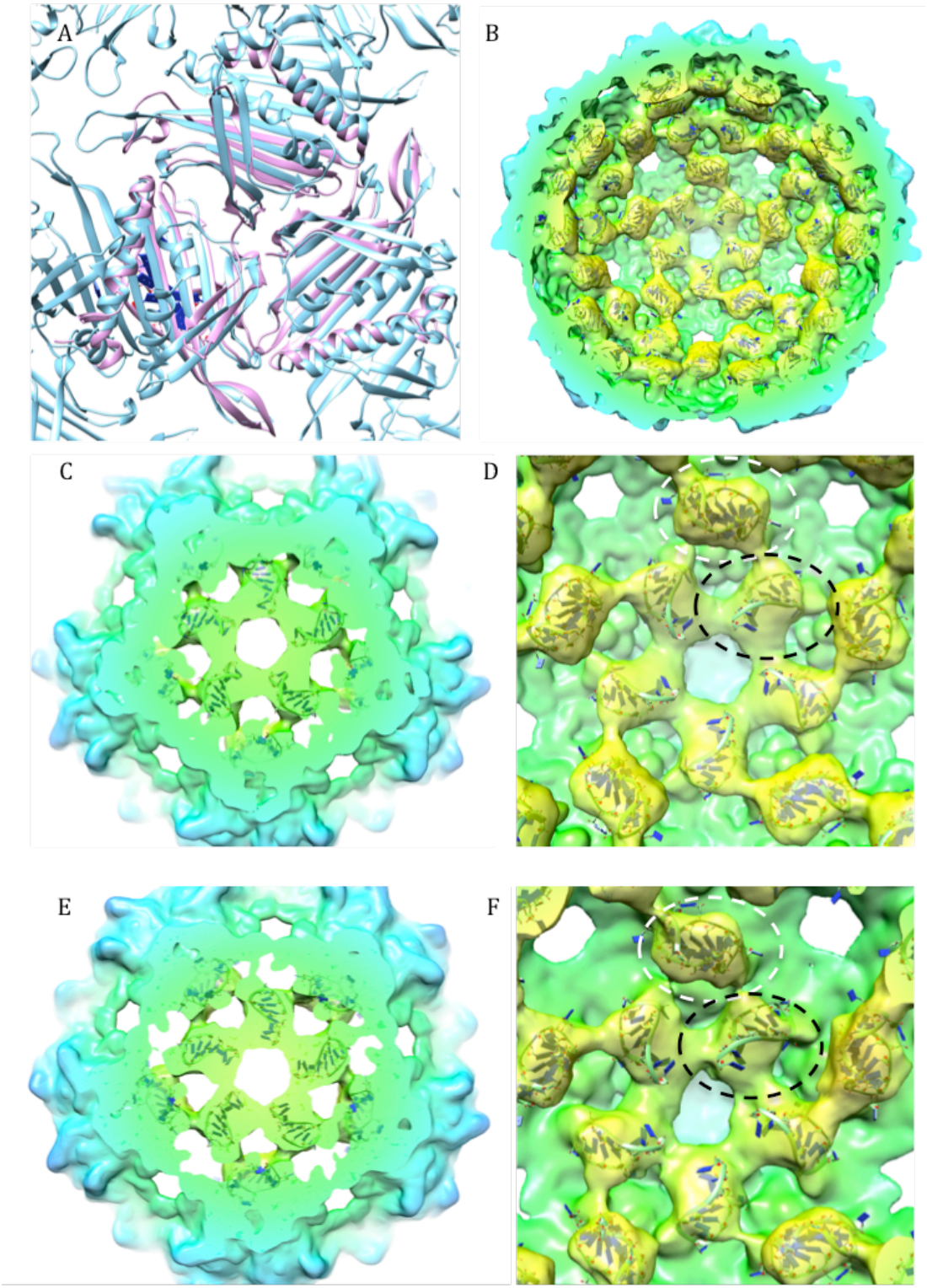

Figure 5-21 Fitting of RNA density into icosahedrally averaged and asymmetric reconstructions of Qβ. A) Crystal structure of MS2 capsid in complex with RNA (1AQ3) (pink) superimposed with crystal structure of Qβ (1QBE)(light blue). Unmasked, unsharpened, icosohedrally averaged (B,C,D) and asymmetric structure (E,F) Qβ structure with crystal structure of MS2 capsid in complex with RNA (1AQ3) fitted but only RNA visualised. View at five fold axis (C,D,E,F) show RNA stem loop density fitted into density corresponding to outer RNA shell. Dashed white circles denote density beneath C/C dimer, black dashed circles A/B dimer.

5.3 Discussion

Here, optimisation of sample preparation and advances in EM hardware and data processing techniques, have allowed the generation a high-resolution structure of wt Qβ. The global resolution of the map is 4.2 Å, but analysis of local resolution reveals that much of the capsid shell is at 3 Å (Figure 5-13, Figure 5-16). Therefore much of the density map is at a resolution very close to the Nyquist limit (2 x sampling = 2.7 Å). At this resolution, secondary structure elements such as α-helices and β strands are beautifully resolved, and tools such as Rosetta can be used to refine X-ray derived atomic models. Here, Rosetta was used to refine the existing crystal structure of the Qβ capsid to significantly improve measures of atomic model quality (Clashscore, MolProbity score), and provide positioning for side chains that were previously only modelled to their Cβ atoms. If future work sought to improve the resolution of the electron density map further, imaging could be performed at a higher Å/pixel sampling, and a larger dataset might be beneficial. However, asymmetric aspects of Qβ including the genome, MP and extended coat protein may limit achievable resolution. The presence of an electron dense genome that does not conform to the icosahedral symmetry of the capsid also may reduce the overall accuracy of angular assignments and slightly skew refinement of the capsid protein, reducing global resolution. An interesting way to test this would be to generate a structure of an empty Qβ capsid, although it is possible that such a capsid would be less stable, or ordered.

Viruses have evolved a broad range of ways to overcome the challenge of encapsidating their genomic material. Many RNA viruses assemble their virions spontaneously, including *Leviviridae*. Data presented here provides insight into how quasi-icosahedral symmetry is propagated as the capsid forms around the genome. Cryo-EM has previously been used to study MS2 (Toropova *et al*., 2008). An icosohedrally averaged, ~ 9 Å structure was obtained, which suggests different density beneath quasi-equivalent A/B and C/C dimers, providing evidence that allosteric dimer switching plays a role in mediating formation of the *T=3* capsid. Here, a structure of Qβ is presented at a significantly improved resolution compared to previous cryo-EM studies. For the first time in Allolevivirus, subtly different density was observed beneath different quasi-equivalent dimer structures, providing evidence for the role in allosteric dimer switching in mediating formation of the *T=3* capsid, and providing evidence that this mechanism is a generic feature of *Leviviridae* capsid assembly.

Another interesting feature of the outer ring of genomic RNA is the suggestion of connectivity between density beneath some dimers (Figure 5-20). This has not been observed previously in *Leviviridae.* It has been previously suggested that all the possible

paths of the genomic RNA through a protein capsid can be modelled using the mathematical principle of Hamiltonian paths (Rudnick & Bruinsma, 2005). The concept of Hamiltonian paths is derived from graph theory, and asks how can each vertex of a graph be visited only once by walking from one vertex to the next along the edges of a polyhedron. When applied to packaging of a genome in members of Levivirus it is assumed the genome must visit each of the 60 A/B coat protein dimers only once (to induce conformational switching from C/C dimer), and any path of the RNA from the outer to the inner shell of RNA returns to the same 5-fold axis in the outer shell. Mathematical modelling using this principle, combined with low-resolution cryo-EM density maps, determined that for MS2 there are 40,678 possible Hamiltonian paths the RNA could take (Dykeman *et al*., 2011). Further computational work combined with an asymmetric structure of MS2 obtained using subtomogram averaing (Dent *et al.,* 2013) has further narrowed the number of Hamiltonian paths that is compatible with experimental evidence to 5 (Geraets *et al.,* 2015). Revisiting the use of Hamiltonian paths with an improved cryo-EM density for the outer shell of RNA may help to further constrain the number of possible Hamiltonian paths the genome may take. This raises the tantilising possibility that the asymmetric reconstruction of Qβ will demonstrate that a single conformation of RNA is present in every virion.

Fundamentally, spherical viruses such as Qβ are asymmetric, both in their genome organisation and protein composition (MP and extended coat protein). The EM maps presented here are all biased by the icosahedral symmetry of the capsid, and do not provide strong clues to the location of the maturation protein or C-terminally extended coat protein. These features are present in one (MP) or low and variable (C-terminally extended coat protein) copy numbers in each virion, and contribute little to the electron density of each particle compared with the mass of the whole capsid. The SPA approach used here is likely, at least in part, to have aligned particles based on the overarching icosahedral symmetry of the particles, even when that symmetry is not imposed. Thus features with low mass are likely somewhat misaligned and lost in the reconstructions. Alternative approaches are needed to locate such asymmetric components. For the MP, this has been tackled by utilising its role in binding virions to pili. In work by Dent *et al,* subtomogram averaging was used to show that the MP replaces one of the dimer subunits (Dent *et al*., 2013). An alternative approach could involve the use of adherons. Adherons could be raised against Qβ, with a negative selection against recombinantly produced capsids, which do not contain the MP. This could yield binders that are specific to the maturation protein. The adheron mass could then be used during classification and alignment to locate the MP.

The asymmetric genomic RNA is packaged with pseudo-icosahedral symmetry, with different sequences bound with different affinity at each symmetry-related binding site. The RNA must therefore be improperly averaged, and/or disordered, and refinement of the structure is biased by the icosahedral structure of the capsid. An interesting approach to tackle such symmetry mis-matches between genome and capsids, and therefore provide structural evidence about genome organisation, is to subtract density associated with the capsid from the raw images, and apply SPA to these new particles to generate a structure containing information relating to the genome. This has been applied to dsRNA cypovirus genomes and associated polymerases in work published recently (Liu & Cheng, 2015). Applying this method to the Qβ genome may yield new insights into genome organisation.

6 Concluding remarks

In this thesis, different cryo-EM methodologies have been utilised to obtain high-resolution information for two different biological systems; amyloid-membrane interactions (tomography) and Qβ bacteriophage (SPA). These two studies illustrate the emerging ability of cryo-EM to provide insightful information for arrange of different biological questions.

Although cryo-EM has been in development since the 1970s, the recent development of improved EMs, DEDs and improved image processing algorithms 'resolution revolution' and flurry of high-resolution structures has promoted increased interest in the technique (Bartesaghi *et al*., 2015; M.G. Campbell *et al*., 2015; Kuehlbrandt, 2014; Hu *et al*., 2015, Hesketh *et al.,* 2015b). Only recently has obtaining sub 10 Å structures by SPA become routine for many macromolecular complexes. Cryo-EM is an emerging method for high-resolution structure determination. The EMDB contains > 2500 released density maps by SPA, with this being the most popular technique for structure determination by EM (Figure 6-1 A). Trends show the number of depositions is growing year on year, with many more high-resolution structures being released (Figure 6-1 B,C). Even at lower resolutions EM structures can be highly informative; density maps ~ 8-20 Å can be used to place crystal or NMR structures of individual complex components into context within a larger macromolecular complex (Dodonova *et al*., 2015; Rawson *et al*., 2015).

While the emergence of cryo-EM and single particle techniques as a powerful tool for high resolution (< 5 Å) structure determination by SPA is exciting and is changing our understanding of a range of macromolecular complexes, cryo-ET and subtomogram averaging, will be the biggest area of growth in the medium term. Due to development of microscopes with increased stage stability, the development of a range of specimen preparation techniques (FIB milling, HPF) and development of complementary technologies (CLEM), cryo-ET can be applied to a range of biological questions in a way that was not previously possible. Cryo-electron tomography uniquely can reveal structural properties of complexes in context and *in situ,* at ~ 5-10 nm resolution range. By providing cellular information at this resolution range, cryo-EM can truly start to fill the void between cell biology and high-resolution structures of individual complexes.

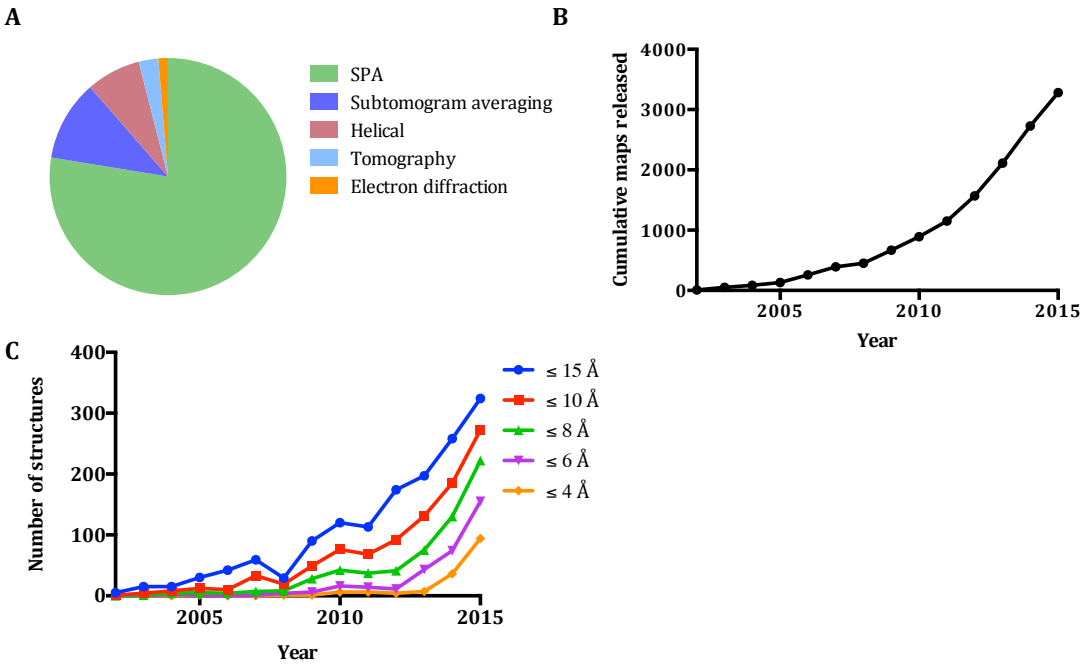

Figure 6-1 Structures in the EMDB. A) Proportion of released maps as a function of EM technique used B) Cumulative map releases in the EMDB between 2002-2015. C) Map releases at given resolution levels between 2002-2015. Statistics from EMDB, accessed November 2015.

In conclusion, over the course of this project, EM has become a technique that can routinely offer high-resolution information for a wide spectrum of specimens. While challenges remain, and improvements can still be made, it is an exciting time to be an electron microscopist.

7 References

Abrescia *et al*. 2012. Structure Unifies the Viral Universe. *Annual Review of Biochemistry, Vol 84*. **81**(1),pp.795–822.

Ackermann, H.W. 2009. Phage Classification and Characterization In Bacteriophages. *Methods in Molecular Biology*. pp. 127–140.

Adrian, M. *et al*. 1984. Cryo-electron microscopy of viruses. *Review Literature And Arts Of The Americas*. **308**(5954),pp.32–36.

Agronskaia, A.V. *et al*. 2008. Integrated fluorescence and transmission electron microscopy. *Journal of Structural Biology*. **164**(2),pp.183–189.

Aguzzi, A. and Falsig, J. 2012. Prion propagation, toxicity and degradation. *Nature Neuroscience*. **15**(7),pp.936–939.

Aits, S. and Jäättelä, M. 2013. Lysosomal cell death at a glance. *Journal of Cell Science*. **126**(Pt 9),pp.1905–1912.

Al-Amoudi, A., Chang, J.J., *et al*. 2004. Cryo-electron microscopy of vitreous sections. *The EMBO journal*. **23**(18),pp.3583–3588.

Al-Amoudi, A., Norlen, L., *et al*. 2004. Cryo-electron microscopy of vitreous sections of native biological cells and tissues. *Journal of Structural Biology*. **148**(1),pp.131–135.

Alikhani, N. *et al*. 2011. Decreased proteolytic activity of the mitochondrial amyloid-β degrading enzyme, PreP peptidasome, in Alzheimer's disease brain mitochondria. *Journal of Alzheimer's disease*. **27**(1),pp.75–87.

Alzheimer's Association 2015. 2015 Alzheimer's disease facts and figures. *Alzheimer's & dementia : the journal of the Alzheimer's Association*. **11**(3),pp.332–384.

Ambroggio, E.E. *et al*. 2005. Direct visualization of membrane leakage induced by the antibiotic peptides: Maculatin, citropin, and aurein. *Biophysical Journal*. **89**(3),pp.1874–1881.

Amos, B. 2000. Lessons from the history of light microscopy. *Nature Cell Biology*. **2**(8),pp.E151–E152.

Anderluh, G. *et al*. 2005. Interaction of human stefin B in the prefibrillar oligomeric form with membranes. Correlation with cellular toxicity. *FEBS Journal*. **272**(12),pp.3042–3051.

Andersen, B.B. *et al*. 2003. Aging of the human cerebellum: a stereological study. *The Journal of comparative neurology*. **466**(3),pp.356–365.

Angot, E. *et al*. 2010. Are synucleinopathies prion-like disorders? *The Lancet*. **9**(11),pp.1128–1138.

Mayer, RJ *et al* 1988. Intermediate filaments and ubiquitin: a new thread in the understanding of chronic neurodegenerative diseases. *Progress in clinical and biological research*. **317**,pp.809–818.

Argiles, A. *et al*. 2002. Phagocytosis of dialysis-related amyloid deposits by macrophages. *Nephrology, dialysis, transplantation : official publication of the European Dialysis and Transplant Association - European Renal Association*. **17**(6),pp.1136–1138.

Astbury, W.T. and Marwick, T.C. 1931. Structure of the Crystal Lattice of Cellulose. *Nature*. **127**(3192),pp.12–13.

Astbury, W.T. and Sisson, W.A. 1935. X-Ray Studies of the Structure of Hair, Wool, and Related Fibres. III. The Configuration of the Keratin Molecule and Its Orientation in the Biological Cell

Astbury, W.T. *et al*. 1935. The X-ray interpretation of denaturation and the structure of the seed globulins. *The Biochemical journal*. **29**(10),pp.2351–2360.1.

Atilla-Gokcumen, G.E. *et al*. 2014. Dividing cells regulate their lipid composition and localization. *Cell*. **156**(3),pp.428–439.

Badtke, M.P. *et al*. 2009. Functional Amyloids Signal Their Arrival. *Science signaling*. **2**(80),pp.pe43–pe43.

Bae, S. *et al*. 2015. Torsion-dependent fluorescence switching of amyloid-binding dye NIAD-4. *Chemical Physics Letters*. **633**,pp.109–113.

Bai, X.C. *et al*. 2013. Ribosome structures to near-atomic resolution from thirty thousand cryo-EM particles W. Kuhlbrandt, ed. *eLife*. **2**,p.e00461.

Bai, X.C., McMullan, G., *et al*. 2015. How cryo-EM is revolutionizing structural biology. *Trends in Biochemical Sciences*. **40**(1),pp.49–57.

Bai, X.C., Yan, C., *et al*. 2015. An atomic structure of human γ-secretase. *Nature*.

Baker, L.A. and Rubinstein, J.L. 2010. Radiation Damage in Electron Cryomicroscopy. *Methods in enzymology*. **481**,pp.371–388.

Baker, T.S. *et al*. 1999. Adding the third dimension to virus life cycles: three-dimensional reconstruction of icosahedral viruses from cryo-electron micrographs. *Microbiology and Molecular Biology Reviews*. **63**(4),pp.862–922– table of contents.

Bakker, S.E. *et al*. 2013. The respiratory syncytial virus nucleoprotein-RNA complex forms a left-handed helical nucleocapsid. *Journal of General Virology*. **94**(Pt 8),pp.1734–1738.

Balch, W.E. and Rothman, J.E. 1985. Characterization of protein transport between successive compartments of the Golgi apparatus: asymmetric properties of donor and acceptor activities in a cell-free system. *Archives of biochemistry and biophysics*. **240**(1),pp.413–425.
Balch, W.E. *et al*. 2008. Adapting proteostasis for disease intervention. *Science*. **319**(5865),pp.916–919.
Ballatore, C. *et al*. 2007. Tau-mediated neurodegeneration in Alzheimer's disease and related disorders. *Nature Reviews Neuroscience*. **8**(9),pp.663–672.
Bartels, T. *et al*. 2011. α-Synuclein occurs physiologically as a helically folded tetramer that resists aggregation. *Nature*. **477**(7362),pp.107–110.
Bartesaghi, A. *et al*. 2015. 2.2 angstrom resolution cryo-EM structure of beta-galactosidase in complex with a cell-permeant inhibitor. *Science*. **348**(6239),pp.1147–1151.
Basnak, G. *et al*. 2010. Viral Genomic Single-Stranded RNA Directs the Pathway Toward a T=3 Capsid. *Journal of Molecular Biology*. **395**(5),pp.924–936.
Baumeister, W. and Walz, J. 1998. The proteasome: paradigm review of a self-compartmentalizing protease. *Cell*.
Bellingham, S.A. *et al*. 2012. Exosomes: vehicles for the transfer of toxic proteins associated with neurodegenerative diseases? *Frontiers in Physiology*. **3**,p.124.
Bence, N.F. *et al*. 2001. Impairment of the ubiquitin-proteasome system by protein aggregation. *Science*. **292**(5521),pp.1552–1555.
Berriman, J.A. *et al*. 2009. Structural organization of Weibel-Palade bodies revealed by cryo-EM of vitrified endothelial cells. *Proceedings of the National Academy of Sciences of the United States of America*. **106**(41),pp.17407–17412.
Berson, J.F. *et al*. 2003. Proprotein convertase cleavage liberates a fibrillogenic fragment of a resident glycoprotein to initiate melanosome biogenesis. *The Journal of Cell Biology*. **161**(3),pp.521–533.
Berthelot, K. *et al*. 2013. What does make an amyloid toxic: Morphology, structure or interaction with membrane? *Biochimie*. **95**(1),pp.12–19.
Bertoncini, C.W. and Celej, M.S. 2011. Small molecule fluorescent probes for the detection of amyloid self-assembly in vitro and in vivo. *Current protein & peptide science*. **12**(3),pp.205–220.
Betzig, E. *et al*. 2006. Imaging intracellular fluorescent proteins at nanometer resolution. *Science (New York, N.Y.)*. **313**(5793),pp.1642–1645.
Bhella, D. and Bakker, S.E. 2013. Pretty Nasty, symmetry in virus architecture. *Biochemist*, 35(2), pp. 14-19.
Biancalana, M. and Koide, S. 2010. Molecular mechanism of Thioflavin-T binding to amyloid fibrils. *Biochimica et Biophysica Acta*. **1804**(7),pp.1405–1412.
Biancalana, M. *et al*. 2010. Minimalist design of water-soluble cross-beta architecture. *Proceedings of the National Academy of Sciences*. **107**(8),pp.3469–3474.
Bianconi, E. *et al*. 2013. An estimation of the number of cells in the human body. *Annals of human biology*. **40**(6),pp.463–471.
Boeré, H. *et al*. 1965. Electron microscopic studies on the fibrillar component of human splenic amyloid. *The Journal of laboratory and clinical medicine*. **66**(6),pp.943–951.
Boland, B. and Campbell, V. 2004. Abeta-mediated activation of the apoptotic cascade in cultured cortical neurones: a role for cathepsin-L. *Neurobiology of Aging*. **25**(1),pp.83–91.
Boland, B. *et al*. 2008. Autophagy induction and autophagosome clearance in neurons: Relationship to autophagic pathology in Alzheimer's disease. *The Journal of Neuroscience*. **28**(27),pp.6926–6937.
Bollback, J.P. and Huelsenbeck, J.P. 2001. Phylogeny, genome evolution, and host specificity of single-stranded RNA bacteriophage (family Leviviridae). *Journal of molecular evolution*. **52**(2),pp.117–128.
Bolognesi, B. *et al*. 2010. ANS Binding Reveals Common Features of Cytotoxic Amyloid Species. *ACS Chemical Biology*. **5**(8),pp.735–740.
Booth, D.S. *et al*. 2011. Visualizing proteins and macromolecular complexes by negative stain EM: from grid preparation to image acquisition. *Journal of visualized experiments : JoVE*. (58),pp.e3227–e3227.
Borbulevych, O.Y. *et al*. 2010. Structures of native and affinity-enhanced WT1 epitopes bound to HLA-A*0201: implications for WT1-based cancer therapeutics. *Molecular immunology*. **47**(15),pp.2519–2524.
Borghi, R. *et al*. 2000. Full length alpha-synuclein is present in cerebrospinal fluid from Parkinson's disease and normal subjects. *Neuroscience Letters*. **287**(1),pp.65–67.
Boya, P. and Kroemer, G. 2008. Lysosomal membrane permeabilization in cell death. *Oncogene*. **27**(50),pp.6434–6451.

Bragg, W.H. and Bragg, W.L. 1913. The reflection of X-rays by crystals. *Royal Society Proceedings A* **88**(605)

Brandenburg, E. *et al*. 2012. Specific in situ discrimination of amyloid fibrils versus α-helical fibres by the fluorophore NIAD-4. *Molecular bioSystems*. **8**(2),pp.557–564.

Brenner, S. and Horne, R.W. 1959. A Negative Staining Method for High Resolution Electron Microscopy of Viruses. *Biochimica et Biophysica Acta*. **34**(1),pp.103–110.

Brown, E. and Verkade, P. 2010. The use of markers for correlative light electron microscopy. *Protoplasma*. **244**(1-4),pp.91–97.

Brown, M.R. *et al*. 2006. Synaptic mitochondria are more susceptible to Ca^{2+}overload than nonsynaptic mitochondria. *Journal of Biological Chemistry*. **281**(17),pp.11658–11668.

Brundin, P. *et al*. 2010. Prion-like transmission of protein aggregates in neurodegenerative diseases. *Nature Reviews Molecular Cell Biology*. **11**(4),pp.301–307.

Buell, A.K. *et al*. 2011. Population of Nonnative States of Lysozyme Variants Drives Amyloid Fibril Formation. *Journal of the American Chemical Society*. **133**(20),pp.7737–7743.

Buell, A.K. *et al*. 2014. Solution conditions determine the relative importance of nucleation and growth processes in alpha-synuclein aggregation. *Proceedings of the National Academy of Sciences of the United States of America*. **111**(21),pp.7671–7676.

Bull, H. *et al*. 2002. Acid phosphatases. *Molecular Pathology* **55**(2):65-72.

Burgess, S.A. *et al*. 2004. The structure of dynein-c by negative stain electron microscopy. *Journal of Structural Biology*. **146**(1-2),pp.205–216.

Butcher, S.J. *et al*. 2011. Lipid-Containing Viruses: Bacteriophage PRD1 Assembly *In*: *Viral Molecular Machines*. Advances in Experimental Medicine and Biology. Boston, MA: Springer US, pp. 365–377.

Campbell, M.G. *et al*. 2015. 2.8 angstrom resolution reconstruction of the Thermoplasma acidophilum 20S proteasome using cryo-electron microscopy. *eLife*. **4**.

Campioni, S. *et al*. 2010. A causative link between the structure of aberrant protein oligomers and their toxicity. *Nature Chemical Biology*. **6**(2),pp.140–147.

Campistol, J.M. 2001. Dialysis-related amyloidosis after renal transplantation. *Seminars in dialysis*. **14**(2),pp.99–102.

Cantalupo, P.G. *et al*. 2011. Raw Sewage Harbors Diverse Viral Populations. *Mbio*. **2**(5),pp.–e00180–11.

Carlson, D.B. and Evans, J.E. 2011. *Low-cost cryo-light microscopy stage fabrication for correlated light-electron microscopy. Journal Visualized experiments* 5;(52)

Carlson, D.B. *et al*. 2013. Laboratory-based cryogenic soft x-ray tomography with correlative cryo-light and electron microscopy. *Microscopy and microanalysis : the official journal of Microscopy Society of America, Microbeam Analysis Society, Microscopical Society of Canada*. **19**(1),pp.22–29.

Carlson, L.A. *et al*. 2010. Cryo electron tomography of native HIV-1 budding sites. *PLoS Pathogens*. **6**(11),p.e1001173.

Carragher, B. *et al*. 2000. Leginon: an automated system for acquisition of images from vitreous ice specimens. *Journal of Structural Biology*. **132**(1),pp.33–45.

Carrell, R.W. 2005. Cell toxicity and conformational disease. *Trends in cell biology*. **15**(11),pp.574–580.

Casey, T.M. *et al*. 2007. Organelle proteomics: identification of the exocytic machinery associated with the natural killer cell secretory lysosome. *Molecular cellular proteomics* . **6**(5),pp.767–780.

Caughey, B. and Lansbury, P.T. 2003. Protofibrils, pores, fibrils, and neurodegeneration: Separating the responsible protein aggregates from the innocent bystanders. *Annual Review of Neuroscience*. **26**(1),pp.267–298.

Chafekar, S.M. *et al*. 2008. Oligomer-specific Abeta toxicity in cell models is mediated by selective uptake. *Biochimica et Biophysica Acta*. **1782**(9),pp.523–531.

Chang, T.-Y. *et al*. 2005. Niemann-Pick Type C Disease and Intracellular Cholesterol Trafficking. *Journal of Biological Chemistry*. **280**(22),pp.20917–20920.

Chang, Y.-W. *et al*. 2014. Correlated cryogenic photoactivated localization microscopy and cryo-electron tomography. *Nature Methods*. **11**(7),pp.737–U179.

Chao, W. *et al*. 2009. Demonstration of 12 nm Resolution Fresnel Zone Plate Lens based Soft X-ray Microscopy. *Optics Express*. **17**(20),pp.17669–17677.

Chapman, M.S. and Liljas, L. 2003. Structural Folds of Viral Proteins *In*: *Virus Structure*. Advances in Protein Chemistry. Elsevier, pp. 125–196.

Charmaine D Rochester, O.A. 2014. Novel and emerging diabetes mellitus drug therapies for the type 2 diabetes patient. *World journal of diabetes*. **5**(3),pp.305–315.

Chase, T.N. 1998. Levodopa therapy Consequences of the nonphysiologic replacement of dopamine. *Neurology*. **50**(5 Suppl 5),pp.S17–S25.

Chebukati, J.N. *et al*. 2010. Bis(monoacylglycero)phosphate and ganglioside GM1 spontaneously form small homogeneous vesicles at specific concentrations. *Biochemical and biophysical research communications*. **394**(3),pp.509–514.

Chen, R.F. and Knutson, J.R. 1988. Mechanism of fluorescence concentration quenching of carboxyfluorescein in liposomes: energy transfer to nonfluorescent dimers. *Analytical biochemistry*. **172**(1),pp.61–77.

Chen, S. *et al*. 2013. High-resolution noise substitution to measure overfitting and validate resolution in 3D structure determination by single particle electron cryomicroscopy. *Ultramicroscopy*. **135**,pp.24–35.

Chen, V.B. *et al*. 2010. MolProbity: all-atom structure validation for macromolecular crystallography. *Acta Crystallographica Section D: Biological Crystallography*. **66**(Pt 1),pp.12–21.

Cheng, L. *et al*. 2010. Backbone model of an aquareovirus virion by cryo-electron microscopy and bioinformatics. *Journal of Molecular Biology*. **397**(3),pp.852–863.

Chiti, F. and Dobson, C.M. 2006. Protein misfolding, functional amyloid, and human disease. *Annual Review of Biochemistry*. **75**(1),pp.333–366.

Chlanda, P. and Sachse, M. 2014. Cryo-electron microscopy of vitreous sections. *Methods in molecular biology*. **1117** (Chapter 10),pp.193–214.

Choo-Smith, L.P. *et al*. 1997. Acceleration of amyloid fibril formation by specific binding of Abeta-(1-40) peptide to ganglioside-containing membrane vesicles. *Journal of Biological Chemistry*. **272**(37),pp.22987–22990.

Ciechanover, A. *et al*. 2000. Ubiquitin-mediated proteolysis: biological regulation via destruction. *Bioessays*.

Clarke, M. *et al*. 2008. F-pili dynamics by live-cell imaging. *Proceedings of the National Academy of Sciences*. **105**(46),pp.17978–17981.

Cleary, J.P. *et al*. 2005. Natural oligomers of the amyloid-beta protein specifically disrupt cognitive function. *Nature Neuroscience*. **8**(1),pp.79–84.

Cluck, M.W. *et al*. 2005. The Regulation of Amylin and Insulin Gene Expression and Secretion. *Pancreas*. **30**(1),p.1.

Cohen, A.S. and Calkins, E. 1959. Electron microscopic observations on a fibrous component in amyloid of diverse origins. *Nature*. **183**(4669),pp.1202–1203.

Cohen, S.I.A. *et al*. 2013. Proliferation of amyloid-beta 42 aggregates occurs through a secondary nucleation mechanism. *Proceedings of the National Academy of Sciences of the United States of America*. **110**(24),pp.9758–9763.

Collins, S.J. *et al*. 2004. Transmissible spongiform encephalopathies. *The Lancet*. **363**(9402),pp.51–61.

Collins, S.R. *et al*. 2004. Mechanism of Prion Propagation: Amyloid Growth Occurs by Monomer Addition. *PLoS Biol*. **2**(10),p.e321.

Correa, I.R.J. 2014. Live-cell reporters for fluorescence imaging. *Current Opinion in Chemical Biology*. **20**,pp.36–45.

Corrigan, F. *et al*. 2014. The neuroprotective activity of the amyloid precursor protein against traumatic brain injury is mediated via the heparin binding site in residues 96-110. *Journal of neurochemistry*. **128**(1),pp.196–204.

Crawford, R. *et al*. 2011. Analysis of lipid nanoparticles by Cryo-EM for characterizing siRNA delivery vehicles. *International journal of pharmaceutics*. **403**(1-2),pp.237–244.

Cremades, N. *et al*. 2012. Direct Observation of the Interconversion of Normal and Toxic Forms of α-Synuclein. *Cell*. **149**(5),pp.1048–1059.

Crowther, R.A. *et al*. 1970. Three dimensional reconstructions of spherical viruses by fourier synthesis from electron micrographs. *Nature*. **226**(5244),pp.421–425.

Cummings, C.J. *et al*. 1999. Mutation of the E6-AP Ubiquitin Ligase Reduces Nuclear Inclusion Frequency While Accelerating Polyglutamine-Induced Pathology in SCA1 Mice. *Neuron*. **24**(4),pp.879–892.

Curd, A. *et al*. 2015. Construction of an instant structured illumination microscope. *Methods (San Diego, Calif.)*.

Dai, W. *et al*. 2013. Visualizing virus assembly intermediates inside marine cyanobacteria. *Nature*. **502**(7473),pp.707.

Dai, W. *et al*. 2014. Zernike phase-contrast electron cryotomography applied to marine cyanobacteria infected with cyanophages. *Nature protocols*. **9**(11),pp.2630–2642.

Danev, R. and Nagayama, K. 2001. Transmission electron microscopy with Zernike phase plate. *Ultramicroscopy*. **88**(4),pp.243–252.

Danev, R. *et al*. 2014. Volta potential phase plate for in-focus phase contrast transmission electron microscopy. *Proceedings of the National Academy of Sciences*.

De Carlo, S. *et al*. n.d. New technologies for Cryo-EM: Volta Phase Plate and Falcon-III Electron Counting. *Microscopy*.

De Kimpe, L. *et al*. 2012. Intracellular accumulation of aggregated pyroglutamate amyloid beta: convergence of aging and Aβ pathology at the lysosome. *AGE* 5(3):673-87.

Debelouchina, G.T. *et al*. 2010. Magic Angle Spinning NMR Analysis of beta(2)-Microglobulin Amyloid Fibrils in Two Distinct Morphologies. *Journal of the American Chemical Society*. **132**(30),pp.10414–10423.

Dehay, B. *et al*. 2010. Pathogenic lysosomal depletion in Parkinson's disease. *The Journal of neuroscience : the official journal of the Society for Neuroscience*. **30**(37),pp.12535–12544.

Dell'Angelica, E.C. *et al*. 2000. Lysosome-related organelles. *FASEB journal*. **14**(10),pp.1265–1278.

Demuro, A. *et al*. 2005. Calcium dysregulation and membrane disruption as a ubiquitous neurotoxic mechanism of soluble amyloid oligomers. *Journal of Biological Chemistry*. **280**(17),pp.17294–17300.

Dent, K.C. *et al*. 2014. Critical step-by-step approaches toward correlative fluorescence/soft X-ray cryo-microscopy of adherent mammalian cells. *Methods in cell biology*. **124**,pp.179–216.

Dent, K.C. *et al*. 2013. The Asymmetric Structure of an Icosahedral Virus Bound to Its Receptor Suggests a Mechanism for Genome Release. *Structure (London, England : 1993)*. **21**(7),pp.1225–1234.

Desplats, P. *et al*. 2009. Inclusion formation and neuronal cell death through neuron-to-neuron transmission of alpha-synuclein. *Proceedings of the National Academy of Sciences of the United States of America*. **106**(31),pp.13010–13015.

Dickson, D.W. *et al*. 2009. Neuropathological assessment of Parkinson's disease: refining the diagnostic criteria. *The Lancet*. **8**(12),pp.1150–1157.

Diestra, E. *et al*. 2009. Cellular electron microscopy imaging reveals the localization of the Hfq protein close to the bacterial membrane. C. Mayer, ed. *PLoS ONE*. **4**(12),p.e8301.

DiMaio, F. *et al*. 2015. Atomic-accuracy models from 4.5-A cryo-electron microscopy data with density-guided iterative local refinement. *Nature Methods*. **12**(4),pp.361–365.

Ding, T.T. *et al*. 2002. Annular alpha-synuclein protofibrils are produced when spherical protofibrils are incubated in solution or bound to brain-derived membranes. *Biochemistry*. **41**(32),pp.10209–10217.

Ding, W. *et al*. 2015. Neurodegeneration and cognition in Parkinson's disease: a review. *European Review for Medical and Pharmacological Sciences*. **19**(12),pp.2275–2281.

Ditaranto, K. *et al*. 2001. Lysosomal membrane damage in soluble Abeta-mediated cell death in Alzheimer's disease. *Neurobiology of Disease*. **8**(1),pp.19–31.

Dobro, M.J. *et al*. 2010. Plunge Freezing for Electron Cryomicroscopy. *Methods in enzymology*. **481**,pp.63–82.

Dobson, C.M. 2003. Protein folding and misfolding. H. Fabian & D. Naumann, eds. *Nature*. **426**(6968),pp.884–890.

Dobson, C.M. 2001. The structural basis of protein folding and its links with human disease. *Philosophical transactions of the Royal Society of London. Series B, Biological sciences*. **356**(1406),pp.133–145.

Dodonova, S.O. *et al*. 2015. Vesicular Transport. A structure of the COPI coat and the role of coat proteins in membrane vesicle assembly. *Science (New York, N.Y.)*. **349**(6244),pp.195–198.

Drenth, J. 2007. *X-Ray Crystallography*. Hoboken, NJ, USA: John Wiley & Sons, Inc.

Dubochet, J. and Lepault, J. 1984. Cryo-electron microscopy of vitrified water. *Journal De Physique*. **9**(45).

Dubochet, J. *et al*. 1988. Cryo-electron microscopy of vitrified specimens. *Quarterly Reviews of Biophysics*. **21**(02),pp.129–228.

Dueholm, M.S. *et al*. 2011. Fibrillation of the Major Curli Subunit CsgA under a Wide Range of Conditions Implies a Robust Design of Aggregation. *Biochemistry*. **50**(39), pp.8281-90

Duin, J. 2006. *Bacteriophages with ssRNA*. Chichester, UK: John Wiley & Sons, Ltd.

Duke, E.M.H. *et al*. 2014. Imaging endosomes and autophagosomes in whole mammalian cells using correlative cryo-fluorescence and cryo-soft X-ray microscopy (cryo-CLXM). *Ultramicroscopy*. **143**,pp.77–87.

Dykeman, E.C. *et al*. 2010. Dynamic Allostery Controls Coat Protein Conformer Switching during MS2 Phage Assembly. *Journal of Molecular Biology*. **395**(5),pp.916–923.

Dykeman, E.C. *et al*. 2013. Packaging Signals in Two Single-Stranded RNA Viruses Imply a Conserved Assembly Mechanism and Geometry of the Packaged Genome. *Journal of Molecular Biology*. **425**(17),pp.3235–3249.

Dykeman, E.C. *et al*. 2011. Simple Rules for Efficient Assembly Predict the Layout of a Packaged Viral RNA. *Journal of Molecular Biology*. **408**(3),pp.399–407.

Eakin, C.M. and Miranker, A.D. 2005. From chance to frequent encounters: origins of beta2-

microglobulin fibrillogenesis. *Biochimica et Biophysica Acta*. **1753**(1),pp.92–99.
Eanes, E.D. and Glenner, G.G. 1968. X-ray diffraction studies on amyloid filaments. *The journal of histochemistry and cytochemistry official journal of the Histochemistry Society*. **16**(11),pp.673–677.
Eichner, T. *et al*. 2011. Conformational Conversion during Amyloid Formation at Atomic Resolution. *Molecular Cell*. **41**(2),pp.161–172.
Eisele, Y.S. *et al*. 2009. Induction of cerebral beta-amyloidosis: intracerebral versus systemic Abeta inoculation. *Proceedings of the National Academy of Sciences*. **106**(31),pp.12926–12931.
Elmlund, D. and Elmlund, H. 2012. SIMPLE: Software for ab initio reconstruction of heterogeneous single-particles. *Journal of Structural Biology*. **180**(3),pp.420–427.
Emmelot, P. *et al*. 1964. Studies on Plasma Membranes. I. Chemical Composition and enzyme content of plasma membranes isolated from rat liver. *Biochimica et Biophysica Acta*. **90**,pp.126–145.
Emsley, P. *et al*. 2010. Features and development of Coot. *Acta Crystallographica Section D: Biological Crystallography*. **66**(Pt 4),pp.486–501.
Engel, M.F.M. *et al*. 2008. Membrane damage by human islet amyloid polypeptide through fibril growth at the membrane. *Proceedings of the National Academy of Sciences of the United States of America*. **105**(16),pp.6033–6038.
Esposito, G. *et al*. 2000. Removal of the N-terminal hexapeptide from human beta2-microglobulin facilitates protein aggregation and fibril formation. *Protein Science*. **9**(5),pp.831–845.
Evans, J.E. and Browning, N.D. 2013. Enabling direct nanoscale observations of biological reactions with dynamic TEM. *Microscopy*. **62**(1),pp.147–156.
Evans, M.L. and Chapman, M.R. 2014. Curli biogenesis: Order out of disorder. *Biochimica Et Biophysica Acta-Molecular Cell Research*. **1843**(8),pp.1551–1558.
Evans, M.L. *et al*. 2015. The Bacterial Curli System Possesses a Potent and Selective Inhibitor of Amyloid Formation. *Molecular Cell*. **57**(3),pp.445–455.
Faruqi, A.R. and McMullan, G. 2011. Electronic detectors for electron microscopy. *Quarterly Reviews of Biophysics*. **44**(3),pp.357–390.
Fernandez, J.J. *et al*. 2008. Sharpening high resolution information in single particle electron cryomicroscopy. *Journal of Structural Biology*. **164**(1),pp.170–175.
Fernández de Castro, I. *et al*. 2014. Metallothioneins for correlative light and electron microscopy. *Methods in cell biology*. **124**,pp.55–70.
Fernández, I.S. *et al*. 2013. Molecular architecture of a eukaryotic translational initiation complex. *Science (New York, N.Y.)*. **342**(6160),p.1240585.
Fernández-Borges, N. *et al*. 2015. Animal models for prion-like diseases. *Virus research*. **207**,pp.5–24.
Ferraz, T.P.L. *et al*. 2004. Comparison of six methods for the extraction of lipids from serum in terms of effectiveness and protein preservation. *Journal of biochemical and biophysical methods*. **58**(3),pp.187–193.
Ferrone, F. 1999. [17] Analysis of protein aggregation kinetics *In*: *Amyloid, Prions, and Other Protein Aggregates*. Methods in Enzymology. Elsevier, pp. 256–274.
Fiers, W. *et al*. 1976. Complete nucleotide sequence of bacteriophage MS2 RNA: primary and secondary structure of the replicase gene. *Nature*. **260**(5551),pp.500–507.
Fischer, N. *et al*. 2015. Structure of the E. coli ribosome-EF-Tu complex at <3 Å resolution by Cs-corrected cryo-EM. *Nature*. **520**(7548),pp.567–570.
Fitzpatrick, A.W.P. *et al*. 2013. Atomic structure and hierarchical assembly of a cross-β amyloid fibril. *Proceedings of the National Academy of Sciences*. **110**(14),pp.5468–5473.
Floege, J. and Ehlerding, G. 1996. Beta-2-Microglobulin-Associated Amyloidosis. *Nephron*. **72**(1),pp.9–26.
Floege, J. and Ketteler, M. 2001. Beta-2-Microglobulin derived amyloidosis: An update. *Kidney International*. **59**(s78),pp.S164–S171.
Floege, J. *et al*. 1991. Clearance and synthesis rates of beta 2-microglobulin in patients undergoing hemodialysis and in normal subjects. *The Journal of laboratory and clinical medicine*. **118**(2),pp.153–165.
Fokine, A. and Rossmann, M.G. 2014. Molecular architecture of tailed double-stranded DNA phages. *Bacteriophage*. **4**(1),p.e28281.
Ford, T. *et al*. 1994. Iodixanol: a nonionic iso-osmotic centrifugation medium for the formation of self-generated gradients. *Analytical biochemistry*. **220**(2),pp.360–366.
Fowler, D.M. *et al*. 2006. Functional amyloid formation within mammalian tissue. *PLoS Biol*. **4**(1),p.e6.
Fowler, D.M. *et al*. 2007. Functional amyloid--from bacteria to humans. *Trends in Biochemical Sciences*. **32**(5),pp.217–224.

Fox, N.C. *et al*. 1999. Correlation between rates of brain atrophy and cognitive decline in AD. *Neurology*. **52**(8),pp.1687–1689.
Förster, F. *et al*. 2008. Classification of cryo-electron sub-tomograms using constrained correlation. *Journal of Structural Biology*. **161**(3),pp.276–286.
Frank, A.O. *et al*. 1997. A finite-element model of oxygen diffusion in the pulmonary capillaries. *Journal of applied physiology (Bethesda, Md. : 1985)*. **82**(6),pp.2036–2044.
Frederick, T.E. *et al*. 2009. Bis(monoacylglycero)phosphate Forms Stable Small Lamellar Vesicle Structures: Insights into Vesicular Body Formation in Endosomes. *Biophysical Journal*. **96**(5),pp.1847–1855.
Freeman, D. *et al*. 2013. Alpha-synuclein induces lysosomal rupture and cathepsin dependent reactive oxygen species following endocytosis. *PLoS ONE*. **8**(4),p.e62143.
Friedman, S.D. *et al*. 2009. Gene Mapping and Phylogenetic Analysis of the Complete Genome from 30 Single-Stranded RNA Male-Specific Coliphages (Family Leviviridae). *Journal of virology*. **83**(21),pp.11233–11243.
Friedman, S.D. *et al*. 2012. Genomic Sequences of two Novel Levivirus Single-Stranded RNA Coliphages (Family Leviviridae): Evidence for Recombination in Environmental Strains. *Viruses-Basel*. **4**(9),pp.1548–1568.
Friedrich, R.P. *et al*. 2010. Mechanism of amyloid plaque formation suggests an intracellular basis of Abeta pathogenicity. *Proceedings of the National Academy of Sciences*. **107**(5),pp.1942–1947.
Frost, B. and Diamond, M.I. 2010. Prion-like mechanisms in neurodegenerative diseases. *Nature Reviews Neuroscience*. **11**(3),pp.155–159.
Frost, B. *et al*. 2009. Propagation of tau misfolding from the outside to the inside of a cell. *Journal of Biological Chemistry*. **284**(19),pp.12845–12852.
Fry, E.E. *et al*. 1999. Virus crystallography. *Molecular biotechnology*. **12**(1),pp.13–23.
Galvagnion, C. *et al*. 2015. Lipid vesicles trigger α-synuclein aggregation by stimulating primary nucleation. *Nature Chemical Biology*. **11**(3),pp.229–234.
Gan, L. and Jensen, G.J. 2012. Electron tomography of cells. *Quarterly Reviews of Biophysics*. **45**(1),pp.27–56.
Gerates *et al.* 2015 Asymmetric Genome Organization in an RNA Virus Revealed via Graph-Theoretical Analysis of Tomographic Data. *PLoS Computational Biology.* **11**(3).
Gerdes, H.-H. 2009. Prions tunnel between cells. *Nature Cell Biology*. **11**(3),pp.235–236.
Gest, H. 2004. *The discovery of microorganisms by Robert Hooke and Antoni Van Leeuwenhoek, fellows of the Royal Society.*
Gharibyan, A.L. *et al*. 2007. Lysozyme Amyloid Oligomers and Fibrils Induce Cellular Death via Different Apoptotic/Necrotic Pathways. *Journal of Molecular Biology*. **365**(5),pp.1337–1349.
Giepmans, B.N.G. *et al*. 2005. Correlated light and electron microscopic imaging of multiple endogenous proteins using Quantum dots. *Nature Methods*. **2**(10),pp.743–749.
Gilbert, P.F. 1972. The reconstruction of a three-dimensional structure from projections and its application to electron microscopy. II. Direct methods. *Proceedings of the Royal Society of London. Series B, Biological sciences*. **182**(1066),pp.89–102.
Gill, S.C. and Hippel, von, P.H. 1989. Calculation of protein extinction coefficients from amino acid sequence data. *Analytical biochemistry*. **182**(2),pp.319–326.
Glabe, C.G. 2006. Common mechanisms of amyloid oligomer pathogenesis in degenerative disease. *Neurobiology of Aging*. **27**(4),pp.570–575.
Glabe, C.G. 2004. Conformation-dependent antibodies target diseases of protein misfolding. *Trends in Biochemical Sciences*. **29**(10),pp.542–547.
Glabe, C.G. 2008. Structural Classification of Toxic Amyloid Oligomers. *The Journal of Biological Chemistry*. **283**(44),pp.29639–29643.
Goldsmith, C.S. and Miller, S.E. 2009. Modern Uses of Electron Microscopy for Detection of Viruses. *Clinical Microbiology Reviews*. **22**(4),pp.552.
Golmohammadi, R. *et al*. 1996. The crystal structure of bacteriophage Q beta at 3.5 A resolution. *Structure*. **4**(5),pp.543–554.
Gonen, T. *et al*. 2005. Lipid-protein interactions in double-layered two-dimensional AQP0 crystals. *Nature*. **438**(7068),pp.633–638.
Goodchild, S.C. *et al*. 2014. β2-Microglobulin Amyloid Fibril-Induced Membrane Disruption Is Enhanced by Endosomal Lipids and Acidic pH. *PLoS ONE*. **9**(8),p.e104492.
Goodsell, D.S. 2010. Mitochondrion. *Biochemistry and molecular biology education : a bimonthly publication of the International Union of Biochemistry and Molecular Biology*. **38**(3),pp.134–140.
Gosal, W.S. *et al*. 2005. Competing pathways determine fibril morphology in the self-assembly of beta2-microglobulin into amyloid. *Journal of Molecular Biology*. **351**(4),pp.850–864.
Gosavi, N. *et al*. 2002. Golgi fragmentation occurs in the cells with prefibrillar alpha-synuclein

aggregates and precedes the formation of fibrillar inclusion. *Journal of Biological Chemistry*. **277**(50),pp.48984–48992.
Grabenbauer, M. *et al*. 2005. Correlative microscopy and electron tomography of GFP through photooxidation. *Nature Methods*. **2**(11),pp.857–862.
Grant, T. and Grigorieff, N. 2015. Measuring the optimal exposure for single particle cryo-EM using a 2.6 Å reconstruction of rotavirus VP6. W. I. Sundquist, ed. *eLife*. **4**,p.e06980.
Grassucci, R.A. *et al*. 2007. Preparation of macromolecular complexes for cryo-electron microscopy. *Nature protocols*. **2**(12),pp.3239–3246.
Greninger, A.L. and DeRisi, J.L. 2015. Draft Genome Sequences of Leviviridae RNA Phages EC and MB Recovered from San Francisco Wastewater. *Genome announcements*. **3**(3),pp.e00652–15.
Haass, C. 2004. Take five-BACE and the γ-secretase quartet conduct Alzheimer's amyloid β-peptide generation. *The EMBO journal*. **23**(3),pp.483–488.
Haass, C. and Selkoe, D.J. 2007. Soluble protein oligomers in neurodegeneration: lessons from the Alzheimer's amyloid beta-peptide. *Nature Reviews Molecular Cell Biology*. **8**(2),pp.101–112.
Haass, C. *et al*. 2012. Trafficking and Proteolytic Processing of APP. *Cold Spring Harbor perspectives in medicine*. **2**(5),p.a006270.
Hagen, C. *et al*. 2012. Correlative VIS-fluorescence and soft X-ray cryo-microscopy/tomography of adherent cells. *Journal of Structural Biology*. **177**(2),pp.193–201.
Haguenau, F. *et al*. 2003. Key events in the history of electron microscopy. *Microscopy and microanalysis* **9**(2),pp.96–138.
Hall, C.E. 1955. Electron Densitometry of stained virus particles. *The Journal of biophysical and biochemical cytology*. **1**(1),pp.1–12.
Hammer, N.D. *et al*. 2007. The curli nucleator protein, CsgB, contains an amyloidogenic domain that directs CsgA polymerization. *Proceedings of the National Academy of Sciences of the United States of America*. **104**(30),pp.12494–12499.
Hardy, J.A. and Higgins, G.A. 1992. Alzheimer's disease: the amyloid cascade hypothesis. *Science*. **256**(5054),pp.184–185.
Harris, J.R. 2015. Transmission electron microscopy in molecular structural biology: A historical survey. *Archives of biochemistry and biophysics*. **581**,pp.3–18.
Harrison, S.C. *et al*. 1978. Tomato Bushy Stunt Virus at 2.9-a Resolution. *Nature*. **276**(5686),pp.368–373.
Hazelton, P.R. and Gelderblom, H.R. 2003. Electron microscopy for rapid diagnosis of infectious agents in emergent situations. *Emerging infectious diseases*. **9**(3),pp.294–303.
Hearing, V.J. 2000. The Melanosome: The Perfect Model for Cellular Responses to the Environment. *Pigment Cell Research*. **13**(s8),pp.23–34.
Hebda, J.A. and Miranker, A.D. 2009. The Interplay of Catalysis and Toxicity by Amyloid Intermediates on Lipid Bilayers: Insights from Type II Diabetes. *Annual Review of Biophysics*. **38**(1),pp.125–152.
Henderson, R. 2013. Avoiding the pitfalls of single particle cryo-electron microscopy: Einstein from noise. *Proceedings of the National Academy of Sciences of the United States of America*. **110**(45),pp.18037–18041.
Henderson, R. 1992. Image contrast in high-resolution electron microscopy of biological macromolecules: TMV in ice. *Ultramicroscopy*. **46**(1-4),pp.1–18.
Henderson, R. 1995. The potential and limitations of neutrons, electrons and X-rays for atomic resolution microscopy of unstained biological molecules. *Quarterly Reviews of Biophysics*. **28**(2),pp.171–193.
Henderson, R. *et al*. 1990. Model for the structure of bacteriorhodopsin based on high-resolution electron cryo-microscopy. *Journal of Molecular Biology*. **213**(4),pp.899–929.
Henderson, R. *et al*. 2011. Tilt-pair analysis of images from a range of different specimens in single-particle electron cryomicroscopy. *Journal of Molecular Biology*. **413**(5),pp.1028–1046.
Herva, M.E. and Spillantini, M.G. 2015. Parkinson's disease as a member of Prion-like disorders. *Virus research*. **207**,pp.38–46.
Hesketh, E.L. *et al*. 2015a. DNA Induces Conformational Changes in a Recombinant Human Minichromosome Maintenance Complex. *Journal of Biological Chemistry*. **290**(12),pp.7973–7979.
Hesketh, E.L *et al.* 2015b Mechanisms of assembly and genome packaging in an RNA virus revealed by high-resolution cryo-EM. *Nature Communications.* **6** p.10113
Hodkinson, J.P. *et al*. 2012. Protein Misfolding and Toxicity in Dialysis-Related Amyloidosis *In*: *Non-fibrillar Amyloidogenic Protein Assemblies - Common Cytotoxins Underlying Degenerative Diseases*. Dordrecht: Springer Netherlands, pp. 377–405.
Hofstetter, H. *et al*. 1974. The readthrough protein A1 is essential for the formation of viable Q beta particles. *Biochimica et Biophysica Acta*. **374**(2),pp.238–251.

Holmes, E.C. 2003. Error thresholds and the constraints to RNA virus evolution. *Trends in Microbiology*. **11**(12),pp.543–546.
Höppener, J.W. *et al*. 1993. Chronic overproduction of islet amyloid polypeptide/amylin in transgenic mice: lysosomal localization of human islet amyloid polypeptide and lack of marked hyperglycaemia or hyperinsulinaemia. *Diabetologia*. **36**(12),pp.1258–1265.
Höppener, J.W.M. and Lips, C.J.M. 2006. Role of islet amyloid in type 2 diabetes mellitus. *The international journal of biochemistry & cell biology*. **38**(5-6),pp.726–736.
Hu, Z. *et al*. 2015. Structural and biochemical basis for induced self-propagation of NLRC4. *Science*. **350**(6259),pp.399–404.
Huang, B. *et al*. 2010. Breaking the Diffraction Barrier: Super-Resolution Imaging of Cells. *Cell*. **143**(7),pp.1047–1058.
Huang, B. *et al*. 2009. Super-resolution fluorescence microscopy. *Annual Review of Biochemistry*. **78**(1),pp.993–1016.
Hurshman, A.R. *et al*. 2004. Transthyretin aggregation under partially denaturing conditions is a downhill polymerization. *Biochemistry*. **43**(23),pp.7365–7381.
Iadanza, M.G. and Gonen, T. 2014. A suite of software for processing MicroED data of extremely small protein crystals. *Journal of applied crystallography*. **47**(Pt 3),pp.1140–1145.
Ibiricu, I. *et al*. 2011. Cryo electron tomography of herpes simplex virus during axonal transport and secondary envelopment in primary neurons. *PLoS Pathogens*. **7**(12),p.e1002406.
Imai, H. *et al*. 2015. Direct observation shows superposition and large scale flexibility within cytoplasmic dynein motors moving along microtubules. *Nature Communications*. **6**,p.8179.
Isobe, I. *et al*. 1999. Enhancement of MTT, a tetrazolium salt, exocytosis by amyloid beta-protein and chloroquine in cultured rat astrocytes. *Neuroscience Letters*. **266**(2),pp.129–132.
Jahn, T.R. and Radford, S.E. 2008. Folding versus aggregation: Polypeptide conformations on competing pathways. *Archives of biochemistry and biophysics*. **469**(1),pp.100–117.
Jahn, T.R. *et al*. 2008. A Common beta-Sheet Architecture Underlies in Vitro and in Vivo beta-2-Microglobulin Amyloid Fibrils. *The Journal of Biological Chemistry*. **283**(25),pp.17279–17286.
Jahn, T.R. *et al*. 2006. Amyloid formation under physiological conditions proceeds via a native-like folding intermediate. *Nature Structural & Molecular Biology*. **13**(3),pp.195–201.
Jahn, T.R. *et al*. 2010. The common architecture of cross-beta amyloid. *Journal of Molecular Biology*. **395**(4),pp.717–727.
Jakhria, T. *et al*. 2014. β2-microglobulin amyloid fibrils are nanoparticles that disrupt lysosomal membrane protein trafficking and inhibit protein degradation by lysosomes. *The Journal of Biological Chemistry*. **289**(52),pp.35781–35794.
Jankovic, J. 2008. Parkinson's disease: clinical features and diagnosis. *Journal of Neurology, Neurosurgery & Psychiatry*. **79**(4),pp.368–376.
Jaunmuktane, Z. *et al*. 2015. Evidence for human transmission of amyloid-β pathology and cerebral amyloid angiopathy. *Nature*. **525**(7568),pp.247–250.
Ji, Z.-S. *et al*. 2002. Apolipoprotein E4 potentiates amyloid beta peptide-induced lysosomal leakage and apoptosis in neuronal cells. *Journal of Biological Chemistry*. **277**(24),pp.21821–21828.
Jin, L.W. *et al*. 2004. Intracellular accumulation of amyloidogenic fragments of amyloid-beta precursor protein in neurons with Niemann-Pick type C defects is associated with endosomal abnormalities (vol 164, pg 975, 2004). *The American journal of pathology*. **165**(4),pp.1447–1447.
Jones, S. *et al*. 2003. Role of the N and C-terminal strands of beta 2-microglobulin in amyloid formation at neutral pH. *Journal of Molecular Biology*. **330**(5),pp.935–941.
Joy, D.C. *et al*. 1986. Principles of analytical electron microscopy.
Jun, S. *et al*. 2011. Direct Visualization of HIV-1 with Correlative Live-Cell Microscopy and Cryo-Electron Tomography. *Structure*. **19**(11),pp.1573–1581.
Kad, N.M. *et al*. 2001. Beta(2)-microglobulin and its deamidated variant, N17D form amyloid fibrils with a range of morphologies in vitro. *Journal of Molecular Biology*. **313**(3),pp.559–571.
Kad, N.M., Myers, S.L., Smith, D.P., Smith, D.A., Radford, S.E. and Thomson, N.H. 2003. Hierarchical assembly of beta(2)-microglobulin amyloid in vitro revealed by atomic force microscopy. *Journal of Molecular Biology*. **330**(4),pp.785–797.
Kaminsky, Y.G. *et al*. 2015. Critical analysis of Alzheimer's amyloid-beta toxicity to mitochondria. *Frontiers in bioscience (Landmark edition)*. **20**,pp.173–197.
Kaplan, B.B. *et al*. 2009. Axonal protein synthesis and the regulation of local mitochondrial function. *Results and problems in cell differentiation*. **48**(Chapter 1),pp.225–242.
Karamanos, T.K. *et al*. 2014. Visualization of Transient Protein-Protein Interactions that Promote or Inhibit Amyloid Assembly. *Molecular Cell*. **55**(2),pp.214–226.
Karch, C.M. and Goate, A.M. 2015. Alzheimer's disease risk genes and mechanisms of disease pathogenesis. *Biological psychiatry*. **77**(1),pp.43–51.

Karran, E. *et al*. 2011. The amyloid cascade hypothesis for Alzheimer's disease: an appraisal for the development of therapeutics. *Nature reviews. Drug discovery*. **10**(9),pp.698–712.
Katou, H. *et al*. 2002. The role of disulfide bond in the amyloidogenic state of beta(2)-microglobulin studied by heteronuclear NMR. *Protein Science*. **11**(9),pp.2218–2229.
Kaufmann, R. *et al*. 2014. Super-Resolution Microscopy Using Standard Fluorescent Proteins in Intact Cells under Cryo-Conditions. *Nano Letters*. **14**(7),pp.4171–4175.
Kausche, G.A. *et al*. 1939. Die Sichtbarmachung von pflanzlichem Virus im Übermikroskop. *Naturwissenschaften*. **27**(18),pp.292–299.
Kawai-Noma, S. *et al*. 2010. In vivo evidence for the fibrillar structures of Sup35 prions in yeast cells. *The Journal of biophysical and biochemical cytology*. **190**(2),pp.223–231.
Kayed, R. *et al*. 2003. Common structure of soluble amyloid oligomers implies common mechanism of pathogenesis. *Science*. **300**(5618),pp.486–489.
Kayed, R. *et al*. 2007. Fibril specific, conformation dependent antibodies recognize a generic epitope common to amyloid fibrils and fibrillar oligomers that is absent in prefibrillar oligomers. *Molecular Neurodegeneration*. **2**(1),p.18.
Kegel, K.B. *et al*. 2000. Huntingtin expression stimulates endosomal-lysosomal activity, endosome tubulation, and autophagy. *The Journal of Neuroscience*. **20**(19),pp.7268–7278.
Kegulian, N.C. *et al*. 2015. Membrane Curvature-sensing and Curvature-inducing Activity of Islet Amyloid Polypeptide and Its Implications for Membrane Disruption. *The Journal of Biological Chemistry*. **290**(43),pp.25782–25793.
Knight, J.D. and Miranker, A.D. 2004. Phospholipid catalysis of diabetic amyloid assembly. *Journal of Molecular Biology*. **341**(5),pp.1175–1187.
Knott, G. and Genoud, C. 2013. Is EM dead? *Journal of Cell Science*. **126**(20),pp.4545–4552.
Knowles, T.P.J. *et al*. 2009. An analytical solution to the kinetics of breakable filament assembly. *Science (New York, N.Y.)*. **326**(5959),pp.1533–1537.
Knowles, T.P.J. *et al*. 2006. Spatial persistence of angular correlations in amyloid fibrils. *Physical review letters*. **96**(23),p.238301.
Knowles, T.P.J. *et al*. 2014. The amyloid state and its association with protein misfolding diseases. *Nature Reviews Molecular Cell Biology*. **15**(6),pp.384–396.
Kobayashi, T. *et al*. 1998. A lipid associated with the antiphospholipid syndrome regulates endosome structure and function. *Nature*. **392**(6672),pp.193–197.
Kobayashi, T. *et al*. 1999. Late endosomal membranes rich in lysobisphosphatidic acid regulate cholesterol transport. *Nature Cell Biology*. **1**(2),pp.113–118.
Kobayashi, T. *et al*. 2002. Separation and characterization of late endosomal membrane domains. *Journal of Biological Chemistry*. **277**(35),pp.32157–32164.
Korinek, A. *et al*. 2011. Computer controlled cryo-electron microscopy-TOM^2 a software package for high-throughput applications. *Journal of Structural Biology*. **175**(3),pp.394–405.
Krahn, P.M. *et al*. 1972. Stages in phage R17 infection: VI. Injection of a protein and RNA into the host cell. *Virology*. **47**(3),pp.628–637.
Kremer, J.R. *et al*. 1996. Computer visualization of three-dimensional image data using IMOD. *Journal of Structural Biology*. **116**(1),pp.71–76.
Kresojević, N. *et al*. 2014. Mutations in Niemann Pick type C gene are risk factor for Alzheimer's disease. *Medical hypotheses*. **83**(5),pp.559–562.
Kucukelbir, A. *et al*. 2014. Quantifying the local resolution of cryo-EM density maps. *Nature Methods*. **11**(1),pp.63–65.
Kuehlbrandt, W. 2014. The Resolution Revolution. *Science*. **343**(6178),pp.1443–1444.
Kukulski, W. *et al*. 2011. Correlated fluorescence and 3D electron microscopy with high sensitivity and spatial precision. *The Journal of Cell Biology*. **192**(1),pp.111–119.
Kukulski, W. *et al*. 2012. Plasma membrane reshaping during endocytosis is revealed by time-resolved electron tomography. *Cell*. **150**(3),pp.508–520.
la Rosa-Trevin, de, J.M. *et al*. 2013. Xmipp 3.0: An improved software suite for image processing in electron microscopy. *Journal of Structural Biology*. **184**(2),pp.321–328.
Labbadia, J. and Morimoto, R.I. 2015. The Biology of Proteostasis in Aging and Disease. *Annual Review of Biochemistry, Vol 84*. **84**(1),pp.435–464.
Ladd, M. *et al*. 2013. *Structure Determination by X-ray Crystallography*. Boston, MA: Springer US.
Ladner, C.L. *et al*. 2010. Stacked sets of parallel, in-register beta-strands of beta2-microglobulin in amyloid fibrils revealed by site-directed spin labeling and chemical labeling. *The Journal of Biological Chemistry*. **285**(22),pp.17137–17147.
Lai, A.Y. *et al*. 2014. scyllo-Inositol Promotes Robust Mutant Huntingtin Protein Degradation. *Journal of Biological Chemistry*. **289**(6),pp.3666–3676.
Larson, S.B. *et al*. 1998. Refined structure of satellite tobacco mosaic virus at 1.8 A resolution. *Journal of Molecular Biology*. **277**(1),pp.37–59.

Lashuel, H.A. and Lansbury, P.T. 2006. Are amyloid diseases caused by protein aggregates that mimic bacterial pore-forming toxins? *Quarterly Reviews of Biophysics*. **39**(2),pp.167–201.
Lashuel, H.A. *et al*. 2002. Alpha-synuclein, especially the Parkinson's disease-associated mutants, forms pore-like annular and tubular protofibrils. *Journal of Molecular Biology*. **322**(5),pp.1089–1102.
Lee, H.J. and Lee, S.J. 2002. Characterization of cytoplasmic alpha-synuclein aggregates - Fibril formation is tightly linked to the inclusion-forming process in cells. *Journal of Biological Chemistry*. **277**(50),pp.48976–48983.
Lee, H.J. *et al*. 2005. Intravesicular localization and exocytosis of alpha-synuclein and its aggregates. *The Journal of Neuroscience*. **25**(25),pp.6016–6024.
Lee, J. *et al*. 2011. Amyloid-beta forms fibrils by nucleated conformational conversion of oligomers. *Nature Chemical Biology*. **7**(9),pp.602–609.
Lee, S. *et al*. 2011. Lysosomal Proteolysis Inhibition Selectively Disrupts Axonal Transport of Degradative Organelles and Causes an Alzheimer's-Like Axonal Dystrophy. *The Journal of Neuroscience*. **31**(21),pp.7817–7830.
Lee, Y.H. *et al*. 2010. Subcellular fractionation methods and strategies for proteomics. *Proteomics*. **10**(22),pp.3935–3956.
Lesne, S. *et al*. 2006. A specific amyloid-beta protein assembly in the brain impairs memory. *Nature*. **440**(7082),pp.352–357.
Levy, E.D. *et al*. 2006. 3D complex: A structural classification of protein complexes. *Plos Computational Biology*. **2**(11),pp.1395–1406.
Leypoldt, J.K. *et al*. 2012. Clearance of middle molecules during haemodialysis and haemodiafiltration: new insights. *Nephrology, dialysis, transplantation* **27**(12),pp.4245–4247.
Li, X. *et al*. 2013. Electron counting and beam-induced motion correction enable near-atomic-resolution single-particle cryo-EM. *Nature Methods*. **10**(6),pp.584–590.
Li, Y. *et al*. 2015. Gaucher-Associated Parkinsonism. *Cellular and molecular neurobiology*. **35**(6),pp.755–761.
Liljas, L. 2004. The role of disordered segments in viral coat proteins. *Conformational proteomics of macromolecular architecture.*
Liljas, L. *et al*. 1994. Crystal structure of bacteriophage fr capsids at 3.5 A resolution. *Journal of Molecular Biology*. **244**(3),pp.279–290.
Liljeroos, L. *et al*. 2011. Electron cryotomography of measles virus reveals how matrix protein coats the ribonucleocapsid within intact virions. *Proceedings of the National Academy of Sciences*. **108**(44),pp.18085–18090.
Lima, S.M.B. *et al*. 2006. Dissecting the role of protein-protein and protein-nucleic acid interactions in MS2 bacteriophage stability. *FEBS Journal*. **273**(7),pp.1463–1475.
Lin, C.-Y. *et al*. 2007. Toxic human islet amyloid polypeptide (h-IAPP) oligomers are intracellular, and vaccination to induce anti-toxic oligomer antibodies does not prevent h-IAPP-induced beta-cell apoptosis in h-IAPP transgenic mice. *Diabetes*. **56**(5),pp.1324–1332.
Linke, R.P. *et al*. 1989. Lysine-specific cleavage of beta 2-microglobulin in amyloid deposits associated with hemodialysis. *Kidney International*. **36**(4),pp.675–681.
Linke, R.P. *et al*. 2000. Production of recombinant human beta2-microglobulin for scintigraphic diagnosis of amyloidosis in uremia and hemodialysis. *European journal of biochemistry- FEBS*. **267**(3),pp.627–633.
Liu, H. and Cheng, L. 2015. Cryo-EM shows the polymerase structures and a nonspooled genome within a dsRNA virus. *Science* . **349**(6254),pp.1347–1350.
Liu, M.L. and Hong, S.T. 2005. Early phase of amyloid beta42-induced cytotoxicity in neuronal cells is associated with vacuole formation and enhancement of exocytosis. *Experimental & molecular medicine*. **37**(6),pp.559–566.
Liu, R.-Q. *et al*. 2010. Membrane localization of beta-amyloid 1-42 in lysosomes: a possible mechanism for lysosome labilization. *The Journal of Biological Chemistry*. **285**(26),pp.19986–19996.
Long, S.C. *et al*. 2005. Assessment of sources and diversity of male-specific coliphages for source tracking. *Environmental Engineering Science*. **22**(3),pp.367–377.
Love, S. *et al*. 1995. Neurofibrillary Tangles in Niemann-Pick Disease Type-C. *Brain*. **118**,pp.119–129.
Low, H.H. *et al*. 2014. Structure of a type IV secretion system. *Nature*. **508**(7497),pp.550–553.
Ltic, S. *et al*. 2004. Alpha-synuclein is expressed in different tissues during human fetal development. *Journal of Molecular Neuroscience* **22**(3),pp.199–204.
Lu, P. *et al*. 2014. Three-dimensional structure of human gamma-secretase. *Nature*. **512**(7513),pp.166–.
Luci c, V. *et al*. 2005. Structural studies by electron tomography: from cells to molecules. *Annual*

Review of Biochemistry. **74**(1),pp.833–865.
Lue, L.F. *et al*. 1999. Soluble amyloid beta peptide concentration as a predictor of synaptic change in Alzheimer's disease. *The American Journal of Pathology*. **155**(3),pp.853–862.
Luk, K.C. *et al*. 2009. Exogenous alpha-synuclein fibrils seed the formation of Lewy body-like intracellular inclusions in cultured cells. *Proceedings of the National Academy of Sciences of the United States of America*. **106**(47),pp.20051–20056.
Lundmark, K. *et al*. 2003. Transmissibility of systemic amyloidosis by a prion-like mechanism. *Proceedings of the National Academy of Sciences*. **100**(6),pp.63013910–3542.
Luzio, J.P. *et al*. 2007. Lysosomes: fusion and function. *Nature Reviews Molecular Cell Biology*. **8**(8),pp.622–632.
Lüllmann-Rauch, R. 2005. History and Morphology of the Lysosome *In*: *Lysosomes*. Boston, MA: Springer US, pp. 1–16.
MacAskill, A.F. and Kittler, J.T. 2010. Control of mitochondrial transport and localization in neurons. *Trends in cell biology*. **20**(2),pp.102–112.
Maji, S.K. *et al*. 2009. Functional amyloids as natural storage of peptide hormones in pituitary secretory granules. *Science*. **325**(5938),pp.328–332.
Malnar, M. *et al*. 2014. Bidirectional links between Alzheimer's disease and Niemann-Pick type C disease. *Neurobiology of Disease*. **72**,pp.37–47.
Mansilla, M.C. *et al*. 2004. Control of membrane lipid fluidity by molecular thermosensors. *Journal of Bacteriology*. **186**(20),pp.6681–6688.
Mao, X.-Y. *et al*. 2010. Association between GBA L444P mutation and sporadic Parkinson's disease from Mainland China. *Neuroscience Letters*. **469**(2),pp.256–259.
Marko, M. *et al*. 2006. Focused ion beam milling of vitreous water: prospects for an alternative to cryo-ultramicrotomy of frozen-hydrated biological samples. *Journal of Microscopy*. **222**(1),pp.42–47.
Martin, C. 2006. The Physiology of Amylin and Insulin Maintaining the Balance Between Glucose Secretion and Glucose Uptake. *The Diabetes Educator*. **32**(Supplement 3),pp.101S–104S.
Mastico, R.A. *et al*. 1993. Multiple presentation of foreign peptides on the surface of an RNA-free spherical bacteriophage capsid. *Journal of General Virology*. **74 (Pt 4)**(4),pp.541–548.
Mastronarde, D.N. 2005. Automated electron microscope tomography using robust prediction of specimen movements. *Journal of Structural Biology*. **152**(1),pp.36–51.
Matsko, N. and Mueller, M. 2005. Epoxy resin as fixative during freeze-substitution. *Journal of Structural Biology*. **152**(2),pp.92–103.
Mazairac, A.H.A. *et al*. 2013. Effect of Hemodiafiltration on Quality of Life over Time. *Clinical journal of the American Society of Nephrology* **8**(1),pp.82–89.
Mazzulli, J.R. *et al*. 2011. Gaucher Disease Glucocerebrosidase and alpha-Synuclein Form a Bidirectional Pathogenic Loop in Synucleinopathies. *Cell*. **146**(1),pp.37–52.
McDonald, K.L. and Auer, M. 2006. High-pressure freezing, cellular tomography, and structural cell biology. *Biotechniques*. 41(2):137
McGough, A. *et al*. 1997. Cofilin changes the twist of F-actin: implications for actin filament dynamics and cellular function. *The Journal of biophysical and biochemical cytology*. **138**(4),pp.771–781.
McLaurin, J. *et al*. 2000. Inositol stereoisomers stabilize an oligomeric aggregate of Alzheimer amyloid beta peptide and inhibit abeta -induced toxicity. *Journal of Biological Chemistry*. **275**(24),pp.18495–18502.
McLean, C.A. *et al*. 1999. Soluble pool of Abeta amyloid as a determinant of severity of neurodegeneration in Alzheimer's disease. *Annals of neurology*. **46**(6),pp.860–866.
McMullan, G. *et al*. 2014. Comparison of optimal performance at 300 keV of three direct electron detectors for use in low dose electron microscopy. *Ultramicroscopy*. **147**,pp.156–163.
McMullan, G. *et al*. 2009. Experimental observation of the improvement in MTF from backthinning a CMOS direct electron detector. *Ultramicroscopy*. **109**(9),pp.1144–1147.
McNaught, K.S.P. *et al*. 2004. Systemic exposure to proteasome inhibitors causes a progressive model of Parkinson's disease. *Annals of Neurology*. **56**(1),pp.149–162.
McNeill, A. *et al*. 2012. A clinical and family history study of Parkinson's disease in heterozygous glucocerebrosidase mutation carriers. *Journal of Neurology, Neurosurgery & Psychiatry*. **83**(8),pp.853–854.
McParland, V.J. *et al*. 2000. Partially unfolded states of beta-2-microglobulin and amyloid formation in vitro. *Biochemistry*. **39**(30),pp.8735–8746.
Medeiros, R. *et al*. 2011. The Role of Tau in Alzheimer's Disease and Related Disorders. *CNS Neuroscience & Therapeutics*. **17**(5),pp.514–524.
Medintz, I.L. *et al*. 2005. Quantum dot bioconjugates for imaging, labelling and sensing. *Nature Materials*. **4**(6),pp.435–446.

Medway, C. and Morgan, K. 2014. Review: The genetics of Alzheimer's disease; putting flesh on the bones. *Neuropathology and Applied Neurobiology*. **40**(2),pp.97–105.
Mercado, G. *et al*. 2013. An ERcentric view of Parkinson's disease. *Trends in Molecular Medicine*. **19**(3),pp.165–175.
Meyer-Luehmann, M. *et al*. 2006. Exogenous induction of cerebral beta-amyloidogenesis is governed by agent and host. *Science*. **313**(5794),pp.1781–1784.
Milanesi, L. *et al*. 2012. Direct three-dimensional visualization of membrane disruption by amyloid fibrils. *Proceedings of the National Academy of Sciences*. **109**(50) pp.20455-20460
Milo, R. 2013. What is the total number of protein molecules per cell volume? A call to rethink some published values. *BioEssays news and reviews in molecular cellular and developmental biology*. **35**(12),pp.1050–1055.
Mindell, J.A. and Grigorieff, N. 2003. Accurate determination of local defocus and specimen tilt in electron microscopy. *Journal of Structural Biology*. **142**(3),pp.334–347.
Miyawaki, A. *et al*. 1997. Fluorescent indicators for Ca2+ based on green fluorescent proteins and calmodulin. *Nature*. **388**(6645),pp.882–887.
Moechars, D. *et al*. 1999. Early phenotypic changes in transgenic mice that overexpress different mutants of amyloid precursor protein in brain. *Journal of Biological Chemistry*. **274**(10),pp.6483–6492.
Monti, M. *et al*. 2005. Limited proteolysis in the investigation of beta2-microglobulin amyloidogenic and fibrillar states. *Biochimica et Biophysica Acta*. **1753**(1),pp.44–50.
Morita, S.-Y. and Terada, T. 2015. Enzymatic measurement of phosphatidylglycerol and cardiolipin in cultured cells and mitochondria. *Scientific reports*. **5**.
Morten, I.J. *et al*. 2007. Investigation into the role of macrophages in the formation and degradation of beta2-microglobulin amyloid fibrils. *The Journal of Biological Chemistry*. **282**(40),pp.29691–29700.
Mossuto, M.E. *et al*. 2011. Disulfide Bonds Reduce the Toxicity of the Amyloid Fibrils Formed by an Extracellular Protein. *Angewandte Chemie*. **50**(31),pp.7048–7051.
Mossuto, M.F. *et al*. 2010. The Non-Core Regions of Human Lysozyme Amyloid Fibrils Influence Cytotoxicity. *Journal of Molecular Biology*. **402**(5),pp.783–796.
Mougenot, A.-L. *et al*. 2011. Prion-like acceleration of a synucleinopathy in a transgenic mouse model. *Neurobiology of Aging*,pp.7–10.
Muench, S.P. *et al*. 2014. PA1b Inhibitor Binding to Subunits c and e of the Vacuolar ATPase Reveals Its Insecticidal Mechanism. *Journal Biological Chemistry*
Mukai, H. *et al*. 2005. Formation of morphologically similar globular aggregates from diverse aggregation-prone proteins in mammalian cells. *Proceedings of the National Academy of Sciences of the United States of America*. **102**(31),pp.10887–10892.
Mulders, H. 2003. *The use of a SEM/FIB dual beam applied to biological samples*. GIT Imaging Microscopy
Murata, K. *et al*. 2010. Zernike Phase Contrast Cryo-Electron Microscopy and Tomography for Structure Determination at Nanometer and Subnanometer Resolutions. *Structure*. **18**(8),pp.903–912.
Murshudov, G.N. *et al*. 1997. Refinement of macromolecular structures by the maximum-likelihood method. *Acta Crystallographica Section D: Biological Crystallography*. **53**(Pt 3),pp.240–255.
Müller, S. *et al*. 2013. Salt-dependent chemotaxis of macrophages. *PLoS ONE*. **8**(9),p.e73439.
Müller, W.G. *et al*. 2012. Towards an atlas of mammalian cell ultrastructure by cryo soft X-ray tomography. *Journal of Structural Biology*. **177**(2),pp.179–192.
Müller-Taubenberger, A. *et al*. 2001. Calreticulin and calnexin in the endoplasmic reticulum are important for phagocytosis. *The EMBO journal*. **20**(23),pp.6772–6782.
Myers, S.L. *et al*. 2006. A systematic study of the effect of physiological factors on beta 2-microglobulin amyloid formation at neutral pH. *Biochemistry*. **45**(7),pp.2311–2321.
Nagler, F.P. and Rake, G. 1948. The Use of the Electron Microscope in Diagnosis of Variola, Vaccinia, and Varicella. *Journal of Bacteriology*. **55**(1),pp.45–51.
Nalivaeva, N.N. and Turner, A.J. 2013. The amyloid precursor protein: A biochemical enigma in brain development, function and disease. *FEBS Letters*. **587**(13),pp.2046–2054.
Naslund, J. *et al*. 2000. Correlation between elevated levels of amyloid beta-peptide in the brain and cognitive decline. *Journal of the American Medical Association*. **283**(12),pp.1571–1577.
Necula, M. *et al*. 2003. Rapid anionic micelle-mediated alpha-synuclein fibrillization in vitro. *Journal of Biological Chemistry*. **278**(47),pp.46674–46680.
Nelson, R. *et al*. 2005. Structure of the cross-beta spine of amyloid-like fibrils. *Nature*. **435**(7043),pp.773–778.
Nesterov, E.E. *et al*. 2005. In vivo optical imaging of amyloid aggregates in brain: design of fluorescent markers. *Angewandte Chemie* . **44**(34),pp.5452–5456.

Nicastro, D. *et al*. 2006. The molecular architecture of axonemes revealed by cryoelectron tomography. *Science* . **313**(5789),pp.944–948.
Nilsson, M.R. 2004. Techniques to study amyloid fibril formation in vitro. *Methods*. **34**(1),pp.151–160.
Nixon, R.A. 2004. Niemann-Pick Type C disease and Alzheimer's disease: the APP-endosome connection fattens up. *The American Journal of Pathology*. **164**(3),pp.757–761.
Nixon, R.A. *et al*. 2005. Extensive involvement of autophagy in Alzheimer disease: An immuno-electron microscopy study. *Journal of Neuropathology and Experimental Neurology*. **64**(2),pp.113–122.
Nomura, S. *et al*. 2013. The E693Δ (Osaka) mutation in amyloid precursor protein potentiates cholesterol-mediated intracellular amyloid β toxicity via its impaired cholesterol efflux. *Journal of Neuroscience Research*. **91**(12),pp.1541–1550.
Novitskaya, V. *et al*. 2006. Amyloid fibrils of mammalian prion protein are highly toxic to cultured cells and primary neurons. *Journal of Biological Chemistry*. **281**(19),pp.13828–13836.
Nucifora, L.G. *et al*. 2012. Identification of Novel Potentially Toxic Oligomers Formed in Vitro from Mammalian-derived Expanded huntingtin Exon-1 Protein. *Journal of Biological Chemistry*. **287**(19),pp.16017–16028.
O'Nuallain, B. and Wetzel, R. 2002. Conformational Abs recognizing a generic amyloid fibril epitope. *Proceedings of the National Academy of Sciences of the United States of America*. **99**(3),pp.1485–1490.
O'Nuallain, B. *et al*. 2004. Seeding specificity in amyloid growth induced by heterologous fibrils. *Journal of Biological Chemistry*. **279**(17),pp.17490–17499.
Ohi, M. *et al*. 2004. Negative Staining and Image Classification - Powerful Tools in Modern Electron Microscopy. *Biological procedures online*. **6**,pp.23–34.
Olsthoorn, R. and Duin, J. 2011. *Bacteriophages with ssRNA*. Chichester, UK: John Wiley & Sons, Ltd.
Olzscha, H. *et al*. 2011. Amyloid-like aggregates sequester numerous metastable proteins with essential cellular functions. *Cell*. **144**(1),pp.67–78.
Ono, K. *et al*. 2003. Susceptibility of lysosomes to rupture is a determinant for plasma membrane disruption in tumor necrosis factor alpha-induced cell death. *Molecular and cellular biology*. **23**(2),pp.665–676.
Orlova, E.V. and Saibil, H.R. 2011. Structural Analysis of Macromolecular Assemblies by Electron Microscopy. *Chemical reviews*. **111**,pp.7710–7748.
Otsubo, S. *et al*. 2009. Characteristics of dialysis-related amyloidosis in patients on haemodialysis therapy for more than 30 years. *Nephrology, dialysis, transplantation* **24**(5),pp.1593–1598.
Paez-Segala, M.G. *et al*. 2015. Fixation-resistant photoactivatable fluorescent proteins for CLEM. *Nature Methods*. **12**(3),pp.215.
Parent, K.N. *et al*. 2014. Three-dimensional reconstructions of the bacteriophage CUS-3 virion reveal a conserved coat protein I-domain but a distinct tailspike receptor-binding domain. *Virology*. **464**,pp.55–66.
Park, S.-H. *et al*. 2013. PolyQ proteins interfere with nuclear degradation of cytosolic proteins by sequestering the Sis1p chaperone. *Cell*. **154**(1),pp.134–145.
Patel, A. *et al*. 2008. Intensive blood glucose control and vascular outcomes in patients with type 2 diabetes. *2572*.
Patwardhan, A. *et al*. 2014. A 3D cellular context for the macromolecular world. *Nature Structural & Molecular Biology*. **21**(10),pp.841–845.
Peccati, F. *et al*. 2015. Disaggregation-induced fluorescence enhancement of NIAD-4 for the optical imaging of amyloid-β fibrils. *Physical chemistry chemical physics* **17**(30),pp.19718–19725.
Pedelacq, J.D. *et al*. 2006. Engineering and characterization of a superfolder green fluorescent protein. *Nature Biotechnology*. **24**(1),pp.79–88.
Persson, M. *et al*. 2013. PRR1 coat protein binding to its RNA translational operator. *Acta Crystallographica Section D: Biological Crystallography*. **69**(Pt 3),pp.367–372.
Persson, M. *et al*. 2008. The Capsid of the Small RNA Phage PRR1 Is Stabilized by Metal Ions. *Journal of Molecular Biology*. **383**(4),pp.914–922.
Pertoft, H. 2000. Fractionation of cells and subcellular particles with Percoll. *Journal of biochemical and biophysical methods*. **44**(1-2),pp.1–30.
Peter Chien *et al*. 2004. Emerging principles of conformation-based prion interitance *Annual Reviews Biochemistry* **73**(1),pp.617–656.
Petersen, O.H. *et al*. 2005. Calcium signalling: Past, present and future. *Cell Calcium*. **38**(3-4),pp.161–169.
Petkova, A.T. *et al*. 2005. Self-propagating, molecular-level polymorphism in Alzheimer's beta-amyloid fibrils. *Science*. **307**(5707),pp.262–265.
Pettersen, E.F. *et al*. 2004. UCSF Chimera-a visualization system for exploratory research and

analysis. *Journal of Computational Chemistry*. **25**(13),pp.1605–1612.
Picone, P. *et al*. 2009. Abeta oligomers and fibrillar aggregates induce different apoptotic pathways in LAN5 neuroblastoma cell cultures. *Biophysical Journal*. **96**(10),pp.4200–4211.
Pieri, L. *et al*. 2012. Fibrillar α-synuclein and huntingtin exon 1 assemblies are toxic to the cells. *Biophysical Journal*. **102**(12),pp.2894–2905.
Pimenta de Castro, I. *et al*. 2012. Genetic analysis of mitochondrial protein misfolding in Drosophila melanogaster. *Cell Death and Differerentiation* **19**(8),pp.1308–1316.
Platt, G.W. and Radford, S.E. 2009. Glimpses of the molecular mechanisms of beta2-microglobulin fibril formation in vitro: aggregation on a complex energy landscape. *FEBS Letters*. **583**(16),pp.2623–2629.
Poirier, J. 2003. Apolipoprotein E and cholesterol metabolism in the pathogenesis and treatment of Alzheimer's disease. *Trends in Molecular Medicine*. **9**(3),pp.94–101.
Polishchuk, R.S. *et al*. 2000. Correlative light-electron microscopy reveals the tubular-saccular ultrastructure of carriers operating between Golgi apparatus and plasma membrane. *The Journal of Cell Biology*. **148**(1),pp.45–58.
Porter, K.R. *et al*. 1945. A study of tissue culture cells by celectron microscopy. *Journal of Experimental Medicine*,pp.233–246.
Porter, M. *et al*. 2011. Characterization of the Response of Primary Cells Relevant to Dialysis-Related Amyloidosis to beta-2-Microglobulin Monomer and Fibrils. *PLoS ONE*. **6**(11).
Pountney, D.L. *et al*. 2004. Annular alpha-synuclein species from purified multiple system atrophy inclusions. *Journal of neurochemistry*. **90**(2),pp.502–512.
Powers, E.T. *et al*. 2009. Biological and Chemical Approaches to Diseases of Proteostasis Deficiency. *Annual Reviews Biochemistry* **78**(1),pp.959–991.
Prince, M. *et al*. 2013. The global prevalence of dementia: A systematic review and metaanalysis. *Alzheimer's & Dementia*. **9**(1)pp.63–75.e2.
Prusiner, S.B. 2012. Cell biology. A unifying role for prions in neurodegenerative diseases. *Science* **336** (6088): 1511-1513
Prusiner, S.B. 1998. Prions. *Proceedings of the National Academy of Sciences of the United States of America*. **95**(23),pp.13363–13383.
Prusiner, S.B. *et al*. 2015. Evidence for α-synuclein prions causing multiple system atrophy in humans with parkinsonism. *Proceedings of the National Academy of Sciences*,p.201514475.
Puchtler, H. *et al*. 1962. On the Binding of Congo Red by Amyloid. *Journal of Histochemistry & Cytochemistry*. **10**(3),pp.355–364.
Qiang, W. *et al*. 2012. Antiparallel β-sheet architecture in Iowa-mutant β-amyloid fibrils. *Proceedings of the National Academy of Sciences*. **109**(12),pp.4443–4448.
Rabindranath, K.S. *et al*. 2006. *Haemodiafiltration, haemofiltration and haemodialysis for end-stage kidney disease* (K. S. Rabindranath, ed.). Chichester, UK: John Wiley & Sons, Ltd.
Rajendran, L. *et al*. 2006. Alzheimer's disease beta-amyloid peptides are released in association with exosomes. *Proceedings of the National Academy of Sciences of the United States of America*. **103**(30),pp.11172–11177.
Rasmussen, S.G.F. *et al*. 2011. Crystal structure of the β2 adrenergic receptor-Gs protein complex. *Nature*. **477**(7366),pp.549–555.
Ravikumar, B. *et al*. 2002. Aggregate-prone proteins with polyglutamine and polyalanine expansions are degraded by autophagy. *Human molecular genetics*. **11**(9),pp.1107–1117.
Rawson, S. *et al*. 2015. Structure of the Vacuolar H+-ATPase Rotary Motor Reveals New Mechanistic Insights. *Structure*. **23**(3),pp.461–471.
Reixach, N. *et al*. 2004. Tissue damage in the amyloidoses: Transthyretin monomers and nonnative oligomers are the major cytotoxic species in tissue culture. *Proceedings of the National Academy of Sciences of the United States of America*. **101**(9),pp.2817–2822.
Relini, A. *et al*. 2006. Collagen plays an active role in the aggregation of beta2-microglobulin under physiopathological conditions of dialysis-related amyloidosis. *The Journal of Biological Chemistry*. **281**(24),pp.16521–16529.
Ren, P.-H. *et al*. 2009. Cytoplasmic penetration and persistent infection of mammalian cells by polyglutamine aggregates. *Nature Cell Biology*. **11**(2),pp.219–225.
Reynaud, E. 2010. Protein misfolding and degenerative diseases. *Nat Education*
Riesner, D. 2003. Biochemistry and structure of PrP(C) and PrP(Sc). *British medical bulletin*. **66**(1),pp.21–33.
Rigacci, S. *et al*. 2008. The (1-63) region of the p53 transactivation domain aggregates in vitro into cytotoxic amyloid assemblies. *Biophysical Journal*. **94**(9),pp.3635–3646.
Rigort, A. and Plitzko, J.M. 2015. Cryo-focused-ion-beam applications in structural biology. *Archives of biochemistry and biophysics*. **581**,pp.122–130.
Rigort, A. *et al*. 2012. Integrative approaches for cellular cryo-electron tomography: correlative

imaging and focused ion beam micromachining. *Methods in cell biology*. **111**,pp.259–281.
Rigort, A. *et al*. 2010. Micromachining tools and correlative approaches for cellular cryo-electron tomography. *Journal of Structural Biology*. **172**(2),pp.169–179.
Risco, C. *et al*. 2012. Ways & Means Specific , Sensitive , High-Resolution Detection of Protein Molecules in Eukaryotic Cells Using Metal-Tagging Transmission Electron Microscopy. *Structure (London, England : 1993)*. **20**(5),pp.759–766.
Rivera, J.F. *et al*. 2011. Human-IAPP disrupts the autophagy/lysosomal pathway in pancreatic beta-cells: protective role of p62-positive cytoplasmic inclusions. *Cell Death Differ*. **18**(3),pp.415–426.
Robert C Piper, D.J.K. 2007. Biogenesis and Function of Multivesicular Bodies. *Annual review of cell and developmental biology*. **23**(1),pp.519–547.
Roberts, A.J. *et al*. 2009. AAA+ Ring and linker swing mechanism in the dynein motor. *Cell*. **136**(3),pp.485–495.
Roberts, J.W. and Steitz, J.E. 1967. The reconstitution of infective bacteriophage R17. *Proceedings of the National Academy of Sciences of the United States of America*. **58**(4),pp.1416–1421.
Rodriguez, J.A. *et al*. 2015. Structure of the toxic core of α-synuclein from invisible crystals. *Nature*.
Rohou, A. and Grigorieff, N. 2015. CTFFIND4: Fast and accurate defocus estimation from electron micrographs. *Journal of Structural Biology*. **192**(2),pp.216–221.
Rosenthal, P.B. and Henderson, R. 2003. Optimal determination of particle orientation, absolute hand, and contrast loss in single-particle electron cryomicroscopy. *Journal of Molecular Biology*. **333**(4),pp.721–745.
Rubinstein, J.L. and Brubaker, M.A. 2015. Alignment of cryo-EM movies of individual particles by optimization of image translations. *Journal of Structural Biology*.
Rubinsztein, D.C. *et al*. 2009. In search of an 'autophagomometer'. *Autophagy*. **5**(5),pp.585–589.
Rudnick, J. and Bruinsma, R. 2005. Icosahedral packing of RNA viral genomes. *Physical review letters*. **94**(3),p.038101.
Rugarli, E.I. and Langer, T. 2012. Mitochondrial quality control: a matter of life and death for neurons. *The EMBO journal*. **31**(6),pp.1336–1349.
Rumnieks, J. and Tars, K. 2014. Crystal Structure of the Bacteriophage Q beta Coat Protein in Complex with the RNA Operator of the Replicase Gene. *Journal of Molecular Biology*. **426**(5),pp.1039–1049.
Rumnieks, J. and Tars, K. 2011. Crystal structure of the read-through domain from bacteriophage Q beta A1 protein. *Protein Science*. **20**(10),pp.1707–1712.
Ruska, E. 1986. The Development of the Electron Microscope and of Electron Microscopy. *Nobel Lecture*.
Ruskin, R.S. *et al*. 2013. Quantitative characterization of electron detectors for transmission electron microscopy. *Journal of Structural Biology*. **184**(3),pp.385–393.
Russo, C.J. and Passmore, L.A. 2014. Electron microscopy. Ultrastable gold substrates for electron cryomicroscopy. *Science* **346**(6215),pp.1377–1380.
Rust, M.J. *et al*. 2006. Sub-diffraction-limit imaging by stochastic optical reconstruction microscopy (STORM). *Nature Methods*. **3**(10),pp.793–795.
S, F. *et al*. 2004. Levodopa and the progression of Parkinson's disease. *The New England Journal of Medicine*. **351**(24),pp.2498–2508.
Saftig, P. and Klumperman, J. 2009. Lysosome biogenesis and lysosomal membrane proteins: trafficking meets function. *Nature Reviews Molecular Cell Biology*. **10**(9),pp.623–635.
Saibil, H.R. *et al*. 2012. Heritable yeast prions have a highly organized three-dimensional architecture with interfiber structures. *Proceedings of the National Academy of Sciences*. **109**(37),pp.14906–14911.
Sancesario, G.M. and Bernardini, S. 2015. How many biomarkers to discriminate neurodegenerative dementia? *Critical reviews in clinical laboratory sciences*,pp.1–13.
Sarafian, T.A. *et al*. 2013. Impairment of Mitochondria in Adult Mouse Brain Overexpressing Predominantly Full-Length, N-Terminally Acetylated Human alpha-Synuclein D. J. Moore, ed. *PLoS ONE*. **8**(5).
Saravanan, B.C. *et al*. 2003. A rapid MTT colorimetric assay to assess the proliferative index of two Indian strains of Theileria annulata. *Veterinary Parasitology*. **113**(3-4),pp.211–216.
Sardiello, M. *et al*. 2009. A gene network regulating lysosomal biogenesis and function. *Science* **325**(5939),pp.473–477.
Sarell, C.J. *et al*. 2013. Expanding the Repertoire of Amyloid Polymorphs by Co-polymerization of Related Protein Precursors. *Journal of Biological Chemistry*. **288**(10),pp.7327–7337.
Sartori, A. *et al*. 2007. Correlative microscopy: bridging the gap between fluorescence light microscopy and cryo-electron tomography. *Journal of Structural Biology*. **160**(2),pp.135–145.
Sasahara, K. *et al*. 2013. Effects of membrane interaction and aggregation of amyloid beta-peptide

on lipid mobility and membrane domain structure. *Physical chemistry chemical physics*. **15**(23),pp.8929–8939.
Sawaya, M.R. *et al*. 2007. Atomic structures of amyloid cross-[bgr] spines reveal varied steric zippers. *Nature*. **447**(7143),pp.453–457.
Sánchez, L. *et al*. 2011. Aβ40 and Aβ42 Amyloid Fibrils Exhibit Distinct Molecular Recycling Properties. *Journal of the American Chemical Society*. **133**(17),pp.6505–6508.
Schaller, S. *et al*. 2015. The main cost drivers in dementia: a systematic review. *International Journal of Geriatric Psychiatry*. **30**(2),pp.111–129.
Schellenberger, P. *et al*. 2014. High-precision correlative fluorescence and electron cryo microscopy using two independent alignment markers. *Ultramicroscopy*. **143**,pp.41–51.
Scheres, S.H. 2014. Beam-induced motion correction for sub-megadalton cryo-EM particles W. Kuhlbrandt, ed. *eLife*. **3**,p.e03665.
Scheres, S.H.W. 2010. Classification of Structural Heterogeneity by Maximum-Likelihood Methods *In*: *Cryo-EM, Part B: 3-D Reconstruction*. Methods in Enzymology. Elsevier, pp. 295–320.
Scheres, S.H.W. 2012. RELION: implementation of a Bayesian approach to cryo-EM structure determination. *Journal of Structural Biology*. **180**(3),pp.519–530.
Scheres, S.H.W. 2015. Semi-automated selection of cryo-EM particles in RELION-1.3. *Journal of Structural Biology*. **189**(2),pp.114–122.
Scheres, S.H.W. and Chen, S. 2012. Prevention of overfitting in cryo-EM structure determination. *Nature Methods*. **9**(9),pp.853–854.
Scheres, S.H.W. *et al*. 2007. Disentangling conformational states of macromolecules in 3D-EM through likelihood optimization. *Nature Methods*. **4**(1),pp.27–29.
Schermelleh, L. *et al*. 2010. A guide to super-resolution fluorescence microscopy. *The Journal of Cell Biology*. **190**(2),pp.165–175.
Schertel, A. *et al*. 2013. Cryo FIB-SEM: volume imaging of cellular ultrastructure in native frozen specimens. *Journal of Structural Biology*. **184**(2),pp.355–360.
Schindelin, J. *et al*. 2012. Fiji: an open-source platform for biological-image analysis. *Nature Methods*. **9**(7),pp.676–682.
Schmidt, H. *et al*. 2009. Enrichment and analysis of secretory lysosomes from lymphocyte populations. *BMC immunology*. **10**,p.41.
Schneider, G. *et al*. 2012. Cryo X-ray microscope with flat sample geometry for correlative fluorescence and nanoscale tomographic imaging. *Journal of Structural Biology*. **177**(2),pp.212–223.
Schon, E.A. and Przedborski, S. 2011. Mitochondria: The Next (Neurode)Generation. *Neuron*. **70**(6),pp.1033–1053.
Schultz, M.L. *et al*. 2011. Clarifying lysosomal storage diseases. *Trends in Neurosciences*. **34**(8),pp.401–410.
Schur, F.K.M. *et al*. 2015. Structure of the immature HIV-1 capsid in intact virus particles at 8.8 angstrom resolution. *Nature*. **517**(7535),pp.505.
Schwartz, C.L. *et al*. 2007. Cryo-fluorescence microscopy facilitates correlations between light and cryo-electron microscopy and reduces the rate of photobleaching. *Journal of Microscopy-Oxford*. **227**(Pt 2),pp.98–109.
Selkoe, D.J. 2003. Folding proteins in fatal ways. *Nature*. **426**(6968),pp.900–904.
Sellinger, O.Z. *et al*. 1960. Tissue fractionation studies. 15. Intracellular distribution and properties of beta-N-acetylglucosaminidase and beta-galactosidase in rat liver. *The Biochemical journal*. **74**,pp.450–456.
Sengupta, P. *et al*. 2007. Lipid rafts, fluid/fluid phase separation, and their relevance to plasma membrane structure and function. *Seminars in cell & developmental biology*. **18**(5),pp.583–590.
Serpell, L. 2014. Amyloid structure. *Essays in biochemistry*. **56**,pp.1–10.
Serpell, L.C. and Smith, J.M. 2000. Direct visualisation of the beta-sheet structure of synthetic Alzheimer's amyloid. *Journal of Molecular Biology*. **299**(1),pp.225–231.
Settembre, C. *et al*. 2013. Signals from the lysosome: a control centre for cellular clearance and energy metabolism. *Nature Reviews Molecular Cell Biology*. **14**(5),pp.283–296.
Settembre, C. *et al*. 2007. Systemic inflammation and neurodegeneration in a mouse model of multiple sulfatase deficiency. *Proceedings of the National Academy of Sciences of the United States of America*. **104**(11),pp.4506–4511.
Settembre, C., Fraldi, A., Jahreiss, L., *et al*. 2008. A block of autophagy in lysosomal storage disorders. *Human molecular genetics*. **17**(1),pp.119–129.
Settembre, C., Fraldi, A., Rubinsztein, D.C., *et al*. 2008. Lysosomal storage diseases as disorders of autophagy. *Autophagy*. **4**(1),pp.113–114.
Shai, Y. 1999. Mechanism of the binding, insertion and destabilization of phospholipid bilayer membranes by alpha-helical antimicrobial and cell non-selective membrane-lytic peptides.

Biochimica Et Biophysica Acta-Molecular Cell Research. **1462**(1-2),pp.55–70.
Shaikh, T.R. *et al*. 2014. Initial bridges between two ribosomal subunits are formed within 9.4 milliseconds, as studied by time-resolved cryo-EM. *Proceedings of the National Academy of Sciences*. **111**(27),pp.9822–9827.
Shaikh, T.R. *et al*. 2008. SPIDER image processing for single-particle reconstruction of biological macromolecules from electron micrographs. *Nature protocols*. **3**(12),pp.1941–1974.
Shewmaker, F. *et al*. 2011. Structural Insights into Functional and Pathological Amyloid. *Journal of Biological Chemistry*.
Shi, D. *et al*. 2013. Three-dimensional electron crystallography of protein microcrystals *eLife*. **2**,p.e01345.
Shimanovich, U. *et al*. 2015. Protein Microgels from Amyloid Fibril Networks. *ACS Nano* **9**(1),pp.43–51.
Shimura, H. *et al*. 2000. Familial Parkinson disease gene product, parkin, is a ubiquitin-protein ligase. *Nature Genetics*. **25**(3),pp.302–305.
Shirahama, T. and Cohen, A.S. 1965. Structure of amyloid fibrils after negative staining and high-resolution electron microscopy. *Nature*. **206**(985),pp.737–738.
Shulman, J.M. *et al*. 2011. Parkinson's disease: genetics and pathogenesis. *Annual Review of Pathology*. **6**(October),pp.193–222.
Sidhu, S.S. *et al*. 2000. Phage display for selection of novel binding peptides. *Methods in enzymology*. **328**,pp.333–363.
Sidransky, E. and Lopez, G. 2012. The link between the GBA gene and parkinsonism. *Lancet Neurology*. **11**(11),pp.986–998.
Sidransky, E. *et al*. 2009. Multicenter analysis of glucocerebrosidase mutations in Parkinson's disease. *The New England Journal of Medicine*. **361**(17),pp.1651–1661.
Siemers, E.R. *et al*. 2015. Phase 3 solanezumab trials: Secondary outcomes in mild Alzheimer's disease patients. *Alzheimer's & dementia : the journal of the Alzheimer's Association*.
Sipe, J.D. and Cohen, A.S. 2000. Review: History of the Amyloid Fibril. *Journal of Structural Biology*. **130**(2-3),pp.88–98.
Sipe, J.D. *et al*. 2014. Nomenclature 2014: Amyloid fibril proteins and clinical classification of the amyloidosis. *Amyloid*. **21**(4),pp.221–224.
Smith, D.P. *et al*. 2003. A systematic investigation into the effect of protein destabilisation on beta 2-microglobulin amyloid formation. *Journal of Molecular Biology*. **330**(5),pp.943–954.
Sorzano, C.O.S. *et al*. 2009. Automatic particle selection from electron micrographs using machine learning techniques. *Journal of Structural Biology*. **167**(3),pp.252–260.
Soto, C. 2012. Transmissible Proteins: Expanding the Prion Heresy. *Cell*. **149**(5),pp.968–977.
Soura, V. *et al*. 2012. Visualization of co-localization in Abeta1-42-administered neuroblastoma cells reveals lysosome damage and autophagosome accumulation related to cell death. *The Biochemical journal*. **441**(2),pp.579–590.
Sparr, E. *et al*. 2004. Islet amyloid polypeptide-induced membrane leakage involves uptake of lipids by forming amyloid fibers. *FEBS Letters*. **577**(1-2),pp.117–120.
Stagg, S.M. *et al*. 2006. Automated cryoEM data acquisition and analysis of 284742 particles of GroEL. *Journal of Structural Biology*. **155**(3),pp.470–481.
Stefani, M. 2010. Biochemical and biophysical features of both oligomer/fibril and cell membrane in amyloid cytotoxicity. *The FEBS journal*. **277**(22),pp.4602–4613.
Stefani, M. and Dobson, C.M. 2003. Protein aggregation and aggregate toxicity: new insights into protein folding, misfolding diseases and biological evolution. *Journal of molecular medicine*. **81**(11),pp.678–699.
Stein, K.C. and True, H.L. 2014. Prion strains and amyloid polymorphism influence phenotypic variation. J. Heitman, ed. *PLoS Pathogens*. **10**(9),p.e1004328.
Stern, G. 2014. Niemann-Pick's and Gaucher's diseases. *Parkinsonism & related disorders*. **20** pp.S143–6.
Steven, A. and Belnap, D. 2005. Electron microscopy and image processing: an essential tool for structural analysis of macromolecules. *Current protocols in protein science editorial board John E Coligan et al*. **Chapter 17**,.Unit 17.2.
Stillwell, W. 2013. *An introduction to biological membranes: from bilayers to rafts*.
Stock-Ley, P.G. *et al*. 1994. Molecular mechanism of RNA phage morphogenesis. *International Journal of Biochemistry*. **26**(10-11),pp.1249–1260.
Stockert, J.C. *et al*. 2012. MTT assay for cell viability: Intracellular localization of the formazan product is in lipid droplets. *Acta histochemica*. **114**(8),pp.785–796.
Stockley, P.G. *et al*. 2007. A Simple, RNA-Mediated Allosteric Switch Controls the Pathway to Formation of a T=3 Viral Capsid. *Journal of Molecular Biology*. **369**(2),pp.541–552.
Stockley, P.G. *et al*. 1993. Molecular mechanism of RNA-phage morphogenesis. *Biochemical Society*

transactions. **21**(3),pp.627–633.
Stockley, P.G. *et al*. 2013. Packaging signals in single-stranded RNA viruses: nature's alternative to a purely electrostatic assembly mechanism. *Journal of Biological Physics*. **39**(2),pp.277–287.
Sui, H. *et al*. 2014. Artifact Correction for Zernike Phase-Plate Cryo-Electron Tomography. *Microscopy and microanalysis* **20**(S3),pp.234–235.
Sulakvelidze, A. 2013. Using lytic bacteriophages to eliminate or significantly reduce contamination of food by foodborne bacterial pathogens. *Journal of the Science of Food and Agriculture*. **93**(13),pp.3137–3146.
Sullivan, K.V. *et al*. 2013. Rapid Detection of Methicillin-Resistant Staphylococcus aureus (MRSA) and Methicillin-Susceptible Staphylococcus aureus (MSSA) Using the KeyPath MRSA/MSSA Blood Culture Test and the BacT/ALERT System in a Pediatric Population. *Archives of Pathology & Laboratory Medicine*. **137**(8),pp.1103–1105.
Suloway, C. *et al*. 2009. Fully automated, sequential tilt-series acquisition with Leginon. *Journal of Structural Biology*. **167**(1),pp.11–18.
Sunde, M. *et al*. 1997. Common core structure of amyloid fibrils by synchrotron X-ray diffraction. *Journal of Molecular Biology*. **273**(3),pp.729–739.
Ta, H.P. *et al*. 2012. A yeast toxic mutant of HET-s amyloid disrupts membrane integrity. *Biochimica et Biophysica Acta (BBA) - Biomembranes*. **1818**(9),pp.2325–2334.
Tang, G. *et al*. 2007. EMAN2: An extensible image processing suite for electron microscopy. *Journal of Structural Biology*. **157**(1),pp.38–46.
Tars, K. *et al*. 2000. Structure determination of bacteriophage PP7 from Pseudomonas aeroginosa: from poor data to a good map. *Acta Crystallographica Section D: Biological Crystallography*. **56**(Pt 4),pp.398–405.
Tars, K. *et al*. 1997. The crystal structure of bacteriophage GA and a comparison of bacteriophages belonging to the major groups of Escherichia coli leviviruses. *Journal of Molecular Biology*. **271**(5),pp.759–773.
Tipping, K.W., Karamanos, T.K., *et al*. 2015. pH-induced molecular shedding drives the formation of amyloid fibril-derived oligomers. *Proceedings of the National Academy of Sciences* p.201423174.
Tipping, K.W., van Oosten-Hawle, P., *et al*. 2015. Amyloid Fibres: Inert End-Stage Aggregates or Key Players in Disease? *Trends in Biochemical Sciences*. **40**(12) pp 719-727
Tivol, W.F. *et al*. 2008. An improved cryogen for plunge freezing. *Microscopy and microanalysis : the official journal of Microscopy Society of America, Microbeam Analysis Society, Microscopical Society of Canada*. **14**(5),pp.375–379.
Toropova, K. *et al*. 2008. The three-dimensional structure of genomic RNA in bacteriophage MS2: implications for assembly. *Journal of Molecular Biology*. **375**(3),pp.824–836.
Toropova, K. *et al*. 2011. Visualising a viral RNA genome poised for release from its receptor complex. *Journal of Molecular Biology*. **408**(3),pp.408–419.
Townsend, M. *et al*. 2006. Effects of secreted oligomers of amyloid beta-protein on hippocampal synaptic plasticity: a potent role for trimers. *Journal of Physiology-London*. **572**(2),pp.477–492.
Toyama, B.H. and Weissman, J.S. 2011. Amyloid Structure: Conformational Diversity and Consequences. *Annual Review of Biochemistry*. **80**(1),pp.557–585.
Trexler, A.J. and Rhoades, E. 2012. N-Terminal acetylation is critical for forming α-helical oligomer of α-synuclein. *Protein science : a publication of the Protein Society*. **21**(5),pp.601–605.
Trinh, C.H. *et al*. 2002. Crystal structure of monomeric human beta-2-microglobulin reveals clues to its amyloidogenic properties. *Proceedings of the National Academy of Sciences of the United States of America*. **99**(15),pp.9771–9776.
Trombetta, E.S. and Parodi, A.J. 2003. Quality control and protein folding in the secretory pathway. *Annual review of cell and developmental biology* **19**
Tsien, R.Y. 1998. The green fluorescent protein. *Annual Review of Biochemistry*. **67**,pp.509–544.
Tycko, R. 2015. Amyloid polymorphism: structural basis and neurobiological relevance. *Neuron*. **86**(3),pp.632–645.
Tycko, R. 2000. Solid-state NMR as a probe of amyloid fibril structure. *Current Opinion in Chemical Biology*. **4**(5),pp.500–506.
Umeda, T. *et al*. 2011. Intraneuronal amyloid β oligomers cause cell death via endoplasmic reticulum stress, endosomal/lysosomal leakage, and mitochondrial dysfunction in vivo. *Journal of Neuroscience Research*
Underwood, E. 2015. Alzheimer's amyloid theory gets modest boost. *Science* **349**(6247),pp.464–464.
Unverdorben, P. *et al*. 2014. Deep classification of a large cryo-EM dataset defines the conformational landscape of the 26S proteasome. *Proceedings of the National Academy of Sciences*. **111**(15),pp.5544–5549.

Uptain, S.M. and Lindquist, S. 2002. Prions as protein-based genetic elements. *Annual Review of Microbiology*. **56**,pp.703–741.
Valegard, K. *et al*. 1990. The three-dimensional structure of the bacterial virus MS2. *Nature*. **345**(6270),pp.36–41.
Valente, E.M. *et al*. 2004. Hereditary early-onset Parkinson's disease caused by mutations in PINK1. *Science (New York, N.Y.)*. **304**(5674),pp.1158–1160.
Valleix, S. *et al*. 2012. Hereditary systemic amyloidosis due to Asp76Asn variant β2-microglobulin. *The New England Journal of Medicine*. **366**(24),pp.2276–2283.
Van Cauwenberghe, C. *et al*. 2015. The genetic landscape of Alzheimer disease: clinical implications and perspectives. *Genetics in medicine* **117**
van den Worm, S. *et al*. 1998. Crystal structures of MS2 coat protein mutants in complex with wild-type RNA operator fragments. *Nucleic Acids Research*. **26**(5),pp.1345–1351.
Van Driel, L.F., Valentijn, J.A., Valentijn, K.M., Koning, R.I. and Koster, A.J. 2009. Tools for correlative cryo-fluorescence microscopy and cryo-electron tomography applied to whole mitochondria in human endothelial cells. *European Journal of Cell Biology*. **88**(11),pp.669–684.
van Heel, M. *et al*. 2000. Single-particle electron cryo-microscopy: towards atomic resolution. *Quarterly Reviews of Biophysics*. **33**(4),pp.307–369.
Van Meer, G. *et al*. 2008. Membrane lipids: where they are and how they behave. *Nature Reviews Molecular Cell Biology*. **9**(2),pp.112–124.
van Rijnsoever, C. *et al*. 2008. Correlative light-electron microscopy (CLEM) combining live-cell imaging and immunolabelling of ultrathin cryosections. *Nature Methods*. **5**(11),pp.973–980.
van Roessel, P. and Brand, A.H. 2002. Imaging into the future: visualizing gene expression and protein interactions with fluorescent proteins. *Nature Cell Biology*. **4**(1),pp.E15–20.
Vargas, K.J. *et al*. 2014. Synucleins regulate the kinetics of synaptic vesicle endocytosis. *The Journal of neuroscience* **34**(28),pp.9364–9376.
Varkey, J. *et al*. 2010. Membrane Curvature Induction and Tubulation Are Common Features of Synucleins and Apolipoproteins. *Journal of Biological Chemistry*. **285**(42),pp.32486–32493.
Vácha, R. *et al*. 2009. Molecular model of a cell plasma membrane with an asymmetric multicomponent composition: water permeation and ion effects. *Biophysical Journal*. **96**(11),pp.4493–4501.
Verdone, G. *et al*. 2002. The solution structure of human beta 2-microglobulin reveals the prodromes of its amyloid transition. *Protein Science*. **11**(3),pp.487–499.
Verma, M. *et al*. 2015. Toxic species in amyloid disorders: Oligomers or mature fibrils. *Annals of Indian Academy of Neurology*. **18**(2),pp.138–145.
Virok, D.P. *et al*. 2011. Protein Array Based Interactome Analysis of Amyloid-β Indicates an Inhibition of Protein Translation. *Journal of Proteome Research*. **10**(4),pp.1538–1547.
Visanji, N.P. *et al*. 2013. The prion hypothesis in Parkinson's disease: Braak to the future. *Acta neuropathologica communications*. **1**(1),p.2.
Vives-Bauza, C. and Przedborski, S. 2011. Mitophagy: the latest problem for Parkinson's disease. *Trends in Molecular Medicine*. **17**(3),pp.158–165.
Volkmann, N. 2002. A novel three-dimensional variant of the watershed transform for segmentation of electron density maps. *Journal of Structural Biology*. **138**(1-2),pp.123–129.
Volkmann, N. 2010. Methods for Segmentation and Interpretation of Electron Tomographic Reconstructions. *Methods in enzymology*. **483**,pp.31–46.
Voorhees, R.M. *et al*. 2014. Structure of the Mammalian Ribosome-Sec61 Complex to 3.4 angstrom Resolution. *Cell*. **157**(7),pp.1632–1643.
Wacker, J.L. *et al*. 2004. Hsp70 and Hsp40 attenuate formation of spherical and annular polyglutamine oligomers by partitioning monomer. *Nature Structural & Molecular Biology*. **11**(12),pp.1215–1222.
Walsh, D.M. *et al*. 2002. Naturally secreted oligomers of amyloid beta protein potently inhibit hippocampal long-term potentiation in vivo. *Nature*. **416**(6880),pp.535–539.
Walsh, P. *et al*. 2014. The mechanism of membrane disruption by cytotoxic amyloid oligomers formed by prion protein(106-126) is dependent on bilayer composition. *The Journal of Biological Chemistry*. **289**(15),pp.10419–10430.
Walther, P. and Ziegler, A. 2002. Freeze substitution of high-pressure frozen samples: the visibility of biological membranes is improved when the substitution medium contains water. *Journal of Microscopy-Oxford*. **208**(1),pp.3–10.
Wang, K. *et al*. 2012. 3D structure determination of native mammalian cells using cryo-FIB and cryo-electron tomography. *Journal of Structural Biology*. **180**(2),pp.318–326.
Wang, Q.J. *et al*. 2006. Induction of autophagy in axonal dystrophy and degeneration. *The Journal of neuroscience : the official journal of the Society for Neuroscience*. **26**(31),pp.8057–8068.
Wang, Y.A. *et al*. 2009. The Structure of F-Pili. *Journal of Molecular Biology*. **385**(1),pp.22–29.

Wasilewski, S. and Rosenthal, P.B. 2014. Web server for tilt-pair validation of single particle maps from electron cryomicroscopy. *Journal of Structural Biology*. **186**(1),pp.122–131.
Weiner, A.M. and Weber, K. 1973. A single UGA codon functions as a natural termination signal in the coliphage q beta coat protein cistron. *Journal of Molecular Biology*. **80**(4),pp.837–855.
Wessman, P. *et al*. 2008. Melittin-Lipid Bilayer Interactions and the Role of Cholesterol. *Biophysical Journal*. **95**(9),pp.4324–4336.
Westermark, G.T. *et al*. 1999. Staining methods for identification of amyloid in tissue. *Methods in enzymology*. **309**,pp.3–25.
White, H.D. *et al*. 2003. A second generation apparatus for time-resolved electron cryo-microscopy using stepper motors and electrospray. *Journal of Structural Biology*. **144**(1-2),pp.246–252.
White, H.E. *et al*. 2009. Globular Tetramers of beta-2-Microglobulin Assemble into Elaborate Amyloid Fibrils. *Journal of Molecular Biology*. **389**(1),pp.48–57.
White, J.A. *et al*. 2005. Differential effects of oligomeric and fibrillar amyloid-beta 1-42 on astrocyte-mediated inflammation. *Neurobiology of Disease*. **18**(3),pp.459–465.
Williams, A. *et al*. 2002. The cell biology of MHC class I antigen presentation. *Tissue Antigens*. **59**(1),pp.3–17.
Williams, D.B. and Carter, B.C. 1996. *Transmission Electron Microscopy- Basics I*. Springer.
Williams, D.B. and Carter, C.B. 2009. *Transmission Electron Microscopy*. Springer Science & Business Media.
Williams, T.L. *et al*. 2015. Europium as an inhibitor of Amyloid-β(1-42) induced membrane permeation. *FEBS Letters*. **589**(21),pp.3228–3236.
Wogulis, M. *et al*. 2005. Nucleation-dependent polymerization is an essential component of amyloid-mediated neuronal cell death. *The Journal of Neuroscience*. **25**(5),pp.1071–1080.
Wong, E. and Cuervo, A.M. 2010. Autophagy gone awry in neurodegenerative diseases. *Nature Neuroscience*. **13**(7),pp.805–811.
Wong, K.D. *et al*. 2004. Neuropathology provides clues to the pathophysiology of Gaucher disease. *Molecular Genetics and Metabolism*. **82**(3),pp.192–207.
Wood, S.J. *et al*. 1996. Seeding of A beta fibril formation is inhibited by all three isotypes of apolipoprotein E. *Biochemistry*. **35**(38),pp.12623–12628.
Wright, A. *et al*. 2009. A controlled clinical trial of a therapeutic bacteriophage preparation in chronic otitis due to antibiotic-resistant Pseudomonas aeruginosa; a preliminary report of efficacy. *Clinical Otolaryngology*. **34**(4),pp.349–357.
Wu, S. *et al*. 2012. Fabs enable single particle cryoEM studies of small proteins. *Structure* **20**(4),pp.582–592.
Xiong, Q. *et al*. 2009. CTF determination and correction for low dose tomographic tilt series. *Journal of Structural Biology*. **168**(3),pp.378–387.
Xue, W.-F. *et al*. 2009. Fibril Fragmentation Enhances Amyloid Cytotoxicity. *Journal of Biological Chemistry*. **284**(49),pp.34272–34282.
Xue, W.-F. *et al*. 2008. Systematic analysis of nucleation-dependent polymerization reveals new insights into the mechanism of amyloid self-assembly. *Proceedings of the National Academy of Sciences*. **105**(26),pp.8926–8931.
Yamamoto, S. *et al*. 2013. Dialysis-Related Amyloidosis: Pathogenesis and Clinical Features in Patients Undergoing Dialysis Treatment. ISBN 978-953-51-1100-9
Yamamoto, S. *et al*. 2009. Recent progress in understanding dialysis-related amyloidosis. *Bone*. **45 1**,pp.S39–S42.
Yamazaki, T. *et al*. 2001. Accumulation and aggregation of amyloid beta-protein in late endosomes of Niemann-Pick type C cells. *Journal of Biological Chemistry*. **276**(6),pp.4454–4460.
Yonetani, M. *et al*. 2009. Conversion of wild-type alpha-synuclein into mutant-type fibrils and its propagation in the presence of A30P mutant. *Journal of Biological Chemistry*. **284**(12),pp.7940–7950.
Yoshioka, C. *et al*. 2010. Cryomesh: a new substrate for cryo-electron microscopy. *Microscopy and microanalysis : the official journal of Microscopy Society of America, Microbeam Analysis Society, Microscopical Society of Canada*. **16**(1),pp.43–53.
Young-Pearse, T.L. *et al*. 2007. A critical function for beta-amyloid precursor protein in neuronal migration revealed by In Utero RNA interference. *The Journal of Neuroscience*. **27**(52),pp.14459–14469.
Zampagni, M. *et al*. 2011. A comparison of the biochemical modifications caused by toxic and non-toxic protein oligomers in cells. *Journal of Cellular and Molecular Medicine*. **15**(10),pp.2106–2116.
Zhang, W. *et al*. 2011. Soluble Aβ levels correlate with cognitive deficits in the 12-month-old APPswe/PS1dE9 mouse model of Alzheimer's disease. *Behavioural Brain Research*. **222**(2),pp.342–350.

Zhang, Y.J. *et al*. 2012. Intra-membrane oligomerization and extra-membrane oligomerization of amyloid-β peptide are competing processes as a result of distinct patterns of motif interplay. *The Journal of Biological Chemistry*. **287**(1),pp.748–756.

Zhang, Y.-W. *et al*. 2011. APP processing in Alzheimer's disease. *Molecular brain*. **4**(1),p.3.

Zhao, W.-Q. *et al*. 2010. Inhibition of Calcineurin-mediated Endocytosis and alpha-Amino-3-hydroxy-5-methyl-4-isoxazolepropionic Acid (AMPA) Receptors Prevents Amyloid beta Oligomer-induced Synaptic Disruption. *Journal of Biological Chemistry*. **285**(10),pp.7619–7632.

Zheng, S.Q. *et al*. 2010. Automated data collection for electron microscopic tomography. *Methods in enzymology*. **481**,pp.283–315.

Zlotnick, A. *et al*. 2000. Mechanism of Capsid Assembly for an Icosahedral Plant Virus. *Virology*. **277**(2),pp.450–456.

Zook, J.M. and Vreeland, W.N. 2010. Effects of temperature, acyl chain length, and flow-rate ratio on liposome formation and size in a microfluidic hydrodynamic focusing device. *Soft Matter*. **6**(6),pp.1352–1360.

8 Appendix

8.1 Appendix A

Over the course of this PhD, imaging of several other biological specimens have been imaged by cryo-EM, work forming part of several publications. Here, this work is detailed.

8.1.1 Cowpea mosaic virus

Cowpea mosaic virus (CPMV), is a member of the Comoviridae subfamily of the plant-infecting Secoviridae. It has a bipartite, positive-sense, single-stranded RNA genome. The two segments, RNA-1 (6kb) and RNA-2 (3.5kb) are encapsidated in separate virions. It forms icosahedral particles that have a maximum diameter of ~30 nm and are comprised of 60 copies each of a Large and Small coat protein. Large and Small coat proteins are processed from a single precursor polyprotein, processed by the action of the RNA-1-encoded 24K proteinase. Particles containing the two different genomic RNAs can readily be purified (CPMV bottom and CPMV middle), along with empty particles (CPMV top), named for the position they adopt . Additionally, empty virus like particles (eVLP) can be produced by the expression of the precursor of Large and Small subunits while co-expressing the viral proteinase to allow correct processing of the polyprotein, using an Agrobacterium-based, pEAQ vector system. The result is efficient release of mature coat protein subunits and large quantities of eVLPs.

Cryo-EM grids were prepared for CPMV bottom, middle and eVLP samples and data collected at the MRC LMB (CPMV bottom, eVLP) or NeCEN, Leiden (CPMV middle, CPMV top) on a Titan Krios microscope equipped with a Falcon II direct detector. Data was processed in RELION by Emma Hesketh. A 3.0 Å structure of the eVLP, 3.4 Å structure of CPMV bottom, and 4.0 Å structures of CPMV middle and top structures were obtained. These structures form part of;

- Emma L. Hesketh, Yulia Meshcheriakova, Kyle C. Dent, Pooja Saxena, **Rebecca F. Thompson**, Joseph J. Cockburn, George P. Lomonossoff & Neil A. Ranson 2015. Mechanisms of assembly and genome packaging in an RNA virus revealed by high-resolution cryo-EM. *Nature Communications* **6** p.10113.

8.1.2 BK Polyomavirus

BK polyomavirus is the causative agent of several diseases in transplant patients and the immunosuppressed. In order to better understand the structure and lifecycle of BK, infectious virions and VP1 only virus-like particles were produced in cell culture, and determined their three-dimensional structures using cryo-electron microscopy and single-particle image processing. The resulting 7.6 Å resolution structure of infections, wild type BK and 8.7 Å resolution of the VLP are the highest resolution cryo-EM structures of any polyomavirus to date. These structures confirm that the architecture of the major structural protein components of these human polyomaviruses are similar to previous structures from other hosts, but give new insight into the location and role of the enigmatic minor structural proteins, VP2 and VP3.
These structures form part of the following publications;

- Daniel L. Hurdiss, **Rebecca F. Thompson**, Ethan L. Morgan, Emma L. Prescott, Margarita M. Panou, Andrew Macdonald & Neil A. Ranson. 2015. New structural insights into the genome and minor capsid proteins of BK polyomavirus using cryo-electron microscopy. Under review, Structure.

8.1.3 Magnetopolymersomes

There is growing interest in functionalising vesicles with magnetic nanoparticles (MNPs), in order to help target therapeutics by localising them using magnetic fields. There is considerable interest in MNP embedded vehicles for nanomedicine, but their development is currently hindered by difficulties producing consistently monodisperse MNPs, and their reliable loading into vesicles. In this work, a tuneable, switchable magnetic delivery vehicle for nanomedical application was developed. These are comprised of tailored polymer vesicles (polymersomes) embedded with superparamagnetic magnetite MNPs (magnetopolymersomes). Cryo-ET was used to characterise the vesicles and their associated MNPs. Tomogram reconstruction enabled both the polymersome membrane ad the MNP, and showed there was no MNPs in the core of the vesicle.
This work forms part of the following publication;

- *In situ* formation of magnetopolymersomes via electroporation for MRI. 2015. Jennifer Bain, Lorena Ruiz-Pérez, Aneurin J. Kennerley, Stephen P. Muench, **Rebecca Thompson**, Giuseppe Battaglia & Sarah S. Staniland. Scientific Reports 5, Article number: 14311

8.2 Appendix B

On the accompanying CD;
This thesis;
Thesis.pdf
Chapter 4
Tilt series and tomograms from Percoll gradient, fraction 9;
Percoll-tilt1.mov
Percoll-tomo1.mov
Percoll-tilt2.mov
Percoll-tomo2.mov
Segmentation of tomogram containing membranes and amyloid fibrils;
Amira.mpg
Tomogram of Sh-SY5Y neuroblastoma cell;
Cell.mov
Soft-X ray microscope of RAW 264.7 cells exposed to Ls-f;
X-ray.mov
Appendix
Tomogram of Magnetopolymersomes;
Magnetosome.mov